



HAL
open science

Optical spectroscopy of heterostructures based on atomically-thin semiconductors

Étienne Lorchat

► **To cite this version:**

Étienne Lorchat. Optical spectroscopy of heterostructures based on atomically-thin semiconductors. Other [q-bio.OT]. Université de Strasbourg, 2019. English. NNT : 2019STRAE035 . tel-03169778

HAL Id: tel-03169778

<https://theses.hal.science/tel-03169778>

Submitted on 15 Mar 2021

HAL is a multi-disciplinary open access archive for the deposit and dissemination of scientific research documents, whether they are published or not. The documents may come from teaching and research institutions in France or abroad, or from public or private research centers.

L'archive ouverte pluridisciplinaire **HAL**, est destinée au dépôt et à la diffusion de documents scientifiques de niveau recherche, publiés ou non, émanant des établissements d'enseignement et de recherche français ou étrangers, des laboratoires publics ou privés.

ÉCOLE DOCTORALE DE PHYSIQUE, CHIMIE PHYSIQUE

Institut de Physique et Chimie des Matériaux de Strasbourg

THÈSE présentée par :

Etienne LORCHAT

soutenue le : 14 mai 2019

pour obtenir le grade de : **Docteur de l'université de Strasbourg**

Discipline/ Spécialité : Physique / Nanophysique

**Optical spectroscopy of heterostructures based
on atomically-thin semiconductors**

THÈSE dirigée par :

M. Stéphane BERCIAUD

Professeur, Université de Strasbourg

RAPPORTEURS :

Mme. Maria CHAMARRO

Professeur, Sorbonne Université

M. Clément FAUGERAS

Chargé de Recherche CNRS, LNCMI-Grenoble

AUTRES MEMBRES DU JURY :

M. Jérémie LEONARD

Chargé de Recherche CNRS, IPCMS

M. Guillaume CASSABOIS

Professeur, Université de Montpellier

M. Kirill BOLOTIN

Professeur, Freie Universität Berlin

1	Introduction	5
2	Selected properties of 2D Materials	11
2.1	Graphene	11
2.1.1	Electronic and optical properties	11
2.1.2	Optical absorption	12
2.2	Transition Metal Dichalcogenides	13
2.2.1	Band structure	13
2.2.2	Spin-orbit coupling, the band fine structure	14
2.2.3	Optical properties	16
2.2.3.1	Absorption	16
2.2.3.2	Emission	17
2.3	Phonons in 2D materials	18
2.3.1	Generalities	18
2.3.1.1	Phonons in graphene	18
2.3.1.2	Phonons in transition metal dichalcogenides	19
2.3.2	Introduction to Raman scattering	20
2.3.3	Raman spectroscopy of graphene	21
2.3.3.1	G-mode and 2D-mode	21
2.3.3.2	Theoretical modelling of the G-mode feature	21
2.3.3.3	Raman spectroscopy as a probe for local doping and strain	23
2.3.4	Raman spectroscopy of TMD	24
2.3.4.1	Layer number determination using Raman spectroscopy	24
2.3.4.2	Doping dependence of TMD Raman modes	24
2.3.4.3	Photodoping in TMD	25
2.4	Excitons in transition metal dichalcogenides	26
2.4.1	Introduction	26
2.4.1.1	Excitons Rydberg series	28
2.4.1.2	Binding energy measurement	29
2.4.1.3	Charged excitons (trions)	32
2.4.2	Excitons dynamics	33
2.4.2.1	Excitons formation	33
2.4.2.2	Excitons dynamics	33

2.4.2.3	Controlling exciton dynamics	36
2.4.2.4	Non linear effect: Auger recombination	36
2.4.3	Spin-valley locking and valley excitons	38
2.4.3.1	Selection rules	38
2.4.3.2	Valley polarization and coherence	40
2.4.4	Exciton pseudo-spin relaxation and decoherence	41
2.4.4.1	Rate equations for the exciton pseudo-spin relaxation	41
2.4.4.2	Rate equation for the exciton decoherence	43
2.4.4.3	State of the art	44
2.5	Van der Waals heterostructures	45
2.5.1	Introduction	45
2.5.2	Transition metal dichalcogenide hetero-bilayer	47
2.5.3	Transition metal dichalcogenide/Graphene heterostructure	48
2.6	Conclusion	53
3	Interlayer coupling in TMD/Graphene heterostructures	55
3.1	Introduction	55
3.2	Experimental approach	56
3.3	Photodoping	58
3.3.1	Evidencing photoinduced charge transfer in MoSe ₂ /Gr heterostructures	58
3.3.1.1	Photodoping in graphene	58
3.3.1.2	Photodoping in MoSe ₂	59
3.3.1.3	Reproducibility	60
3.3.2	Environmental and substrate induced effects	62
3.3.2.1	Measurement in ambient air vs in vacuum	62
3.3.2.2	Substrate effects	64
3.3.2.3	Photodoping in other TMD/Graphene heterostructures	67
3.3.3	Discussion	70
3.3.3.1	Results summary	70
3.3.3.2	Mechanism	72
3.3.4	Conclusion	73
3.4	Exciton dynamics in MoSe ₂ /graphene heterostructures	73
3.4.1	Room temperature exciton dynamics	74
3.4.2	Temperature dependence	76
3.4.2.1	SiO ₂ supported heterostructure	76
3.4.2.2	Encapsulated heterostructure	77
3.4.2.3	Temperature dependent PL intensity	78
3.4.3	Distance dependent exciton dynamics	79
3.4.4	Conclusion	80
3.5	Neutralizing a TMD monolayer with graphene	84
3.5.1	Room temperature hints of TMD neutralization	84
3.5.2	Characterization of MoSe ₂ /graphene PL emission	86

3.5.3	Doping homogeneity in MoSe ₂ /graphene heterostructure	87
3.5.4	Exciton and trion dynamics	91
3.5.5	Generalization to other TMD	92
3.6	Conclusion	93
4	Valley physics in TMD heterostructures	95
4.1	Valley Polarization and Coherence in TMD/Graphene van der Waals Heterostructures	97
4.1.1	Mueller algebra and Muller polarimetry	97
4.1.2	Valley contrast in heterostructures	100
4.1.3	Temperature dependence of valley contrast	104
4.1.4	Discussion	107
4.1.5	Conclusion	109
4.2	Chiral Coupling of Valley Excitons with Spin-Momentum Locked Surface Plasmons	110
4.2.1	Plasmonics in a nutshell	110
4.2.1.1	Surface plasmons	110
4.2.1.2	Plasmonic arrays	111
4.2.2	Geometrical phase in plasmonic array	112
4.2.3	Chiral coupling in a WS ₂ /plasmonic array heterostructure	113
4.2.4	Discussion	116
4.3	Conclusion	119
5	Conclusion and perspectives	121
6	Résumé détaillé	125
A	Building van der Waals heterostructure	143
A.1	Exfoliation	143
A.1.1	Graphene and Boron Nitride	143
A.1.2	Transition Metal Dichalcogenides	144
A.2	Van der Waals heterostructure assembly	145
A.2.1	Recipe for the Polycarbonate stamp	145
A.2.2	The transfer station	146
A.2.3	Pick up	147
B	Setup	149
B.1	Optical measurements at IPCMS, a versatile system	149
B.1.1	Excitation	150
B.1.2	Microscopy	151
B.1.2.1	Measurements in ambient condition	151
B.1.2.2	Measurements in vacuum at variable temperature	151
B.1.3	Detection	152
B.1.3.1	Spectrometer	152
B.1.3.2	Grating	152

B.1.4	Hyperspectral mapping	153
B.1.4.1	Data processing	153
B.2	Angle resolved polarimetric setup at ISIS	154
B.3	Time resolved Photo Luminescence at LPCNO	154
B.3.1	Streak camera	155
C	Samples list	157

1

Layered materials, such as graphite, are composed of bi-dimensional (2D) layers of atoms covalently bound, stack on top of each other and hold by van der Waals interaction. Being able to isolate one of these 2D layer has been a challenge ever since we understand the crystalline structure of those layered compounds. Bottom-up and top-down approaches have been tried to reach this goal. The bottom-up approach consists of combining molecular precursor together to finally get the 2D crystalline layer. One of these techniques is the Chemical Vapour Deposition (CVD) growth, in which methane molecules are decomposed into carbon and hydrogen at high temperature. Carbon atoms then precipitate on a copper surface to form the 2D graphite layer called graphene. In contrary, the top-down approach starts from a bulk layered compound that is then peeled off "layer by layer" to obtain the monolayer compound. Even though such an approach seems tedious, it is universal and works for any layered compound. This technique has been successfully applied to a wide range of layered compound such as graphite, boron nitride and transition metal dichalcogenide [1], using tape to peel bulk crystals off. This has been a major breakthrough that lead to Geim and Novoselov's Nobel prize in 2010.

Bulk layered materials have been extensively studied and people already knew which type of materials they can isolate (Fig. 1.1). 2D materials can be insulator such as hexagonal boron nitride, semimetal like graphene (Gr), semiconductor as a subset of transition metal dichalcogenide (TMD) (Fig. 1.1). Moreover, they could also be superconductor or metallic. 2D materials are therefore a great tool kit that allows people to study the effect of strong vertical confinement on such physical properties.

In addition, TMD are subject to polytypism, for instance semiconducting hexagonal (2H) MoTe_2 becomes metallic when its crystalline structure becomes distorted octahedral (1T'). Interestingly, MoTe_2 can be switched from one structure to the other, which brings us to the main interest of the 2D materials, their tunability. Graphene electrical and optical properties can be tuned by an electrical field and MoS_2 undergoes an electrical field induced superconducting transition. Since those systems are 2D electron gas directly in contact with their environment, changing the latter will modify material physical properties. In addition, most of 2D materials can sustain quite strong strain.

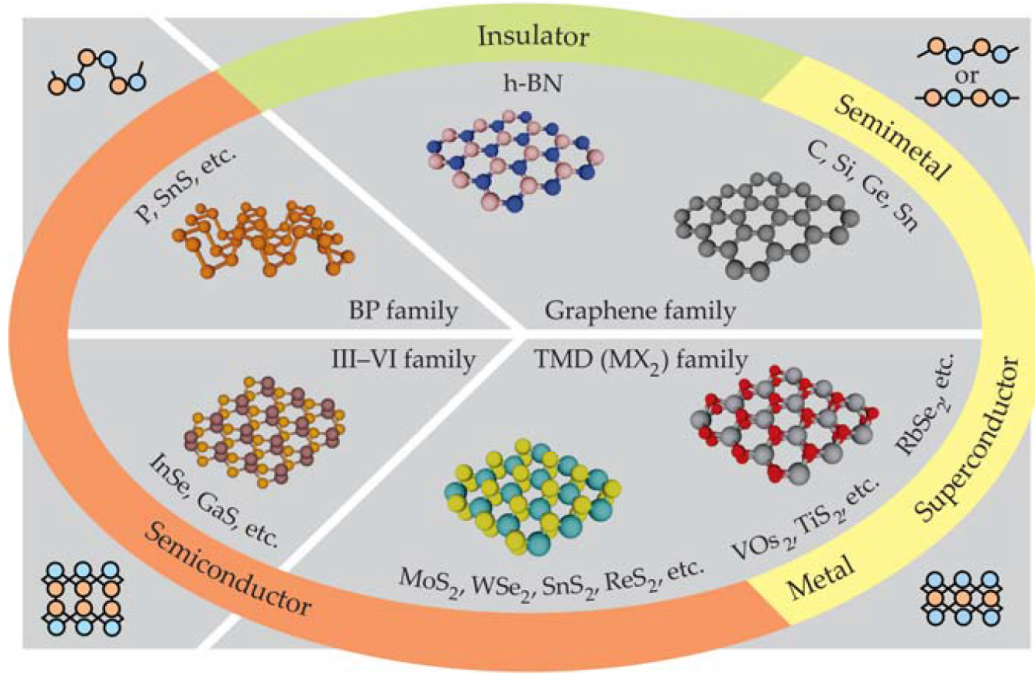


Figure 1.1: Adapted from[2].

History of 2D materials

In 2010, Mak and co-workers exfoliated a MoS_2 monolayer and demonstrated that it is a direct gap semiconductor [3]. Even though its multilayer structure is a semiconductor. The intense Lorentzian Photo-Luminescence (PL) peak displayed by the MoS_2 monolayer indicated an excitonic nature the emission and room temperature stable excitons. However, the presence of excitons has been demonstrated experimentally only in 2014 [4] with the observation of the excitonic Rydberg series, proof of the excitonic nature of the PL emission in TMD. In addition, for excitons to be stable at room temperature, their binding energy have to be larger than $k_b T$ (30 meV). Even though the exact binding energy of TMD excitons remains a partially opened question, recent work brings valuable information in this topic using magneto-PL measurement [5].

The strong spin-orbit coupling alongside with the TMD crystal symmetry properties lead to the splitting of the spin sub band in TMD. This splitting gives the TMD the ability to emit PL with the same polarization as the excitation light. This effect has been both theoretically predicted and experimentally observed in 2012 [6, 7]. Moreover, the band splitting gives rise to a complex excitonic manifold with different optical selection rules for different excitons. To observe this complex manifold, one needs narrow emission peak and clean optical signature from the TMD. However, such high quality optical response from TMD have been obtained only recently in BN capped TMD samples. This approach has been developed by Cadiz and co-workers [8]. Finally, in such system, people have been able, in 2017, to find optical signature of the dark exciton which can actually couple to an electric field perpendicular to the TMD plane [9–11]. Interestingly, these three groups use three different methods to brighten the dark exciton. In [10], the authors make

use of an in plane magnetic field to couple bright and dark exciton leading to the detection of PL coming from the dark exciton. In [11], the dark exciton is coupled in the near field to a surface plasmon that is then decoupled into the far field using a scatterer into the metallic film. Lastly, in [9] the authors bring an electric field perpendicular to the sample by using a side excitation instead of the usual normal excitation.

Another key feature of the excitons is their lifetime. Even if their room temperature lifetime is long and therefore easy to measure, it has been tricky to get their intrinsic radiative lifetime. It has been done in 2016 [12] and the authors report a 1.8 ps radiative lifetime for MoSe₂. Finally, the TMD optical properties have been well characterized and one of the biggest question that remains open is the exciton creation mechanism.

One of the strength of 2D materials is their lack of out of plane dangling bonds. This allows us to stack various 2D materials together to form the so called van der Waals heterostructure. Technique that provides sharp and atomically clean interfaces between different materials have been reported in 2014 [13], attracting a lot of interest. Giving the large variety of physical properties of those materials, van der Waals heterostructures are an interesting playground. Several devices have been demonstrated using van der Waals heterostructure. In 2014, a photodetector based on MoS₂/graphene heterostructure has been achieved [14]. They demonstrated a photogating effect even at low photon flux. In 2016, another photodetector has been demonstrated with a picosecond time response consisting of a TMD slab (from 100 nm to one monolayer) sandwich between two graphene layers [15]. In the monolayer case, a strong quenching of the PL emission has been recorded showing the strong interaction between the TMD monolayer and the graphene. However, this interaction has not been characterized yet.

Furthermore, strong light matter coupling has been demonstrated between a Fabry-Pérot cavity and a MoS₂ monolayer in 2015 [16]. This brings the attention of the nano-photonic community on 2D materials. In 2017 strongly-coupled WS₂ monolayer displays valley polarized excitation up to room temperature even though those properties were vanishing above 200 K for monolayers. People then started to use TMD multilayer as chiral emitters to study directional coupling between chiral optical mode and chiral TMD excitation [17]. The same kind of directional coupling has been demonstrated just before using a WS₂ monolayer [18].

Finally, in ten years, TMD photophysics has been extensively studied. Even though a few questions remain on the exciton formation mechanism, the exciton radiative lifetime has been measured, their binding energy has been characterized and the exciton manifold has been unveiled. Optical control of the exciton valley number has been demonstrated. However, protecting these properties up to room temperature is still a challenge which has been partially overcome only within the strong coupling regime. But if the coupling with a cavity is not an option, getting room temperature valley polarized exciton remains a challenge.

With the rise of van der Waals heterostructures, many devices have been demonstrated and most of them use graphene as an electrode either to contact TMD slabs or as backgate [28].

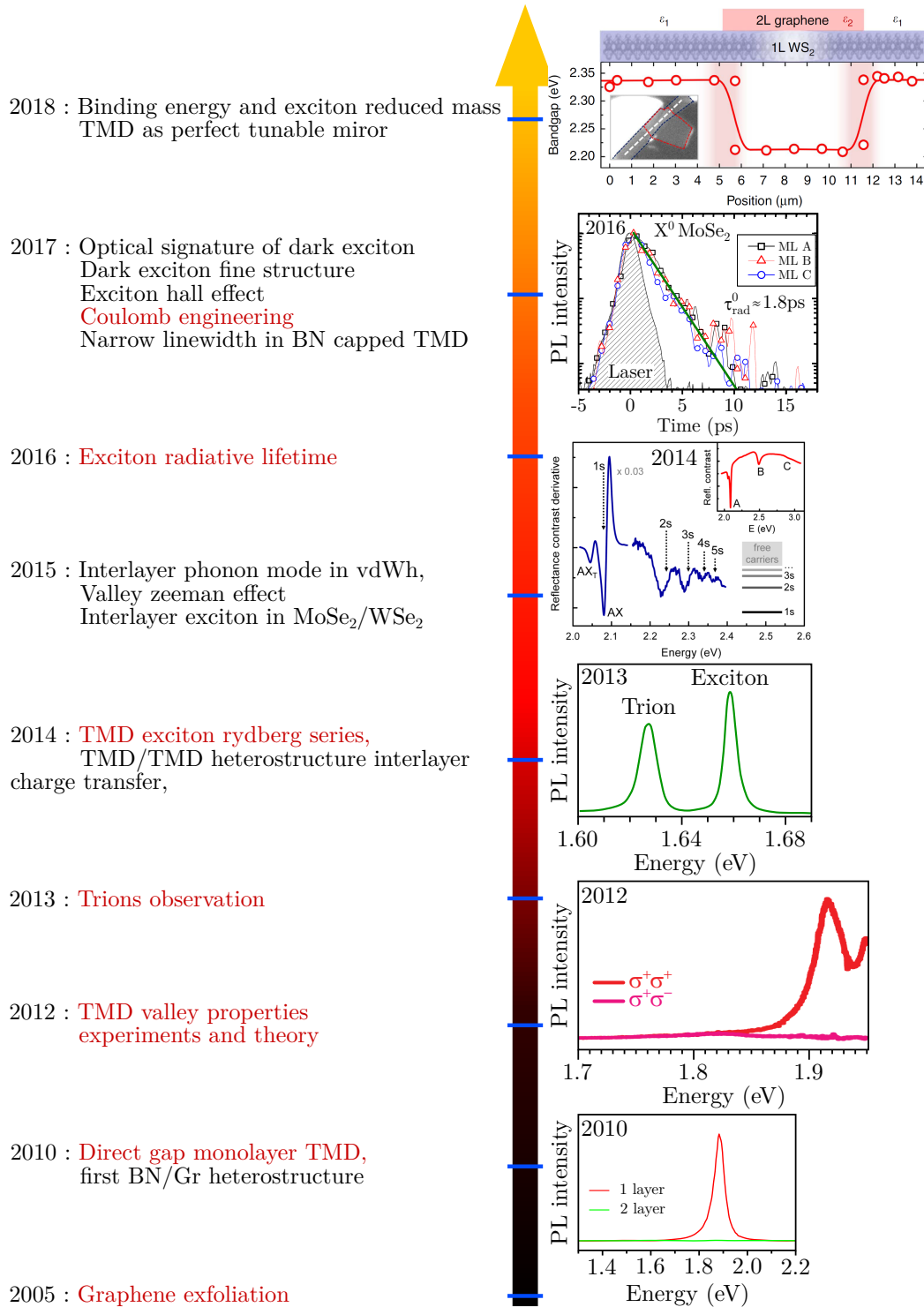


Figure 1.2: Timeline and landmarks paper in the 2D material research focused on spectroscopy. The most important paper for this work are highlighted in red and illustrated on the right side. From bottom to top, topics have been covered in those references: 2005 [1], 2010 [3, 19], 2012 [6, 7], 2013 [20], 2014 [4, 21], 2015 [22–24], 2016 [12], 2017 [8, 9, 25–27], 2018 [5, 28].

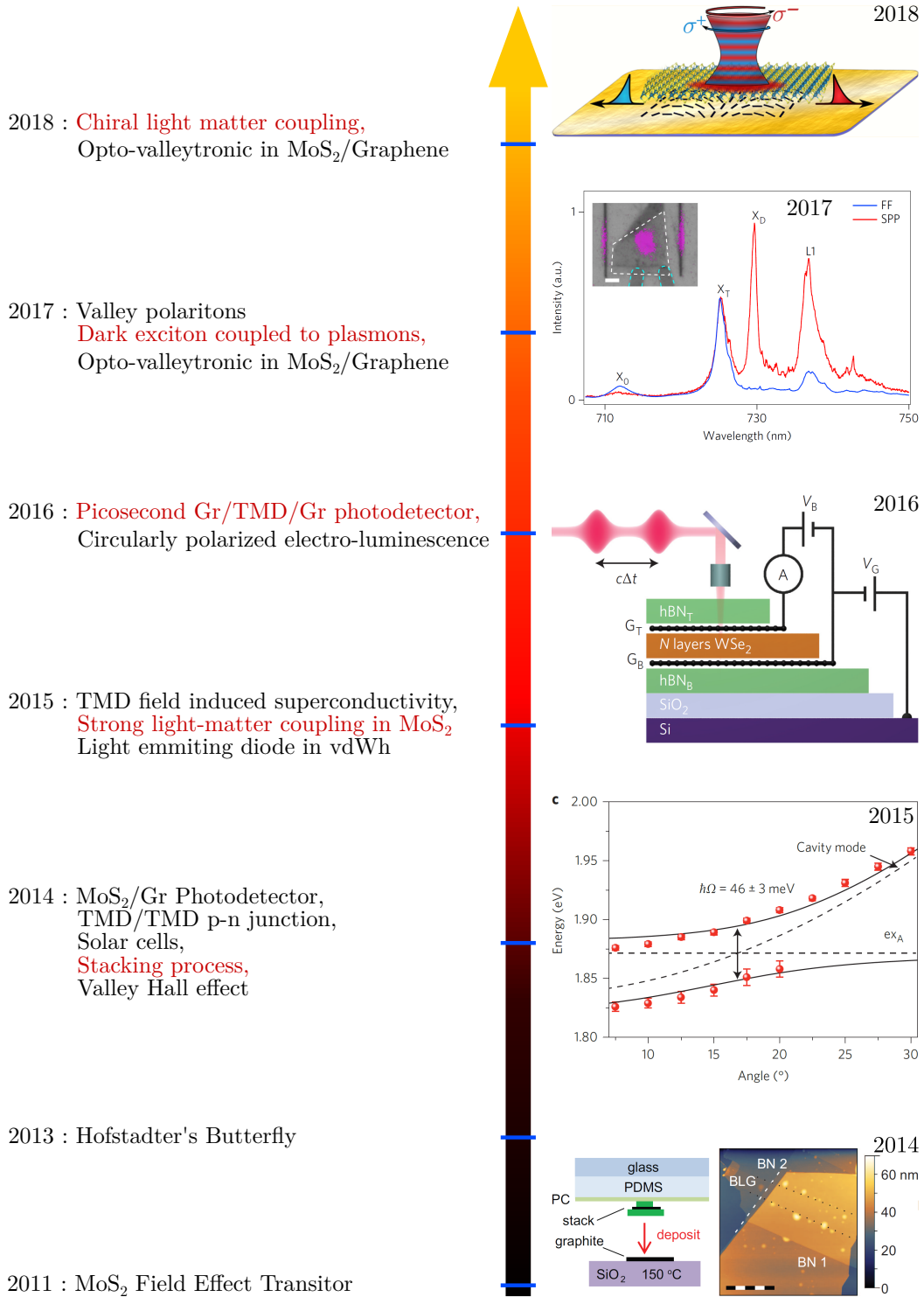


Figure 1.3: Timeline and landmarks paper in the 2D material research focused on devices and nano-photonics. The most important paper for this work are highlighted in red and illustrated on the right side. From bottom to top, topics have been covered in those references: 2011 [29], 2013 [30], 2014 [13, 14, 31–33], 2015 [16, 34, 35], 2016 [15, 36], 2017 [11, 37, 38] 2018 [18].

However, the interaction between TMD and graphene has not been well characterized yet.

Manuscript organization

Most of devices based on 2D materials rely on the interaction between the different materials.

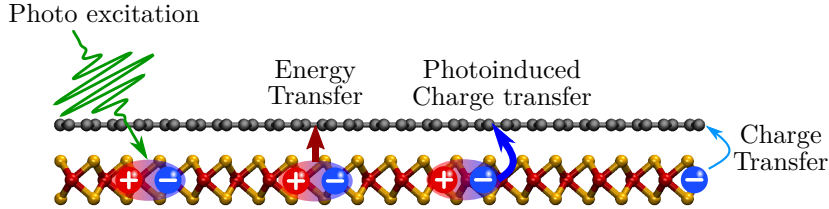


Figure 1.4: *Different interlayer interactions in TMD/graphene heterostructure.*

However, such interactions are poorly characterized and very little is known about them. In the following we will focus on the monolayer TMD/monolayer graphene heterostructure. The different interactions between 2D materials are mainly interlayer energy transfer, interlayer photoinduced charge transfer or charge transfer from the TMD to the graphene presented in (Fig. 1.4). Each of these interactions are present but their relative amplitude remains unknown.

Chapter 2 introduces the physical properties of graphene and TMD that are relevant in our work. We will also introduce in this chapter the doping measurement protocol we have followed to characterize graphene Fermi energy based on Raman spectroscopy.

Chapter 3 is focusing on the interlayer interactions in the monolayer TMD/monolayer graphene heterostructure. We carried out photoluminescence as well as Raman spectroscopy measurements to unveil and characterize a photoinduced net charge transfer from TMD to graphene. To better understand the interlayer energy transfer, we measure the TMD exciton dynamics in TMD/graphene heterostructure. Finally, we will monitor the TMD native doping in such structure.

Chapter 4 is dealing with the TMD/graphene heterostructure valley properties using a comprehensive polarimetric setup: the Mueller matrix measurement. We will also show that exciton valley properties can be protected by coupling the TMD layer to a plasmonic cavity. In this system we show evidence of spin momentum lock PL emission from the TMD.

Chapter 5 brings the conclusion and some perspective to this work.

2

2.1 Graphene

2.1.1 Electronic and optical properties

Graphene is a 2D crystal made of sp^2 hybridized carbon atoms meaning that each carbon atom will form three localized σ -bonds and one delocalized π -bond. The carbon atoms σ -bonds are arranged in a honeycomb lattice with two inequivalent sites, namely S_A and S_B (Fig. 2.1 a) and therefore 2 atoms per unit cell. At the corner of the Brillouin zone (Fig. 2.1 b), the so called $\pm K$, the conduction band and the valence band touch each other on one single point giving to graphene a semi-metallic character. The cone-shaped dispersion relation at the K points gives several interesting properties to graphene (Fig. 2.1 c). First, at the K point, graphene electron mass goes to zero giving them relativistic properties. Second, electrons in graphene are fast, up to one percent of the speed of light and have huge mobility, up to $200\,000\text{ cm}^2 \cdot \text{V}^{-1} \cdot \text{s}^{-1}$ at room temperature [39].

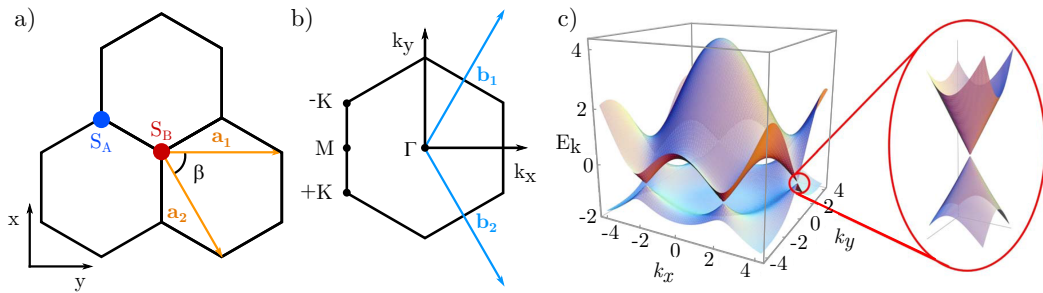


Figure 2.1: a) Real space sketch of the graphene lattice with A and B inequivalent sites. a_1 and a_2 are the real space lattice vectors. b) Reciprocal lattice, with the $\pm K$, M and Γ high symmetry point and its lattice vectors b_1 and b_2 . c) Electronic dispersion relation of graphene. Adapted from [39].

Electronic properties are determined by the band structure and the Fermi level. Due to the cone shape of the electronic dispersion and the absence of gap at K , it is therefore easy to tune graphene electronic properties via electric field effect (Fig. 2.2 a). Since optical properties

depend on the electronic properties, graphene optical properties are also gate tunable (Fig. 2.2 b).

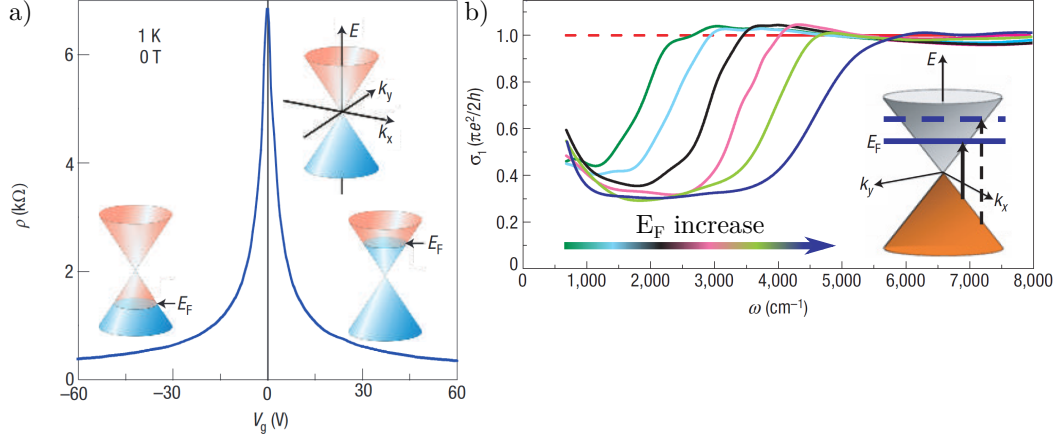


Figure 2.2: a) Gate dependent graphene channel resistance adapted from [40]. b) Graphene optical conductivity with respect to the incident photon wave-number. Increasing graphene Fermi level forbid some interband transitions adapted from [41].

2.1.2 Optical absorption

Optical absorption in graphene is mainly due to interband and intraband transitions. However, for photon energy above 50 meV, interband transitions are the dominant absorption processes, for momentum conservation reasons. This optical absorption is mediated by in plane electrical dipole excitation.

Optical absorption coefficient is defined by the incident power over absorbed power ratio. The incident power for a normal incidence is given by $W_i = c |\Theta|^2 / 4\pi$ with $\vec{\theta}$ the electric field. Moreover, the absorbed power can be written as $W_a = \eta \hbar \omega$ with η the photon absorption rate. η can be calculated with Fermi golden rule, $\eta = (2\pi/\hbar) |M|^2 D$ with M the matrix element of the 2D Dirac electron light matter interaction Hamiltonian [39, 42] and D the density of state for graphene. The density of state in graphene can be written as $D = \hbar\omega / \pi \hbar^2 v_F^2$. Finally the matrix element M can be written as

$$|M|^2 = \frac{|\Theta|^2 e^2 v_F^2}{8\omega^2} \quad (2.1)$$

We can now express the absorbed power W_a as

$$W_a = \frac{2\pi}{\hbar} \frac{|\Theta|^2 e^2 v_F^2}{8\omega^2} \frac{\hbar\omega}{\pi \hbar^2 v_F^2} \hbar\omega = \frac{e^2}{4\hbar} |\Theta|^2 \quad (2.2)$$

$$\mathcal{A} = \frac{W_a}{W_i} = \frac{e^2 |\Theta|^2}{4\hbar} \frac{4\pi}{c |\Theta|^2} = \pi\alpha \approx 2.3\% \quad (2.3)$$

with α the fine structure constant. In first approximation, graphene absorbs 2.3% (Fig. 2.2 b) of the incoming light in this MIR to UV range but this is actually qualitatively valid only from near infra-red to optical wavelength. The low graphene absorption combined with its high conductivity, makes it an interesting gate or contact electrode especially for other 2D materials because it can make ohmic contact with them [43]. It is worth mentioning that nowadays, the 2D materials community tends to use graphite back gate instead of the usual silicon gate electrode defined by the substrate because the former is more efficient than the latter[44]. In addition, such graphite back gates can be easily insert in a van der Waals heterostructures.

2.2 Transition Metal Dichalcogenides

Transition Metal Dichalcogenide (TMD) is a vast materials family with various crystalline structures and physical properties. Those materials present mostly an hexagonal (2H), octahedral (1T) or distorted octahedral (1T') crystalline phase. Some of those materials (e.g. MoS₂ ...) can undergo a chemically induced phase transition from 2H to 1T which also changes their semiconductor character to a metallic one. This allows to make low resistance contacts [45]

On the electronic point of view, they can be metallic such as NbS₂ or semiconductor as 2H MoSe₂. They could present superconductivity (NbSe₂) at low temperature, charge density wave (TaSe₂)... 2D materials have many different properties and are definitely an interesting playground for a physicist. In addition, all those materials could be exfoliated down to the monolayer; inducing a strong vertical confinement in all those systems.

Giving the wide range of physical phenomenon present in TMD, we will focus on a particular set of TMD: the 2H semiconductors especially MoS₂, MoSe₂, MoTe₂, WS₂ and WSe₂. We choose them because they are all semiconductors with a rich photophysics that we will detail in the following.

2.2.1 Band structure

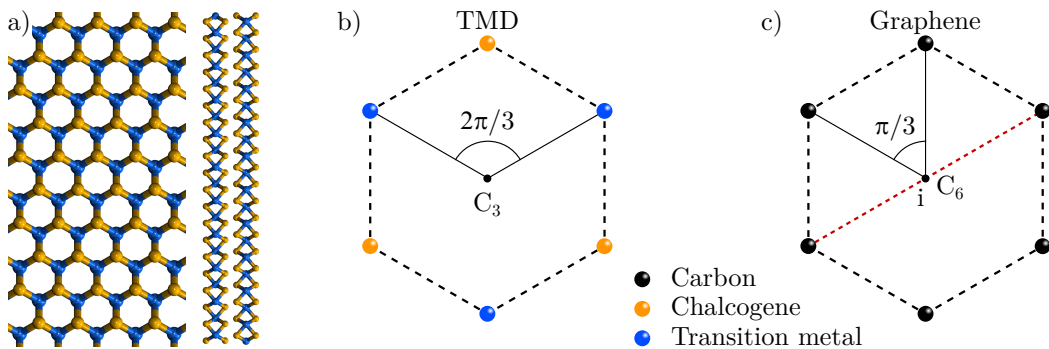


Figure 2.3: a) 2H-TMD crystalline structure, top and side view b) TMD unit cell with its C_3 principal rotation axis and no inversion symmetry. c) Graphene unit cell with its C_6 principal rotation axis and an inversion symmetry since inequivalent sites are populated with the same carbon atom.

From now on, we will refer to the sole subset of transition metal dichalcogenide that we have studied as TMD. 2H-TMD present the same honeycomb lattice as graphene. However, the A and B site of the lattice are occupied by different atoms, breaking the inversion symmetry and reducing the principal rotation symmetry axis from C_6 to C_3 (Fig. 2.3).

Those TMD undergo an indirect (in multilayer) to direct bandgap (in monolayer) transition (Fig. 2.4). Therefore, a TMD monolayer becomes a 2D electron system analogue to the III-V quantum well.

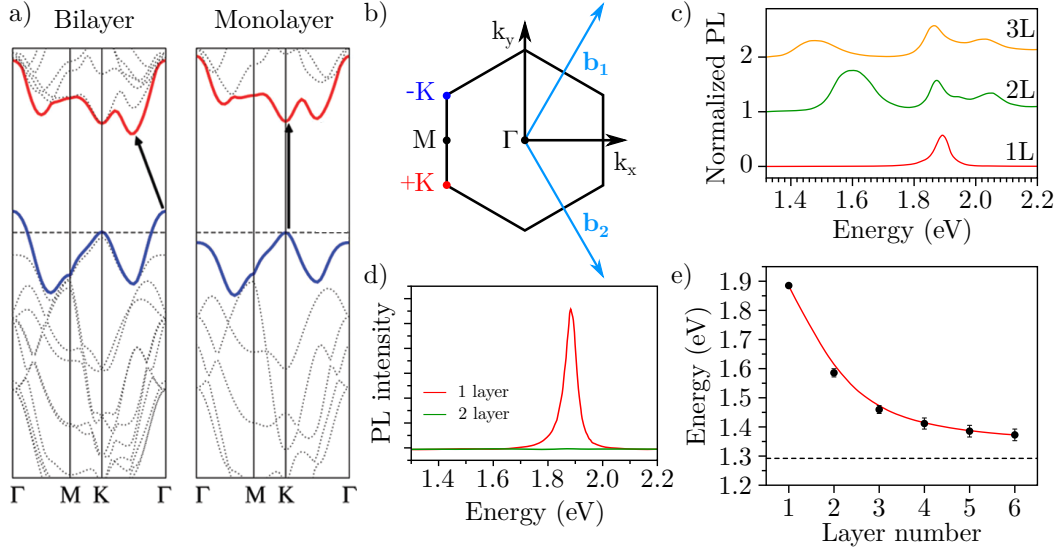


Figure 2.4: a) MoS_2 band structure for a bi and monolayer, the gap is indicated by the solid line arrow. b) reciprocal lattice sketch with the high symmetry point Γ , $\pm K$ and M . c) Mono-, bi- and tri-layer MoS_2 PL spectra in red, green, and orange respectively. Each spectrum is normalized to one. d) PL intensity of a mono- and bi-layer MoS_2 in red and green acquired in the same conditions. e) Lowest energy PL peak with respect to the layer number. c, d and e) are adapted from [3].

The reduction of the PL intensity between a mono- and a bi-layer TMD is the smoking gun evidence of the indirect to direct bandgap transition but we will develop this later. In (Fig. 2.4 a) we present a MoS_2 dispersion relation without spins. However, due to the massive transition metal atoms in those systems, a strong spin-orbit coupling will occur in TMD.

2.2.2 Spin-orbit coupling, the band fine structure

Spin-orbit interaction \mathcal{H}_{SO} couples the angular momentum \mathbf{L} with the spin momentum \mathbf{S} by $\mathcal{H}_{SO} \propto \mathbf{L} \cdot \mathbf{S}$. Since \mathbf{L} could be rewritten as $\mathbf{L} = \mathbf{r} \times \hbar \mathbf{k}$, the spin-orbit interaction couples the electron wavevector \mathbf{k} with its spin as

$$\mathcal{H}_{SO} \propto \mathbf{r} \times \mathbf{k} \cdot \mathbf{S} \quad (2.4)$$

From (Eq. 2.4) we find opposite effect for opposite spins or \mathbf{k} vector giving

$$\mathcal{H}_{\text{SO}}(\mathbf{k}, \uparrow) = \mathcal{H}_{\text{SO}}(-\mathbf{k}, \downarrow) = -\mathcal{H}_{\text{SO}}(\mathbf{k}, \downarrow) = -\mathcal{H}_{\text{SO}}(-\mathbf{k}, \uparrow) \quad (2.5)$$

Those relations, combined with the lack of inversion symmetry imply $E(\mathbf{K}, \uparrow) \neq E(\mathbf{K}, \downarrow)$. This lead to a spin splitting at the K point and the opposite one at the -K point. In (Fig. 2.5), we present MoS₂ band structure and a close up around the conduction band at the K point for both MoS₂ and WS₂. The valence band is qualitatively the same for any TMD, since they have the same spin sub-band energy hierarchy. However, in tungsten based TMD, the lowest conduction spin sub-band has opposite spin compare to the molybdenum lowest conduction one.

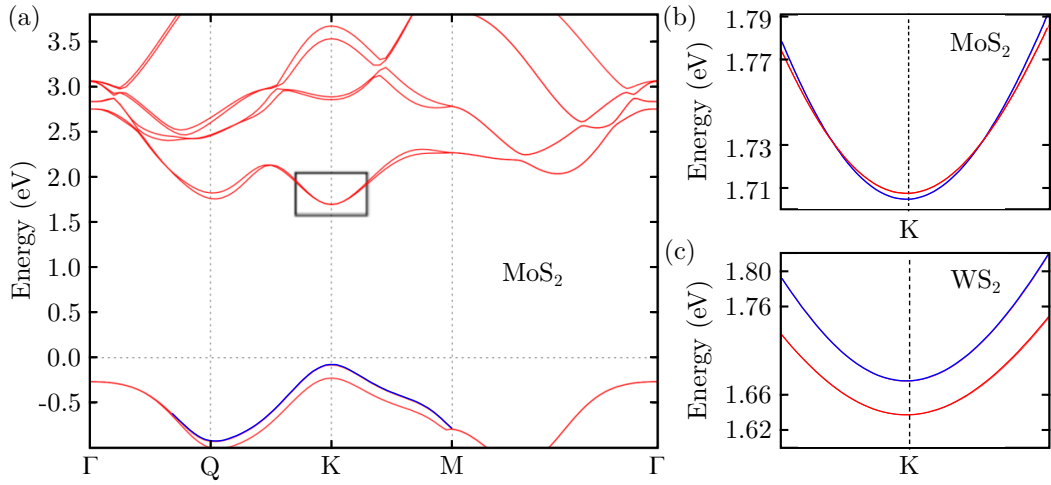


Figure 2.5: a) MoS₂ band structure, centred at K, calculated by Density Functional Theory including spin-orbit interaction. The spin up valence band is presented in blue. A zoom on the black rectangle is presented in (b). b) Zoom on the MoS₂ conduction band minimum around the K point, the spin down band is shown in blue. c) Same as (b) for WS₂. Figure adapted from [46].

TMD are then separated in two classes, the so-called bright and dark TMD. This nomenclature comes from optical properties that will be discuss later. A bright TMD presents the same spin splitting order in the conduction and valence band while a dark TMD presents an opposite spin splitting in conduction compared to valence band. The different spin splitting are summarized in Table 3.1

It seems that Molybdenum based TMD are bright unlike Tungsten based that are dark. However, recent work from Molas and co-workers [49] brings debate on the bright character of MoS₂ which is predicted to be bright in tight binding or DFT calculation but only with a few meV energy difference between both spins. Interband transitions in electronic band structure define absorption lines. Such interband absorption relies on free carrier absorption. However, TMD absorption is dominated by excitonic effect instead of free carrier absorption.

	MoS ₂	MoSe ₂	MoTe ₂	WS ₂	WSe ₂
Δ_{CB}	-3	-20 to -22	-32 to -36	29 to 32	36 to 38
Δ_{VB}	138 to 150	180 to 202	213 to 269	379 to 433	400 to 510
class	B or D	B	B	D	D

Table 2.1: Spin splitting at the K point in the conduction (Δ_{CB}) and valence (Δ_{VB}) band induced by spin orbit coupling. Those data are taken from [47] and [48]. We indicate in the last line the bright or dark character of each TMD. B and D stands for bright or dark character of the TMD.

2.2.3 Optical properties

2.2.3.1 Absorption

TMD band structure, especially the splitting in the valence band due to the spin-orbit coupling, gives rise to two different electronic transitions. These two transitions therefore lead to two different optical absorption bands, the A and B ones. The A optical absorption line corresponds to the lowest energy transition while the B one is the highest energy transition (Fig. 2.6).

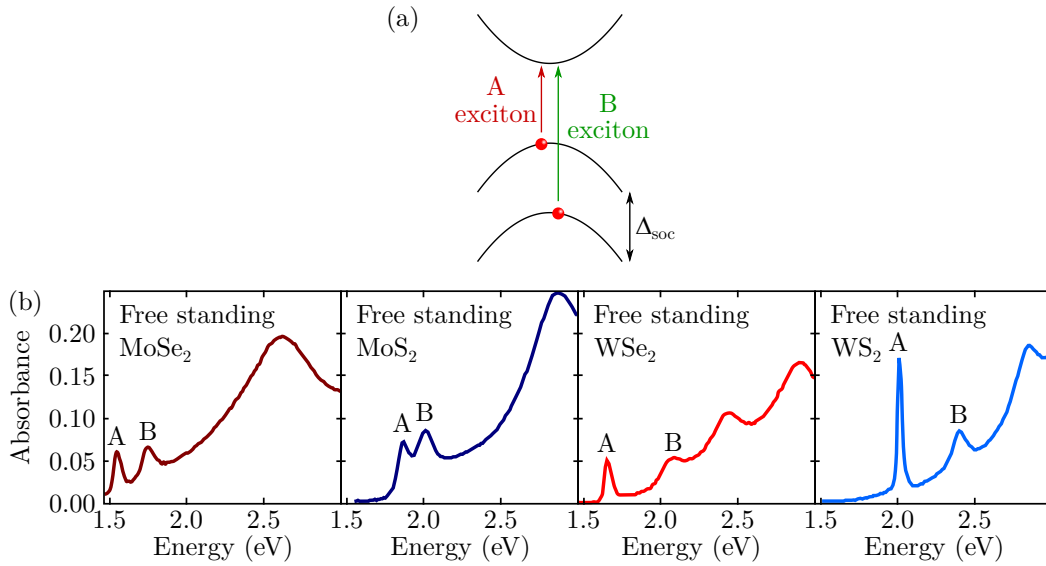


Figure 2.6: a) TMD band structure with the spin orbit splitting. The transition labelled A and B are the electronic transition underlying the two A and B peak in (b). b) Absorption measurement reproduced from [50]. These data have been taken on free standing samples.

From reflectivity measurement, we can extract the absorption coefficient for each material. The reflectivity is linked to the real part of the refractive index by the Snell Descartes laws. Using the Kramers-Kronig relation on the real part of the refractive index n , we get access to the imaginary part of the refractive index κ . In addition, the refractive index allows us to compute the imaginary part of the dielectric function ϵ'' with $\epsilon'' = 2n\kappa$. Finally, using the dielectric function imaginary part ϵ'' and the refractive index real part, we can compute the absorption α as

$$\alpha(\omega) = \frac{\omega}{n(\omega)c} \varepsilon''(\omega) \quad (2.6)$$

with ω the incoming photon frequency and $n(\omega)$ the frequency dependent refractive index. The light absorption of TMD layer strongly depends on the photon energy and presents several peaks (Fig. 2.6 c). Each peak corresponds to an excitonic transition which comes from the spin band structure. Actually, each exciton is related to an electronic transition in the conduction band however, the absorption for an exciton occurs below the electronic gap energy (Fig. 2.6 a).

2.2.3.2 Emission

On one hand, the TMD PL emission is dominated by the A exciton (Sect. 2.4) at room temperature. On the other hand, A exciton as well as its charged counterpart, the trion and defect related emission dominate at low temperature (Fig. 2.7). However, BN encapsulation gives sharper and cleaner emission peaks getting rid of the defect emission. BN encapsulated TMD A exciton emission width even approaches the homogeneous limit (Fig. 2.7) [8, 28, 51]. The effect is particularly impressive on MoS₂ since the width is divided by 4 when encapsulated in BN and the intensity is roughly one order of magnitude higher. This highlights the cleaning effect induced by the encapsulation, further confirmed by the absence of defect related emission at low energy.

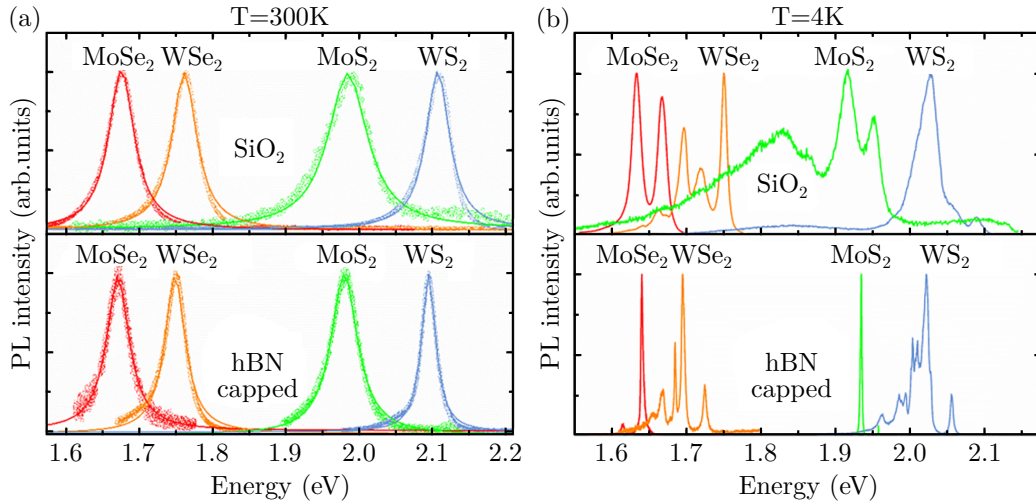


Figure 2.7: a) Room temperature PL emission, the width is reduced for BN-capped samples. b) Low temperature PL emission for various TMD supported on SiO₂ and encapsulated in BN. In BN, optical signature are much cleaner with much narrower peak and complex peak structure unveiled. Figure reproduced from [8].

On WS₂ and WSe₂, the prominent emission peak usually assigned to the trion emission merged with some defect emission finally reveals a complex structure of many different peaks. The reproducibility and steadiness of those emission peak energies suggest a phonon assisted emission from momentum indirect exciton [52, 53].

We will come back to the difference between exciton and free electron hole pair in section 2.4. Before going any further, we will introduce the 2D materials vibrational properties.

2.3 Phonons in 2D materials

2.3.1 Generalities

In a crystal, vibrations can be decomposed on a normal mode basis, each normal mode being called phonon. The number of phonons N_{ph} depends on the number of atom per unit cell N in the crystal as $N_{\text{ph}} = 3N$. Each phonon has its own frequency that depends on the material weight since mechanical resonator frequency ω depends on its spring constant k , which depends on the phonon mode and its mass m as $\omega \propto \sqrt{\frac{k}{m}}$. In addition, the spring constant can be changed by strain effect, depending on the considered mode.

Interestingly, vibrational properties of a crystal depend on the electronic properties via electron phonon coupling. This gives rise to the temperature dependent electronic properties and to the doping dependence of the phonon frequencies which is modulated by the environmental condition, doping.

2.3.1.1 Phonons in graphene

With two atoms per unit cell, graphene hosts 6 different phonon modes. Their frequencies are changed by 3% per % of strain in the material. Therefore, such effect can be used as a probe for the strain if the phonon frequency is high enough to get measurable shifts. Phonon frequencies have been calculated [54] and we report their dispersion relation in (Fig. 2.8).

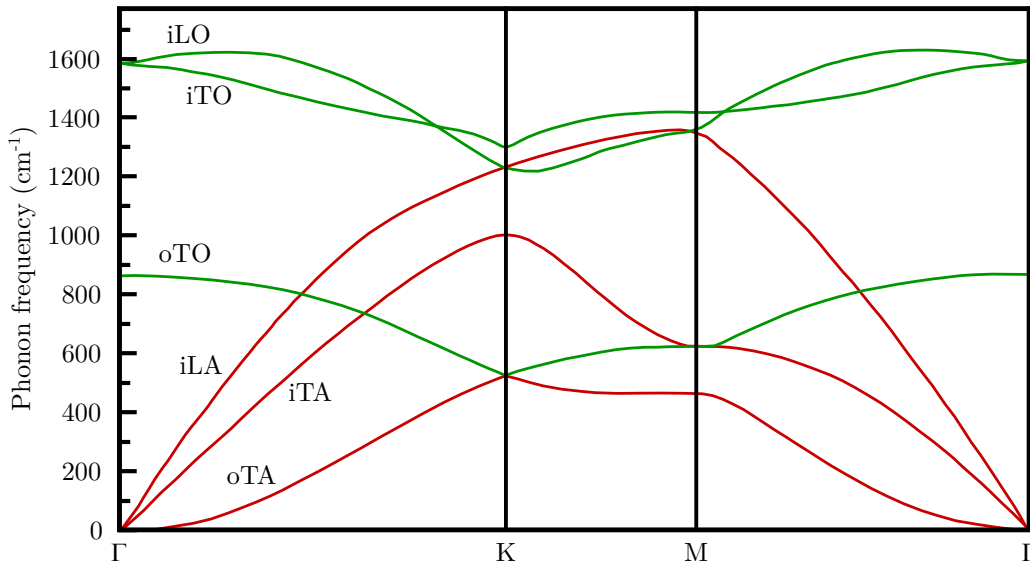


Figure 2.8: Phonon dispersion relations along high symmetry lines and at high symmetry Γ , K and M point adapted from [54]. Modes are labelled by i or o for in or out of plane modes, L and T stands for longitudinal and transverse and finally A and O refer to acoustic or optical phonons.

The highest frequency phonons are the iLO and iTLO modes ranging from 1200 to 1600 cm^{-1} giving shifts up to 45 cm^{-1} per strain% which is easily measurable [55].

For graphene, the influence of the doping on the phonon frequency is typically 1% per 10^{13} cm^{-2} which induced measurable 15 cm^{-1} shift of the iTLO and iLO modes in graphene [56]. Therefore, iTLO and iLO frequency could be a useful probe to monitor doping in graphene. However, to achieve this goal, we need an experimental technique that can be sensitive to iTLO and iLO phonons.

2.3.1.2 Phonons in transition metal dichalcogenides

TMD vibrational properties are similar to the graphene ones. However, with 3 atoms per unit cell, one transition metal and two chalcogene for a monolayer, a monolayer TMD hosts 9 different vibrational modes (Fig. 2.10). Since TMD atoms are much heavier than graphene ones, the TMD phonon frequencies are lowered compared to graphene ranging from 150 (19meV) to 500 cm^{-1} (62 meV) for MoS_2 optical phonons [57]. Furthermore, acoustic phonon range from 0 to 150 cm^{-1} (19 meV). Depending on the TMD composition, the upper bounds could be changed.

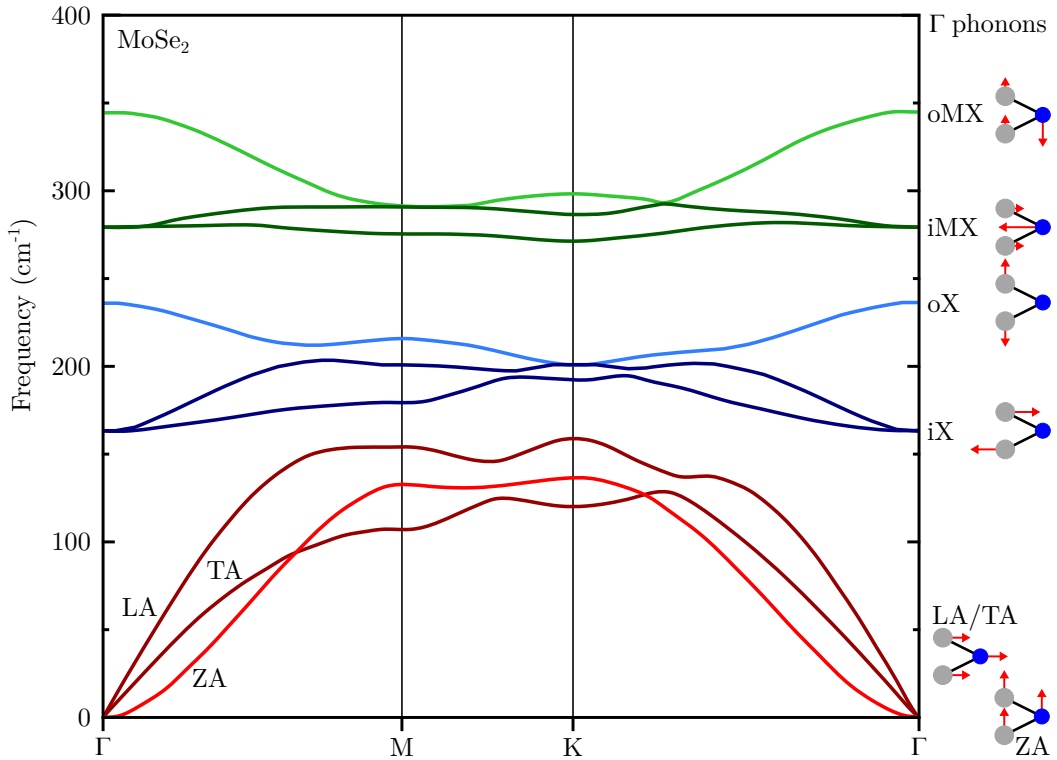


Figure 2.9: Phonon dispersion relation calculated for MoSe_2 monolayer. We also show the atomic displacement involved by each phonon at the Γ point where in plane modes are doubly degenerated. Adapted from [57].

Finally, for both graphene and TMD, increasing the number of layer, increases the number of atoms per units cells and hence the number of phonons.

2.3.2 Introduction to Raman scattering

Raman spectroscopy is an optical spectroscopy technique that gives access to the phonon frequencies and therefore to the doping strain environmental condition ... In a semi-classical picture, it relies on the inelastic light scattering of photons by the crystal giving rise to peaks that are shifted by the phonon frequency from the incident laser frequency (Fig. 2.10 a).

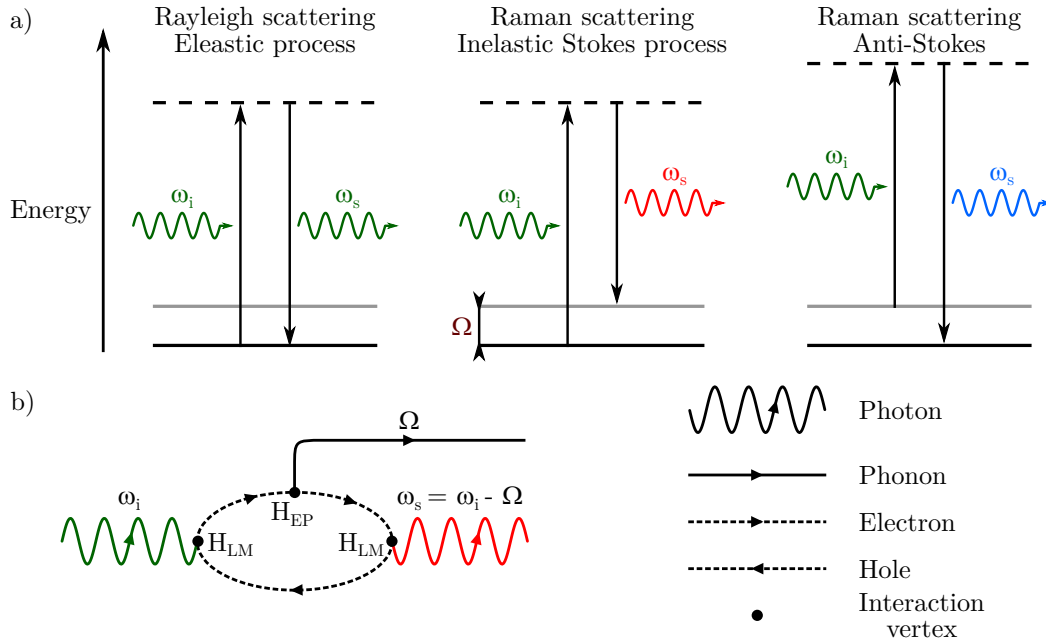


Figure 2.10: a) Elastic and inelastic light scattering processes represented in a semi-classical picture. Solid black lines are electronic states while the gray ones are vibronic ones. The dashed lines represent the intermediate states that can be virtual states. Ω is the phonon frequency. b) Quantum description of the Raman process using Feynman diagram. The incoming phonon creates a virtual electron hole pair that interacts with a photon before recombining radiatively emitting a photon at a different frequency. Adapted from [58].

The quantum description of the Raman process is as follows. An incident photon is absorbed, creating a virtual electron-hole pair that absorbs or creates a phonon via electron-phonon coupling. Finally, the electron-hole pair recombines radiatively, emitting a photon shifted compared to the excitation light frequency (Fig. 2.10 b). Such process is in general inefficient and only one photon per million undergoes inelastic scattering. For Raman interaction, a phonon needs to satisfy conditions on the dipole it induced. If this condition is fulfilled, the phonon is said Raman active. This activity can be calculated from group theory calculations developed in [59].

On the one hand, the dipolar condition state if a given phonon can interact with the electromagnetic field or not. On the other hand, the momentum conservation imposes other conditions on the phonons. For first-order processes (i.e. involving only one phonon), the momentum conservation is written

$$\mathbf{k}_i \pm \mathbf{q} = \mathbf{k}_s \quad (2.7)$$

with \mathbf{k}_i , \mathbf{k}_s the incident and scattered photons wavevectors and \mathbf{q} the phonon wavevector. The maximum phonon momentum is roughly $\mathbf{q}_{\max} = a^{-1} = 3 \times 10^9 \text{ m}^{-1}$ with a the lattice constant. To compare with the photon momentum which is roughly $\lambda^{-1} = 2 \times 10^6 \text{ m}^{-1}$. Since $\mathbf{q}_{\max} \gg \mathbf{k}_s$ it becomes clear that we have only access to the lowest momentum phonon in lattices meaning that we are probing the phonon dispersion relations in the vicinity of the Γ point.

This analysis is valid for first order Raman processes. However, for n-th order processes (i.e. involving n phonons) the momentum conservation law becomes

$$\mathbf{k}_i + \sum_{j=1}^n \mathbf{q}_j = \mathbf{k}_s \quad (2.8)$$

Finally, the momentum matching condition becomes $\sum_{j=1}^n \mathbf{q}_j \approx 0$. Therefore, higher order Raman processes are sensitive to phonons within the whole phonon dispersion as long as the sum over all their momentum is vanishing.

2.3.3 Raman spectroscopy of graphene

2.3.3.1 G-mode and 2D-mode

Phonon frequencies are sensitive to the doping and hence to the Fermi energy. Therefore, we will probe graphene Fermi energy using the two prominent features of the graphene Raman spectrum, the so called G- and 2D-mode (Fig. 2.11).

The G-mode is a first order process which has been described above and corresponds to iTO and iLO doubly degenerated phonon mode at Γ . However, the 2D-mode is peculiar. It is a second order Raman process, which involves phonons at the K point. Moreover, both excitations and desexcitations have to be resonant to get a finite intensity [60].

2.3.3.2 Theoretical modelling of the G-mode feature

A combination of theoretical and empirical modeling [56, 61–64] gives a protocol to extract the graphene Fermi level from its Raman characterization using both G- and 2D-mode features. The G-mode features are theoretically described but the 2D-mode features is more complicated to described theoretically and its behavior with strain and doping is known empirically. In first approximation, the G-mode FWHM Γ_G is inversely proportional to its lifetime. Since this phonon energy is roughly 0.2 eV, it can decay into an electron-hole pair as long as this mechanism is not Pauli-blocked. Therefore, the neutral graphene G-mode is wider compared to the doped graphene G-mode. The variation of the G-mode width $\Delta\Gamma_G$ due to this effect can be written as

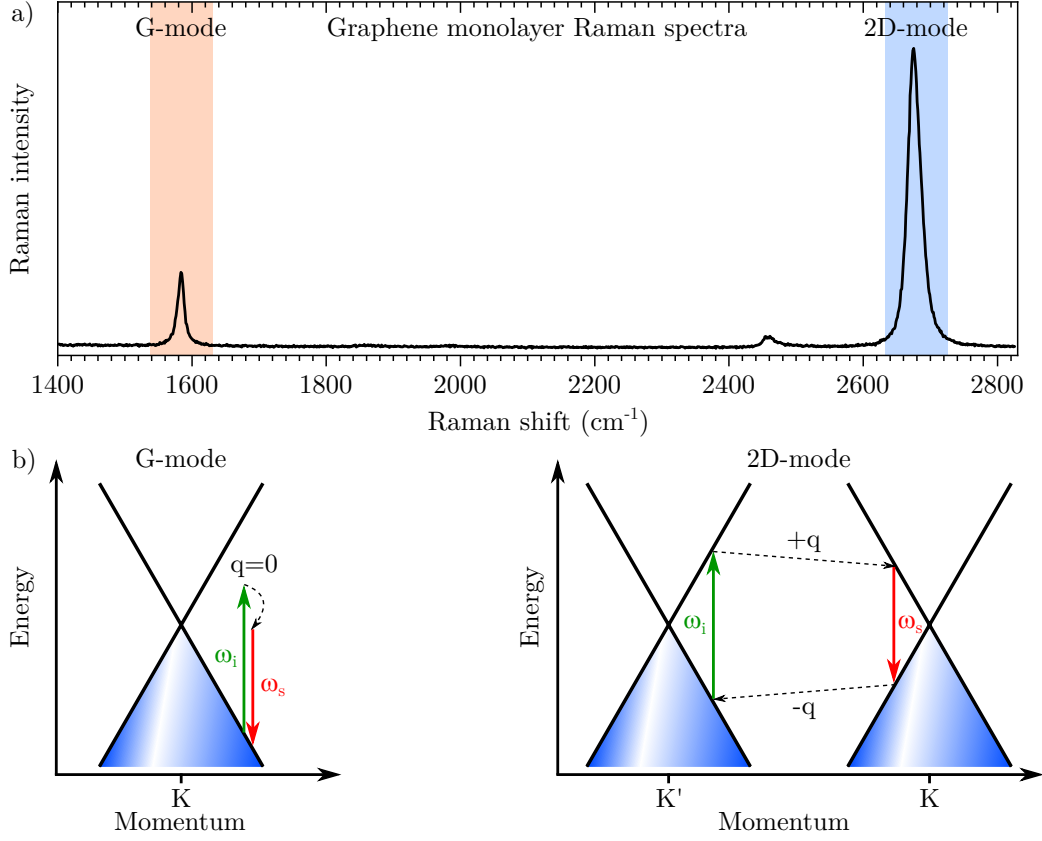


Figure 2.11: a) Graphene monolayer Raman spectrum. The reddish region highlights the G-band while the blueish corresponds to the 2D-band. b) First order Raman process corresponding to the G-mode. Second order doubly resonant Raman process underlying the 2D-mode.

$$\Delta\Gamma_G = \Gamma_G - \Gamma_0 = \frac{\lambda_\Gamma}{4} \omega_G^0 \left[f\left(-\frac{\hbar\omega_G^0}{2} - E_F\right) - f\left(\frac{\hbar\omega_G^0}{2} - E_F\right) \right] \quad (2.9)$$

with ω_G^0 the G mode frequency at zero doping, $f(E)$ the Fermi-Dirac distribution and λ_Γ the dimensionless parameter that reflects the electron-phonon coupling. Γ_0 takes into account every sources of broadening except the doping. Hence, it is the G-mode FWHM at high doping, when Γ_G is vanishing.

We can define in the same way the difference between the G-mode frequency induced by doping $\Delta\omega_G$. However, this quantity can be separated into two different contributions: $\Delta\omega_G = \Delta\omega_G^A + \Delta\omega_G^{NA}$. $\Delta\omega_G^A$ corresponds to the so called adiabatic frequency shift which takes into account the change in the graphene equilibrium lattice parameters due to the doping. However, this term brings negligible correction for small doping ($E_F < 1$ eV). Moreover, $\Delta\omega_G^{NA}$ is the non-adiabatic frequency shift that takes into account the phonon energy renormalization due to the phonon interaction with virtual electron-hole pair. This renormalization will be larger when the electron density increases. Finally, $\Delta\omega_G^{NA}$ could be expressed as

$$\Delta\omega_G^{\text{NA}} = \frac{\lambda_\Gamma}{2\pi\hbar} \int_{-\infty}^{+\infty} \frac{[f(E - E_F) - f(E)] E^2 \text{sgn}(E)}{E^2 - (\hbar\omega_G^0/4)} dE \quad (2.10)$$

with f the Cauchy principal value.

2.3.3.3 Raman spectroscopy as a probe for local doping and strain

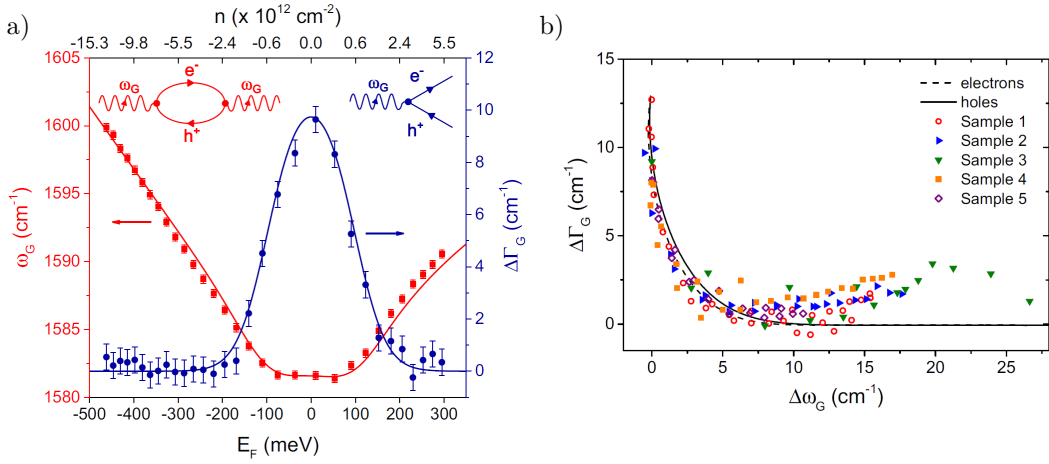


Figure 2.12: a) G-mode frequency and width in red and blue respectively with respect to the Fermi energy. The solid red lines corresponds to (2.10) while the blue one comes from (2.9). The right inset is the Feynman diagram of the phonon electron-hole pair interaction leading to the increase of the G mode frequency while the right one corresponds to the decay of a phonon to an electron hole pair. b) G-mode width with respect to its frequency. The solid and dashed lines correspond to a fit based on (2.10) and (2.9) for the hole and electron doped graphene respectively. Adapted from [56].

Data from (Fig. 2.12) have been recorded using an ionic top gate to control the Graphene Fermi energy and the theory agrees well with those data. Finally, the last tool is semi-empirical. The G-mode frequency correlation with the 2D-mode frequency gives insights on the nature of the dopant and on the graphene strain. The slope described by this correlation gives this information (Fig. 2.13)

In a nutshell, an increase of the G-mode frequency alongside a decrease of its width indicates a doping of the graphene. The 2D-mode, G-mode frequency correlation allows us to determine the nature of the graphene dopant. Finally, the fitting of the G-mode width against frequency correlation using Eq. (2.9) and (2.10) allows us to quantitatively measure the graphene Fermi energy. Even though this protocol cannot be adapted to TMD, Raman spectroscopy can give insight on its doping level. For the same reason we can measure graphene doping level thanks to Raman spectroscopy.

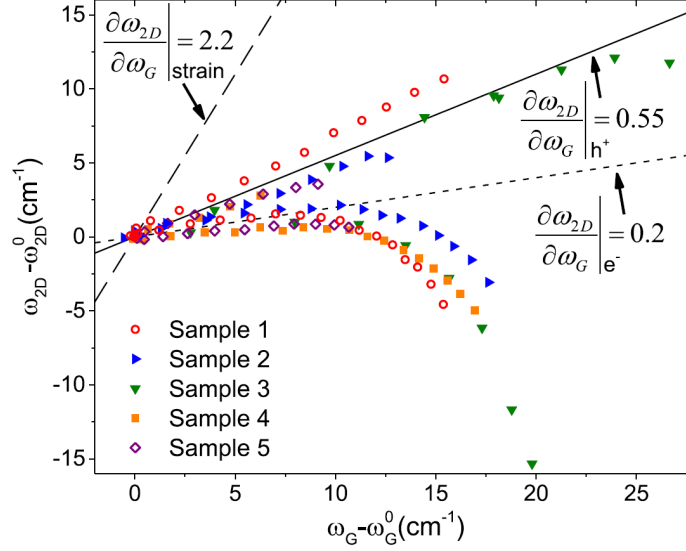


Figure 2.13: 2D-mode frequency with respect to the G mode frequency. The dashed line highlights the correlation behaviour when strain is increased. The solid line corresponds to a hole doping while the dotted line follows an electron doping behaviour. Adapted from [56].

2.3.4 Raman spectroscopy of TMD

2.3.4.1 Layer number determination using Raman spectroscopy

We have thoroughly studied the N-layer Raman response of different TMD [65?], especially the N-layer MoTe₂ Raman response for N=1 to 12 and the bulk [65]. From the 4 Raman active modes in the monolayer, each duplicate following the the Davidov splitting while new low frequency mode appearing below 40 cm⁻¹ in the multilayer samples. These low frequency modes consist of the movement of one layer with respect to the other as a whole (Fig. 2.14).

To go further, we modelize the TMD slab as a finite linear chain of coupled mechanical oscillators. Each atom is represented by a material point linked to its nearest and second nearest neighbour by a spring. We use four different spring constant within the bulk, two for the nearest neighbours and two for the second nearest neighbour. The edge effects are taken into account by two additional spring constants (Fig 2.15 a)

Using this model, we were able to fit with the same force constant for each mode (Fig. 2.15 b-d). Even though we present only the data on the out-of-plane modes, the model fits also in-plane modes [65]. However, different force constants have to be used. In the following, we will focus on the oX and iMX phonon modes since they are at relatively high frequencies and intensity for any TMD.

2.3.4.2 Doping dependence of TMD Raman modes

To characterize doping in TMD, we will make use of the oX mode (A'_1) Raman mode [66, 67] (Fig. 2.14). Using an ionic top gate, Miller and co-workers demonstrated that the A'_1 mode frequency of an MoS₂ layer depends on the doping level (Fig. 2.16 a). The A'_1 mode shift by 3 cm⁻¹ by

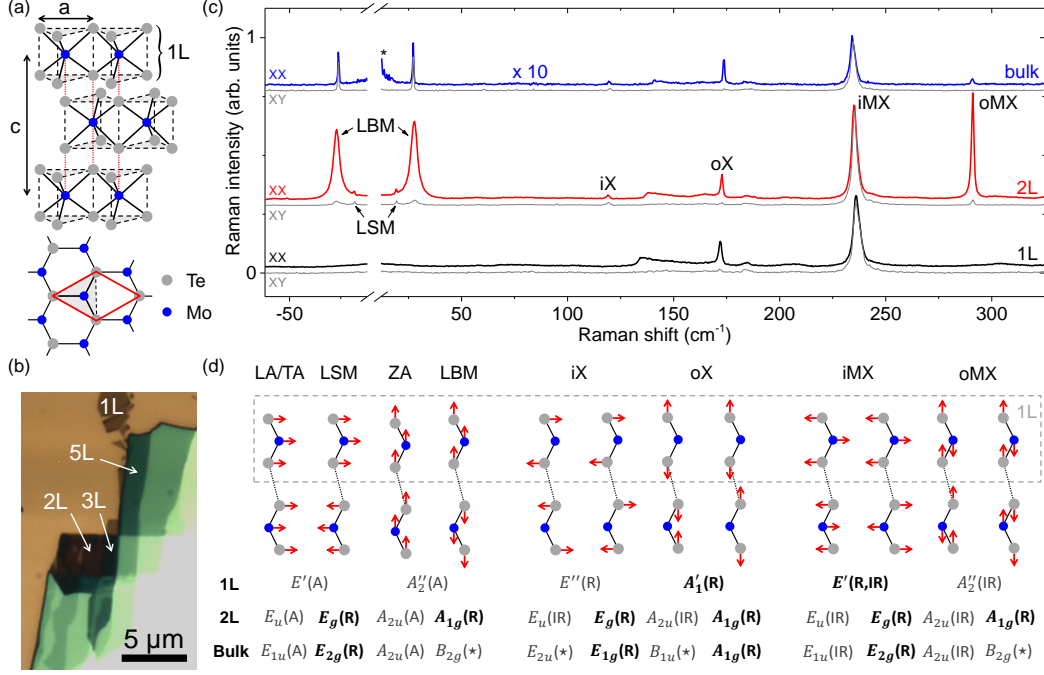


Figure 2.14: *a)* Side and top view of the crystal structure of 2H-MoTe₂. The red rhombus represents the unit cell. *b)* Optical image of a *N*-layer MoTe₂ crystal deposited onto a Si/SiO₂ substrate. *c)* Raman spectra of monolayer, bilayer and bulk MoTe₂ in the parallel (XX, thick colored solid lines) and perpendicular (XY, thin grey lines) polarization configuration. The spectra are vertically offset for clarity and the asterisk highlights residual contributions from the exciting laser beam. *d)* Atomic displacements and irreducible representations associated with the Γ point phonon modes in monolayer, bilayer and bulk MoTe₂. The Raman (R) and/or infrared (IR) activity are indicated, and stars denote silent modes. The zero frequency acoustic modes (LA, TA, ZA) and their irreducible representations are also shown for clarity. Figure reproduced from [65].

injecting $1.5 \times 10^{13} \text{ cm}^{-2}$ dopant density in the MoS₂ layer. This gives a 0.5% frequency shift per $\times 10^{13}$ electron per cm².

2.3.4.3 Photodoping in TMD

Once the doping dependence of the A'₁ mode frequency has been characterized, the photodoping of MoS₂ can be unravelled by measuring Raman spectra at different photon fluxes. By doing so, a decrease of the A'₁ frequency has been revealed (Fig. 2.16 b) which is the proof of a photoinduced electron doping in MoS₂. By performing this study on various samples and in vacuum or in air, the photodoping is attributed to desorption of electronegative species such as water or oxygen molecules.

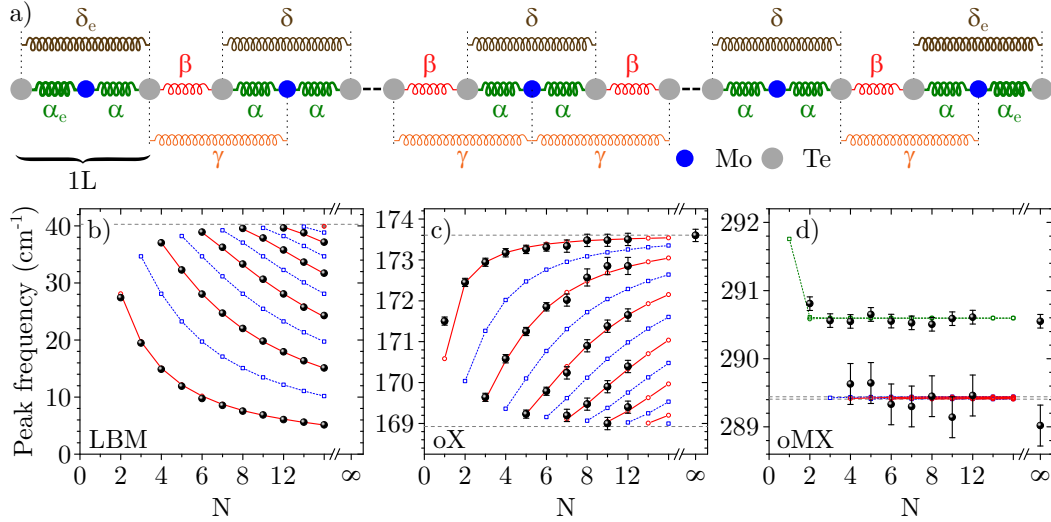


Figure 2.15: a) Schematic of the finite linear chain model discussed in the text. b) Layer Breathing Mode (LBM) c) oX and d) oMX Raman mode with respect to the sample number of layers. Each open squares (circles) correspond to a Raman inactive (active) mode calculated from our model. The black dots correspond to the value extracted from a fit of Raman spectra. The gray dashed line shows the limit in the bulk of the mode frequency. The solid red and dashed blue lines are guide to the eye that connect the different calculated phonon values. In (d) the green dashed line and open symbols are the surface mode. Figure adapted from [65].

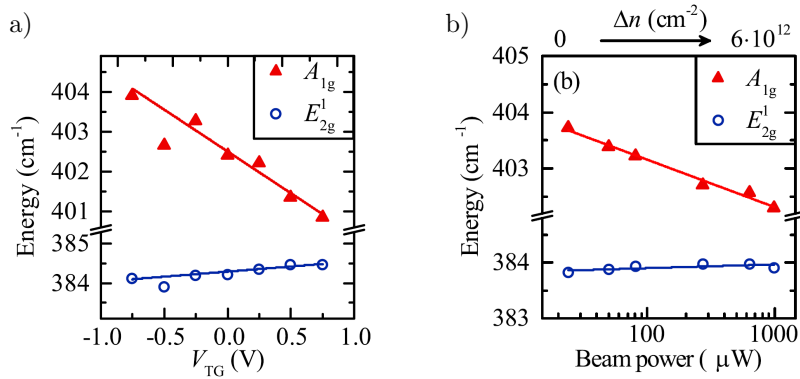


Figure 2.16: a) oX MoS_2 mode frequency with respect to the top gate voltage. b) oX mode frequency with respect to the incoming laser power. Figure adapted from [66].

2.4 Excitons in transition metal dichalcogenides

2.4.1 Introduction

Let us now differentiate the free carrier absorption from the excitonic absorption in a direct gap semiconductor. In the free carrier absorption, the photon energy is transferred to an electron lying in the valence band, promoting it to conduction band and leaving a hole in the valence band. This absorption can only occur for photon energy at least equal to the electronic bandgap. Before going any further, we would like to emphasize that the electronic gap energy E_g corresponds to

the single particle gap E_{g_s} renormalized by the electron electron interaction E_{e-e} . Therefore, the electronic gap is higher than the single particle gap and could be written as $E_g = E_{g_s} + E_{e-e}$. For photon energy higher than the electronic gap E_g , electrons (hole) will quickly decay to the bottom (top) of the conduction (valence) band by interaction with phonon before recombining radiatively (excluding non-radiative mechanism) from this position. Since holes and electrons do not interact with each other, they can be represented in a one particle representation (Fig. 2.17 a). This process has a rather flat absorption spectrum since the absorption is proportional to the density of state which is constant for 2D system, with parabolic dispersion.

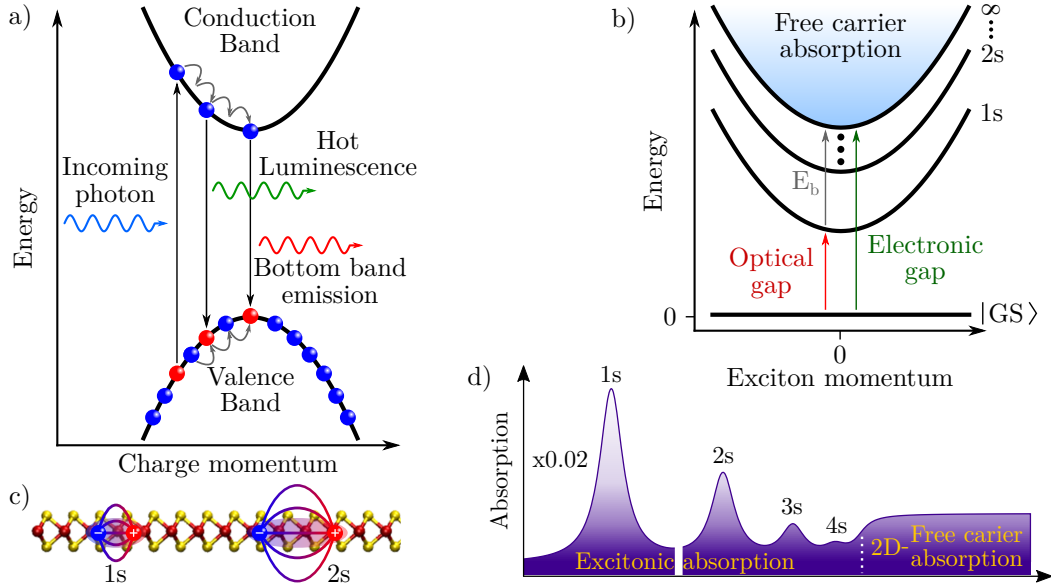


Figure 2.17: a) Free carrier absorption sketch, blue (red) dots represent electron (holes). The black vertical arrows represent the photo-induced transition. Small grey curved arrows represent the electron phonon interaction guiding the electron (hole) to the bottom (top) of the conduction (valence) band. The wavy blue arrow is the photon used to excite electron-hole pair while the green and red ones are the photon re-emitted by the semiconductor. The green one represents hot luminescence from carrier that are not fully relaxed yet while the red one comes from fully relaxed electron hole pair. b) Excitonic representation of bounded electron hole pairs, red (green) arrow is the optical (electronic) gap. The binding energy is represented by the gray arrow. c) Real space representation of exciton with different principal quantum number in a TMD layer, the 1s state electrical field line lies mostly in the layer while the 2s lies more outside of it. d) Sketch of the excitonic optical absorption. The 1s state absorption is divided by 50 since it absorbs much more than the other exciton Rydberg state.

We described free carrier absorption but electrons and holes have opposite charge and therefore, they can attract each other's by Coulomb interaction. If this interaction is strong enough, an electron-hole bound state could arise. At this point, the electron hole pair cannot be considered as two different particles anymore but the pair should rather be considered as a single quasi-particle, the exciton. The exciton properties are defined by its constituents and then, the exciton centre of mass is the electron-hole centre of mass. The exciton momentum is $\mathbf{K} = \mathbf{k}_e + \mathbf{k}_h$ with \mathbf{k}_e (\mathbf{k}_h)

the electron (hole) momentum and its mass is $M = m_e + m_h$ with m_e (m_h) the electron (hole) effective mass. An exciton is a strong dipole and hence it can absorb light efficiently and its absorption is peaked around the energy $E_{\text{exc}} = E_g - E_b$ with E_b (E_g) the binding (electronic gap) energy (Fig. 2.17 b). The lowest exciton energy E_{exc} is called optical gap. The binding energy E_b also defines the exciton stability with respect to the temperature. Hence in order to get a finite absorption at room temperature the binding energy has to verify $E_b > k_B T$.

2.4.1.1 Excitons Rydberg series

As hydrogen atoms, excitons have Rydberg series. The lowest energy state is the 1s and the equivalent of the ionization energy is the electronic bandgap since an ionized exciton is actually a free electron hole pair. In addition, the quasi-particle has its own dispersion relation which depends quadratically on its momentum \mathbf{K} (Fig. 2.17 b). The binding energy is an important characteristic for an exciton. They are usually not stable at room temperature, so let us approximate this value for TMD.

Assuming a 2D hydrogen model with a homogeneous effective dielectric constant, the exciton binding energy for each exciton Rydberg state E_b^n is written as follows [68]

$$E_b^n = \frac{e^2}{8\pi\epsilon_{\text{eff}}a_0} \cdot \frac{1}{\left(n + \frac{1}{2}\right)^2} \quad (n \in \mathbb{N}). \quad (2.11)$$

with e the electron charge, a_0 the exciton Bohr radius and ϵ_{eff} the effective dielectric constant averaging the dielectric constant outside and inside the TMD. The binding energy is then E_b^0 . However, to properly estimate this energy, we first need the exciton Bohr radius which could be written as

$$a_0 = \frac{4\pi\epsilon_{\text{eff}}\hbar^2}{\mu e^2} \quad (2.12)$$

with μ the exciton reduced mass. The effective electronic and hole mass in a TMD is roughly half of the electron rest mass and then μ is around 0.25 electron rest mass [69]. The exciton Bohr radius will strongly depend on the coulomb interaction intensity which in return depends on the dielectric screening. Lesser screening implies stronger Coulomb interaction and then smaller Bohr radius. Here, we consider that the layer is surrounded by vacuum. Giving the monolayer dielectric constant $> 10\epsilon_0$ [70] we estimate the effective dielectric constant to $5\epsilon_0$. Finally, this gives an exciton Bohr radius around 1nm and then an exciton binding energy $E_b^0 = 0.5\text{eV}$ which leads to stable exciton at room temperature. For comparison, we report in (Table 3.2) the reduced mass μ , the surrounding dielectric constant ϵ_{eff} , the exciton binding energy and Bohr radius for three dimensional III-V semiconductor (GaAs), AlGaAs/GaAs quantum well and finally TMD

We can now write the full exciton dispersion relation for any exciton state and momentum (Fig. 2.17 b).

$$E_{\text{exc}}^n = E_g + \frac{\hbar^2 \mathbf{K}^2}{2M} - E_b^n. \quad (2.13)$$

	E_g (eV)	μ	ϵ_{eff}	E_B (meV)	a_0 (nm)
3D GaAs [71]	1.56 (@4 K)	0.0632	12.85	4.3	11.2
2D AlGaAs/GaAs	1.42	0.060	12.5	21	11
2D MoSe ₂	~ 2	0.25	5	500	1

Table 2.2: μ is given in electronic mass and ϵ_{eff} in vacuum permittivity

2.4.1.2 Binding energy measurement

To test the 2D hydrogen model and measure the exciton binding energy, we need to access the exciton Rydberg series up to the highest principal quantum number possible. Each transition of the exciton series absorbs light. Therefore, the energy of the exciton level could be accessed by Photo Luminescence Excitation experiment (PLE). This experiment consists of sweeping the excitation energy across the different optical resonances. Since absorption is higher when the excitation is resonant with an excitonic state, this will induce a larger, lowest lying exciton, PL intensity [72]. Since each exciton state absorbs light, it could be recorded via direct absorption measurement. Such experiments are difficult to carry out due to the large absorption intensity discrepancies between the first and the n -th exciton states. However, it has been done by A.Chernikov and co-workers [4]. They used reflectance spectroscopy to get access to the exciton Rydberg series (Fig. 2.18 a) and finally tested if the model could reproduce those data. It appears that this model is quantitatively agreeing only with the highest excitonic state but not with the two first states (Fig. 2.18 b).

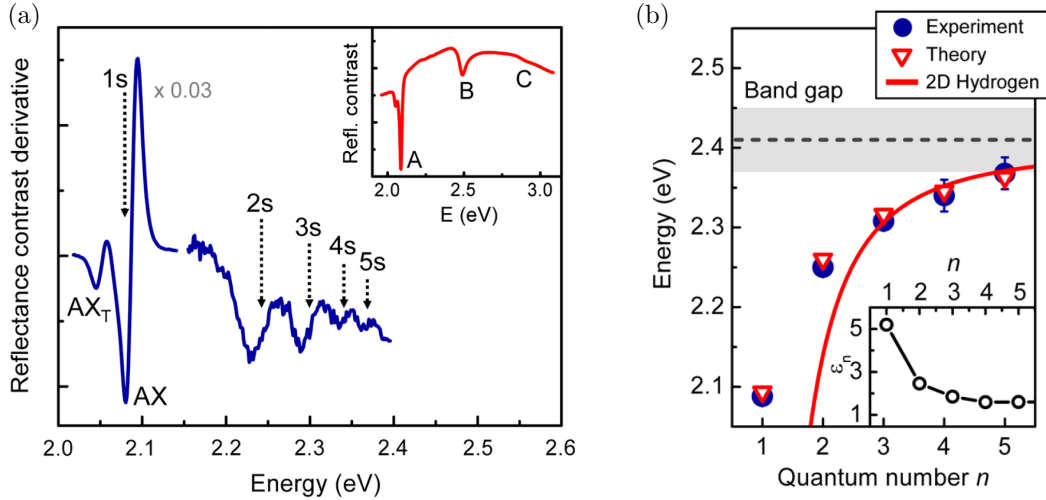


Figure 2.18: *a)* Reflectance contrast derivative with respect to energy. Below 2.15eV, the spectrum is divided by 30 for clarity. The inset is the full reflectance spectrum. *b)* Comparison between theory and experiment, blue dots correspond to experiment extracted from a) the red line corresponds to the 2D hydrogen model while the red triangle stands for the Keldysh potential based theory. The electronic bandgap presented here is a fitting parameter of the theory. The inset presents the effective dielectric constant needed seen by the exciton for different Rydberg state. Adapted from [4].

Higher Rydberg states have also larger Bohr radii, but this is already taken into account in the 2D hydrogen model. Furthermore, a larger Bohr radius implies that electric field lines generated by the exciton dipole leak more and more outside the TMD layer (Fig. 2.17 c). Finally, the effective dielectric screening affecting the electron hole pair is decreasing while the Bohr radius increases. This effect is not taken into account in the 2D hydrogen model and leads to the hydrogen model breakdown. To take this effect into account, a new Hamiltonian [69] was proposed using Keldysh potential [73] describing the interaction between charges in a 2D electron gas with high dielectric contrast. This is typically the case of a TMD layer in contact with air. Even though this potential allows us to describe qualitatively the exciton Rydberg series, the potential describing quantitatively the screening effect in TMD excitons has not been found yet

Interestingly, from those data, we can extract the exciton binding energy and therefore the electronic gap, 2.4 eV for WS₂ in air supported on SiO₂. It is important to specify the dielectric environment for characteristic value such as gap energy because it is possible to tune those parameters by changing the dielectric environment. From Eq. 2.11 and 2.12, we found that increasing the dielectric screening reduces the exciton binding energy and therefore it should increase the emission energy. However, increasing the dielectric screening actually reduces the emission energy by roughly 10meV. This could be explained by the effect of the screening on the electronic bandgap itself, since in Eq. 2.13 both term E_g and E_b are affected by the dielectric screening and both by a reduction. At the end of the day, the effect on the electronic gap is larger than on the binding energy, reducing the TMD emission energy (Fig. 2.20 a). Finally, it is the energy difference Δ_{2s-1s} between the 1s and 2s exciton state that will undergo the largest change in the optical properties.

The same type of measurements has been carried out recently on TMD encapsulated in BN since this encapsulation leads to sharper optical resonances. Sharper excitonic resonance should give us an easier access to the exciton Rydberg series as presented in (Fig. 2.18). In [5] Stier and co-workers carried out magnetoabsorption experiment. A given exciton state energy $E(B)$ will depend on the magnetic field as $E(B) = E_0 + \Delta E_{\text{dia}} + g_\nu \mu_B B$ where the last term takes the Zeeman splitting into account with μ_B the Bohr magneton and g_ν the exciton valley g-factor. ΔE_{dia} the exciton diamagnetic shift which depends quadratically on the magnetic field B .

$$\Delta E_{\text{dia}} = \frac{e^2}{8\mu} \langle r_\perp^2 \rangle B^2 \quad (2.14)$$

The quadratic dependence with magnetic field gives access to the root mean-square of the exciton radius while the linear one gives access to the exciton Landé factor (Fig. 2.19).

Keldysh potential takes into account non isotropic dielectric function. Therefore we can extract both binding and electronic gap energy: 1.890eV for BN capped WSe₂.

In (Fig. 2.20 b) we report the energy difference Δ_{2s-1s} for different dielectric environments. TMD layers are usually supported on SiO₂ which has a dielectric constant of 3.9. On the other hand, boron nitride which is extensively used nowadays as substrate for TMD, has a slightly higher dielectric constant, 5.09 [75]. Therefore, Δ_{2s-1s} for WSe₂ supported on SiO₂ is roughly

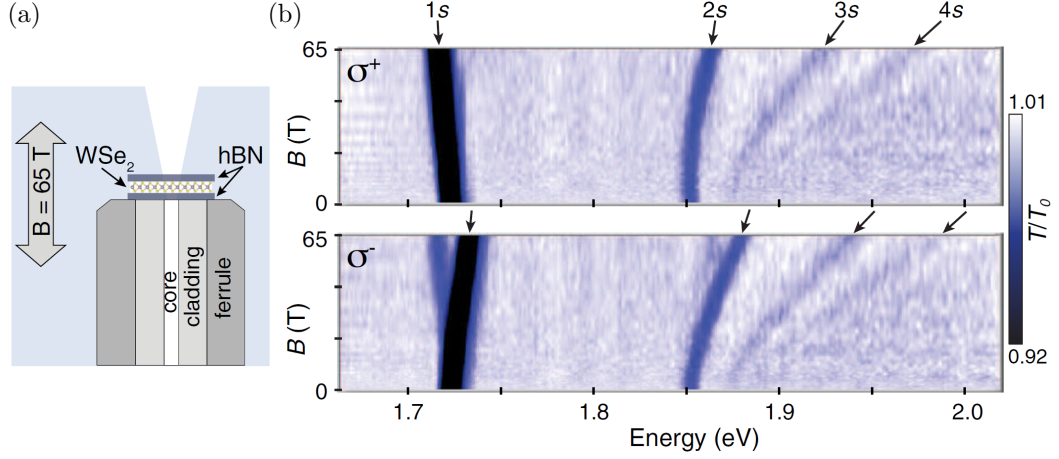


Figure 2.19: a) Sample scheme, the encapsulated layer is deposited on a optical fibre to be compatible with the high magnetic field setup. b) Magneto absorption data reproduced from [5].

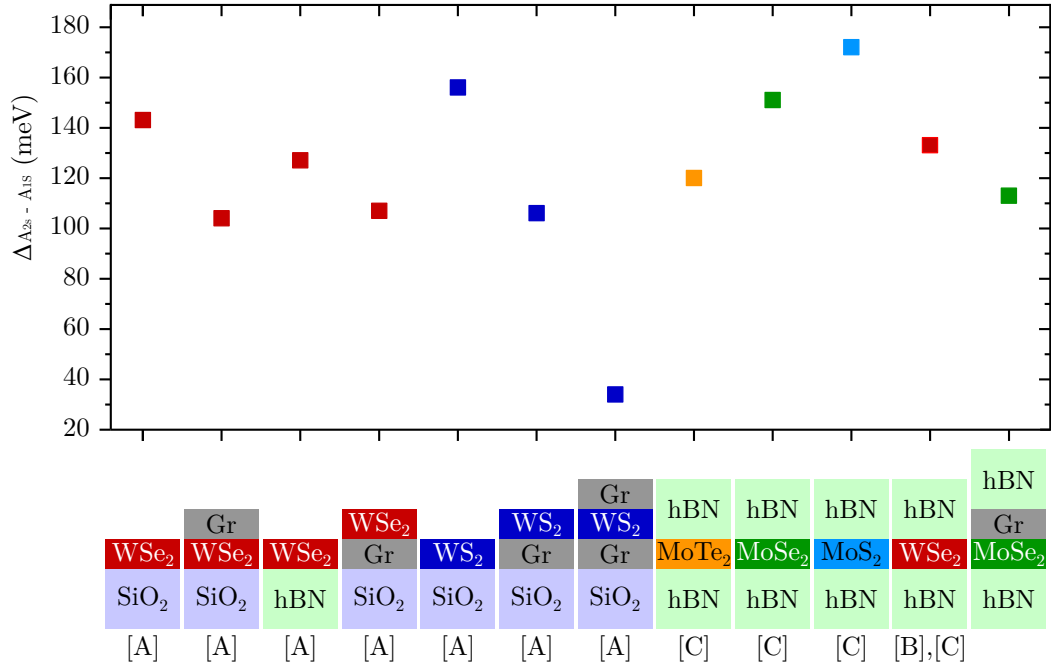


Figure 2.20: Table of the energy difference between the first and second excitonic Rydberg states for different TMD in different dielectric environment. Those data come from different references, [A] is [25], [B] come from [5] and [C] from [74]. The last value comes from our work.

10meV higher than WSe₂ on h-BN. However, adding a graphene monolayer with its high dielectric function changes the splitting Δ_{2s-1s} by 40meV for a sole monolayer.

Within the 2D hydrogen model, the binding energy of the 2s state E_b^1 can be written as $E_b^1 = \frac{1}{9}E_b^0$ with E_b^0 the 1s binding energy. Therefore, the 1s state binding energy can be written as $E_b^0 = \frac{9}{8}\Delta_{2s-1s}$. However, using the Keldysh potential based Hamiltonian, the 1s state binding energy becomes, empirically $E_b^0 = 2\Delta_{2s-1s}$ [4, 25].

2.4.1.3 Charged excitons (trions)

We introduced excitons which are bound states between electron and hole. In addition, three charges bound state could also exist and are called trions. It is worth mentioning that for high electron density compare to the exciton density, the existing bound state are attractive and repulsive polaron instead of trion and exciton respectively. However, we will refer to this species as trion and exciton. Even bi-excitons and charged bi-excitons have been reported in TMD recently [76]. Trions can be seen at room temperature, however bi-excitons are stable only at low temperature. Trions have a binding energy around 30 meV for any TMD which is sufficient to be stable at room temperature (Fig. 2.21 a).

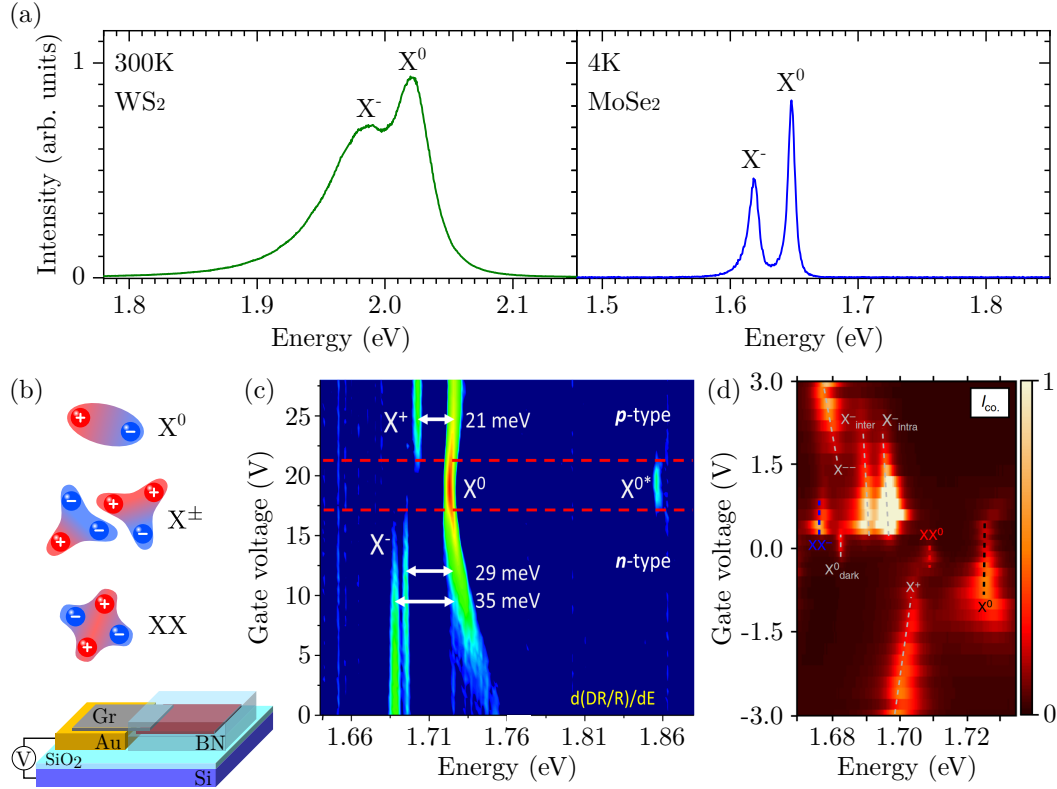


Figure 2.21: a) WS₂ room temperature PL emission in green and MoSe₂ PL emission at 4K. The trion is highlighted by X⁻ and the neutral exciton by X⁰. b) Exciton, positive and negative trion, and bi-exciton representation. At the bottom, we show the scheme of the charge adjustable device used in (c) and (d). The red layer is the TMD. c) Gate dependent differential reflectivity intensity on WSe₂ at 4K. X^{0*} is the neutral exciton second Rydberg state. X⁻ presents two branches because of the many different possible negative trions. d) Gate tunable WSe₂ PL emission, XX and XX[±] refer to neutral bi-excitons and charged bi-excitons respectively.

A strong trion emission and absorption at higher doping is shown in (Fig. 2.21 c-d). The neutral PL exciton intensity decreases when doping increases while charged excitons PL intensity increases. It is then interesting that doping can be measured by reflectivity or trion PL intensity. However, it is in general difficult to find on a sample a perfectly neutral area and most of the time a residual doping induces a residual trion emission even without sizeable trion absorption in

the neutral regime. Finding ways to regulate doping in TMD is then important.

2.4.2 Excitons dynamics

2.4.2.1 Excitons formation

Exciton creation mechanism is an active research field and several mechanisms have been discussed depending on the excitation energy and excitation intensity. At low intensity, photons can be absorbed in linear processes. However, high excitation intensity can lead to non linear absorption processes. Therefore, it can perform second harmonic generation or two-photon absorption, two non linear processes. In the following we will discuss TMD linear absorption mechanisms.

Since TMD present roughly a 500 meV exciton binding energy, the A1s excitonic absorption is 500 meV below the free electron hole pair absorption. Therefore, it is easy to excite the TMD above the A1s absorption but below the free carrier absorption. Moreover, the exciton creation mechanism remains unclear when exciting in between different exciton rydberg state. However, there will always be some residual absorption coming from the different excitonic state. Therefore, we should create excitons. Finally, exciting between the optical and electronic gap should induce the direct creation of higher lying exciton that will then cascade via exciton phonon interaction to the A1s state. However, we do not know which phonon is involved in this mechanism neither its efficiency.

Furthermore, a TMD excited above the electronic gap should create free electron-hole pairs that will then form bound states and decay non radiatively to the A1s state. Such creation mechanism should be slower than the direct exciton creation since the exciton is not created directly. However, it has been demonstrated that exciton creation time from a population of unbound electron hole pairs happen within a sub-picosecond timescale [77].

Once the electron hole-pair decays to the A1s exciton state, it will live a given time before decaying. Recording the A exciton PL time trace can give insight on the exciton creation mechanism, creation time and exciton lifetime.

2.4.2.2 Excitons dynamics

To study the intrinsic exciton lifetime we need a time resolved technique. Among them, femtosecond transient absorption spectroscopy (pump probe) has the smallest temporal Instrumental Response Function (IRF), 100 fs resolution for a commercial system. However, transient absorption and more broadly non-linear spectroscopy rely on high fluence pulses. Therefore, monolayer TMD could perform two photon absorption or second harmonic generation since it is non centrosymmetric crystal. These effects will blur the excitation energy. In addition, high fluences also imply large exciton density leading to exciton-exciton interactions that end up in a very complex dynamic. This is why we will not use this type of technique.

Contrary to the non-linear spectroscopy, Time Resolve Photo-Luminescence (TRPL) needs a detector with a time resolution and then high frequency (THz) electronic which is uncommon

and tricky to realize for direct detection with Avalanche Photo Diode (APD) (cf Appendix B). Detection with a streak camera is different and relies on the same principle as oscilloscope (cf. Appendix B). TRPL has therefore a 500 fs temporal IRF at best with a state of the art streak camera. But more commonly it has a ~ 5 ps IRF. The relatively long IRF is compensated by the possibility to maintain a linear excitation to record PL time trace.

To get insights into a material radiative lifetime, it is better to perform TRPL measurements at low temperature to avoid any temperature effects on the TRPL dynamics. However, at low temperature the TMD exciton dynamics is very fast and below the standard 5 ps resolution [78]. Hence it is only recently that low temperature dynamics has been uncovered [12] using state of the art TRPL setup. Those measurements have been performed on MoSe₂ at different temperatures, from 4K up to room temperature.

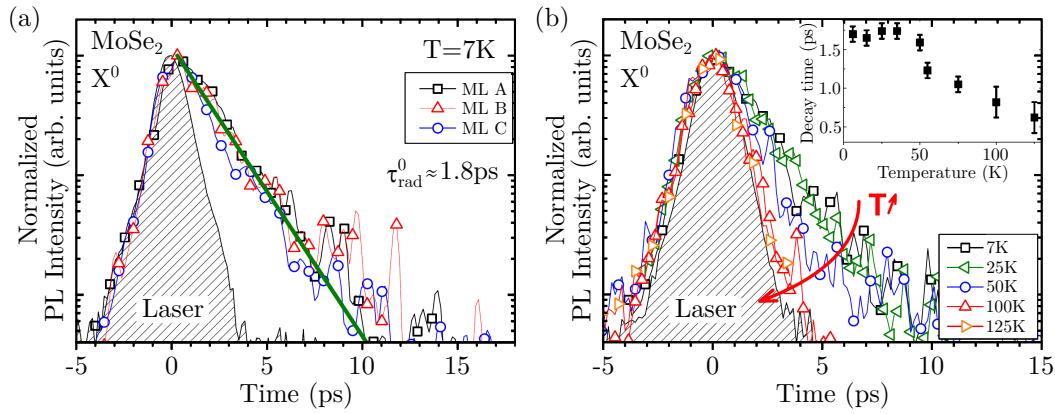


Figure 2.22: a) Time resolved photoluminescence of the MoSe₂ A exciton for three different monolayers coming from different sources. Flakes are supported on SiO₂. The exciton lifetime is 1.8ps and is assumed to be the exciton radiative lifetime. b) A exciton TRPL at different temperatures, the inset represents the decay time evolution with the temperature. For both panel, the Instrumental Response Function is highlighted by the hatched area. The excitation energy is 1.746 eV. Figure reproduced from [12].

In (Fig. 2.22) the extracted exciton lifetime on MoSe₂ is 1.8ps. The exciton lifetime is different from the exciton radiative lifetime in general. However, each decay time involves a new exponential decay in the PL time trace. The absence of any longer decay time in their data, the rise of a secondary longer time around 100 K (Fig. 2.23) and the temperature independence of the exciton lifetime below 40K give them arguments to consider this short decay time to be the radiative decay time τ_{rad}^0 . It is then reasonable to think that they have measured radiative decay time even if there is no indisputable evidence of this. In addition, this short decay time combined with the excitation energy below the free carrier absorption indicate that the emission comes from a non-thermalized exciton population at low momentum. We have to emphasize now that an exciton can emit a photon only if it fulfills a momentum matching condition with the photon dispersion relation $\omega_{\text{ph}} = ck_{\text{ph}}$. If the exciton momentum is too high, it will not couple to light and therefore it will not emit light.

Between 40K and 100K, the exciton lifetime starts to decrease due to the exciton-phonon inter-

action that kicks exciton out of the light cone. This should induce a second longer decay time but the population that leaves the light cone is too small to be detected. Finally, above 100K this population is large enough to be recorded (Fig. 2.23) and gives rise to a PL time trace with a short and a long decay time. The short decay time corresponds to a non-thermalized emission while the longer one corresponds to the thermalized population.

At this point, we have to emphasize that rising time (the time needed to reach the time trace maximum) is not resolved on the time trace. Therefore, the exciton creation time is below the IRF, giving a 0.5 ps upper bound to the exciton creation time.

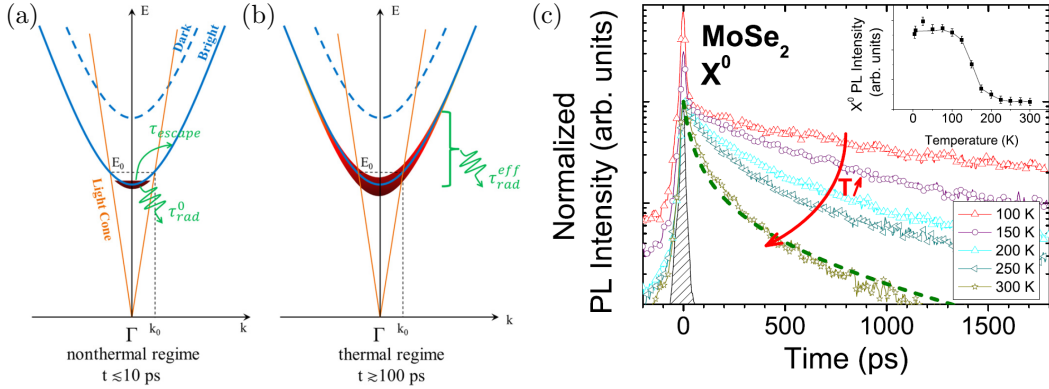


Figure 2.23: (a) Low temperature exciton population, a non thermalized population lies at the bottom of the exciton dispersion relation (blue solid line) inside the light cone (orange line). The dark exciton dispersion relation is the dashed blue line. b) Same as (a) for a thermalized population that spreads outside of the light cone. Photoluminescence time traces from 100K to Room temperature. Figure reproduced from [12].

Increasing the temperature increases the thermalized over non-thermalized population ratio as well as the effective radiative lifetime $\tau_{\text{rad}}^{\text{eff}}$ corresponding to the thermalized population radiative decay rate. This lifetime increases because the exciton Boltzmann distribution explores larger K when temperature increases. In addition, the escape time outside of the light cone becomes shorter and shorter. Finally, the effective radiative lifetime is

$$\tau_{\text{rad}}^{\text{eff}} = \frac{3k_B T}{2E_0} \tau_{\text{rad}}^0 \quad (2.15)$$

with k_B the Boltzmann constant and E_0 the maximum kinetic energy for an exciton to couple to light (Fig. 2.23 a,b) [12]. Eq.(2.15) gives a linear dependence of the exciton effective radiative lifetime due to the thermalization. Therefore, the lifetime should increase with temperature above 100 K. However, with increasing temperature, excitons diffuse more and more. Hence, they are more likely to collide with each other. This could induce exciton-exciton annihilation (EEA) also known as Auger recombination.

2.4.2.3 Controlling exciton dynamics

Before going further, we have to mention that recent TRPL measurements on BN encapsulated MoSe₂ layer bring new insights on the excitonic dynamics in TMD monolayers [79]. First we need to emphasize that the radiative lifetime τ_{rad}^0 depends on the dielectric environment as

$$\tau_{\text{rad}}^0 = \frac{\varepsilon m_e}{E_g \hbar k_0} \left(\frac{E_{X^0}}{e} \right)^2 a_0^2 \quad (2.16)$$

with E_{X^0} the exciton emission energy and $k_0 = E_{X^0} \sqrt{\varepsilon} / \hbar c$ the light wavevector in the dielectric environment. From (2.16) we found that radiative lifetime increases with the dielectric screening. However, BN defines an optical cavity (Fig. 2.24 a) that impacts the radiative lifetime through Purcell effect.

For practical reason, when people perform such TRPL experiment, the excitation laser energy is most of the time off resonant. Therefore, a photon has to be absorbed while a phonon is created in the material (Fig. 2.24 b) to finally create an exciton. These leads to the formation of a high momentum exciton population which are not optically active since such exciton are outside of the lightcone. Such high momentum population will form a reservoir. Excitons in the reservoir will be bring to the bottom of the exciton dispersion relation via exciton-phonon interaction at a rate Γ_{relax} . Once inside the lightcone, an exciton can desexcite radiatively at a rate Γ_X . Solving the rate equation model presented in (Fig. 2.24 c) gives the time dependent population of the optically active state $n_X(t)$

$$n_X(t) = \frac{n_R^0}{\tau_{\text{relax}} - \tau_X} \left[\exp\left(\frac{-t}{\tau_{\text{relax}}}\right) - \exp\left(\frac{-t}{\tau_X}\right) \right] \quad (2.17)$$

with n_R^0 the population in the exciton population in the reservoir at $t = 0$, τ_X and τ_{relax} the characteristic time associated with Γ_{relax} and Γ_X respectively. Remarkably, Eq. (2.17) depends only on $|\tau_{\text{relax}} - \tau_X|$ as shown in (Fig. 2.24 d). in addition, a bare TMD layer supported on SiO₂, has a τ_{relax} much below the experimental sensitivity and cannot be resolved. Therefore, in this condition, the time trace is a mono-exponential decay with a characteristic time τ_X . However, when encapsulated into BN, the exciton phonon coupling is soften and τ_{relax} can be measured. For BN encapsulated samples, the relaxation time becomes actually larger than the exciton desexcitation time and has been measured in (Fig. 2.24 e). Finally, by modulating the bottom BN thickness, the cavity can be tuned on and off resonant modulating the radiative lifetime of the exciton (Fig. 2.24 f).

2.4.2.4 Non linear effect: Auger recombination

Auger recombination is a non linear process involving two different excitons that interact together. One of them decays non radiatively by transferring its energy to the second via dipole/dipole interaction. Therefore, the second becomes a free electron hole pair (Fig. 2.25).

Auger recombination will be more likely to happen at high exciton density, but also for highly diffusive exciton. Since an exciton that diffuses more is more likely to interact with another one. The exciton-exciton annihilation is a non linear effect that depends on the square of the exciton

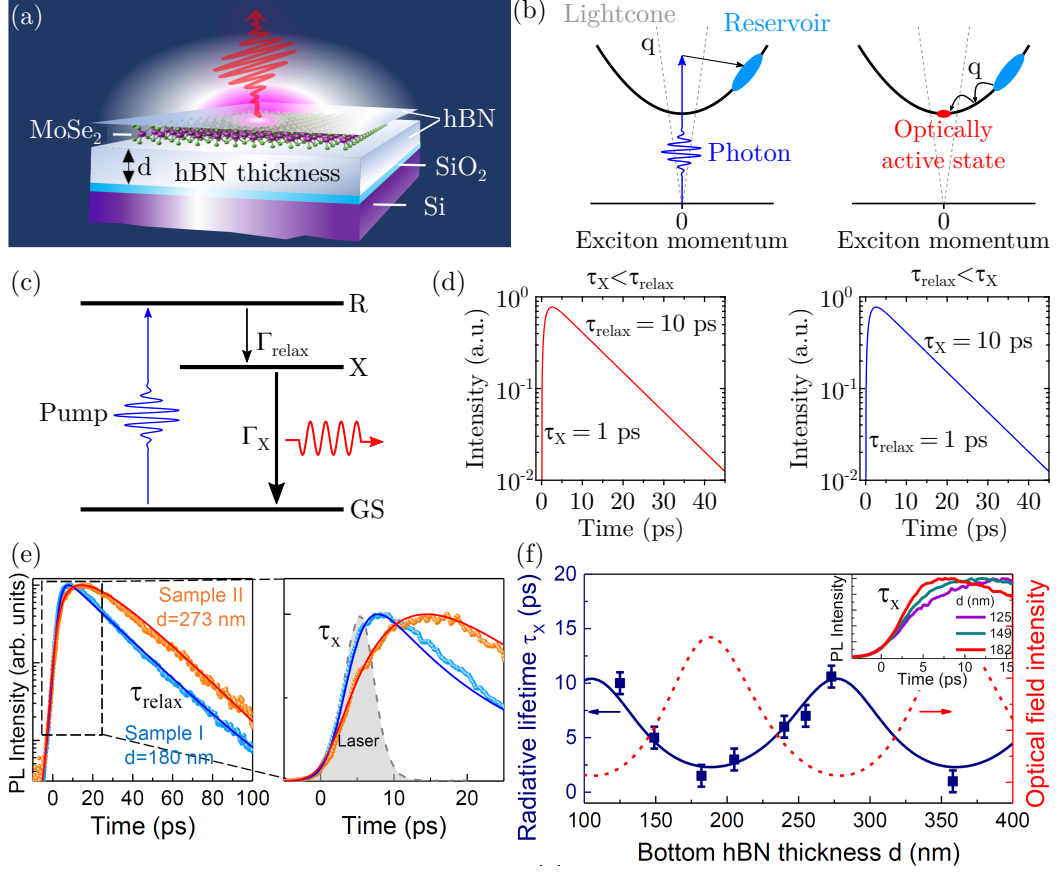


Figure 2.24: a) Scheme of the samples studied. the MoSe_2 is deposited on different BN thickness and then encapsulated with a thin BN layer. b) Excitation of high momentum exciton creating an exciton reservoir in blue. Second panel, decay of excitons from the reservoir to the optically active state in red via exciton phonon coupling. c) Rate equation model of the exciton dynamics for a BN encapsulated MoSe_2 . d) Simulation of optically active exciton population given by Eq. 2.17 for different values of τ_{relax} and τ_X . e) MoSe_2 PL decay time of a flake on 273nm (180nm) BN in orange (blue) the second panel corresponds to a zoom around the short time, the grey area represents the IRF. Rise times are slightly out of the IRF while the decay time is fully resolved. f) Radiative lifetime extracted from different BN thickness. The solid line corresponds to the lifetime calculated, taking into account the cavity effect (Purcell effect) induced by the thick BN. Dots are the experimental points. Figures are reproduced from [79].

population. Therefore, EEA can be brought to light by increasing the photon flux. A non linear behavior with respect to excitation intensity is the indubitable proof of exciton non linear decay mechanism such as Auger recombination.

The Auger effect has been studied in detail in [80], extracting from their experiment the exciton diffusion coefficient (Fig. 2.26 a).

Interestingly, the time trace reported in (Fig. 2.26) shows a dip appearing at sufficiently high excitation energy density. In real space this corresponds to a ring shape emission pattern. Such pattern is due to the increase of the diffusion coefficient thanks to the Auger effect (exciton-exciton annihilation). The effective diffusion coefficient modified by the Auger effect is $D_{\text{eff}} =$

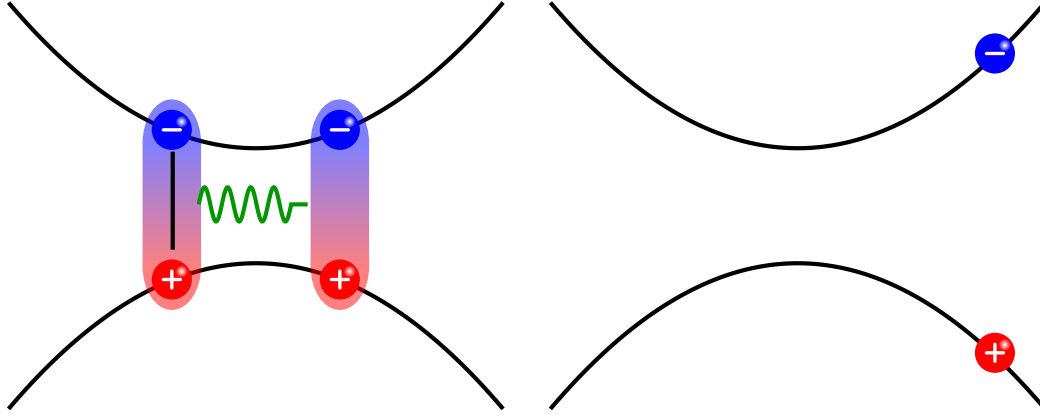


Figure 2.25: Exciton decaying via Auger recombination.

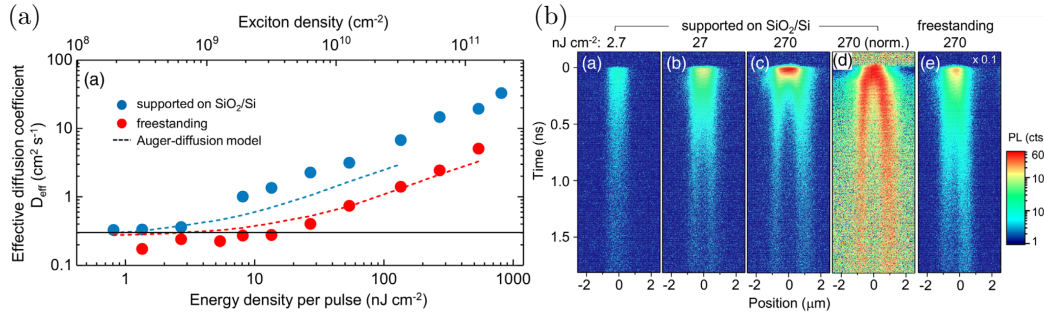


Figure 2.26: a) Exciton diffusion coefficient with respect to the pump fluence. b) time evolution of the exciton population with respect to position along a direction. Adapted from [80].

$D + R_A n_0 w_0^2 / 16$ with R_A the Auger coefficient, n_0 and w_0 the initial peak density and width of the exciton distribution. Exciton-exciton annihilation will occur between two near excitons and diffusion could bring them close together. On the other hand, an Auger recombination will give a kick to the exciton increasing its momentum and therefore its diffusion coefficient. This is how this effect is understood.

We have a picture of the exciton decay mechanism and dynamics, but many questions about the exciton creation mechanism and dynamics remain unanswered. The exciton creation time is shorter than one ps. However, this is just an upper bound and there is no clear exciton creation mechanism yet. In addition, given the high exciton binding energy, exciting below or above the free carrier absorption could change the exciton formation mechanism and finally very little is known about this.

2.4.3 Spin-valley locking and valley excitons

2.4.3.1 Selection rules

We already emphasized the effect of the valence band splitting that lead to the energy difference between A and B exciton (cf Section 2.2.3). However, we did not discuss yet the effect of the

conduction band splitting. Since this splitting is small, both transitions could be possible leading to different exciton split by few tens meV. However, the total angular momentum has to be conserved. Therefore, an optical selection rule rises for photon incidence perpendicular to the TMD plane.

$$m_h + m_e = m_{ph} \pmod{3} \quad (2.18)$$

with m_e (m_h) the electron in the conduction band (hole in the valence band) angular momentum and $m_{ph} = \pm 1$ the photon total angular momentum. The mod 3 takes into account the three fold rotation symmetry of the system [81]. The valence (conduction) band angular momentum has been calculated to be 2 (0) [48, 82]. Combined with the electron spin, we end up with the total angular momentum given in (Fig. 2.27). We remind that total angular momentums are given for electrons in the valence and conduction bands. However, holes in the valence band have opposite quantum numbers compared to the electron in valence band. Therefore, in the valence band, $m_h = -m_e$. Finally, using Eq.(2.18) we have $m_h_{\Gamma_{10,11}} + m_e_{\Gamma_7} = -5/2 + 1/2 = 1 \pmod{3}$ therefore, the bands labeled Γ_{10} and Γ_{11} couple to Γ_7 , while the bands labeled Γ_{12} and Γ_9 couple to Γ_8 (Fig. 2.27).

The transition previously described can be addressed by photons with a given circular polarization determined by m_{ph} in Eq.(2.18). Therefore, excitons in a monolayer TMD can be created in a given valley, and are then said *valley-polarized*. Moreover, optical transitions between opposite spin sub-band are forbidden, since orbital momentum cannot be conserved. Such spin forbidden transitions are called dark, or gray [9, 27] excitons ¹. If the lowest energy A exciton couples to light, the TMD is then called bright and should emit better at low temperature because at room temperature the inactive transition could be thermally populated decreasing the yield of the photoluminescence (Fig. 1.18). On the contrary, if the lowest energy transition is dark, the TMD is called dark and will emit better at room temperature because the optically active transition will be thermally populated. Bright TMD are Molybdenum based while dark ones are Tungsten based TMD even if there remains a controversy on the bright character of MoS₂.

Before going further, we would like to emphasize that valley selectivity in monolayer TMD should not be present in any multilayer sample. By a simple symmetry argument, we can show that even number of layers TMD should not display valley polarization. However, odd numbers of layers present this polarization. This is due to the presence or absence of an inversion center. Since its presence, in even number of layer TMD samples, imposes that spin up sub-band energy at K $E(\mathbf{K}, \uparrow) = E(-\mathbf{K}, \uparrow)$. This should unprotect the valley polarization and destroy valley properties. However, reports of robust valley polarization in bilayer TMD exist [83]. Such polarized emission could be explained by extrinsic factors such as defect or strain that locally break the inversion symmetry of the system. It could also rise from the intrinsic physics of the spin-orbit coupling [84] that has been predicted to give circularly polarized PL emission for bilayer TMD up to 93%.

¹Gray because those excitons do not couple to in plane electric field. However, they do couple to electric field normal to the plane. Therefore, a high numerical aperture objective can excite and detect this type of excitons.

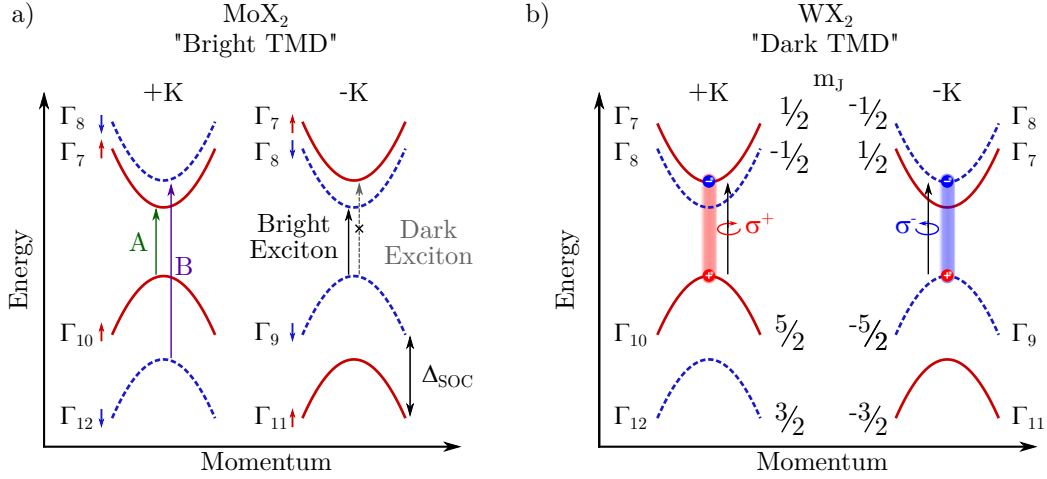


Figure 2.27: The red and blue arrows correspond to the electron spin direction. a) Spin structure sketch of a Molybdenum based TMD. Optically active A and B exciton are presented on the left side. Here A excitons are bright and so are Molybdenum based TMD. However, B excitons are dark. $\pm K$ valley has opposite spin structure but the transition energy still the same for both valley. b) Spin structure for a dark TMD. Optical selection rules are presented for both valleys. The spin value is reported on the right hand side of the band structure.

2.4.3.2 Valley polarization and coherence

Using circularly polarized light, it is possible to create an exciton population in a given valley giving rise to the valley pseudo-spin ± 1 . Let us define an exciton with ± 1 pseudo-spin as $|\pm 1\rangle$, a right or left polarized photon as $|\sigma^\pm\rangle$ and finally a vertically (horizontally) polarized photon as $|V\rangle$ ($|H\rangle$). We can use Jones formalism to map any perfectly polarized states on a two dimension vector space, usually people use the $\{|V\rangle, |H\rangle\}$ basis but $\{|\sigma^+\rangle, |\sigma^-\rangle\}$ basis could be used instead of the previous one¹. In this basis we can express the vertically and horizontally polarized photon as follow,

$$|V\rangle = \frac{i}{\sqrt{2}} (|\sigma^+\rangle - |\sigma^-\rangle) \quad (2.19)$$

$$|H\rangle = \frac{1}{\sqrt{2}} (|\sigma^+\rangle + |\sigma^-\rangle). \quad (2.20)$$

A linear polarization is then a sum of both circular polarizations with a fixed phase relation between them, which is by definition a coherent superposition of circularly polarized photons. Therefore, using linear polarization to excite the A exciton, results in the creation of a coherent superposition of exciton at + and $-K$ valley. This superposition for vertical or horizontal polarizations is then written as

¹Actually any opposite pole of the Poincaré sphere can be used as a basis not only linearly or circularly polarized states

$$|V\rangle \longleftrightarrow \frac{i}{\sqrt{2}} (|+1\rangle - |-1\rangle) \quad (2.21)$$

$$|H\rangle \longleftrightarrow \frac{1}{\sqrt{2}} (|+1\rangle + |-1\rangle) \quad (2.22)$$

Excluding every spin relaxation and decoherence mechanisms for excitons, the photon absorbed by the excited state will then be re-emitted as it was absorbed i.e. circularly polarized for a exciton in a given valley and linearly polarized for a coherent superposition of excitons. But there is obviously spin relaxation and decoherence mechanism that will be discussed in the following.

2.4.4 Exciton pseudo-spin relaxation and decoherence

Spin relaxation mechanisms in transition metal dichalcogenide is still an active topic and the question « what are the spin relaxation mechanisms? » has no clear answer yet, but there is few mechanisms that are discussed in the literature.

First, the electron phonon interaction could give rise to a spin flip and could have enough momentum to change electron valley number however, this phonon mediated process is likely to happen for a single charge but unlikely to happen for a whole exciton because electron and hole has to be scattered at the same time. Due to its phononic nature, this process should be thermally activated.

Second, the Coulomb exchange interaction could also play a key role here. Since excitons in 2D system present large binding energy and small Bohr radii, the exchange interaction will be important in TMD. Such interaction will link the + and - K valley together via dipole-dipole interaction. This process is somewhat similar to a Förster energy transfer and should vanish at $K = 0$ [85, 86]. In the end, it is rather complicated to determine an analytical form of those decay mechanism. Most of the time an effective model and rate equations are used to describe this physics.

2.4.4.1 Rate equations for the exciton pseudo-spin relaxation

Even though it is complicated to understand which mechanism is destroying the valley polarization, by performing polarization resolve measurement in the steady state, we can extract the valley lifetime by using rate equations that give the dynamics of population with a given spin n_{\pm} . First the observable is the contrast ρ between emitted light intensity in both circular polarization for a given circular excitation ($I_{\sigma^{\pm}}(\sigma^{\pm})$), and is defined by,

$$\rho = \frac{I_{\sigma^+}(\sigma^+) - I_{\sigma^+}(\sigma^-)}{I_{\sigma^+}(\sigma^+) + I_{\sigma^+}(\sigma^-)} = \frac{n_+ - n_-}{n_+ + n_-}. \quad (2.23)$$

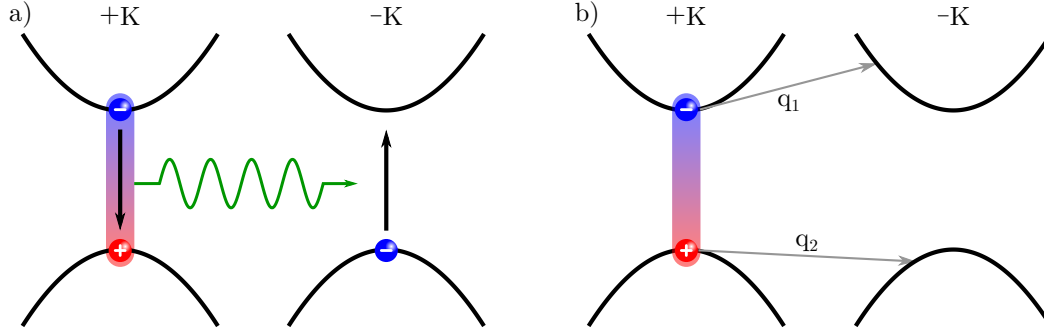


Figure 2.28: a) Coulomb exchange interaction leading to the switch of the electron hole pair valley index. b) Same as a for phonon mediated process. phonons are represented by grey arrows.

Once a valley is optically pumped, the created exciton could either decay from this valley or first be exchanged to the other valley and then decay. The rate equation governing the exciton pseudo-spin population dynamic, and moreover the exciton population dynamics, could be written as [87]

$$\begin{cases} \dot{n}_+ = A\phi + \Gamma_s n_- - \Gamma_s n_+ - \Gamma_d n_+ \\ \dot{n}_- = \Gamma_s n_+ - \Gamma_s n_- - \Gamma_d n_- \end{cases} \quad (2.24)$$

with A the TMD absorption, Γ_s the exchange rate between the exciton pseudo-spin up and down and Γ_d the total (radiative and non-radiative) decay rate. In the steady state, the time variation disappears and Eq. (2.24) becomes,

$$\begin{cases} \Gamma_s n_+ + \Gamma_d n_+ = A\phi + \Gamma_s n_- \\ \frac{\Gamma_s + \Gamma_d}{\Gamma_s} n_- = n_+ \end{cases} \quad (2.25)$$

Combining Eq. (2.23)) and (2.25) allow us to rewrite the contrast ρ in terms of decay and exchange rate as follow,

$$\rho = \frac{1}{1 + \frac{2\Gamma_s}{\Gamma_d}} \quad (2.26)$$

However, Eq. (2.26) stands for excitation that creates population in a given valley. This is valid for purely resonant excitation. Furthermore, such measurements are most of the time done slightly of resonant and therefore, it could be possible in the exciton creation mechanism to marginally populate the second valley. Therefore, we can introduce a $\rho_0 < 1$ term that will takes this effect into account transforming eq.(2.26) into

$$\rho = \frac{\rho_0}{1 + \frac{2\Gamma_s}{\Gamma_d}} \quad (2.27)$$

2.4.4.2 Rate equation for the exciton decoherence

We can measure the coherence in the steady state, the same way we measure the polarization defining a new ratio γ which depends on the co (I_{XX}) and cross (I_{XY}) polarization intensity.

$$\gamma = \frac{I_{XX} - I_{XY}}{I_{XX} + I_{XY}}. \quad (2.28)$$

The same way we express ρ with respect to population, we will express γ with respect to the coherent (n_c) and incoherent (n_u) populations. Let us assume that no pure dephasing mechanisms are at work here. If a coherent state undergoes an intervalley scattering, it will lose its coherence but a coherent state will not be retrieved after an intervalley scattering of an incoherent state (Fig. 2.29 b).

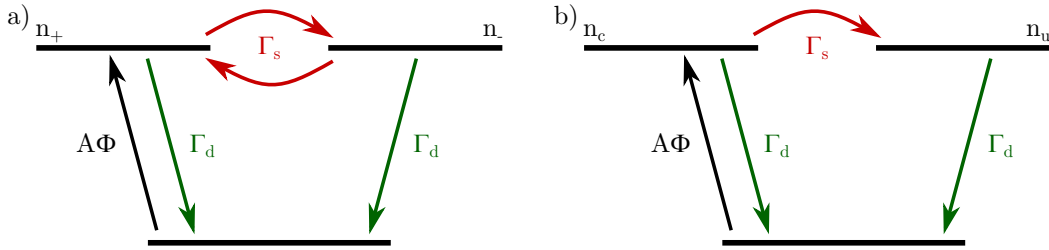


Figure 2.29: a) Population rate equation model for a σ^+ excitation, red arrow represents the intervalley scattering rate Γ_s , the black one is the pumping term and the green the desexcitation rate. b) Same as (a) for coherent superposition obtain by shining linear polarized light on the sample.

The copolarized intensity contain the whole luminescence emitted by the coherent population by definition but also half of the incoherent population since incoherent light has fifty percent photons with a given polarization and fifty percent in the orthogonal polarization (i.e. 50% vertically and 50% horizontally polarized photons). The copolarized intensity could be written as $I_{XX} = n_c + \frac{1}{2}n_u$. For the same reason, I_{XY} contain only half of the incoherent population emission and $I_{XY} = \frac{1}{2}n_u$. The valley coherence could be written as,

$$\gamma = \frac{n_c}{n_c + n_u}. \quad (2.29)$$

The rate equations in the steady state are

$$\begin{cases} A\phi = \Gamma_s n_c + \Gamma_d n_c \\ n_u = \frac{\Gamma_s}{\Gamma_d} n_c. \end{cases} \quad (2.30)$$

The valley degree of coherence γ , by combining Eq. (2.29) and (2.31), then becomes,

$$\gamma = \frac{1}{1 + \frac{\Gamma_s}{\Gamma_d}} \quad (2.31)$$

This shows that coherence is longer lived than the spin population as long as no other dephasing

mechanisms are present.

2.4.4.3 State of the art

Valley contrast have been tracked in many different samples. The first report of valley polarization has been done in 2012 [87] and valley coherence in 2013 [88].

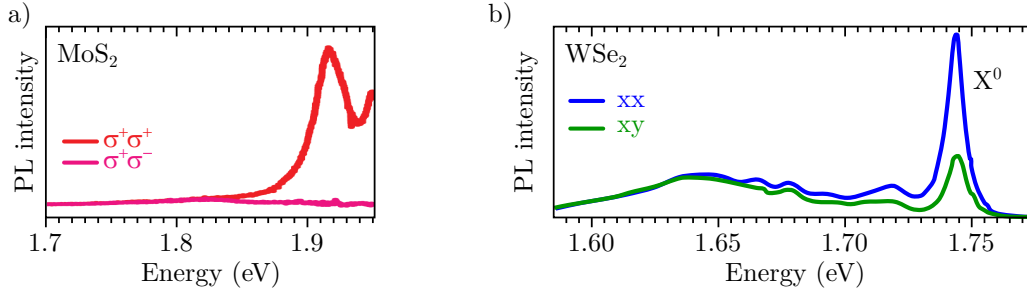


Figure 2.30: a) MoS_2 monolayer PL emission at 14 K excited with a σ^+ polarized light and analysed with a σ^+ (red) and σ^- (pink) polarization. Adapted from [87] b) WSe_2 monolayer PL emission at 30 K excited with a vertical polarization analysed on a vertical (blue) and horizontal (green) polarization basis. Adapted from [88].

On MoS_2 , the PL emission is perfectly circularly polarized (Fig. 2.30 a). However, the same year and for the same material (MoS_2) at least three different values has been reported: 100% [82, 87], 50% [89] and 32% [90]. Those data then need to be taken cautiously. Moreover, the PL emission of WSe_2 when excited with a linear polarization is linearly polarized even if it is not perfectly polarized. Here, a 35% valley coherence degree have been reported (Fig. 2.30 b).

	MoS_2	$MoSe_2$	WS_2	WSe_2	$MoTe_2$
ρ	1; 0.3*	<0.05	0.4	0.5	0
γ	0.55*	<0.05	0.04	0.35	0

Table 2.3: State of the art value of the valley polarization and coherence at low temperature for different TMD. The value followed by a star * have been obtained in BN capped samples.

We reported in Table 3.2 the state of the art values for ρ and γ the degree of valley polarization and coherence. Those data have been extracted from the literature, MoS_2 (BN capped) : [8], WS_2 : [83], WSe_2 : [88], $MoSe_2$: [91], $MoTe_2$: [92]. All those data have been taken at low temperature. However, report of room temperature valley polarization have been done but they all rely on defective samples [93, 94]. Since highly defective sample are short lived, they could display non vanishing valley polarization contrast. However, the valley coherence is fragile and can be destroyed by scattering on any defects. Therefore, low quality samples do not display valley coherence which remains elusive at room temperature. The protection of these properties up to room temperature stills a challenge. We will go back to this problematic in Chapter 4.

2.5 Van der Waals heterostructures

2.5.1 Introduction

Semiconductor heterostructures have been grown for decades, using 3D semiconductor grown on top of each other (e.g. GaAs/AlGaAs). Even if each semiconductor slab can be grown as thin as it is needed, out of plane dangling bonds will remain as the signature of their 3D nature. Therefore, the dangling bonds of the two semiconductors will form covalent bonds. Hence, such structure could be called covalent heterostructure. For thick semiconductor layer, the strain will relax within a μm . However, to get thin heterostructure, the dangling bonds impose drastic conditions on lattice mismatch. Since few percent lattice mismatch between the two semiconductors could lead to cracks in the atomic structure with dramatic effect on the electronic and optical properties of the 2D system.

In addition, 2D materials have no-out-of plane dangling bonds and can therefore be stacked together without lattice mismatch problem. Since there are no covalent bounds, the 2D materials are held together by van der Waals interaction and virtually any 2D material can be stack on a together. Therefore, such structures are called van der Waals heterostructure. In the following, we will make use of different 2D materials to realize those heterostructure. The different materials properties are summarized in table 2.4

	Optical bandgap @300K (eV)	optical dielectric constant	lattice constant (\AA)
1L TMD	1.1 (MoTe ₂) to 2.0 (WS ₂)	6 (WS ₂) to 10 (MoTe ₂)	3.19 (WS ₂) to 3.55 (MoTe ₂)
Graphene	0	-	2.46
h-BN	5.7	3	2.51

Table 2.4: *The optical dielectric constant is taken perpendicular to the layer for BN , the optical gap value is taken from [95]. The dielectric constant values comes from [96].*

Even with lattice mismatch as high as 44%, the crystalline structure of the 2D materials will be minimally altered in such structure. Beside their easy implementation as compared to covalent heterostructures, van der Waals heterostructures allow us to improve 2D materials properties. A TMD encapsulated in BN get sharper optical resonance (cf Sect. 2.4) [8].

More interestingly, those structures can form moiré pattern that can give new properties such as superconductivity in twisted bilayer graphene [97] (Fig. 2.31 a). Giving the large range of properties covered by layered compound, Van der Waals structure allows us to create sharp and clean interfaces between different 2D electron gas, tune the distance between them and study interactions between them in a way that was not possible before.

The simplest case of van der Waals heterostructure is the encapsulation in hexagonal boron nitride (BN). BN is an interesting layered material, insulator with a dielectric constant of 4 slightly higher than the silicon dioxide one in the visible range. It could be exfoliated down to a monolayer giving a very nice tool to control the distance between two materials. As a

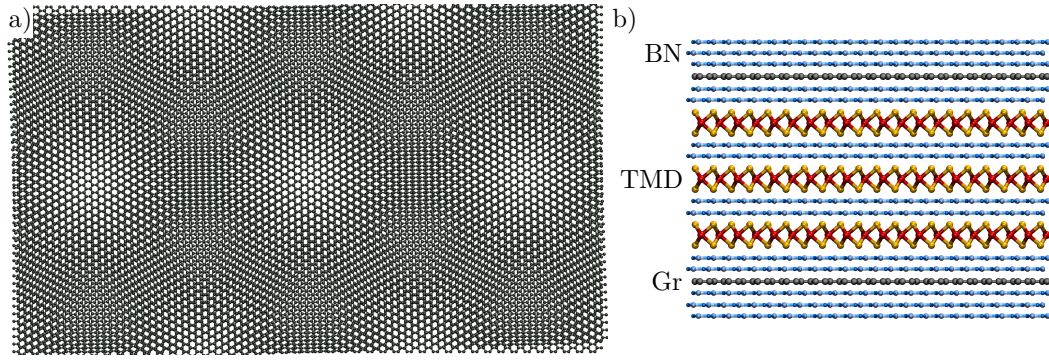


Figure 2.31: a) bilayer graphene twisted by 2° forming a Moiré pattern. b) Van der Waals heterostructure based light emitting diode [34]. Graphene layers are contacted to be used as electrodes.

substrate, BN is perfectly flat and crystalline and when stacked with other TMD or graphene, usual assembly technique allows to agglomerate dirt and dust in big pocket leaving perfectly flat and clean interface (Fig. 6.6) behind [13, 98, 99]. BN encapsulation removes all the adsorbate on both side enhancing 2D material properties. Graphene encapsulation enhances its mobility to the state of the art suspended graphene mobility [19, 100].

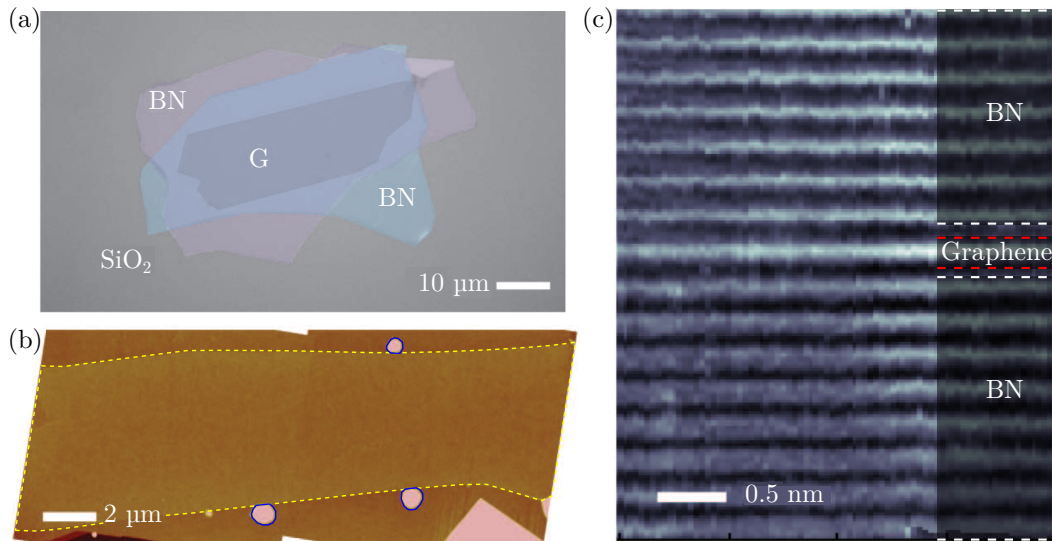


Figure 2.32: a) optical micrograph of a BN encapsulated graphene sample. The full stack is supported on SiO_2 . b) AFM topography of the graphene region. No bubbles or residue can be seen. c) TEM image of a cut normal to the substrate. BN is present between white dashed lines and graphene between the red dashed lines. No residue can be seen. Figure adapted from [101].

In (Fig. 6.6 b) the AFM image shows a flat landscape except three bubbles highlighted in blue aside the graphene layer highlighted in yellow. The TEM image of the stack along the stacking direction also shows no adsorbate between the BN and the graphene (Fig. 6.6 c). This cleaning effect can be observed on any 2H-TMD, graphene or BN interface.

2.5.2 Transition metal dichalcogenide hetero-bilayer

Despite its effect on optical or electronic properties, the effect of BN is to remove any adsorbate from the layer it encapsulates and by this mean enhance the layer properties. However, the BN itself do not interact with the material it encapsulates. It is the BN flatness, its layered character and finally its crystalline structure: hexagonal with a given lattice parameters that impact the capped layer. Even in the case of Moiré lattices, it is only the lattice constant that matters.

Even though BN does not interact with TMD nor graphene layers, a TMD layer can interact with another one in heterobilayer. Each TMD can host strong dipole due to excitonic effect and they can interact together leading to Förster Energy transfer. Semiconductor can be doped and therefore charges can be exchange between the two layers. It is also possible to define pn junction in such system. Moreover, TMD always form type 2 heterojunction (Fig. 2.33) with top valence band in one material while the lowest conduction band is in the other one. This will lead to various effects that we will discuss in the following.

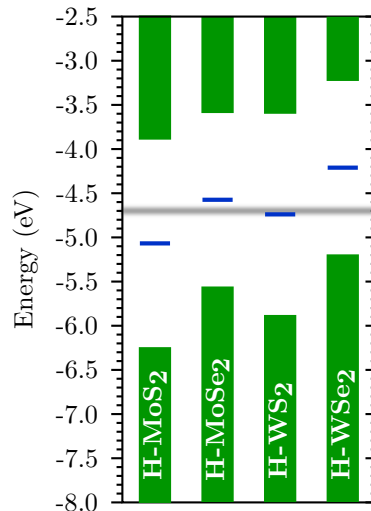


Figure 2.33: Valence, conduction band and Fermi energy in green and blue respectively for different TMD calculated *ab initio* without GW correction adapted from [102]. The grey line correspond to the neutral graphene Fermi energy measured by KPFM [103].

First, both TMD photo-luminescence are quenched. Second, a new peak can appear corresponding to interlayer excitons with an electron in one layer and a hole in the other. This highlights a real interaction between TMD layers as long as charges are transferred from a TMD layer to the other. This charge transfer acts as a new decay mechanism, which explains the PL quenching (Fig. 2.34).

The band alignment between WSe₂ and MoSe₂ is type II. In this configuration charges can be transferred from one material to the other and interlayer exciton can be created between the two charges hosted in the two different layers. MoSe₂ in plane crystalline axis length is 3.33 Å while the WSe₂ one is 3.33 Å as well. Therefore, An angle $n\pi/3$ between the WSe₂ and MoSe₂ crystalline axis, stacks $\pm K$ point of each Brillouin zone on top of each other.

With such alignment, the exciton momentum will vanish leading to the interlayer exciton light

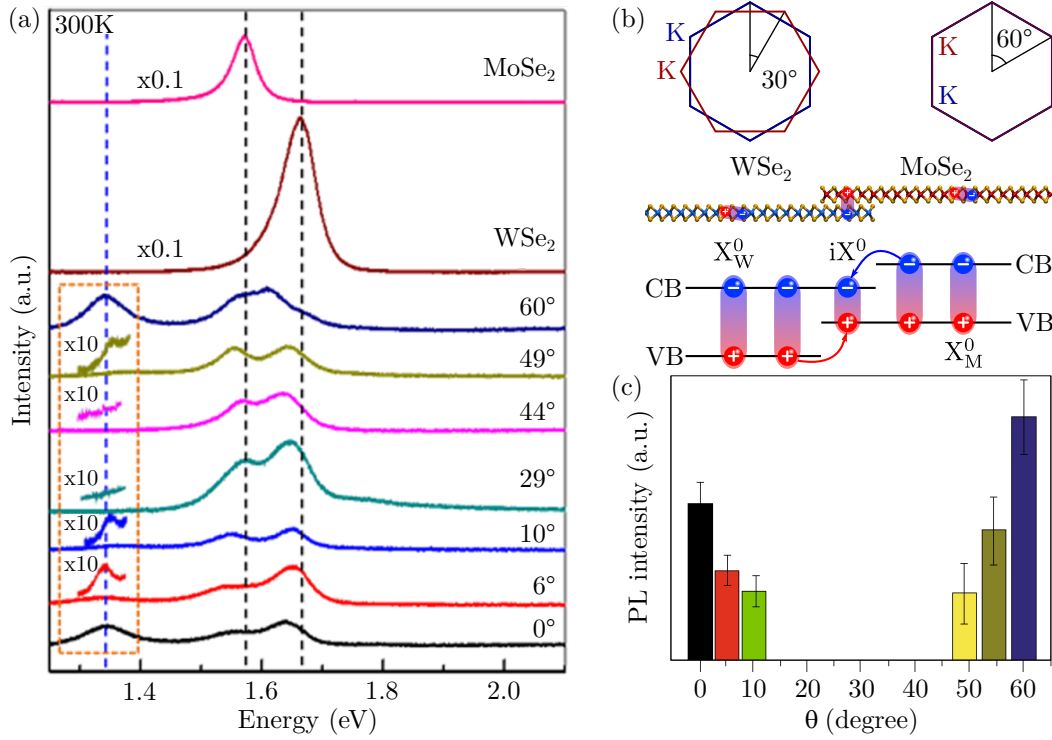


Figure 2.34: *a) Room temperature PL spectra of a $WSe_2/MoSe_2$ with respect to the crystalline axis angle. b) sketch of the band edge alignment of $MoSe_2$ in blue and WSe_2 in red. At the bottom, we show WSe_2 and $MoSe_2$ neutral exciton with the interlayer exciton after a charge transfer process. c) Interlayer exciton intensity with respect to the angle between $MoSe_2$ and WSe_2 crystalline axis. (a) and (c) are reproduced from [104].*

emission. However, as the angle between TMDs crystalline axis tends to 30° , the interlayer exciton PL intensity decreases. In this case, the PL reduction is due to the misalignment between the crystalline axis that increase the exciton momentum until it gets out of the light cone. At this point, the exciton is no more able to decay radiatively (Fig. 2.34 a,c).

It is also interesting to note that TMD neutral exciton PL intensity is always reduced. The quenching factor range from 40 with perfectly aligned bilayer ($\theta = 60^\circ$) to 20 for perfectly misaligned bilayer ($\theta = 30^\circ$). This suggests that, charges can circumvent the momentum mismatch for misaligned hetero-bilayer [105] via electron defect scattering. Alternatively, it could also be the smoking gun of an energy transfer from a TMD to the other [106].

2.5.3 Transition metal dichalcogenide/Graphene heterostructure

To further study the interaction between two dimensional layers, we study the TMD/Graphene heterostructure. Graphene is a semimetal, easy to contact on which local technique to study doping and strain have been developed (cf. Chapter 3). Graphene is usable as an electrode to create ohmic contact with TMD. A TMD monolayer displays large exciton PL intensity. However, when interfaced with graphene the TMD PL yield drops dramatically (Fig. 2.35), with a quenching factor of 300. This highlights the strong interaction between those two materials.

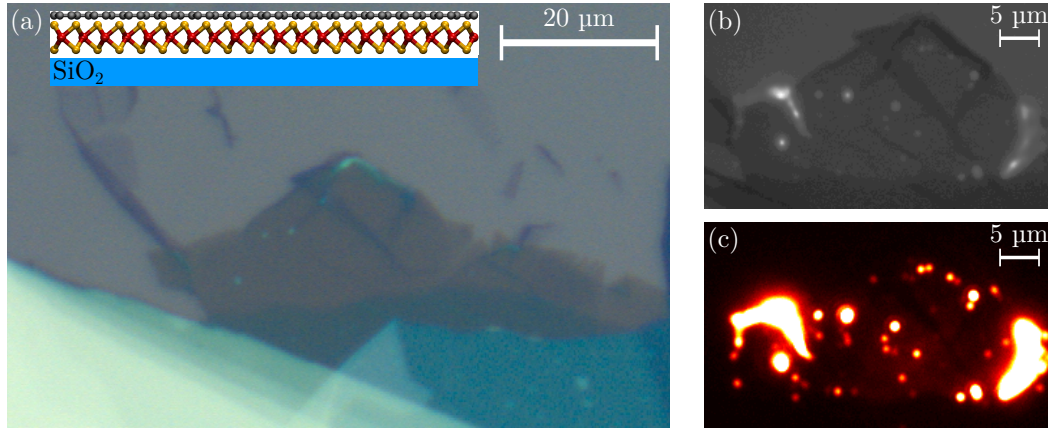


Figure 2.35: a) optical micrograph of sample S3 (cf Appendix C). $\text{SiO}_2/\text{MoSe}_2/\text{graphene}$ heterostructure. The brown area correspond to the TMD. b) False color PL and whitelight image. c) wide field PL image of the sample. the dark red region correspond to the TMD coupled to graphene region while the more intense dot comes from bubbles where TMD and graphene are decoupled.

The interactions between TMD and graphene are basically the same as TMD/TMD. The PL quenching can originate from a charge transfer from the TMD to graphene, or it could also be the signature of an energy transfer since graphene. Since graphene has been demonstrated to be a good Förster energy transfer at least for semiconductor quantum dot or nano platelet [107].

In the following, we will only consider photoinduced charge transfer. We will completely overlook static charge transfer of the native TMD doping to graphene. Even though it could occur, it will take place as soon as the graphene layer touches the TMD one. Therefore, we will not be able to study this.

Here charge transfer refer to any mechanism that increase the Fermi energy of graphene in our case. The charge transfer from TMD to graphene could be extrinsic (slow and mediated by defects, adsorbate...) or intrinsic, induced by charge separation and is a much faster process [15]. However, both mechanisms are photo-induced. The extrinsic effect could be (among many different scenarios) desorption of electronegative species such as water or dioxygen molecule. Such electronegative molecule attract electrons to them and hole-dope the graphene layer, shining light on the stack will desorb molecules and release electrons they was trapping into the graphene (Fig. 2.36 b).

Moreover, The intrinsic mechanism relies on the light excitation of excitons in the TMD that will transfer one of their charges into graphene, electron or hole, depending on the out of plane hopping term for the two species and the band alignment between TMD and graphene (Fig. 2.36 a). The charge transfer from TMD to graphene is a tunnel process and hence its efficiency decays exponentially with the interlayer distance.

Finally, both extrinsic and intrinsic charge transfer are reversible in air but the desorption of molecule is not reversible in vacuum.

Energy transfer process consists of transferring an excitation from a donor to an acceptor.

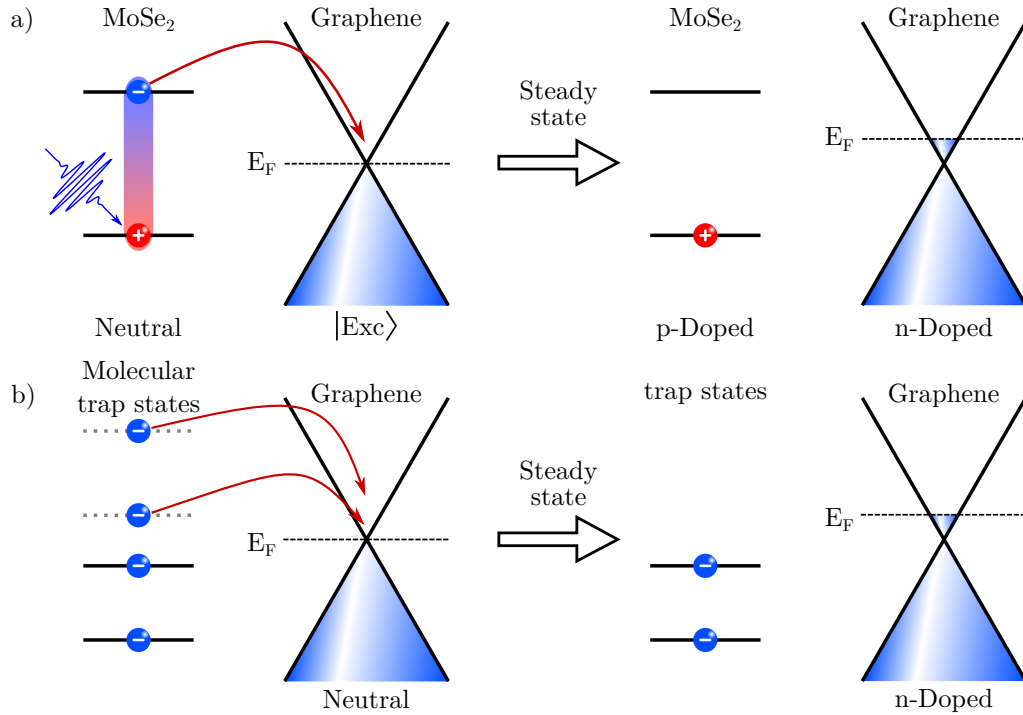


Figure 2.36: a) *intrinsic charge transfer, under illumination excitons are created (left panel) and then electrons (holes) are transferred to graphene. In steady state (right panel), graphene should be n-(p-)doped and the TMD p-(n-)doped.* b) *black lines correspond to molecular trap energy level and gray dashed lines to molecular trap removed by the light induced desorption of molecules. This will release electrons in the graphene. In the steady state, graphene is n-doped and less molecule are adsorb on the graphene.*

Such transfer could be mediated by many different process such as dipole-dipole interaction called Förster type energy transfer (Fig. 2.37 a) or Dexter type energy transfer that regroup dipole-multipole, multipole-multipole interaction and charge exchange (Fig. 2.37 b). The former is relatively long range and can be efficient up to 10 nm while the latter has 1 nm range.

Both Förster and Dexter type energy transfer are non radiative processes. On the first hand, Dexter energy transfer is a short range process depending on the wave functions overlap between donor and acceptor and its efficiency decay exponentially with the distance between donor and acceptor. On the other hand, Förster type energy transfer is quite long range and depends on the spectral overlap between the donor luminescence and the acceptor absorption and their dipole relative orientation. For point like donor and acceptor at a distance larger than 2 nm, the Förster transfer rate $\Gamma_F \propto R^{-6}$ with R the distance between donor and acceptor. Being extensively used in biology, this configuration of energy transfer has been largely studied both experimentally and theoretically but in our case, the distance between donor and acceptor is short, around 7 Å and both donor and acceptor are 2 dimensional. Therefore, the distance dependence of the Förster energy transfer rate should be $\Gamma_F \propto R^{-4}$. This case has not been studied in depth experimentally mainly because it is difficult to find a model system. However, van der Waals heterostructure could be an interesting platform to study this high dimension Förster energy transfer. Few pioneer works exist already though [108, 109].

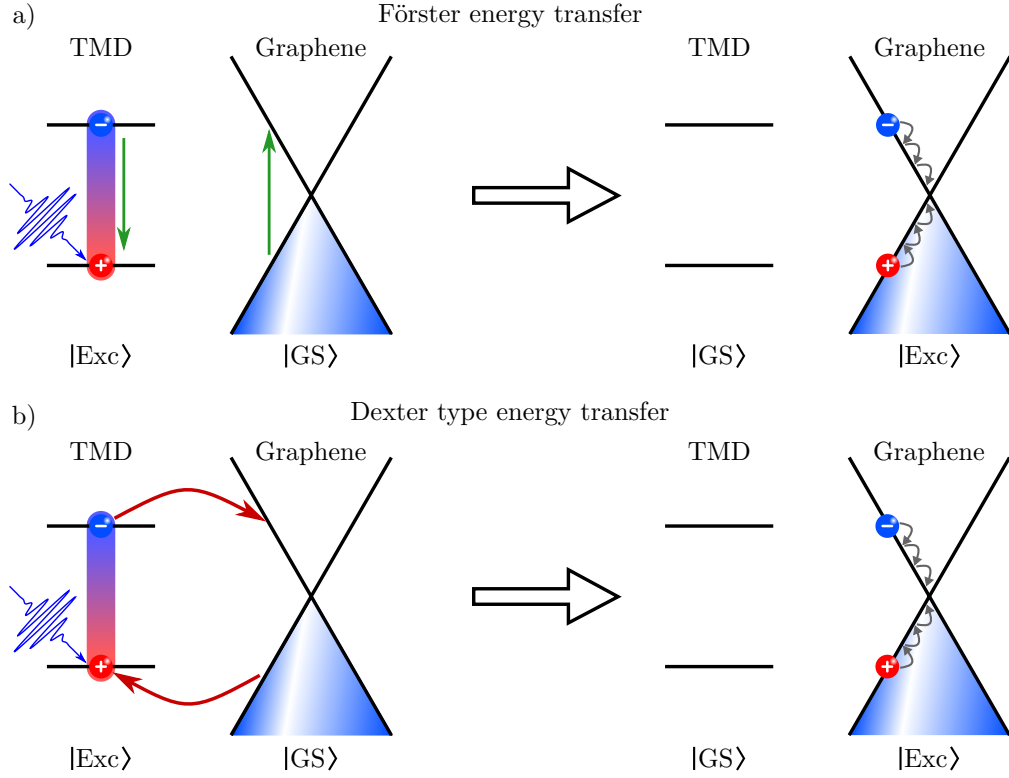


Figure 2.37: a) Förster energy transfer b) Dexter type energy transfer. The half filled conical dispersion represent neutral graphene on the left panel, The graphene is in the ground state, while the TMD is in excited state. On the right panel the graphene is excited while the TMD is in the ground state and hence the excitation has been transferred from the left to the right and energy has been transferred from TMD to graphene.

Since graphene is used in various devices, the interlayer interaction between TMD and graphene has already been studied using several experimental techniques. Spectroscopists make use of pump probe experiments [110, 111], while other groups make use of electrical measurement in TMD/graphene based devices [14].

The pump probe experiments bring insights into the TMD dynamics when interfaced or not with graphene (Fig. 2.38). Those experiments have been carried out at room temperature.

As stated before, pump probe experiment needs high fluence to get a measurable signal. Therefore, the exciton lifetime for the bare WS_2 layer, 21 ps, is rather short compare to usual ns lifetime [12, 112] of the WS_2 measured by TRPL (Fig. 2.38 a). However, this time becomes even shorter when WS_2 is interfaced with graphene, highlighting the effect of graphene on the WS_2 excitons (Fig. 2.38 c). The similar results on graphene on SiO_2 and graphene on WS_2 when pumped below the optical gap further confirm that electron hole pair are transfered to graphene and the massive PL quenching (fator 200) (Fig. 2.38 b,d,e,f). The interlayer interaction has been assigned to a fast electron transfer from TMD to graphene with a ps^{-1} rate. However, energy transfer have been completely ignored in this work.

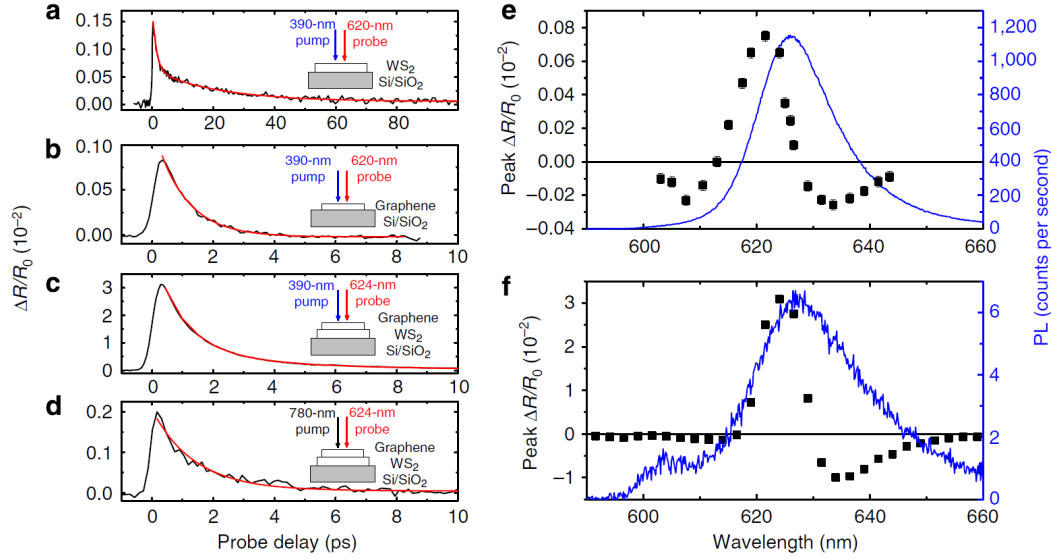


Figure 2.38: a) Differential reflection (DR/R_0) measured from a monolayer WS_2 flake with a 390 nm pump and a 620 nm probe pulse. The red line indicates a biexponential fit with time constants of 1.3 and 21 ps. b) The same measurement as (a) performed with a monolayer graphene sample. The red line is a single-exponential fit of 1 ps. c) The same measurement as (a) performed with a heterostructure sample of graphene and monolayer WS_2 , and with a 624 nm probe pulse. The signal decays biexponentially with time constants of 1 and 3.5 ps. d) The same measurement as (c) but with a 780 nm pump pulse. The red line indicates a 1.4 ps exponential decay. e) Peak differential reflection from the monolayer WS_2 as a function of the probe wavelength (symbols, left axis) and PL of the same sample under 405 nm laser excitation. The error bars indicate the uncertainties due to noise. f) Same as (e) but for the heterostructure sample. Figure taken from [110].

Furthermore, a photoinduced net charge transfer has been demonstrated in an MoS_2 /graphene heterostructure [14]. The samples are made of cm^2 scale CVD grown MoS_2 and graphene.

In this work, the measure of the source drain with respect to the gate voltage gives a charge neutrality point for the graphene at $V_g = 5$ V in air. On the other hand, when the sample is illuminated, the charge neutrality point is reached for $V_g = -20$ V. This proves the net charge transfer from the MoS_2 to the graphene. Therefore, the authors attribute the exciton lifetime shortening to this charge transfer. However, it appears that the charge neutrality point in the dark under vacuum is shifted to $V_g = -15$ V, while it goes to $V_g = -20$ V under illumination, same as in air. Such changes with the experimental conditions could be a hint of extrinsic charge transfer.

Finally, the effect of energy transfer even though it has been shown to play an important role in colloidal quantum dot graphene [107] and in TMD/TMD heterostructure [106] is not discussed in any of these works.

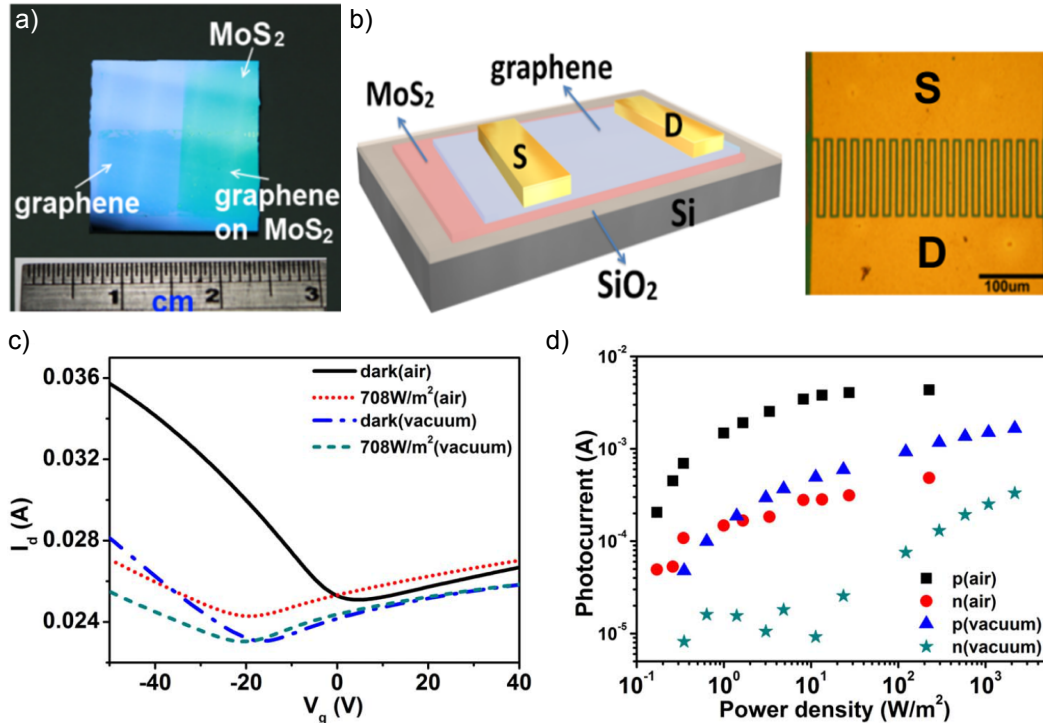


Figure 2.39: a) image of the sample before contact evaporation. Both film are CVD grown. b) Sample scheme and micrograph with the evaporated contact. c) Graphene source drain intensity with respect to the gate voltage in different conditions. d) Power dependent photo current in different conditions. Figure adapted from [14].

2.6 Conclusion

We overviewed graphene and TMD properties and introduce interlayer interaction in TMD/graphene heterostructure.

Graphene is a semimetal that absorbs 3% over a broadband from infra-red to visible range making it a good Förster type energy acceptor. On the other hand, its semimetallic character makes it a good Dexter type energy acceptor. Then we discussed the graphene vibrational properties, we introduced an optical technique relying on Raman spectroscopy to quantitatively measure the graphene Fermi level.

TMD, with their high spin-orbit coupling and the lack of inversion symmetry show a non spin-degenerate band structure giving rise to the so called valley properties. The strong confinement inherent to their 2D nature allows strongly bound exciton to appear. Those excitons dominate the optical absorption spectrum and the luminescence comes mostly of the lowest energy exciton. We also review excitons properties, their valley pseudo-spin inherited from the TMD electronic valley properties and excitons selection rules. And lastly the decoherence and depolarization mechanism in TMD.

Finally, we gave some insights on different interaction mechanisms between graphene and TMD in van der Waals heterostructure: interlayer charge or energy transfers. we also emphasized the difference between Dexter and Förster type energy transfer their donor/acceptor distance dependence and underlying mechanism.

Since TMD graphene heterostructure are used to demonstrate new type of devices, it is mandatory to understand interlayer interaction in those systems. In order to do so, we will measure the graphene Fermi energy using Raman spectroscopy to characterize interlayer charge transfer in TMD/Graphene. Since we can control the interlayer distance with a BN spacer, we will also be able to get insight on the energy transfer especially Förster type energy transfer which can be relatively long range. Thanks to the trion emission, we can monitor the TMD doping level at low temperature to understand what happen to the TMD native doping. Finally, we will introduce some ways to recover TMD valley contrast at room temperature using TMD/graphene heterostructure or by coupling TMD to cavity.

Related publications

- G. Froehlicher, [E. Lorchat](#), F. Fernique, C. Joshi, A. Molina-Sánchez, L. Wirtz, S. Berciaud
Unified description of the optical phonon modes in N-layer MoTe₂,
Nano Lett., 15, 6481-6489 (2015)
- [E. Lorchat](#), G. Froehlicher, S. Berciaud
Splitting of interlayer shear modes and photon energy dependent anisotropic raman response in N-layer ReSe₂ and ReS₂,
ACS nano, 10, 2752-2760 (2016)
- G. Froehlicher, [E. Lorchat](#), S. Berciaud
Direct versus indirect band gap emission and exciton-exciton annihilation in atomically thin molybdenum ditelluride (MoTe₂),
Phys. Rev. B, 94, 085429 (2016)
- G. Froehlicher, [E. Lorchat](#), O. Zill, M. Romeo, S. Berciaud
Rigid-layer Raman-active modes in N-layer transition metal dichalcogenides: interlayer force constants and hyperspectral Raman imaging,
Journal of Raman Spectroscopy, 49, 91-99 (2018)

3

Interlayer coupling in TMD/Graphene heterostructures

3.1 Introduction

Graphene and TMD are basic building blocks for complex structures. For example, graphene is used as a very high quality back gate for electrical control of TMD monolayer or graphene bilayer properties [44][28]. However, interactions between TMD and graphene are poorly characterized even though the different types of interaction are well known. In such semiconductor/metal heterostructure, charge and energy transfer are the main interaction mechanism.

On the one hand, charge transfer will always modify the Fermi energy of both TMD and graphene. This effect can be seen for any transfer rate. In addition, with a charge transfer rate comparable to the exciton recombination rate, charge transfer could lead to the reduction of the exciton lifetime. On the other hand, energy transfer, which consist in the transfer of an electron hole pair from an acceptor (e.g. TMD) to an acceptor (e.g. graphene) would lead to the emission of the acceptor. However, graphene is a semi-metal and therefore will not emit any light from this transfer since any electron hole pair in graphene decay non radiatively much faster than the radiative recombination. In addition as for the charge transfer, a fast energy transfer will result in a shorter excitonic lifetime in TMD.

All recent observations of modified exciton dynamics in TMD/graphene heterostructure have been attributed to charge transfer with a $\sim 1 \text{ ps}^{-1}$ rate and no further discussion for the microscopic mechanism [111][110]. In addition, a photoinduced net charge transfer from TMD to graphene has been demonstrated [110][113]. However, it has also been shown in Graphene quantum dot heterostructures that graphene can be a good Förster energy transfer acceptor [107][114]. Since TMD exciton are very strong in-plane dipoles and graphene dipoles are in-plane as well, it is likely that Förster type energy transfer occur, since Förster energy transfer is dipole mediated (cf Chapter 2). Such interaction mostly affects TMD exciton dynamics and is rather long range. A second type of energy transfer exists, the Dexter energy transfer. This transfer is mediated by electron and needs spatial overlap of the graphene and TMD electronic wavefunction to occur. Finally, TMD could transfer charges to graphene and vice versa. This charge transfer can be photoinduced [14], a photoexcited exciton is broken to transfer one of its charges to graphene (cf

chapter 2). For each electron transferred to graphene by this mechanism, a hole is left in the TMD. This charge transfer mechanism is also a non radiative decay mechanism. Such net charge transfer induces a change in the materials Fermi level and could be photoinduced or rely on native doping from the TMD layer.

To properly characterize interlayer interaction in TMD/Graphene heterostructures, we combine Raman, PL and Time Resolved PL (TRPL) spectroscopy. Raman spectroscopy gives us insight on the material doping. It can be used to quantitatively measure the graphene Fermi level (cf chapter 2) or to measure the TMD doping trends. Net charge transfer mechanism can therefore be characterized by Raman spectroscopy. On the other hand, PL spectroscopy gives access to the exciton dynamics. The time resolved spectroscopy allows us to quantitatively record exciton dynamics since it is longer than one picosecond. However, Steady state PL spectroscopy gives insight on the exciton dynamics. Since a change in intensity denotes a change in the exciton dynamics if nothing, (e.g. Absorption ...) had change.

3.2 Experimental approach

To study interlayer coupling, we choose MoSe₂/Graphene heterostructures as a model system. First, we simply fabricate a monolayer MoSe₂/Graphene heterostructure supported on SiO₂. We characterize it using Atomic Force Microscopy (AFM) PL and Raman spectroscopy (Fig. 3.1). From the AFM measurement, we found that in the area within the dashed line contour (Fig. 3.1 a), the graphene layer is only 6.5Å away from the TMD while it is 2.2 nm away from TMD elsewhere. This is the difference between what we will call coupled and decoupled region respectively.

In (Fig. 3.1 d,f) we observe a 300 times quenching of the PL on the coupled region compared to the bare TMD which is a 99.7% quenching efficiency. This also suggests a lifetime reduction by the same factor. We will investigate the change in the TMD dynamics when interface with graphene in (Sect. 3.4). The quenching comes along with a minor red shift of the exciton emission energy $\sim 10\text{meV}$ (cf. Chapter 2). This shift is expected since graphene has a large dielectric constant and therefore modifies the exciton binding energy [115]. In addition, the PL lineshape on the bare and decoupled TMD present a shoulder on the red side of the spectra. This shoulder can be attributed to the trion emission. However, this shoulder is absent on the heterostructure, suggesting the TMD neutralization by graphene. This effect is very small but we will come back to it in (Sect. 3.5)

The strong PL quenching goes along with modification of the graphene Raman spectra. The most striking is the 2D-mode increased frequency (Fig. 3.1 e,i) by 20 cm^{-1} . The 2D-mode frequency can be approximated [116] by

$$\omega_{2D} = \omega_{2D}^0 + 2 \frac{v_{TO}}{v_F} \omega_1 \quad (3.1)$$

with ω_{2D}^0 the intrinsic 2D mode frequency (cf Chapter 2), v_{TO} the transversal optical phonon velocity and v_F the graphene Fermi velocity. The increase of the 2D-mode frequency could ei-

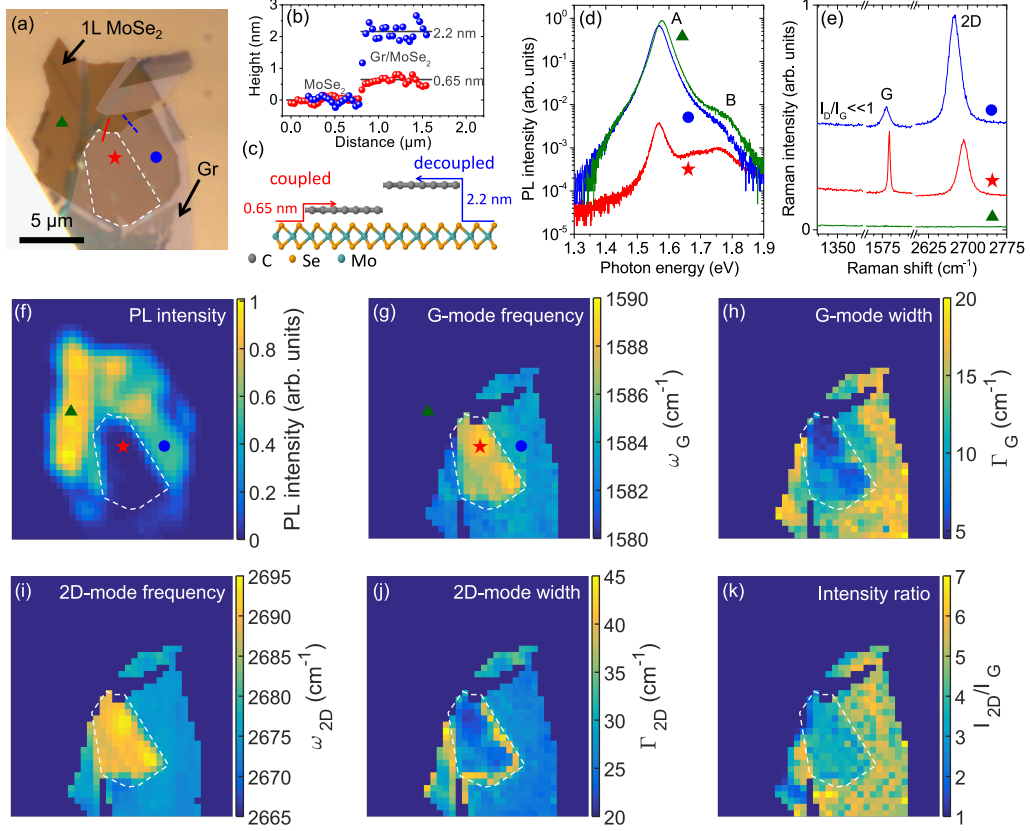


Figure 3.1: Data taken on the sample *S1*, monolayer MoSe_2 /graphene heterostructure supported on Si/SiO_2 substrate. *a)* Sample optical micrograph, the coupled part is highlighted by the white dashed line. *b)* AFM profile taken along the red and blue dashed line drawn in *(a)*. *c)* Schematic of the heterostructure, the red arrow highlights the coupled region step while the blue corresponds to the uncoupled one. *d)* PL spectra taken on the different sample region: green triangle blue circle and red star presented in *(a)*. The green triangle is the bare MoSe_2 , the blue circle corresponds to the uncoupled MoSe_2 /graphene region while the red star corresponds to the coupled TMD/Graphene region. *e)* Same as *(d)* for the Raman spectra. *f)* Hyperspectral PL intensity map of the whole sample, the white dashed line corresponds to the coupled region. *g-k)* Hyperspectral Raman map for the G-mode frequency (*g*), G-mode width (*h*), 2D-mode frequency (*i*), 2D-mode width (*j*) and finally G-mode/2D-mode intensity ratio. All maps have the same scale bar as *(a)*. Map have been recorded using cw 2.33 eV (532 nm) laser excitation at a photon flux $\Phi_{\text{ph}} = 2 \times 10^{19}$ and $\Phi_{\text{ph}} = 2 \times 10^{22} \text{ cm}^{-2} \cdot \text{s}^{-1}$ for the PL map and the Raman map respectively. Figure reproduced from [108]

ther come from the decrease of the Fermi velocity or from the increase of the transverse optical phonon velocity [117]. Such change can be induced by the change of the dielectric screening when graphene is interfaced with TMD [118, 119]. However, there is no effect on the 2D-mode when graphene is decoupled from the MoSe_2 . In addition, the exciton emission energy is shifted due to the dielectric change induced by graphene for both coupled and decoupled spectra. Therefore, the change in the 2D-mode frequency is not well understood yet and deserves more studies to conclude on its origin.

The G-mode width reduction by $\sim 10 \text{ cm}^{-1}$ alongside the G mode frequency increase by 8 cm^{-1}

indicates a doping of the graphene layer (Fig. 3.1 e,g,h). Finally, the intensity ratio between the 2D- and the G-mode is also reduced on the heterostructure, additional proof of the graphene doping. This photoinduced doping will be characterized in the following section (Sect. 3.3) using this characterization method and the graphene doping measurement scheme present in Chapter 2.

3.3 Photodoping

3.3.1 Evidencing photoinduced charge transfer in MoSe₂/Gr heterostructures

3.3.1.1 Photodoping in graphene

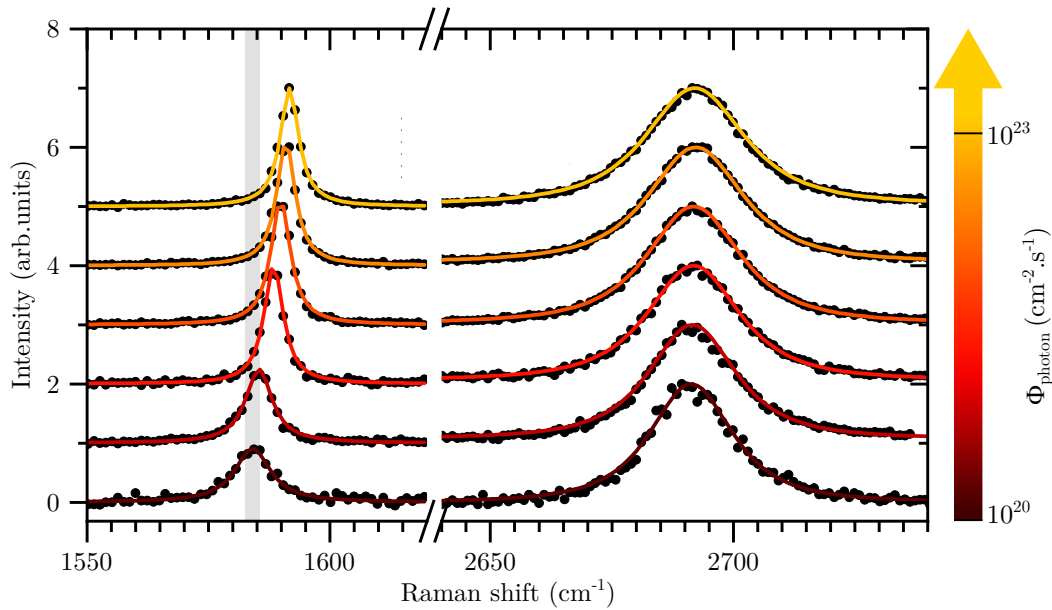


Figure 3.2: Raman spectra taken on MoSe₂/Graphene heterostructure (S1) coupled region at different photon flux. The black dots correspond to the data point while the solid line are Lorentzian fit of the G- and 2D-modes.

To properly characterize the graphene doping mechanism, we perform graphene Raman spectroscopy at different photon flux (Fig. 3.2) to get insight on the microscopic mechanism. We extract fitting parameters from (Fig. 3.2) and report them in (Fig. 3.3). We found photo induced effect only on the coupled region while uncoupled or bare graphene region display photon flux independent behavior.

The increase of the G-mode frequency as well as the width reduction with the photon flux indicate a photoinduced doping of the graphene (Fig. 3.3 a,b). The 0.11 slope in the ω_{2D} , ω_G correlation (Fig. 3.3 e) is the signature of an electronic doping (cf chapter 2). Finally, we perform these measurements increasing and then decreasing the excitation intensity. We record no difference in the Raman features proving the reversible nature of the photodoping effect in our measurement conditions. In (Fig. 3.3) we found that graphene Fermi energy seems to saturate. In addition, even if graphene is known to photodope in presence of oxygen or moisture [120], there

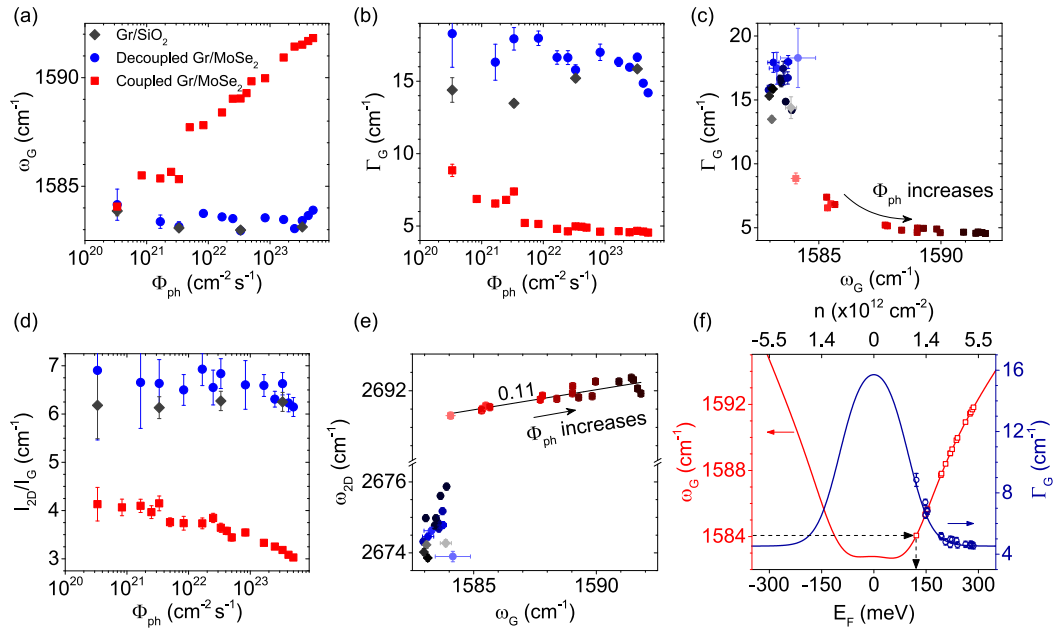


Figure 3.3: Data taken on MoSe₂/graphene (S1) a) G-mode frequency ω_G at different photon flux, the red squares correspond to the coupled region the blue circles to the decoupled region and the gray diamonds to the bare graphene. b) same as (a) for the G-mode width Γ_G . c) Correlation between Γ_G and ω_G for decoupled region blue circles and coupled region red squares. The color gradient highlights the photon flux, darker symbols correspond to higher photon flux. d) Photon flux dependent intensity ratio between 2D- and G-mode. e) Same as (c) for the 2D-mode frequency and G-mode frequency. The solid line corresponds to a linear fit of the data taken on the coupled region. The slope is 0.11. f) Fit (solid line) of the G-mode width (open circle) in blue. Extraction of the graphene Fermi energy via the G-mode frequency (red open squares) with the theoretical G-mode frequency, red solid line (cf Chapter 2). Figure reproduced from [108]

is no effect on graphene on SiO₂. This highlight that MoSe₂ play a role in the doping mechanism.

Finally, we extract the flux dependence of the graphene photodoping. We display the results in (Fig. 3.4)

The Fermi energy saturates at 280 meV. Different scenarios can be imagine to explain this saturation. However, we should first get insights into the photodoping mechanism, extrinsic and mediated by desorption or intrinsic and due to exciton electron transfer to the graphene. To better understand this, we will monitor the photoinduced doping in the TMD layer, looking for a hole doping.

3.3.1.2 Photodoping in MoSe₂

Since the doping is efficient only when MoSe₂ is interfaced with graphene, we should find the trace of a hole doping in the TMD, since graphene is electron doped. It has been demonstrated that the A'₁ monolayer TMD Raman mode could be used as a doping probe [66]. A'₁ mode frequency decreases and its width increases while it is doped by electron. Since A'₁ mode has a much lower

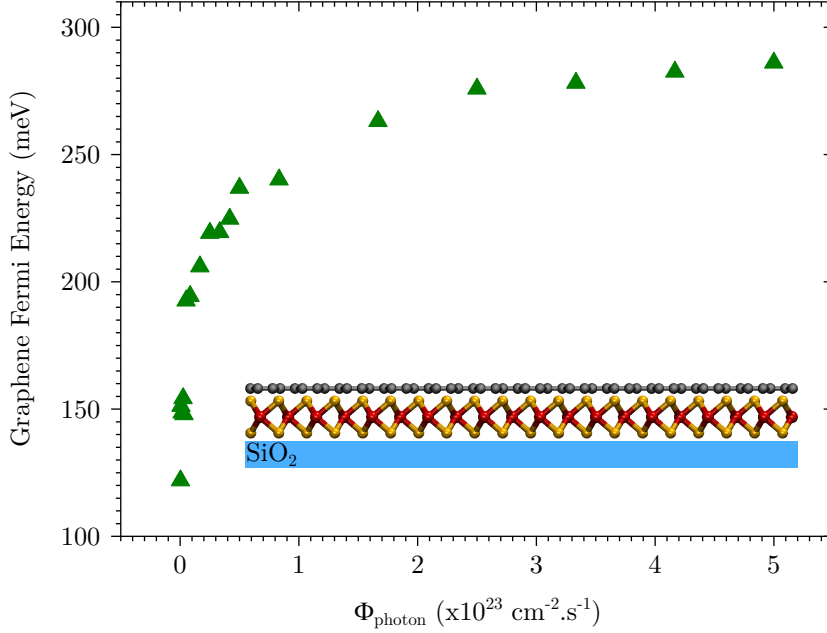


Figure 3.4: Graphene Fermi energy with respects to the incident photon flux for S1 in ambient air. S1 is a monolayer MoSe₂/graphene heterostructure supported on Si/SiO₂ substrate.

frequency (240 cm^{-1}) the absolute value of the shift will be much smaller.

In (Fig. 3.5 b), we found that A'₁ mode frequency is sharper and its frequency is higher at any photon flux. This suggests an electron transfer in the dark from the TMD to the graphene. Since pristine MoSe₂ is usually n-doped [20], MoSe₂ is probably neutralized by graphene. However, the same trend is recorded for the coupled MoSe₂/graphene region than for the other (decoupled and bare MoSe₂) indicating an electron doping in MoSe₂. On the other hand, as the photon flux increase, the difference between the coupled MoSe₂/graphene and the bare MoSe₂ A'₁ frequency (width) increases (decreases). This is the signature that MoSe₂ coupled to graphene is less photodoped with the photon flux, corresponding to a net hole transfer from the graphene to the MoSe₂.

3.3.1.3 Reproducibility

We have well characterized the photodoping effect on one sample. However, before going further, we characterize several samples and extract their Fermi energy with respect to the photon flux

In (Fig. 3.6) we uncover for each sample a saturation level within 250 ± 50 highlighting the reproducibility of the photodoping mechanism. More interestingly, for the same photon flux, each sample displays a different doping. The different sensitivity of our heterostructures highlights the sample dependent efficiency of the net charge transfer process. The similarity in the saturation limit points toward an intrinsic doping saturation mechanism. However, the different efficiency of the doping mechanism is most likely due to the extrinsic nature of the doping mechanism. We will prove the extrinsic nature of the doping mechanism by performing the same measurement in different environments.

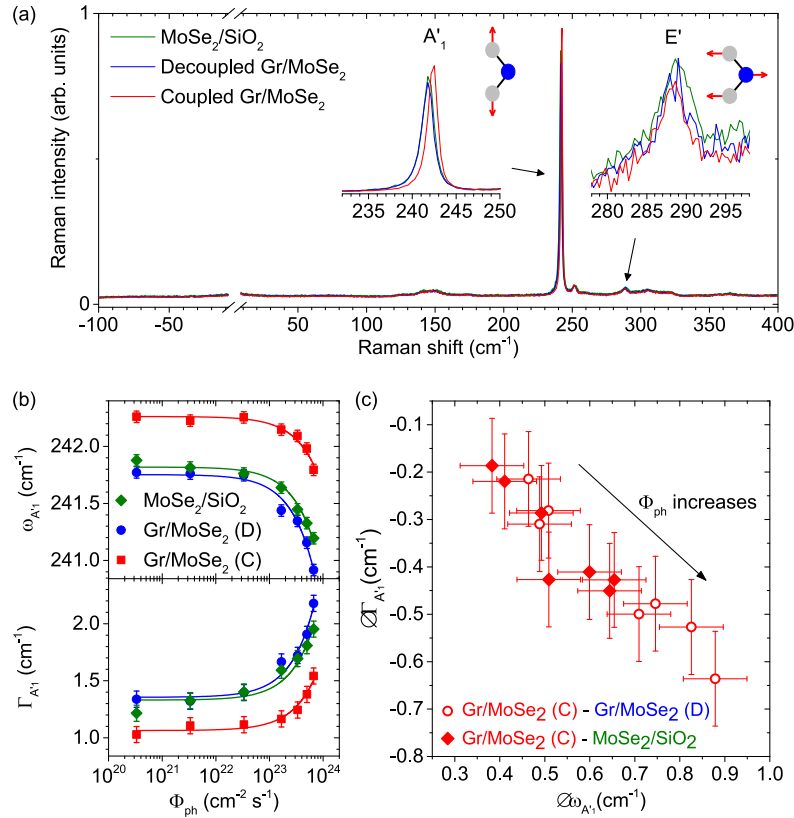


Figure 3.5: *a) MoSe₂ Raman spectra on different regions, coupled decoupled and on bare TMD in red blue and green respectively. The left inset is a zoom on the prominent peak A'₁ corresponding to the out of plane movement of the chalcogen atom. The right inset is a zoom on the E' mode indicated by an arrow. It corresponds to the in plane movement of each atom b) TMD Raman mode A'₁ frequency and width, this give a qualitative measure of the doping in the TMD. The coupled, uncoupled and bare MoSe₂ regions are represented in red, blue and green respectively. The Raman mode frequency is decreasing while the width is increasing, sign of an electron doping for any region even though this effect is smaller for the coupled region. c) Correlation between the width and the frequency of the A'₁. To compare what happens in the coupled with respect to the uncoupled region, we represent the difference between coupled and uncoupled region or coupled and bare MoSe₂ region. Figure reproduced from [108]*

In the following we will test the role of adsorbate by measuring the doping level in air and in vacuum. The doping should be reversible in air since desorption can be balance with absorption for a given flux while it should be irreversible in vacuum because no molecule can be reabsorb after desorption.

Because SiO₂ is much rougher than two-dimensional materials there could be adsorbate trapped in between the layered compound and the substrate. To get rid of those adsorbates, we will deposite a BN/TMD/Gr stack on SiO₂ and fully encapsulate one of our heterostructure in BN. Finally, to check the role of band offset between the semiconducting layer and the graphene, we measure the photodoping effect for different TMD.

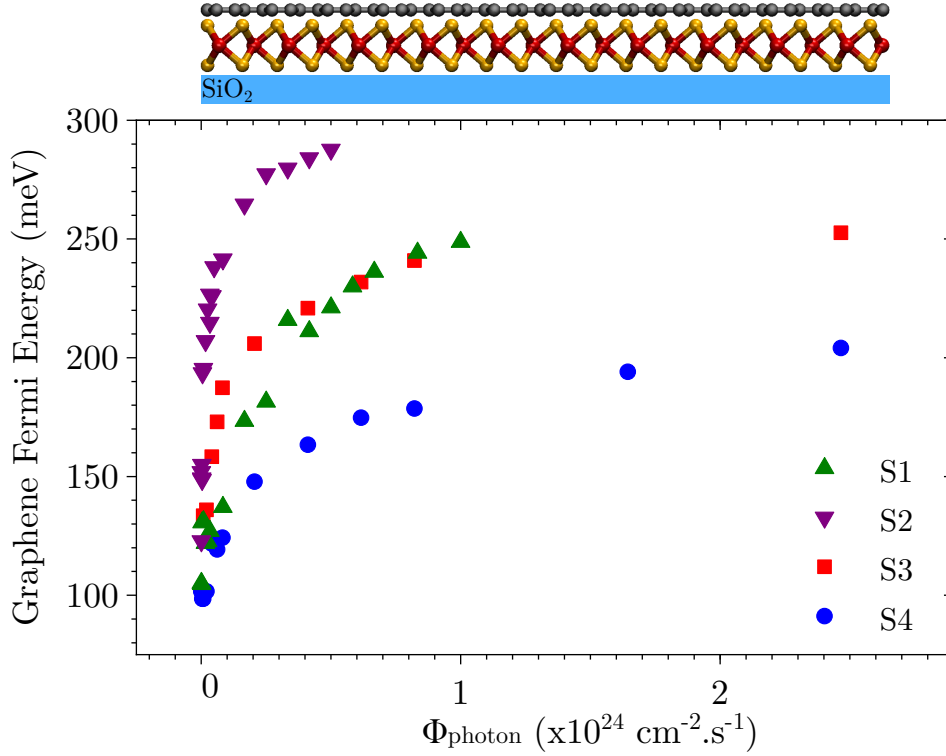


Figure 3.6: Graphene Fermi energy with respects to the incident photon flux for S1 in ambient air. S1 is a monolayer MoSe₂/graphene heterostructure supported on Si/SiO₂ substrate.

3.3.2 Environmental and substrate induced effects

3.3.2.1 Measurement in ambient air vs in vacuum

To check the effect of adsorbates in the photodoping effect, we measure graphene Fermi energy while sweeping the incident photon flux. We therefore carried out the same measurement under vacuum. Since changing environment is an easy way to verify the intrinsic character of an effect.

Under vacuum, the PL quenching is smaller than under ambient condition (Fig. 3.7 a). However, the B exciton is more prominent under vacuum than in ambient conditions. This is the smoking gun of a reduction of the A exciton lifetime which is probably due to an efficient non-radiative decay mechanism. Since there is less adsorbate at the surface under vacuum than in ambient conditions, exciton diffuses on larger distances. Finally, the Auger recombination will be more efficient under vacuum than in ambient conditions.

It is interesting to note that every G-mode characteristics are almost pinned at their extreme value (Fig. 3.7 b-d). In addition, when we ramp up the photon flux, the G-mode frequency increases. However, when we ramp down the power, the G mode frequency is pinned to its maximum value. This shows that the net charge transfer mechanism is irreversible, meaning the absence of charge leaking channel.

We acquire Raman spectra on the fly after insulating the sample for the first time at $t=0$

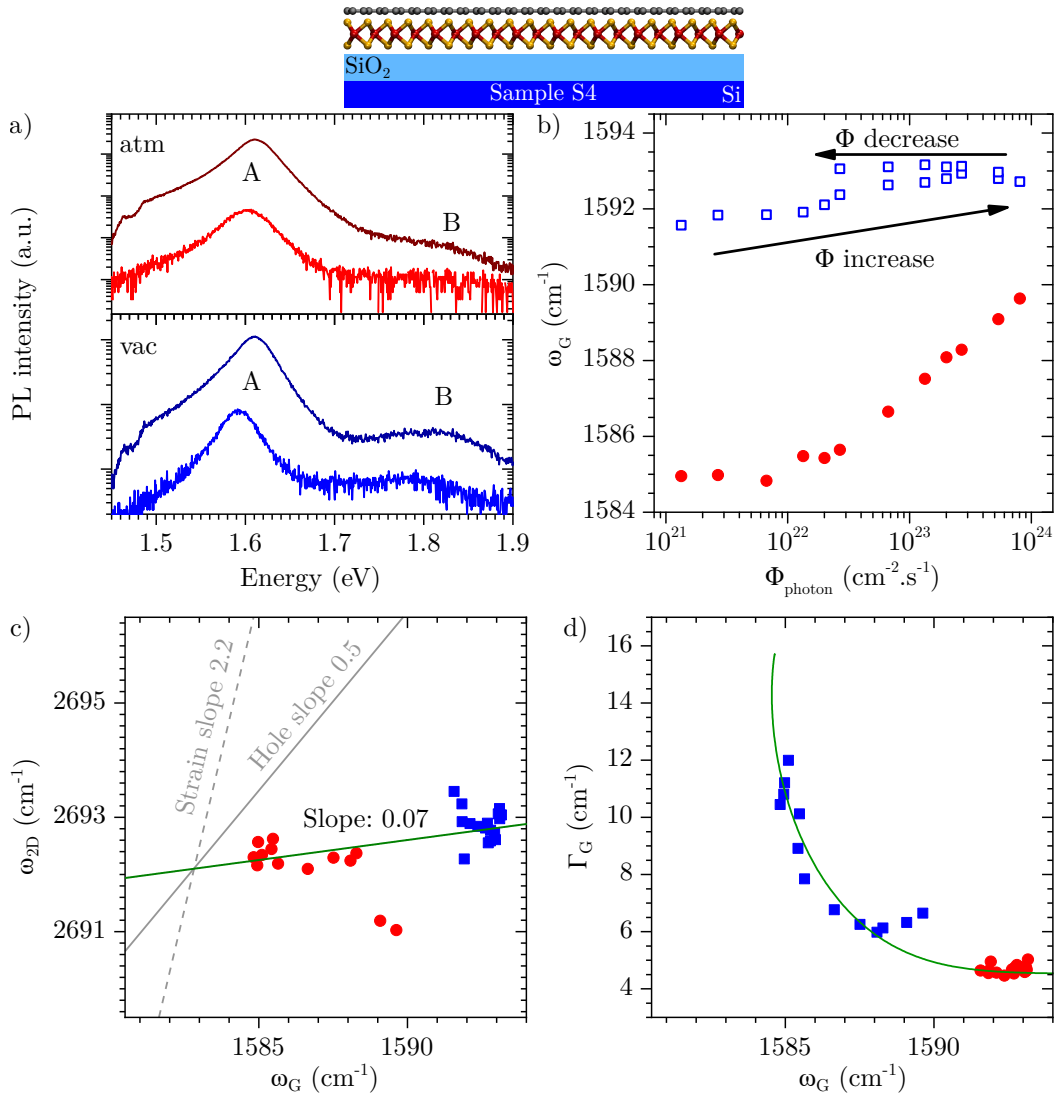


Figure 3.7: Data taken on sample S4 a) PL spectra recorded at $3 \times 10^{20} \text{ cm}^{-2} \cdot \text{s}^{-1}$ photon flux on MoSe₂ presented in dark blue or dark red and MoSe₂/Graphene in blue or red. The top panel has been recorded in ambient conditions while the lower one corresponds to vacuum. A and B denote the A and B exciton. b) G-mode frequency with respect to the power, blue square data are taken under vacuum while the red circles correspond to ambient conditions measurement. c) 2D- and G-Mode correlation, the green line is a fit of all the data since they have been taken on the same sample. The slope indicates an electron doping. The gray line correspond to hole doping slop and the dashed line correspond to strain. d) Frequency with correlation of the G mode indicating doping. The green line corresponds to the fit of the G-mode width and frequency using (EQ.(2.9) and EQ.(2.10)).

and acquiring spectrum every 30 or 60 second, trying to get insight on the doping mechanism efficiency. Using a cw laser excitation, we record spectrum using high photon flux $8 \times 10^{23} \text{ cm}^{-2} \cdot \text{s}^{-1}$ (Fig. 3.8) to get a measurable signal within the 30 or 60 s camera exposure.

We found that G-mode frequency and therefore doping increase slowly while the sample is insulated. Given the absence of leaking channel that would allow the extraction of charges from

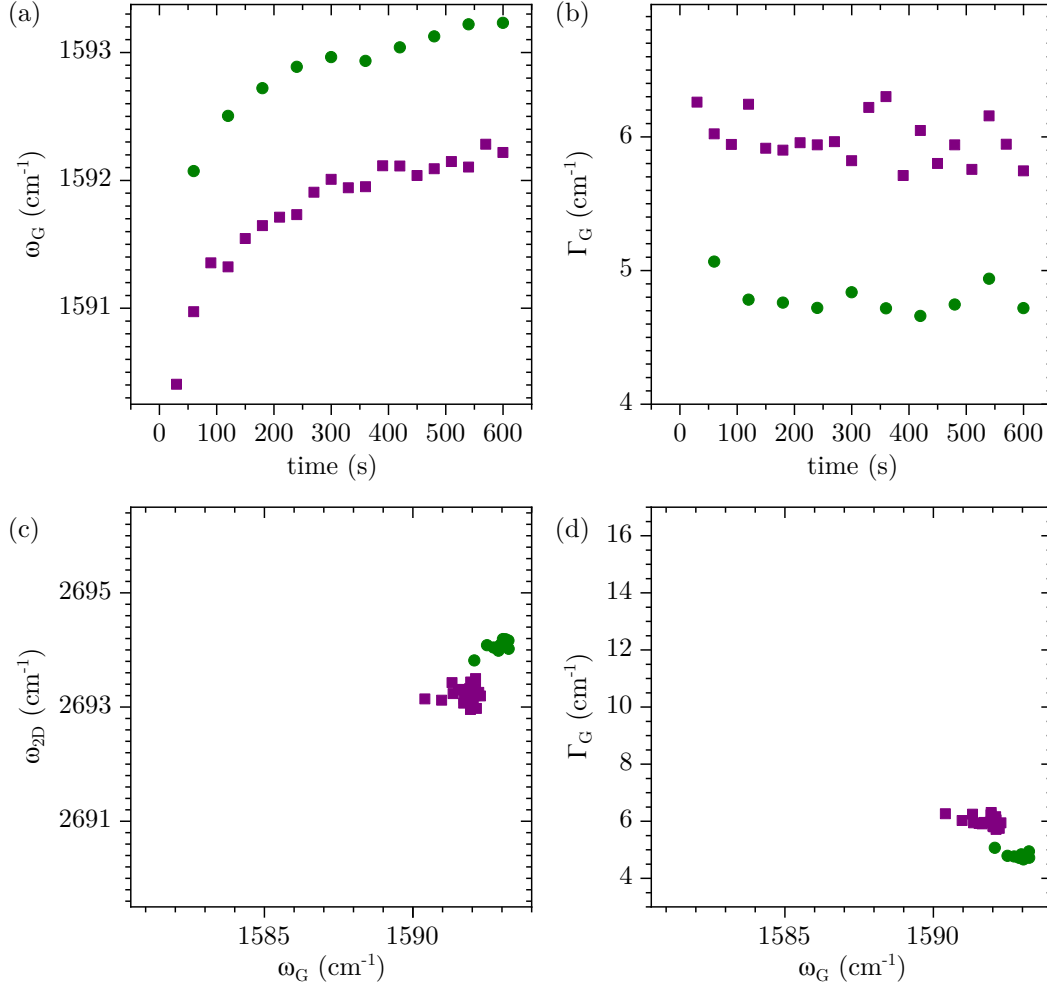


Figure 3.8: Data taken on S_4 under vacuum at $3 \times 10^{22} \text{ cm}^{-2} \cdot \text{s}^{-1}$ photon flux on two different points. a) G-mode frequency ω_G with respect to insulation time. Each spectrum is integrated for 30 s (60 s) for the purple squares (green circles). b) Same as (a) for the G-mode FWHM Γ_G . c) 2D- and G-mode frequency correlation. d) G-mode frequency and FWHM correlation.

the graphene, the net charge transfer is a slow process.

The net charge transfer mechanism could be related to desorption of electronegative molecule adsorbate at the surface. In ambient condition desorption can be quickly compensated by the absorption of another molecule. Therefore, an equilibrium between absorption and desorption give the doping level. However, under vacuum molecule will not be reabsorb easily, finally leading to a slow increase of the doping level up to the saturation value. To test our hypothesis, we choose to change substrate.

3.3.2.2 Substrate effects

We first choose to measure Raman characteristic of a Graphene/MoSe₂ heterostructure supported on Si/SiO₂ substrate (Fig. 3.9). The stacking order is then the following: SiO₂/Graphene/MoSe₂/air.

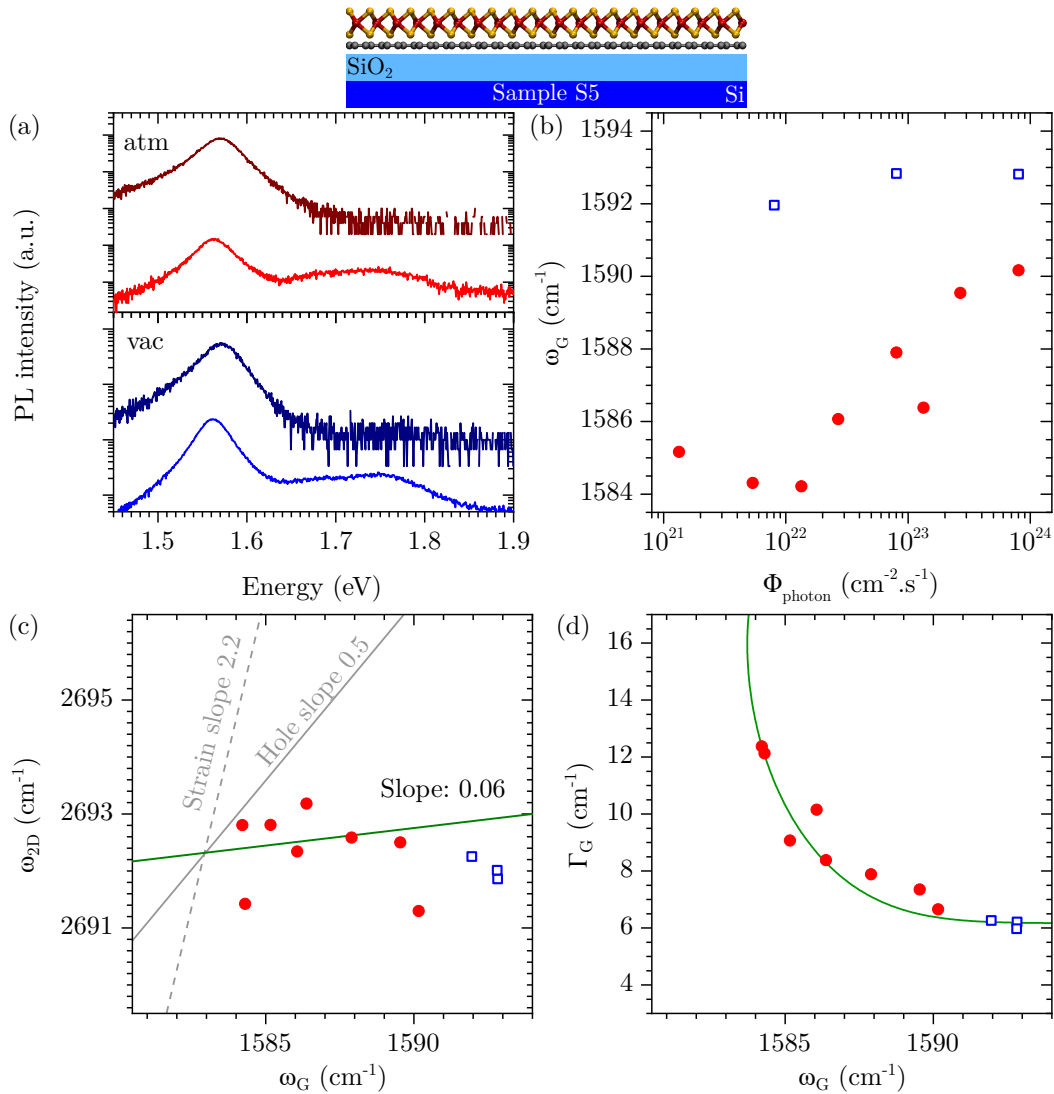


Figure 3.9: Data taken on sample S5 a) PL spectra recorded at $3 \times 10^{20} \text{ cm}^{-2} \cdot \text{s}^{-1}$ photon flux on MoSe₂ presented in dark blue or dark red and MoSe₂/Graphene in blue or red. The top panel has been recorded in ambient conditions while the lower one corresponds to vacuum. A and B denote the A and B excitons. b) G-mode frequency with respect to the power, blue square data are taken under vacuum while the red circles correspond to ambient conditions measurement. c) 2D- and G-Mode correlation, the green line is a fit of all the data since they have been taken on the same sample. The slope indicates an electron doping. The gray line corresponds to hole doping slop and the dashed line correspond to strain. d) Frequency/FWHM correlation of the G mode indicating doping. The green line corresponds to the fit of the G-mode width and frequency.

We found that there is no difference between MoSe₂/graphene and graphene/MoSe₂ heterostructures. However, both structure are directly in contact with air and SiO₂. Since SiO₂ is a rough substrate, compared to the atomic flatness of 2D materials, adsorbate could also reside in between the bottom layer and the substrate.

To completely screen our structure from the outer world, we encapsulate it into BN. Since

BN is atomically flat and presents the same cleaning effect as TMD interfaced with graphene, the interlayer distance in this case tends to zero. Hence, the interface is perfectly clean.

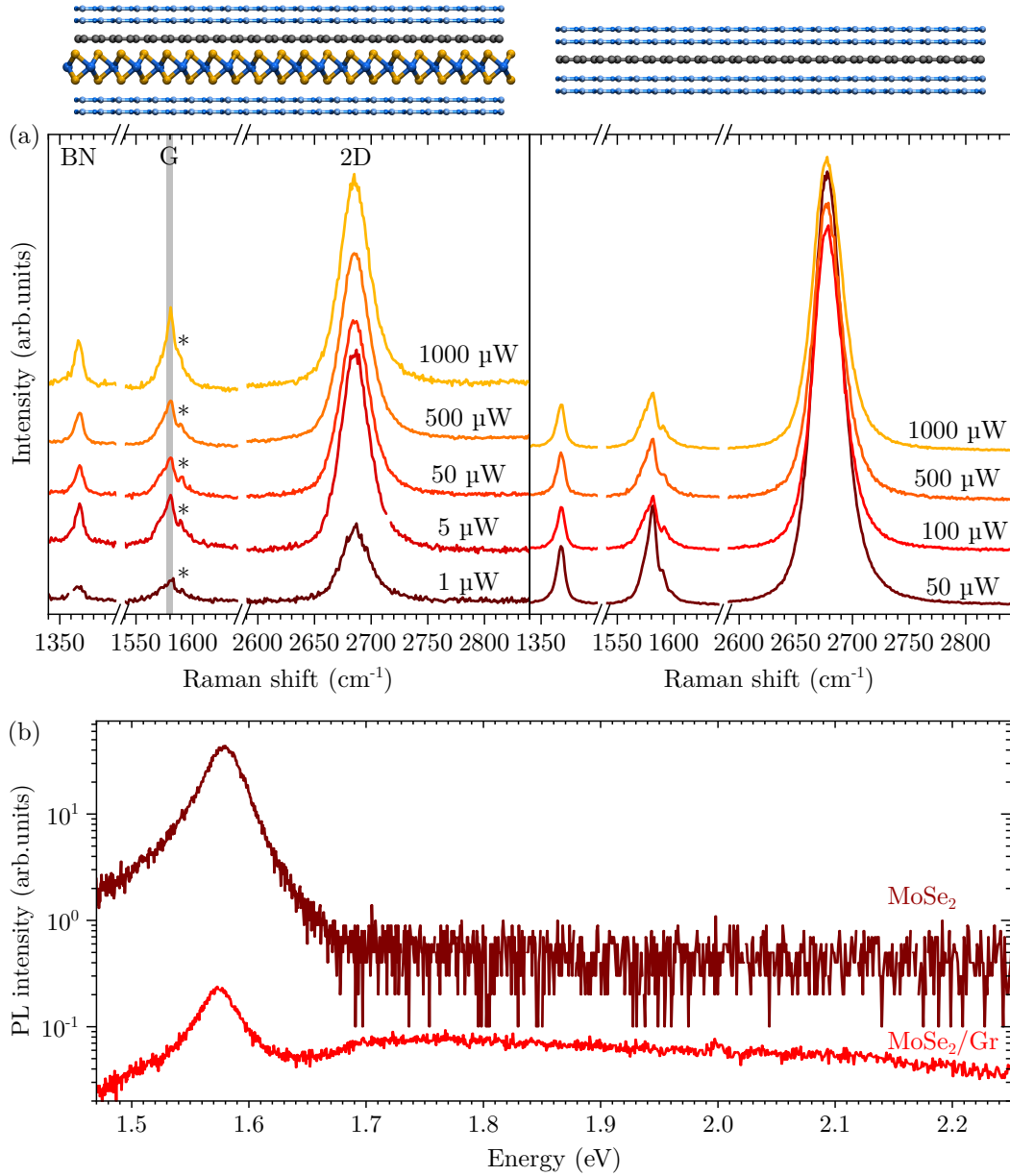


Figure 3.10: data taken on S6: BN capped MoSe₂/graphene heterostructure. a) Raman spectra taken on the heterostructure (BN capped graphene) on the right (left) panel with at different excitation power, 1 μW corresponds to 3×10^{20} photons.cm⁻².s⁻¹. The asterisk denotes a side peak induced by a Moiré lattice between the top BN layer and the graphene layer underneath. b) PL spectra in ambient air (under vacuum) displayed on the right (left) panel.

In the encapsulated heterostructure, the G-mode frequency remains wide at 1582 cm⁻¹ showing an undoped character and no more photodoping is visible (Fig. 3.10). The side peak on the G mode marked by an asterisk (Fig. 3.10 a) is the signature of a Moiré lattice between the top BN layer and the graphene layer underneath [121]. It is present for angles between graphene and

BN lattice vector smaller than 2° . Since we do not give a particular attention to the alignment, we were first confused to find such a peak. However, it has been demonstrated that thermodynamically, graphene on BN is stable if the graphene/BN lattice vector angle is 0° and metastable for a 30° angle. If the stack is heated above 100°C , it will spontaneously rotate to adopt one of the configuration [122]. Since we heat our sample up to 180° during the fabrication process, we do expect the graphene to rotate and adopt the Moiré lattice configuration.

The PL lineshape is a bit broader under vacuum, this probably come from the sample inhomogeneity since both spectra have been taken on different sample region. Finally, the net charge transfer effect is absent when the heterostructure is encapsulated, pointing again toward a adsorbate mediated process.

In the previous experiment, we demonstrate that MoSe_2 play a role in the doping mechanism. We recorded graphene photoinduce doping as long as MoSe_2 is in contact with SiO_2 or air.

Therefore, we do not expect to find doping if we remove the BN top layer to get an heterostructure that look like this: $\text{SiO}_2/\text{BN}/\text{MoSe}_2/\text{graphene}$. Since it is impossible to just remove the BN capping layer on our previous sample, we fabricate a new one to test this idea. As expected, graphene does not display any change of the graphene G-mode. This shows that doping is not photomodulated in graphene. In addition, a wide G mode ($\text{FWHM} > 12$) combined with its small frequency ($\omega_G < 1583$) indicates a neutral graphene (Fig. 3.11).

3.3.2.3 Photodoping in other TMD/Graphene heterostructures

The saturation Fermi level, if it relies on band alignment or intrinsic mechanism, should be different for different TMD. We then perform our characterization on various TMD/graphene heterostructure, starting with $\text{WSe}_2/\text{graphene}$ structure. Intriguingly, $\text{WSe}_2/\text{graphene}$ heterostructure has the same behavior than $\text{MoSe}_2/\text{graphene}$. PL is quenched by two orders of magnitude. Electrons are transferred to graphene, in a reversible manner in ambient condition while it is not under vacuum. Finally, the doping level saturate at ≈ 300 meV (Fig. 3.12).

We then go for $\text{WS}_2/\text{graphene}$ heterostructures with the same approach.

WS_2 PL emission occurs at 2 eV. In addition, graphene 2D-mode energy is ≈ 330 meV. Since we usually use a 2.33 eV (532 nm) laser excitation to record Raman response, the 2D-mode is drown in the WS_2 PL signal. Therefore, we are not able to record the 2D mode using 2.33 eV (532 nm) laser excitation. To get rid of this problem, we also use a slightly sub resonant excitation at 1.96 eV (633 nm). Using such excitation, we found the same increase (decrease) of the G-mode frequency (width) with increasing power (Fig. 3.13 b-d). The G- 2D-mode correlation in ambient condition has a 0.08 slope indicating an electron doping. However, under vacuum the 2D-mode frequency is down shifted probably because the measurements have not been carried out on the same point. Hence strain could change the 2D-mode frequency.

We found on WS_2 the same doping behavior than on other TMD and again the same saturating value of the G-mode and therefore of the graphene Fermi level with respect to the photon flux. We have again transfer electron to graphene

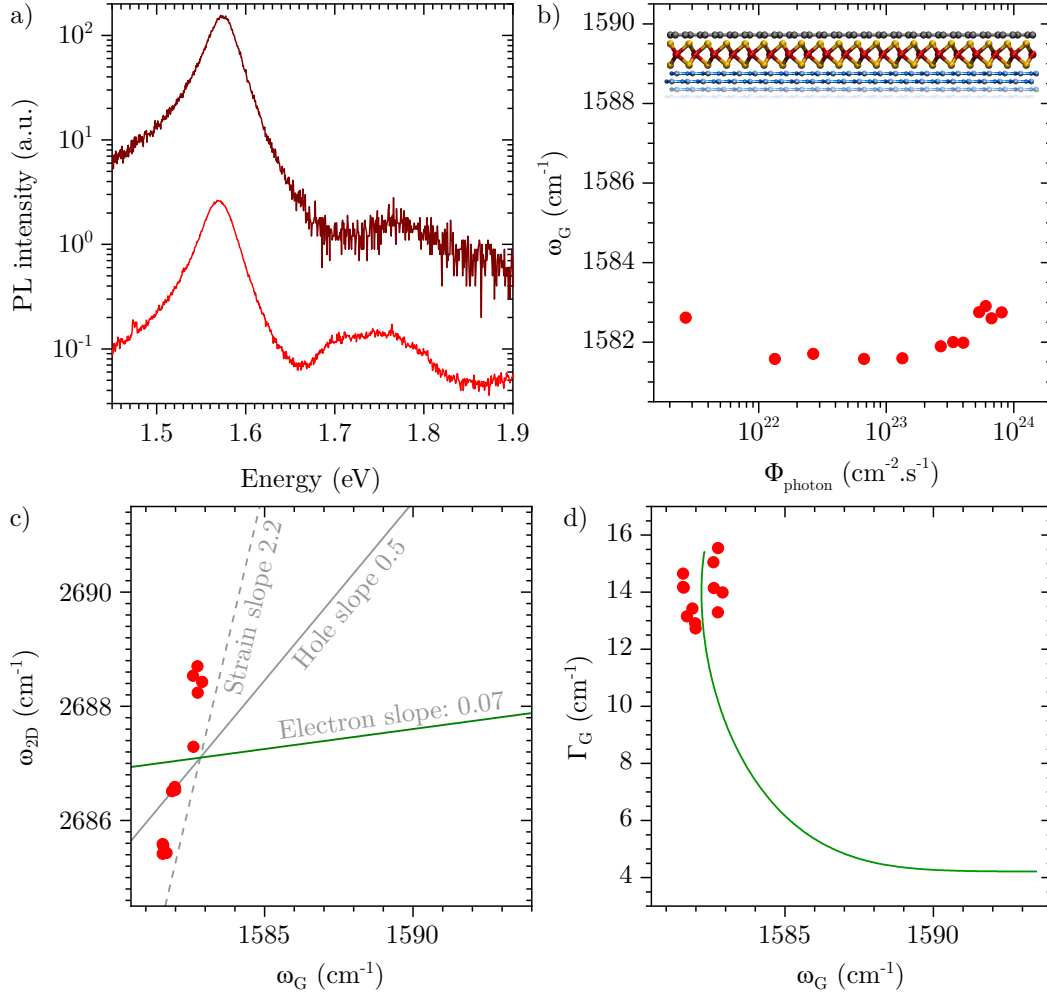


Figure 3.11: Data taken on sample S7, a SiO₂/BN/MoSe₂/graphene sample. a) PL spectra recorded at 3×10^{20} cm⁻².s⁻¹ photon flux on MoSe₂ presented in dark blue or dark red and MoSe₂/Graphene in blue or red. The top panel has been recorded in ambient condition while the lower one corresponds to vacuum. A and B denote the A and B excitons. b) G-mode frequency with respect to the power, blue square data are taken under vacuum while the red circle correspond to ambient conditions measurement. c) 2D- and G-Mode correlation. d) Frequency/linewidth correlation of the G mode indicating a neutral graphene.

Finally, MoS₂/graphene heterostructure is the only heterostructure that behaves differently from the MoSe₂/graphene one.

First, the quenching factor is only one order of magnitude on MoS₂ compare to the usual 2 order of magnitude. This is not that surprising since the B exciton on MoS₂ has a measurable intensity contrary to the MoSe₂. This highlight the poor radiative decay efficiency compare to the non radiative one on the bare MoS₂. The G mode frequency does not increase with the photon flux anymore. On the other hand, the G mode frequency (1586 cm⁻¹) and width (≈ 10 cm⁻¹) indicate a probable doping of the graphene layer (Fig. 3.14 b,d). Since we do not dope the graphene, it is impossible to make use of the 2D-, G-mode frequency correlation to get the

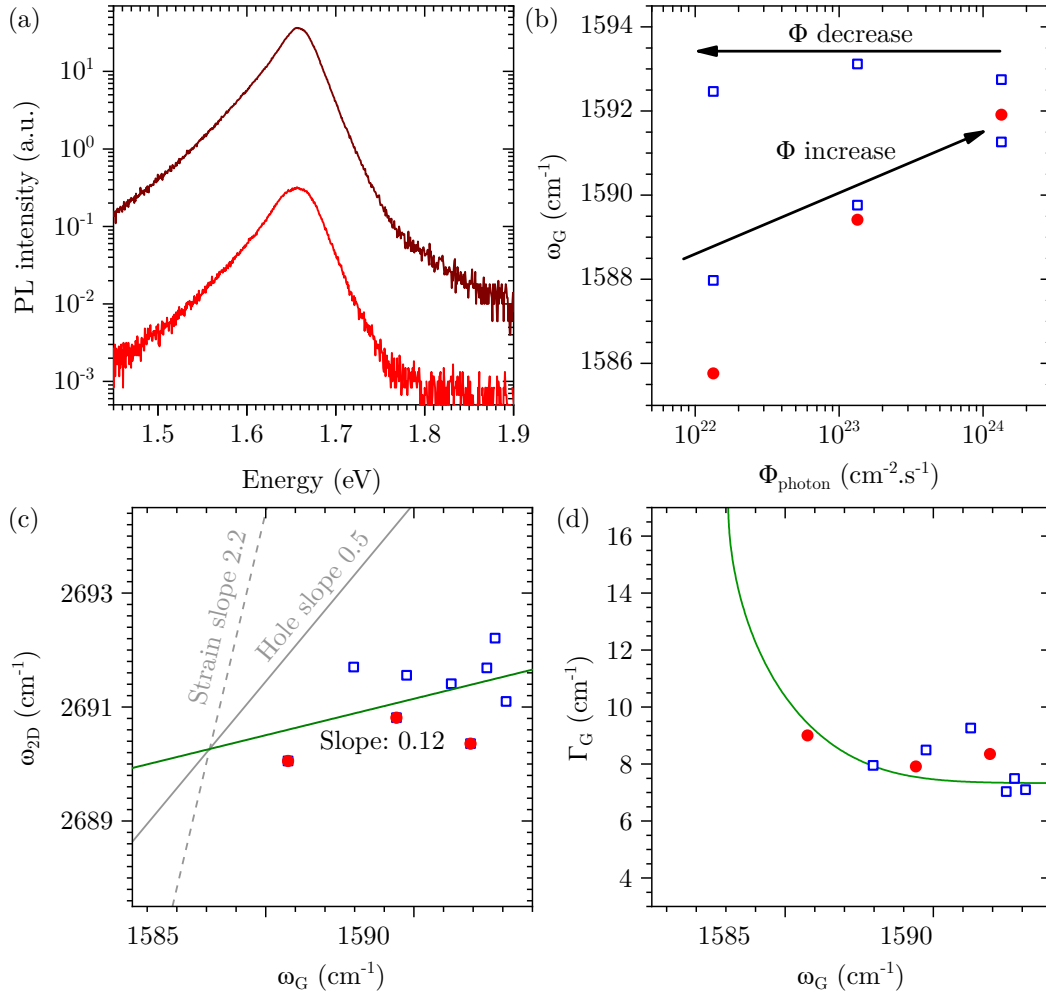


Figure 3.12: Data taken on sample S8 (WSe₂/Gr heterostructure) a) PL spectra recorded at 3×10^{20} cm⁻².s⁻¹ photon flux on WSe₂ presented in dark blue or dark red and MoSe₂/Graphene in blue or red. The top panel has been recorded in ambient condition while the lower one corresponds to vacuum. A and B denote the A and B excitons. b-d) Open blue square data are taken under vacuum while the full red circle correspond to ambient conditions measurement. b) G-mode frequency with respect to the power. c) 2D- and G-Mode correlation, the green line is a fit of all the data since they have been taken on the same sample. The slope indicates an electron doping. d) Frequency/linewidth correlation of the G mode indicating doping.

nature of the dopant (Fig. 3.14 c). Interestingly, the PL intensity of MoS₂ present a shoulder on the red part of the spectrum which correspond to the trion emission. However, this shoulder is totally absent from the MoS₂/graphene heterostructure. Therefore, it is probable that the slight non photoinduced doping in graphene is actually coming from MoS₂ neutralization by graphene.

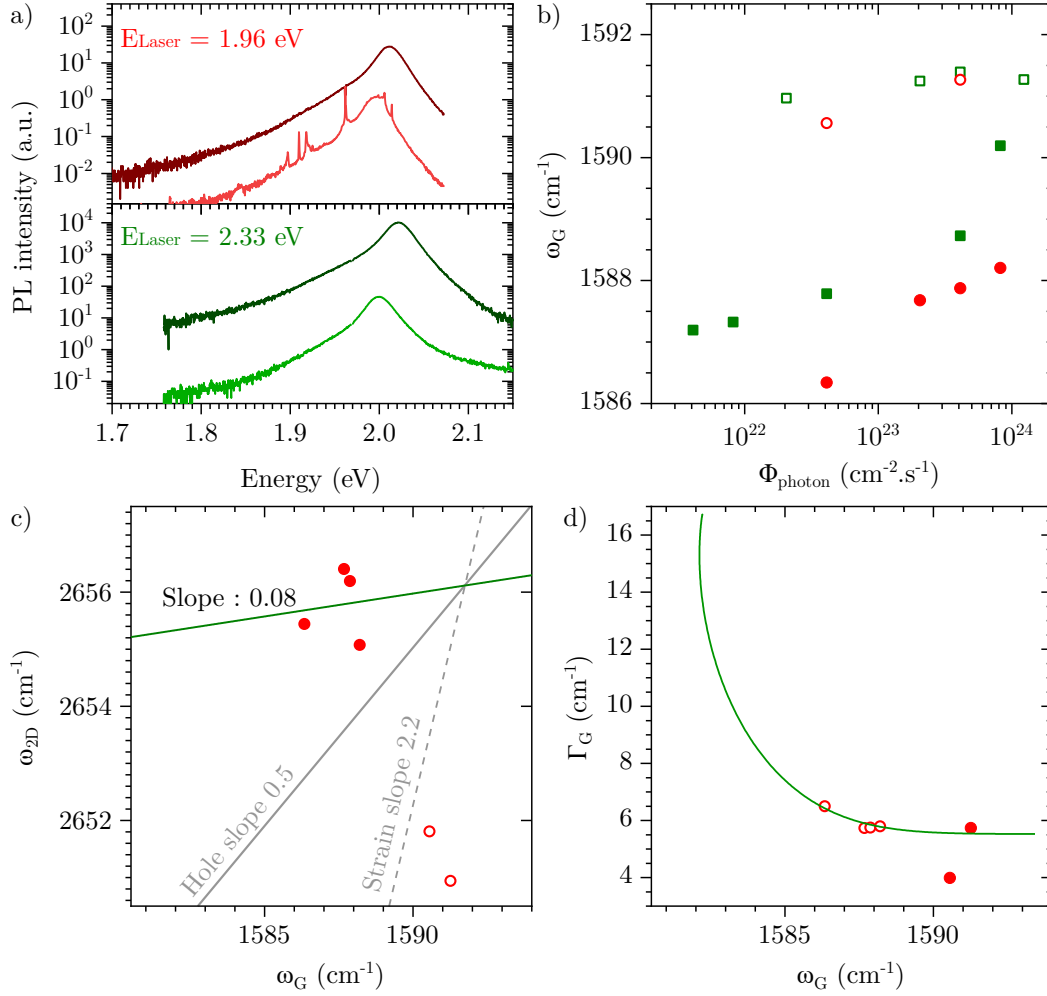


Figure 3.13: Data taken on sample S9 (WS₂/Gr heterostructure) a) upper panel, PL spectra recorded under 1.96 eV (633 nm) laser excitation WS₂ presented in dark red and WS₂/graphene in red. The peaks superimposed on the PL signal correspond to WS₂ Raman signal. The lower panel is the same excited at 2.33 eV (532 nm). Both have been recorded in ambient conditions. b-d) Full (open) symbol stand for measurement done in ambient (vacuum) condition. Green symbol have been recorded at 2.33 eV laser excitation and red at 1.96 eV. b) G-mode frequency with respect to the power c) 2D- and G-Mode correlation, the green line is a linear fit of the data taken in ambient conditions. d) Frequency/FWHM correlation of the G mode indicating doping.

3.3.3 Discussion

3.3.3.1 Results summary

We have evidence the graphene electron photodoping when interfaced with MoSe₂ in air. Since it is photo induced, the graphene Fermi energy depends on the photon flux and saturate at 300 meV at photon flux $> 10^{24}$ cm⁻².s⁻¹. Since TMD are known to be photodopable [66, 123], we also demonstrate the TMD photodoping. However, this effect is less pronounced when the MoSe₂ is interfaced with graphene than for bare MoSe₂ confirming the electron transfer from the TMD to the graphene. This two photodoping effect are reversible in air.

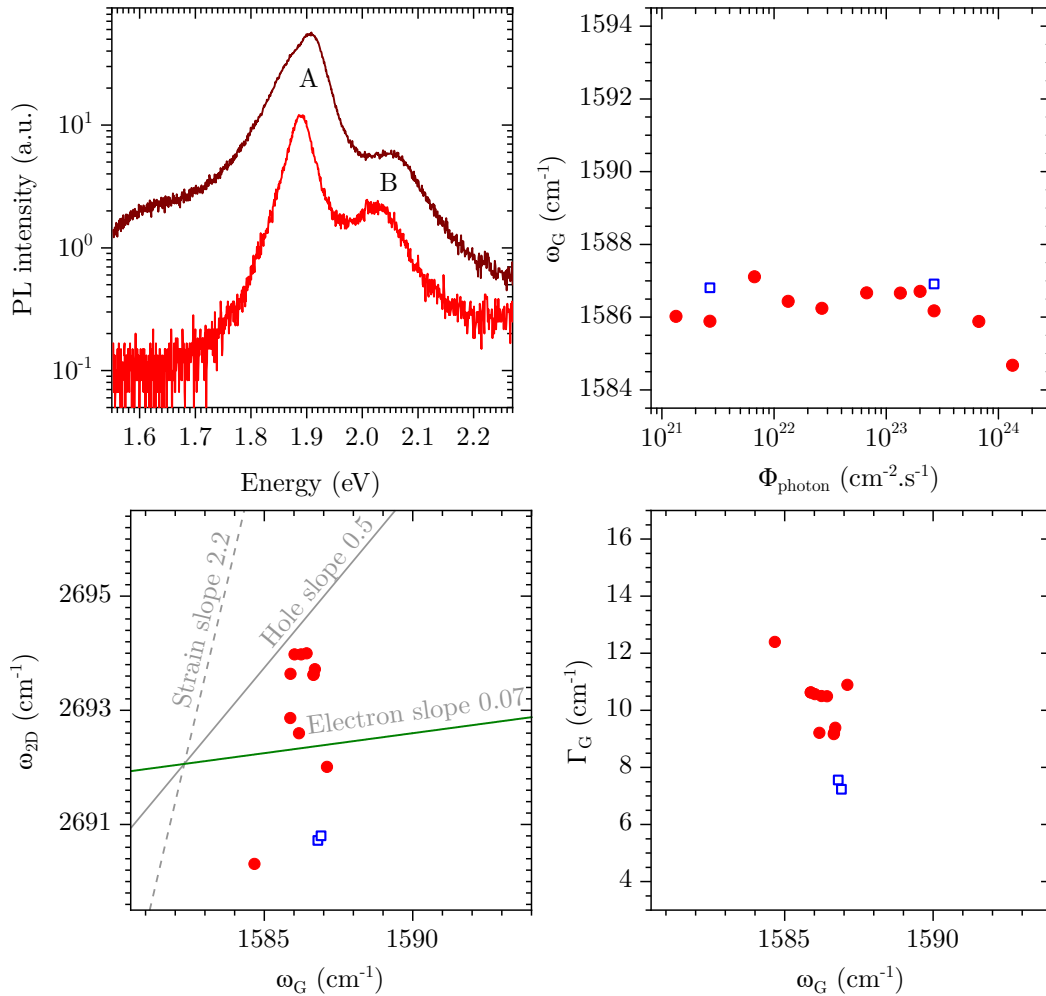


Figure 3.14: Data taken on sample S10 (MoS₂/Gr heterostructure) a) PL spectra recorded in ambient condition, dark red correspond to MoS₂ while the red correspond to MoS₂/graphene. b-d) Full (open) symbol stand for measurement done in ambient (vacuum) condition. Green symbol have been recorded at 2.33 eV laser excitation and red at 1.96 eV. b) G-mode frequency with respect to the power c) 2D- and G-Mode correlation. d) Frequency/FWHM correlation.

On the other hand, graphene Fermi energy saturate at any photon flux under vacuum as long as we insole the heterostructure long enough. We also demonstrate that even at $8 \times 10^{23} \text{ cm}^{-2} \cdot \text{s}^{-1}$ photon flux, the doping reach the saturation within five to ten minutes. In addition, once we reach the saturation level, turning off the light for one minute do not reduce significantly graphene doping level.

Going further, we completely screen the TMD/graphene heterostructure from the outer world by encapsulating it in BN flakes. In this structure, we found no evidence of doping meaning that graphene Fermi energy remain in between $\pm 100 \text{ meV}$, since our doping measurement technique is not sensitive enough to measure such doping. Finally, we prepare a BN/TMD/graphene sample. In this condition, the TMD layer still free from adsorbate thanks to self cleaning mechanism in van der Waals heterostructure. However, the graphene layer remain in contact with air so the heterostructure itself is not screened from the outer world. In this condition, we still not able to

record any doping. We have summarized this results in the table 3.1

E_F	SiO ₂ /MoSe ₂ /Gr	SiO ₂ /Gr/MoSe ₂	SiO ₂ /BN/MoSe ₂ /Gr/BN	SiO ₂ /BN/MoSe ₂ /Gr
Air	250±50 meV (R)	300 meV (R)	<100 meV	<100 meV
Vacuum	250±50 meV (I)	300 meV (I)	<100 meV	<100 meV

Table 3.1: *Graphene doping level reached at the saturation for each type of MoSe₂ based heterostructure we have measured. R and I stands for Reversible and Irreversible respectively.*

Finally, we demonstrate the exact same effect in the same proportion on WSe₂ and WS₂ graphene heterostructure deposited on Si/SiO₂ substrate. The same 300 meV doping level in graphene has been measured on this sample. This mechanism is reversible in air while irreversible under vacuum. However, we have not been able to demonstrate photodoping effect in MoS₂/graphene heterostructure which is the only structure that do not display the same behavior as the MoSe₂/Gr heterostructure. Even though small photoinduced doping as already been observed in this system even at low photon flux [110, 113].

3.3.3.2 Mechanism

We will discuss this results using a toy model to describe the temporal evolution of the graphene doping level \dot{n} .

$$\dot{n} = \alpha\Phi - \Gamma_{\text{leak}}n \quad (3.2)$$

With Φ the incident photon flux, α a coefficient that represent the photodoping efficiency and Γ_{leak} the dopant leak rate from the graphene. Such model cannot reproduce the saturation except if α depends on the population n but we have no clue of this dependence.

First, the photodoping of the TMD has been attributed to desorption of electronegative species from the TMD [66] that will release electron in the TMD. It is this free electron that will then be transferred to the graphene. This mechanism also suggest that native doping should be transferred to graphene leaving the TMD neutral (cf Sect. 3.5).

In air, the competition between the desorption and adsorption of molecules on TMD gives a non-vanishing Γ_{leak} and leads to a steady state value for the graphene Fermi energy (E_F) at a given photon flux. Therefore, the saturation happen when the photon flux is high enough to desorb every molecule adsorb on the TMD surface leading to the maximum graphene doping level.

Contrary to measurement in air, under vacuum no molecule can be adsorbed on the TMD once they have been desorbed from the TMD. Therefore, Γ_{leak} is vanishing leading to the saturation at any photon flux and the irreversibility we found under vacuum. The irreversibility under vacuum also demonstrate that $\Gamma_{\text{leak}} < 1 \text{ min}^{-1}$ in eq.(3.2) since the doping level do not change over several minutes in the dark.

We have the same results for SiO₂/MoSe₂/Gr and SiO₂/Gr/MoSe₂ samples, indicating that adsorbate are either at the air TMD interface, or at the TMD/SiO₂ interface, which is expected

since SiO₂ is a rough substrate. However, removing adsorbate thanks to the self-cleaning effect in van der Waals heterostructure block graphene photodoping below our 100 meV sensitivity and most likely block completely this mechanism.

The doping is actually found only when TMD or graphene is in contact with SiO₂. Therefore, this effect could also be induced by the interaction between TMD or graphene and SiO₂. The saturation mechanism that lead to the same doping level for MoSe₂, WSe₂ and WS₂ graphene heterostructure remain unclear. If each of these materials has the same adsorbate density or it could also be some kind of band alignment that underlies this effect. Finally, the MoS₂/graphene heterostructure behavior also remain a mystery. Even though [110] using electrical measurement shows that graphene doping density saturate below 10^{12} cm^{-2} for $10^{16} \text{ cm}^{-2} \cdot \text{s}^{-1}$ photon flux. In this condition, our method could not be used since Raman spectrum integration time at $10^{20} \text{ cm}^{-2} \cdot \text{s}^{-1}$ photon flux is already two hours. Therefore at $10^{16} \text{ cm}^{-2} \cdot \text{s}^{-1}$ photon flux, we would have to integrate over years !

3.3.4 Conclusion

In conclusion, we have demonstrated a photoinduced net charge transfer from MoSe₂, WSe₂ and WS₂ to graphene. However, we have not been able to show it in MoS₂/graphene heterostructure. We attribute this charge transfer to the desorption of electronegative species such as water or oxygen molecules that release electron into the TMD. Therefore, the photodoping is an extrinsic mechanism as well as a marginal effect even though it is easily measurable. It is marginal since the photon flux we are using are typically $10^{23} \text{ cm}^{-2} \cdot \text{s}^{-1}$ while the transferred electron density is typically $5 \times 10^{12} \text{ cm}^{-2}$

To further confirm our mechanism, we expect to recover photodoping as long as the TMD layer is in contact either with air or SiO₂. Therefore we would like to perform our characterization on SiO₂/TMD/Gr/BN and SiO₂/BN/Gr/TMD samples. The presence of photodoping effect in these samples would confirm our hypothesis.

3.4 Exciton dynamics in MoSe₂/graphene heterostructures

We have demonstrated that net charge transfer is a marginal effect. The accumulation of a finite charge density under laser illumination is slow and can not be the main quenching mechanism that removes 99% of the excitons at room temperature for any environmental conditions. Therefore it cannot explain the massive PL quenching. This could be the fingerprint of both, Dexter or Förster energy transfer (cf. Chapter 2). To differentiate all those effect, we choose to study the temperature and TMD-graphene distance dependence of the exciton dynamics in MoSe₂/Graphene heterostructure. Even though the particular case of TMD/Graphene heterostructure has not been extensively studied theoretically, people start to address temperature and distance dependence of Förster energy transfer [109].

3.4.1 Room temperature exciton dynamics

For high excitation intensity, non linear desexcitation mechanism arise (i.e. Auger effect) resulting in the sub-linearity of the PL intensity with the excitation photon flux. Therefore, we first perform steady state PL measurement at different photon flux in order to check the importance of non linear effect in the PL.

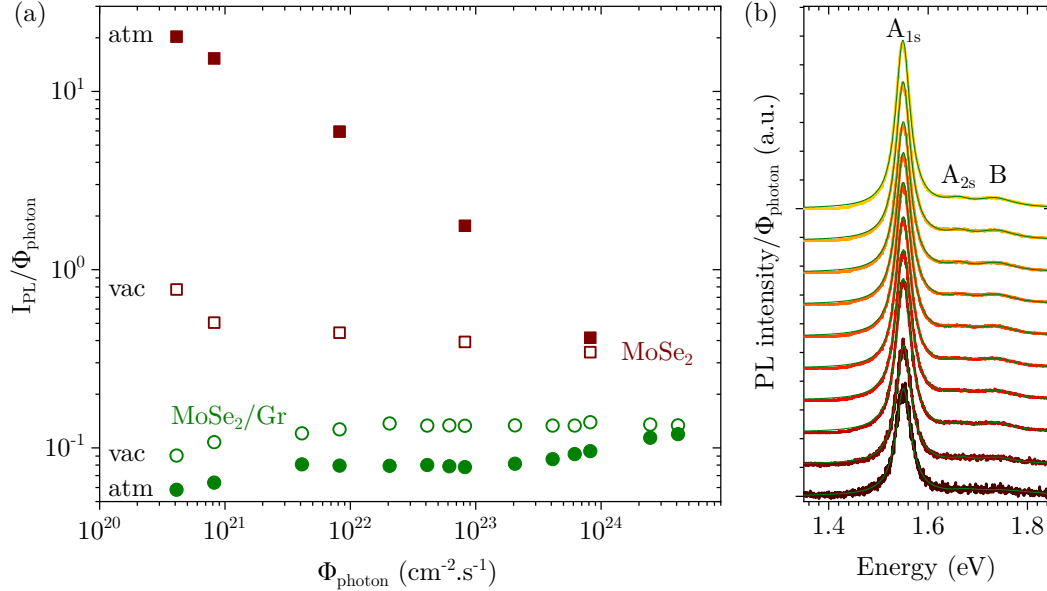


Figure 3.15: Data taken on *S3*. a) Integrated PL intensity for MoSe_2 ($\text{MoSe}_2/\text{graphene}$) in dark red squares (green circles), in air and under vacuum with full and open symbols respectively. Increasing trends denote supra-linear intensity, flat ones to linear behaviour while decreasing trends highlight sub-linear PL intensity. b) PL intensity divided by the photon flux with respect to energy for $\text{MoSe}_2/\text{graphene}$. The green line corresponds to a triple Lorentzian fit to take into account the prominent A_{1s} exciton, the A_{2s} and the B exciton.

The MoSe_2 PL intensity is highly sub-linear in air while it is weakly sub-linear at the lowest excitation intensity under vacuum before going linear (Fig. 3.15 a). This is most likely due to the removal of adsorbate under vacuum allowing exciton to diffuse more since there is less scattering center. Therefore, excitons are more likely to collide and undergo an Auger effect leading to the non radiative destruction of an exciton. Finally, exciton dynamic in bare TMD is mostly governed by Auger effect. In addition, the PL intensity on the heterostructure is linear. Therefore, the heterostructure exciton dynamics is governed by the graphene induced desexcitation rate.

To measure the exciton dynamics, we carried out TRPL measurements in collaboration with Xavier Marie's group at LPCNO in Toulouse.

To extract the exciton lifetime, we fit the time trace with a convolution of an hyperbolic secant ($1/\cosh(x)$) to take into account the IRF and an exponential decay. First, the exciton lifetime on the heterostructure is completely mixed up with the IRF. Therefore, we cannot extract exciton lifetime. However, the exciton lifetime is resolved on the bare TMD. Here we can extract a 63

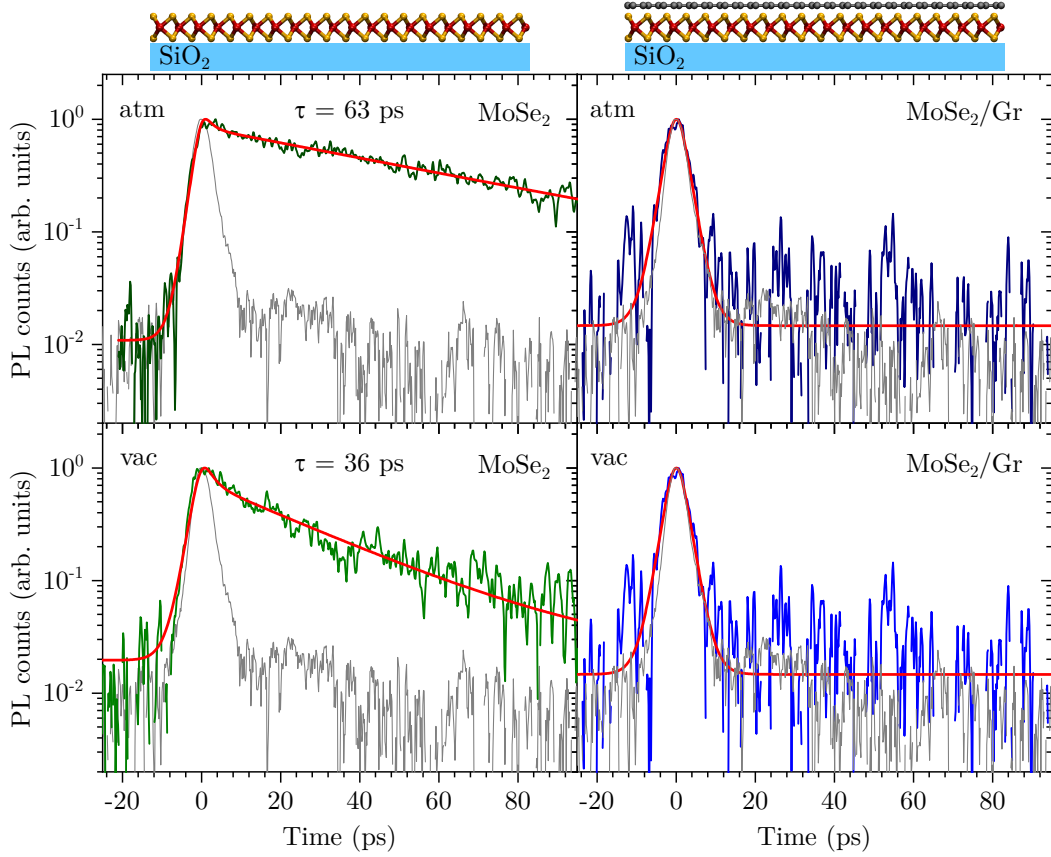


Figure 3.16: Data taken on S3. Left panels correspond to the MoSe₂ exciton decay time recorded at room temperature while the right panels are recorded on MoSe₂/graphene. Upper panels are recorded in air and the bottom in vacuum. The grey line corresponds to the IRF, the green or blue line to the data and the red one to the fit. Those data have been recorded using a 705 nm excitation.

ps and 36 ps lifetime for the exciton in air and under vacuum respectively. Compare to the 1 ns measured on bare MoSe₂ using a 633 nm (1.96 eV) excitation in [108] this 63 ps measured with a 705 nm (1.76 eV) laser excitation is rather odd. However, the latter present a quenching factor of only 20, highlighting either the reduction of the bare MoSe₂ quantum yield after cooling the sample down to 4K and bringing it back to ambient conditions or the signature of non linear effect such as Auger recombination (cf Chapter 2). In the other hand, we have already evidence such excitation energy dependent quenching factor for WS₂ (Fig. 3.13) with a 300 quenching factor excited at 532 nm (2.33 eV) while the quenching factor is only 20 for a 633 nm (1.96 eV) laser excitation.

For freshly exfoliated sample excited at 532 nm (2.33 eV) with a cw laser, the quenching factor depends strongly on the photon flux since Auger recombinations play a key role in the excitonic dynamic. Finally, we measure the quenching factor using 100 nW beam focalized on a μm^2 resulting in a 200 W.cm^{-2} power density. Using this excitation power, we extract the quenching factor in air for different TMD and we summarized it in table 3.2.

	MoSe ₂	WS ₂	WSe ₂	MoS ₂
quenching factor in air	300	300	150	10

Table 3.2: Exciton quenching factor for various TMD using 532 nm (2.33 eV) laser excitation and 200 W.cm⁻² excitation power density

Finally, it is hard to understand the influence of Auger recombination on the TMD photo-physics. Therefore, it will be easier to measure intrinsic properties at low temperature. The exciton lifetime will be much shorter lived at 4K (~ 1 ps) than at room temperature (~ 1 ns) forbidding the accumulation of exciton in the TMD and the rise of non linear recombination.

3.4.2 Temperature dependence

3.4.2.1 SiO₂ supported heterostructure

We perform the TRPL measurements on S3 samples on bare MoSe₂ and MoSe₂/graphene region. The exciton dynamics is the same on both regions below 80K. The only difference is a second longer decay time on bare MoSe₂ compared with the heterostructure. This faint longer lived population is probably due to exciton localization (Fig. 3.17).

We fit the experimental PL time trace using the same method described above and report them in Fig. 3.18.

The exciton dynamic from 14 to 80 K, Fig. 3.18, is in perfect agreement with previously reported 2 ps lifetime at 4 K measured in [12]. Interestingly the MoSe₂ lifetime is the same as the exciton lifetime on the heterostructure. Therefore, the new decay time τ_G induced by the graphene has to be slower than the radiative decay time. This already puts a lower bound to τ_G at 2 ps at 4 K. The lifetime then decreases with temperature to enter the IRF at temperature higher than 80 K for both MoSe₂ and heterostructure. To further characterize τ_G we continue to sweep the temperature from 90 K to 250 K Fig. 3.19.

A long excitonic lifetime starts to rise on MoSe₂ at 90 K due to the thermalization of the exciton population. However, the excitonic lifetime on the heterostructure remains below the IRF. Since we show that τ_G is larger than 2 ps at 14 K, and that graphene does not impact exciton lifetime from 14 K to 80 K, we expect to resolve the exciton lifetime above 90 K. Therefore, its absence denotes that τ_G has been reduced when temperature increases. Or the decay mechanism is highly wavevector dependent since the long lived thermalized exciton population has large wavevector contrary to the short lived non thermalized excitation (cf Chapter 2).

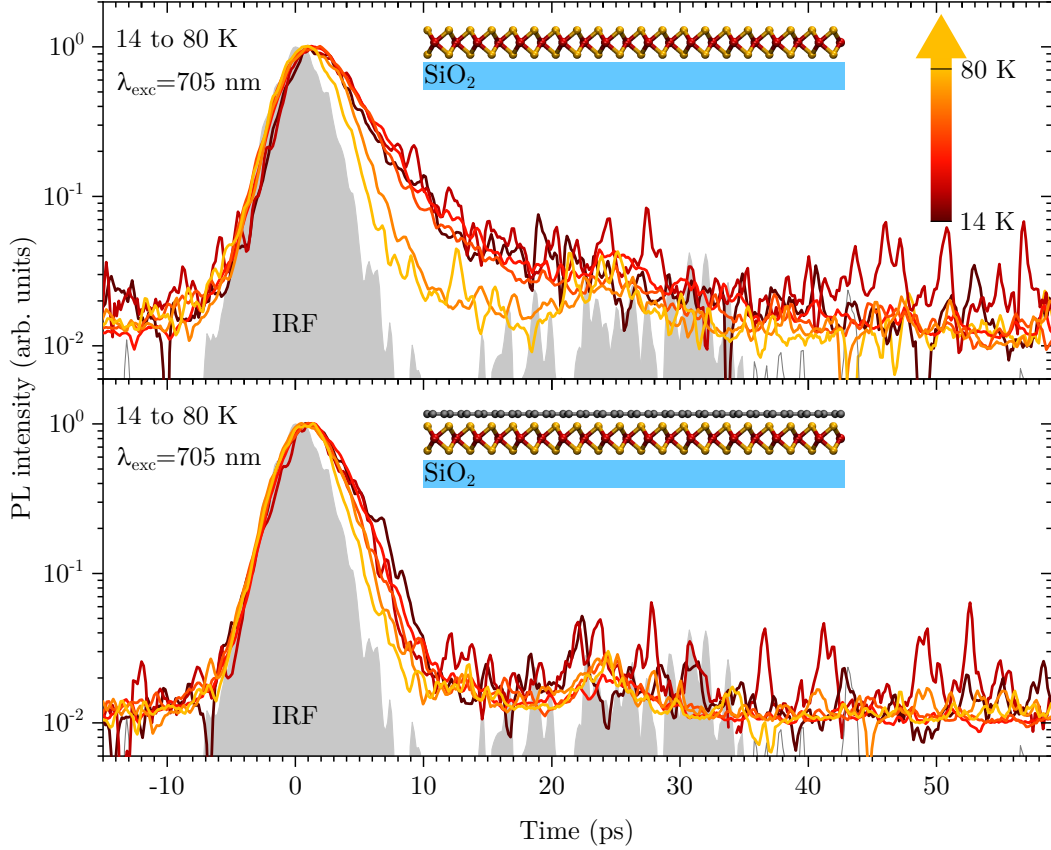


Figure 3.17: Data taken on S3 ($\text{SiO}_2/\text{MoSe}_2/\text{Graphene}$). Upper panel, TRPL spectrum for MoSe_2 from 14 K (in dark red) to 80 K (in yellow). The grey line is the IRF of our system. The lower panel is dedicated to the $\text{MoSe}_2/\text{Graphene}$ heterostructure where no longer lifetime is seen. However the lifetime is above the IRF up to 80K and is comparable to the bare MoSe_2 lifetime. The excitation wavelength is 705 nm

3.4.2.2 Encapsulated heterostructure

To get better optical properties we choose to encapsulate our sample in boron nitride.

Encapsulation into boron nitride removes all the adsorbate at the TMD surface. Therefore, the relaxation time from a reservoir of high momentum exciton to the A exciton emissive state is increased (cf. 2.4.2.3). In (Fig. 3.20) we show that graphene reduce the MoSe_2 relaxation time when it is encapsulated in BN. On MoSe_2 both rise and decay time are resolved corresponding to the exciton recombination time and relaxation time respectively. Since the effective radiative lifetime τ_0^{eff} depends on the dielectric environment as $\tau_0^{\text{eff}} = \sqrt{\epsilon} \tau_0^{\text{vac}}$ with τ_0^{vac} the excitonic lifetime in vacuum, the MoSe_2 lifetime should increase when encapsulated in BN. Interestingly, The A exciton dynamic in $\text{MoSe}_2/\text{graphene}$ encapsulated in graphene is similar to the dynamic without encapsulation.

At higher temperature, the heterostructure behaves as the non encapsulated heterostructure

On encapsulated $\text{MoSe}_2/\text{graphene}$, we found again no clues of larger lifetime induced by the exciton population thermalization spreading exciton momentum outside of the light cone and therefore increasing the exciton lifetime at higher temperature (Fig. 3.21). This raises the ques-

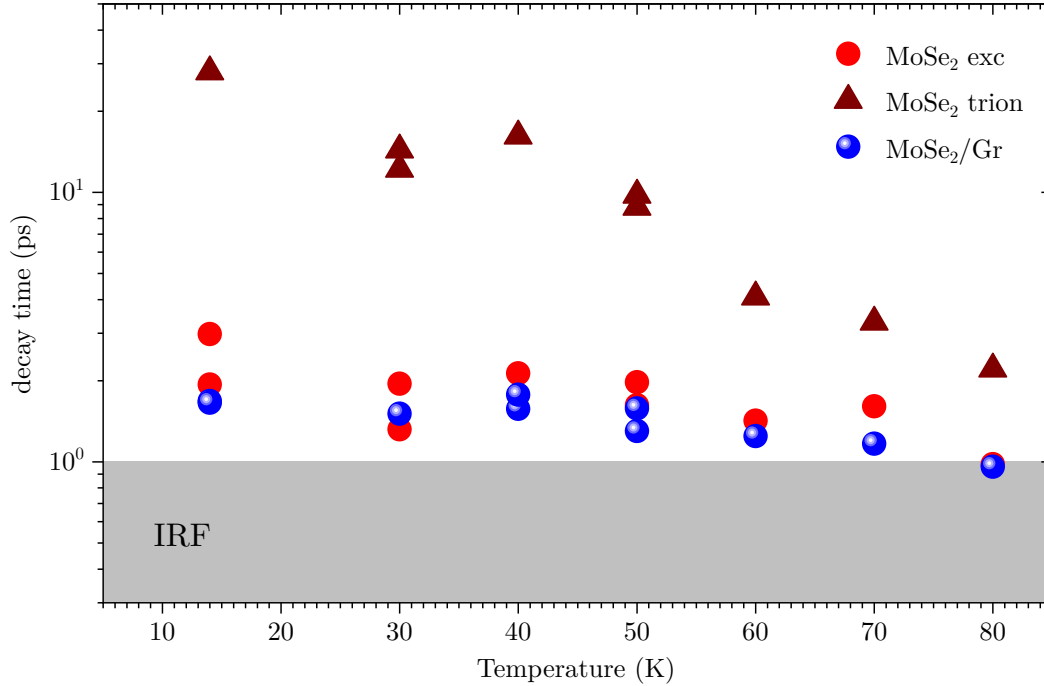


Figure 3.18: Data taken on S3 ($\text{SiO}_2/\text{MoSe}_2/\text{Graphene}$). MoSe_2 exciton and trion lifetime plotted with red circle and dark red triangle respectively. The exciton lifetime we present is the short lived part of the time trace. The heterostructure exciton lifetime are represented by the blue sphere. We give value within 0.2 ps. We do not display the error bar because of the log scale.

tion of the exciton thermalization. Most likely, the exciton population is not thermalized in the heterostructure since thermalized population has a much longer lifetime, only the non thermalized exciton can emit otherwise they are destroyed via non radiative decay through graphene. However, if thermalized, the exciton population should not spill out of the light cone. Therefore the exciton population temperature has to be low.

3.4.2.3 Temperature dependent PL intensity

Exciton and trion are two independent populations meaning that trion is not formed from an exciton population eg. from the trapping of an exciton onto a trapped charge in the TMD. Therefore, the oscillator strength is distributed between the exciton and the trion depending on the doping level. However, we have no control on the doping level of our samples and the quantum yield of the trion is not known. Since the doping level is not the same for MoSe_2 and for $\text{MoSe}_2/\text{Graphene}$, (Sect. 3.5), there is an unknown offset in the exciton PL intensity which forbids us to conclude on the quenching factor. To exploit PL intensity data, the first thing is to compare the PL intensity at the same doping level. Therefore, charge adjustable sample are mandatory for such experiment.

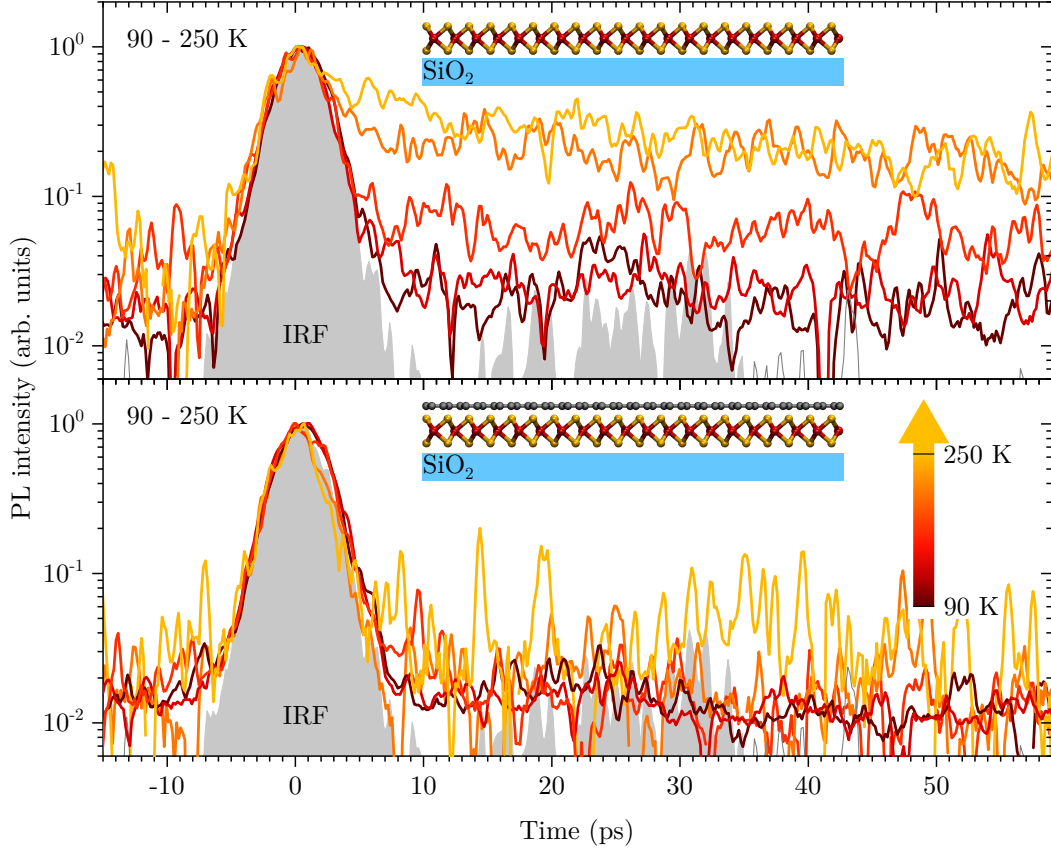


Figure 3.19: Data taken on S3. Upper panel, TRPL spectrum for MoSe₂ from 90 K (in dark red) to 250 K (in yellow). The grey line is the IRF. The lower panel is dedicated to the MoSe₂/Graphene heterostructure where the exciton time trace is merged with the IRF.

3.4.3 Distance dependent exciton dynamics

Graphene induces a new decay channel Γ_{gr} which depend on the temperature and distance between TMD and graphene. From the room temperature exciton dynamics, we extracted $\Gamma_{\text{gr}}(d = 0, T = 300) \sim 1 \text{ ps}^{-1}$. At 4K $\Gamma_{\text{gr}}(d = 0, T = 4) > 0.5 \text{ ps}^{-1}$. However, the temperature dependence of the excitonic lifetime does not bring valuable information to better understand the mechanism underlying $\Gamma_{\text{gr}}(d, T)$. Hence, we fabricate samples consisting of an encapsulated MoSe₂/Graphene heterostructure with a BN spacer in between TMD and graphene. To quantitatively measure the lifetime reduction induced by the graphene at a given distance, it is mandatory to have a reference on BN encapsulated MoSe₂ monolayer. However, none of the sample we fabricate has a proper reference. Since the BN capped MoSe₂ always emits less light with a shorter lifetime than the TMD/BN/graphene region. Even though we do not have proper reference on our sample, we were able to measure the decay time of the TMD distant of 5 nm from the graphene (Fig. 3.22 a). We compare our results to the sample S1 time trace. We use very low fluence to record the dark red exciton decay (Fig. 3.22 b) as well as the decay on the reference S1.

The exciton lifetime with 5 nm BN between the TMD and the graphene is slightly reduced compare to our reference. Such results point toward a relatively efficient long range decay channel

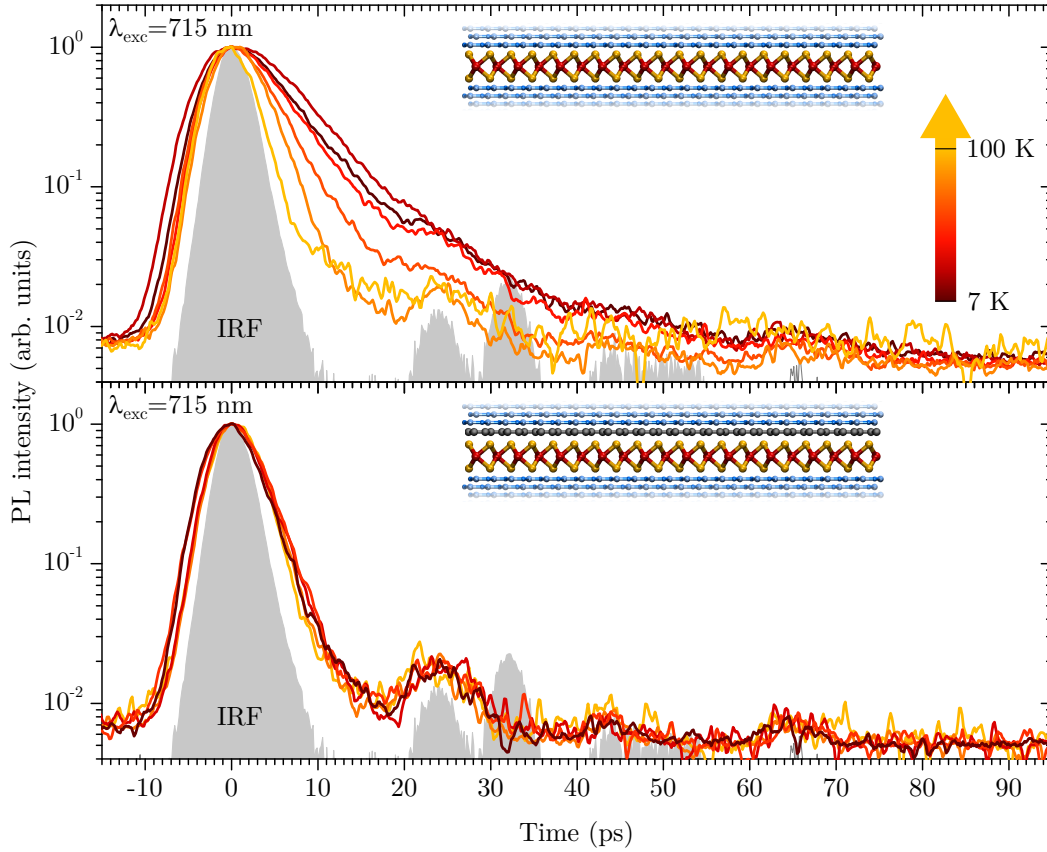


Figure 3.20: Data taken on S11 a) Upper panel, MoSe_2 A exciton time trace from 7 to 100K. The lower panel is dedicated is the same as (a) for $\text{MoSe}_2/\text{Graphene}$ heterostructure. for every panel, the gray curve correspond to the IRF.

as Förster energy transfer. However, at short distances, the Förster energy transfer is probably not the dominant mechanism since the excitonic lifetime is almost recovered at 5 nm from graphene.

3.4.4 Conclusion

A TMD interfaced with graphene undergoes a strong PL quenching. We try to characterize the mechanism responsible for this quenching. First, we demonstrate that charges were transferred from TMD to graphene when they were in contact. Raman spectroscopy allows us to unveil and study this net charge transfer. We determine the nature of the dopant, electrons, and we extract the Fermi energy of the graphene layer. This doping effect is seen in various experimental conditions, in air or under vacuum and for different TMD/Graphene heterostructures. However, its dynamics change drastically depending on the conditions, highlighting its extrinsic nature. Despite this extrinsic nature, a TMD layer is needed to achieve the high amplitude we observe and finally, the role of the TMD in this effect is not completely clear yet. Therefore, we need to perform new experiments on samples such as $\text{SiO}_2/\text{BN}/\text{Graphene}/\text{TMD}$ and $\text{SiO}_2/\text{TMD}/\text{Graphene}/\text{BN}$ to understand how the TMD layer dopes the graphene and the role of adsorbate in this mechanism. However, we were able to show that this mechanism is a marginal effect with 10^{12} electron. cm^{-2} transferred to graphene compare to the 10^{22} photon. cm^{-2} photon flux used to excite the TMD.

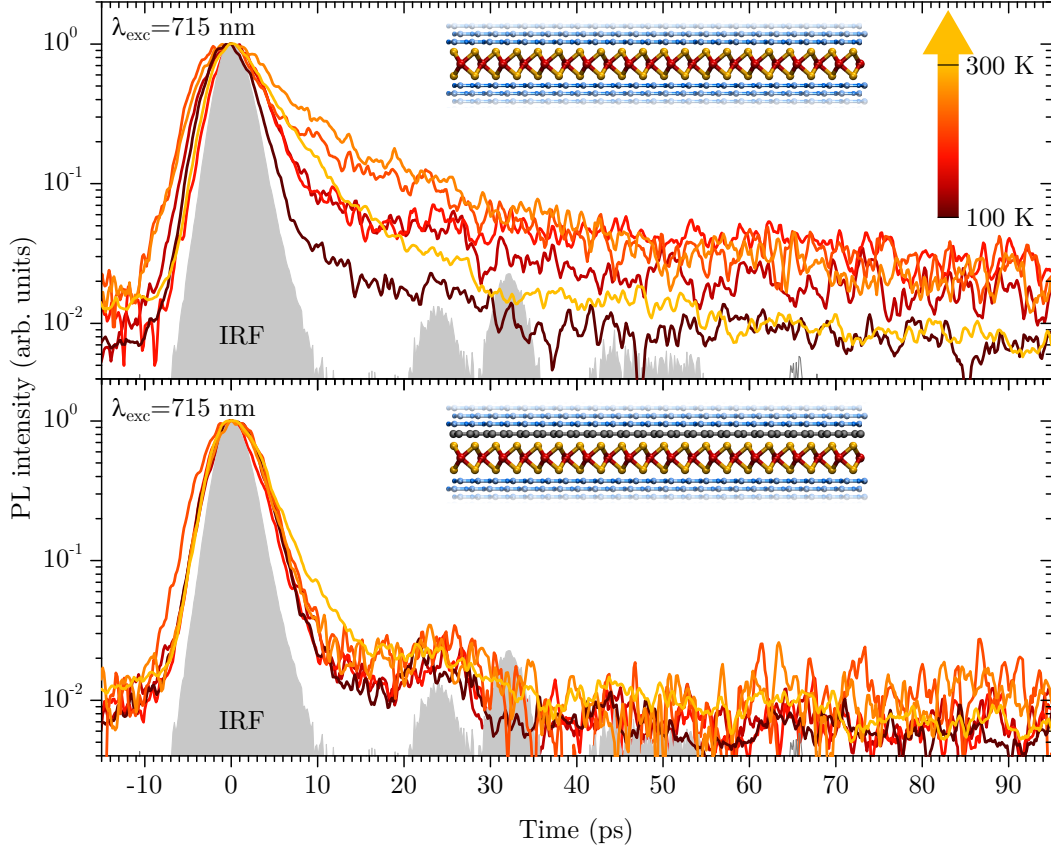


Figure 3.21: Data taken on S11 a) Upper panel, MoSe_2 A exciton time trace from 100 to 300K. The lower panel is dedicated is the same as (a) for $\text{MoSe}_2/\text{Graphene}$ heterostructure. for every panel, the gray curve corresponds to the IRF.

At this point, we still don't know how TMD excitons are quenched by graphene. To characterize the exciton decay mechanism, we perform PL and TRPL experiments. We demonstrate that whatever the PL intensity is, the exciton lifetime is not impacted by the graphene at low temperature. With increasing temperature, the exciton lifetime reduces but remains equal between the bare MoSe_2 and the heterostructure merging with the IRF (≈ 1 ps) at 80 K. However, around 100 K, a longer lifetime starts to rise on the bare MoSe_2 corresponding to the emission of a thermalized population with an effective lifetime much larger than the non thermalized exciton PL intensity. At this point, the heterostructure excitons remain short lived (< 1 ps). Therefore, we conclude that the graphene induced exciton decay mechanism is either very sensitive to the exciton momentum, since thermalized exciton have a much larger momentum distribution than the non thermalized exciton. Or it could also be the smoking gun of the temperature dependence of this effect expected for a Förster energy transfer between TMD and graphene [109].

Finally, since Förster-type energy transfer is more efficient at room temperature, we perform TRPL with a BN spacer between the TMD and the graphene layer. However, a sample fabrication issue forbid us to get an intern reference on encapsulated MoSe_2 . Therefore, our results

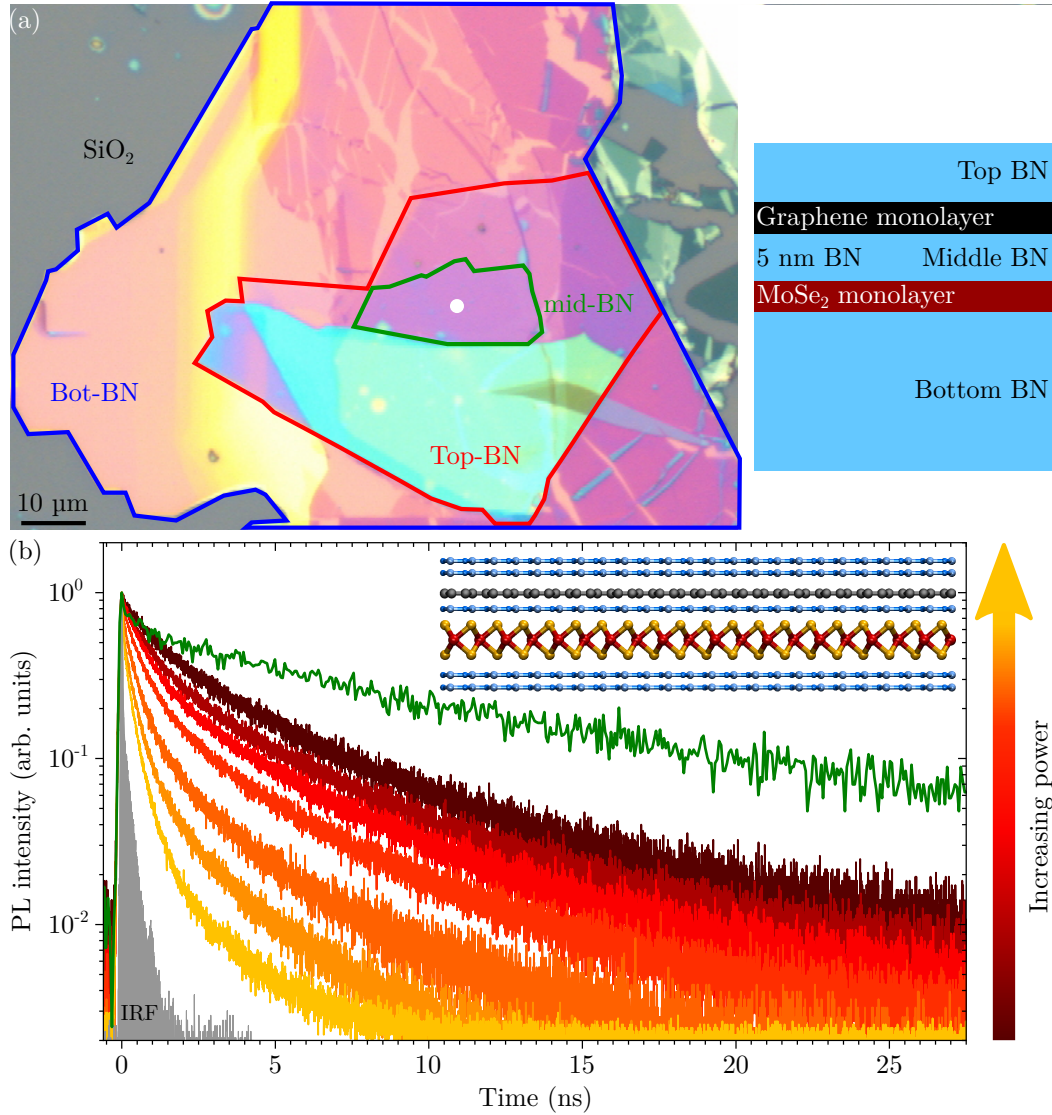


Figure 3.22: Data recorded on S15 and S1 in ambient conditions. a) Sample S11 micrograph, the blue, green and red highlight the bottom, middle and top BN layer. b) Fluence dependent TRPL recorded on S15 and displayed in the dark red ($4 \times 10^{10} \text{ cm}^{-2}$ fluence) to yellow ($3.5 \times 10^{13} \text{ cm}^{-2}$ fluence) colour gradient. Each of this time trace is recorded using a 2.58 eV (480 nm) laser energy. As an indication, we also display the time trace of the of a MoSe₂ supported on SiO₂ recorded using a 1.96 eV (633 nm) laser energy at $2.2 \times 10^{11} \text{ cm}^{-2}$ fluence. This last trace is not directly comparable to the others.

are difficult to interpret even if we can make use of an external reference. First, we found that exciton are long lived ≈ 0.5 ns for a TMD decoupled from the graphene by 5 nm BN. However, the exciton decay time induced by Förster energy transfer to graphene is calculated to be ≈ 10 ps [109] pointing toward a non Förster mediated decay mechanism. On the other hand, comparing our results with the external reference, we found a lifetime reduction between them highlighting a probable effect of the graphene on the lifetime.

Graphene induced decay mechanism is most likely an energy transfer. However, giving its

exact microscopic description remain an open question. The Förster-type energy transfer require strong in plan dipole which is one of the main characteristic of the TMD excitons. In addition, this transfer has been demonstrate in similar system. With 5 nm distance between the TMD and the graphene we expect a factor two quenching of the PL for a Förster-type energy transfer. The difficulty to have a proper internal reference make such small quenching difficult to be observed. In addition, the PL intensity rise drastically with a 2 nm BN spacer. This probably indicates that at least a part of the quenching is due to a Dexter-type energy transfer which rely on a charge exchange between the TMD and the graphene. Giving the relative weight of each mechanism would be difficult. Though, we have demonstrate that energy transfer wether it is charge or dipole mediated process, play a key role in the exciton dynamics of TMD/Graphene heterostructures.

3.5 Neutralizing a TMD monolayer with graphene

Transition metal dichalcogenide are natively doped even if the exfoliation process is carefully carried out. This doping is strongly inhomogeneous and gives a hard time to an experimentalist to reach the sample neutrality point in a given region, and forbids us to achieve a fully neutral system over several microns. At the end of the day, the neutrality point can only be reached for small almost homogeneous regions which give rise to a "sweet spot" physics with huge reproducibility issue. This problem could be addressed by interfacing the TMD with graphene as long as it can act as a local charge reservoir to collect TMD charges (Fig. 3.23). To monitor the TMD doping, we choose to cool down our samples and use the strong trion emission from TMD, to locally estimate the charge inhomogeneity through the local change of the exciton trion/intensity ratio. We map several different samples including encapsulated and non encapsulated samples and results are essentially the same at the sole difference that the TMD is heavily doped in non encapsulated TMD almost hiding the excitonic part of the spectrum.

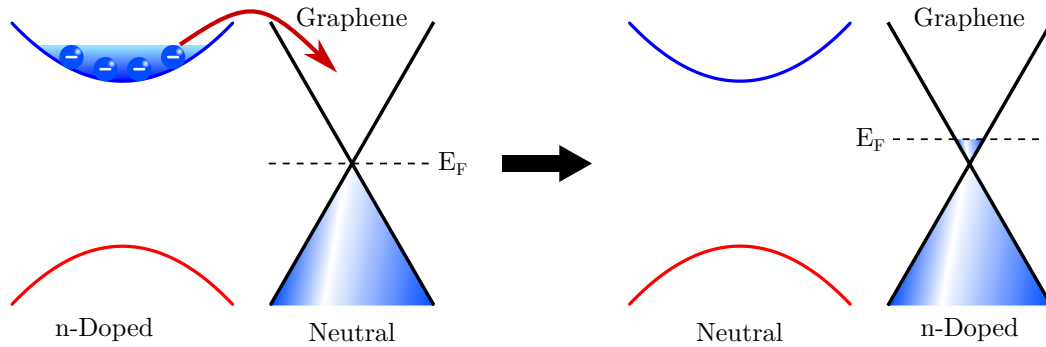


Figure 3.23: Sketch of electron transfer from a doped TMD to the neutral graphene.

3.5.1 Room temperature hints of TMD neutralization

We observe already in section 3.3 some hints of the TMD neutralization when interfaced with graphene. The exciton trion energy difference is ≈ 30 meV for every TMD. Such energy difference is slightly higher than the room temperature thermal energy, 25 meV. Therefore the trion could be seen at room temperature even though it is weakly stable. In (Fig. 3.24) we report PL spectra for bare TMD and TMD/graphene heterostructure recorded using photon flux $< 10^{21}$ cm $^{-2}$ and a 2.33 eV (532 nm) laser excitation. Bare MoSe $_2$ is recorded almost in the linear regime since the B exciton is not rising above the noise. Therefore, the A exciton is long lived, it undergoes very few Auger effect. However, a shoulder is visible on the red side of the A exciton (Fig. 3.24 a). Hence, we fit the spectrum with two Lorentzians that appear to be separated by 30 meV. Thus we attribute the shoulder to the trion. The absence of such shoulder on the heterostructure is a hint that TMD is actually neutral or very weakly doped when interfaced with graphene. For MoS $_2$ (Fig. 3.24 b), we observe trion A exciton and B exciton. On the other hand, the trion is not visible on the red side of the exciton. Again this is a hint of the MoS $_2$ neutrality. The WS $_2$ presents only one peak, the A exciton. However, the A exciton presents a shoulder for the bare

WS₂ PL spectrum which is not visible when interfaced with graphene (Fig. 3.24 c).

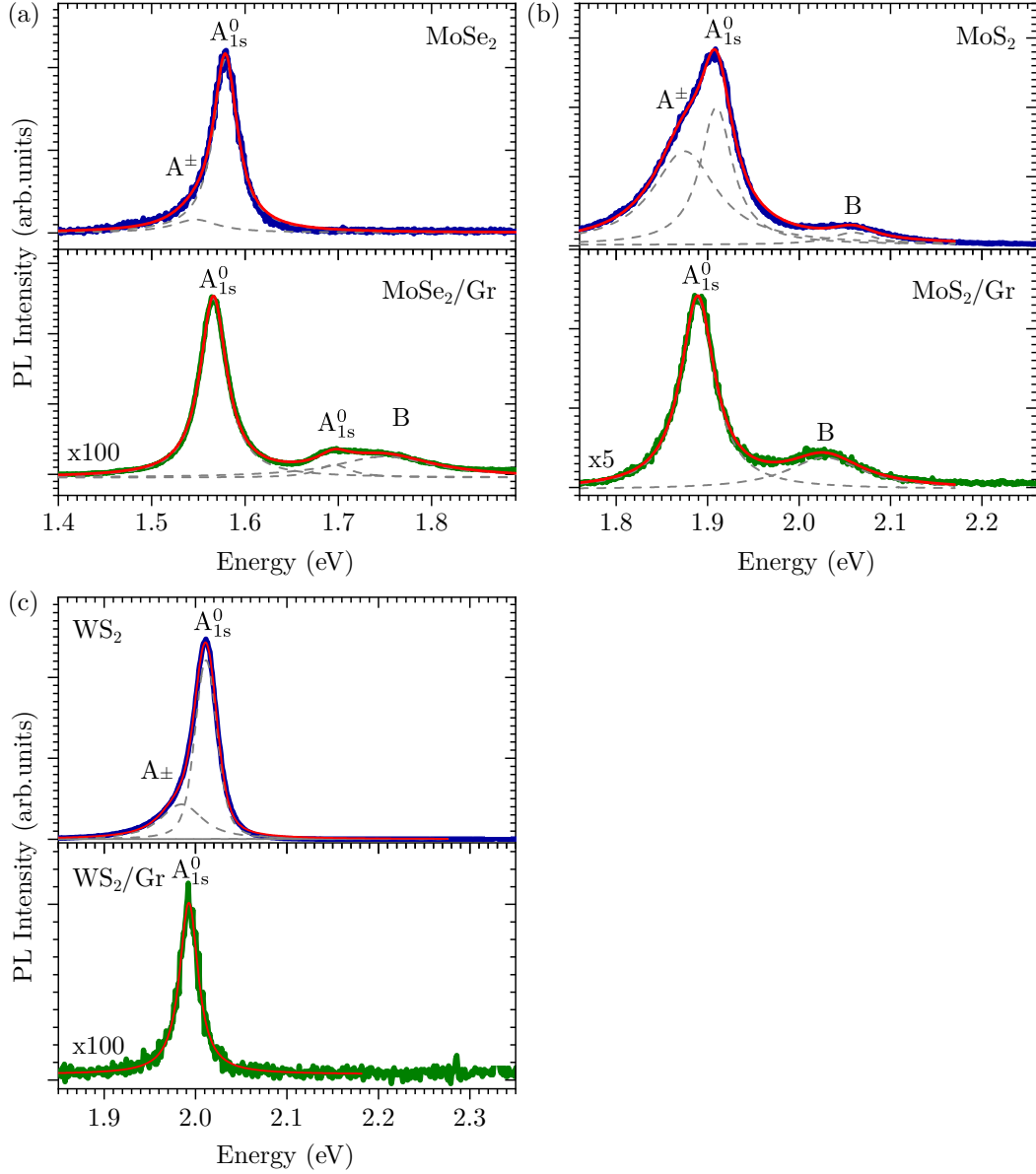


Figure 3.24: Spectra displayed in dark blue correspond to bare TMD while it is shown in green for TMD/graphene heterostructure. Spectra have been recorded in ambient conditions. a) Data taken on S11. Bare MoSe₂ spectrum has been fitted by two Lorentzian one to take into account the red shoulder attributed to the trion. The second is the 1s state of the A exciton b) Data taken on S10. The bare MoS₂ spectrum is fitted with three Lorentzian, one for the trion one for the A exciton and the last for the B exciton. Since there is no shoulder on the heterostructure spectrum, we fit the spectrum with only two Lorentzians, the A and B exciton. c) Data taken on S12. The bare WS₂ spectrum is fitted by two Lorentzian, one for the A exciton and one for the trion component. This component is absent on the heterostructure spectrum.

Finally, we record the opposite behavior on WSe₂ which present a shoulder on the red side of the A exciton PL emission for both the heterostructure and the bare TMD. We have hints that MoS₂, MoSe₂ and WS₂ are neutralized by graphene since we do not record, on the heterostructure,

the shoulder we measure at the trion energy on bare TMD.

3.5.2 Characterization of MoSe₂/graphene PL emission

Before going any further, we will demonstrate that PL emission from the heterostructure originates from the A exciton radiative decay whatever the temperature. Therefore, we record the temperature PL dependence of the heterostructure and reference TMD (Fig. 3.25).

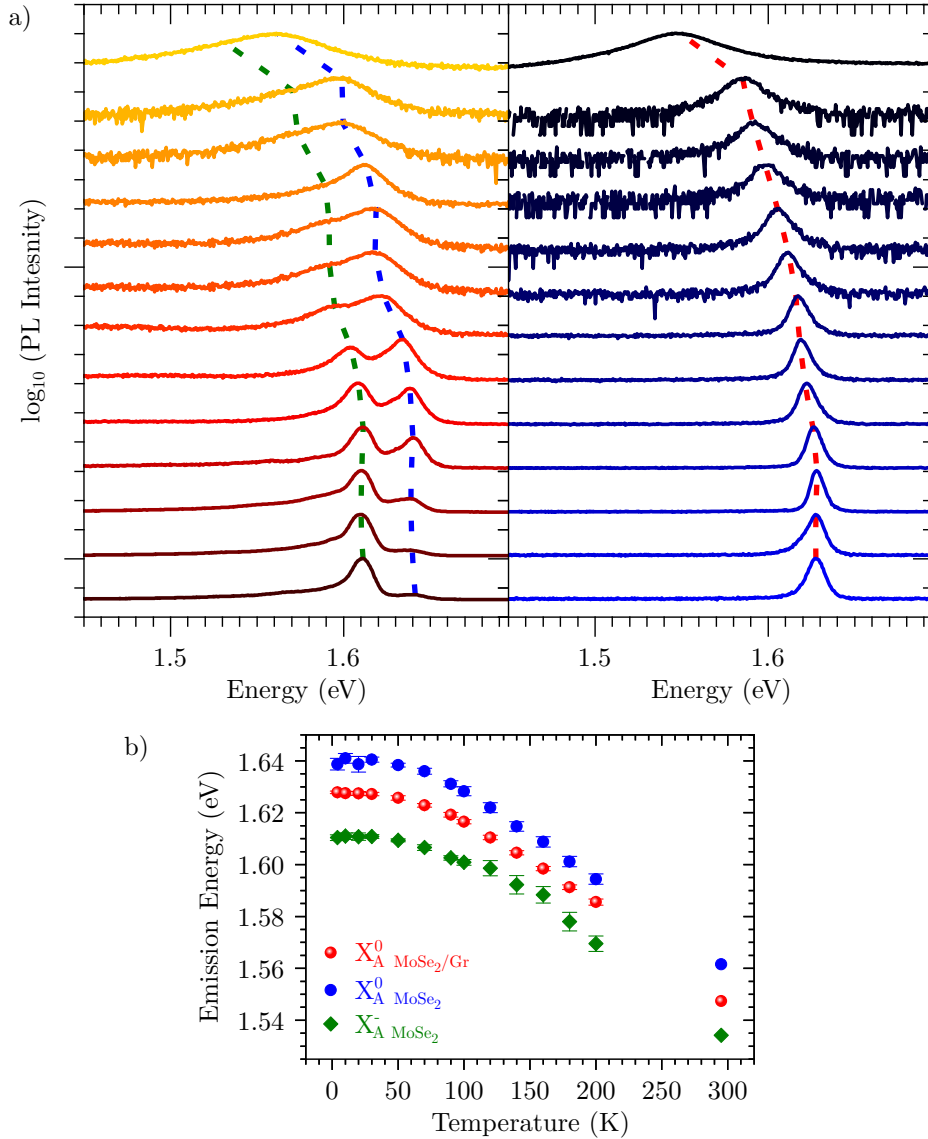


Figure 3.25: Data taken from S3. a) MoSe₂ and MoSe₂/Graphene temperature dependent PL spectra, from dark red to yellow for MoSe₂ and from dark blue to light blue for MoSe₂/Graphene. b) Average MoSe₂ exciton and trion emission energy and average MoSe₂/Graphene exciton emission energy. Data point are average over few tens of spectra and the error bar correspond to the standard deviation, which is most of the time smaller than the data point.

At 4K, We found only one peak on the heterostructure PL spectrum (Fig. 3.25 b). Since graphene has a large dielectric constant, we expect the exciton to redshift compared to the bare

TMD exciton [25]. Since, the trion is also red shifted compared to the exciton this emission peak could also be the trion. However, the emission peak energy from the heterostructure is always more energetic than the trion and slightly less energetic than the exciton on the bare TMD at 4 K (Fig. 3.25 a). An emission coming from the TMD trion on the heterostructure would have been red shifted compare to the trion line on the bare TMD for the same dielectric constant reason. Hence, we can attribute the PL emission of the heterostructure to the exciton since its emission energy is higher than the trion disqualifying it to be the origin of the sample PL. Finally, we extract the PL emission energy for the bare TMD exciton and trion and from the heterostructure peak. We report the results in (Fig. 3.25 c). We show the same behaviour for the three and the heterostructure emission energy remains in between the bare TMD exciton and trion. This gives a final proof to the excitonic nature of our PL emission.

The trion intensity is vanishing on the heterostructure, with a trion over exciton intensity ratio below 10^{-3} . Hence, either the TMD is neutral when interfaced with graphene or the trion is completely quenched by the graphene. We carried out reflectivity measurement at 4K coupled with PL spectroscopy (Fig. 3.26) on BN encapsulated sample to get sharper optical resonance.

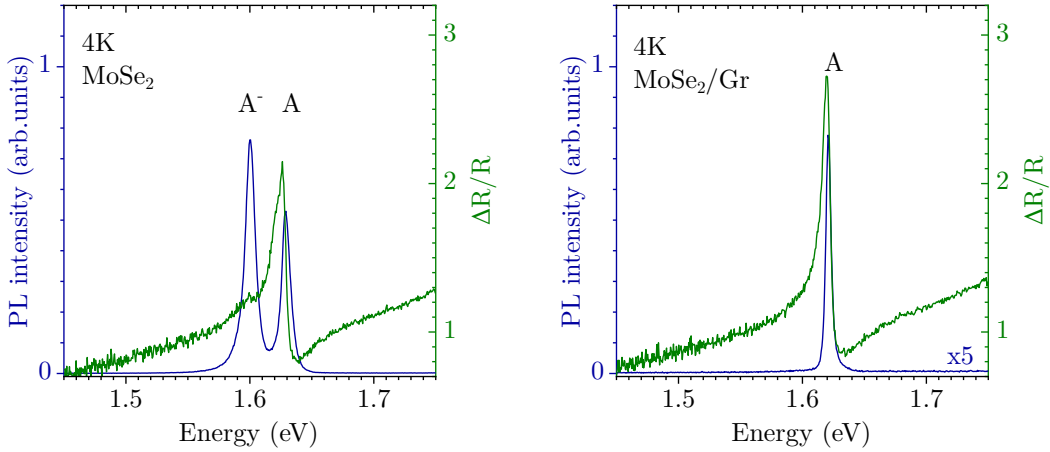


Figure 3.26: Data taken on S11 a) BN encapsulated MoSe_2 PL spectrum in blue and reflectivity in green. b) same as (a) for MoSe_2 graphene heterostructure.

The BN capped MoSe_2 display a strong trion emission slightly larger than the exciton emission. In addition we observe a small bump in the reflectivity at the trion energy plus a larger resonance at the exciton energy. This demonstrate the doping in MoSe_2 . On the other hand, the heterostructure display only one peak. In addition, the reflectivity measurements display only one sharp resonance at the excitonic resonance. This is prove of the TMD neutrality when interfaced with graphene.

3.5.3 Doping homogeneity in MoSe_2 /graphene heterostrucutre

The careful reader should also note that the A exciton PL intensity is quenched by roughly a factor of ten on the TMD/Graphene region compare to the TMD alone and this quenching factor becomes twice bigger if we consider the total photoluminescence signal. Because we pump above

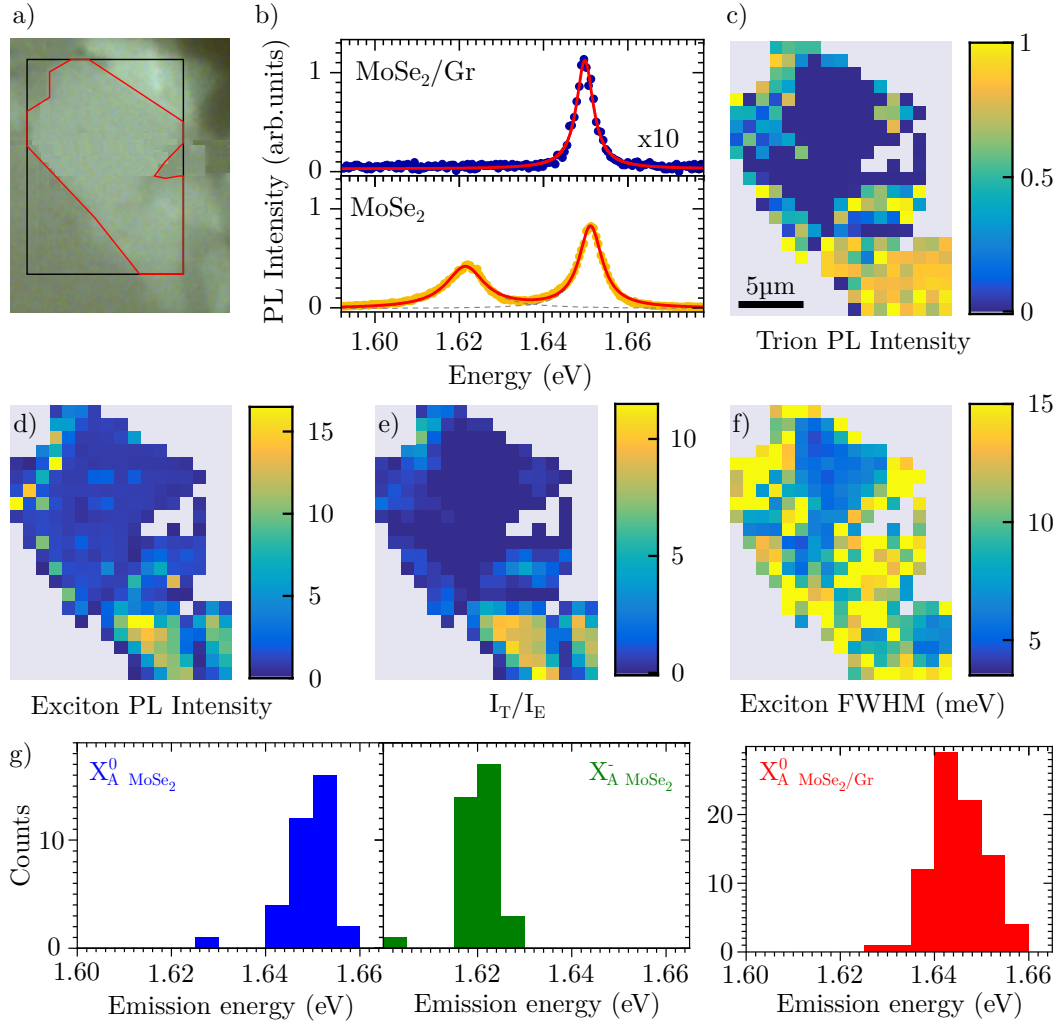


Figure 3.27: Data taken from S11 a) sample optical micrograph, the red line highlight MoSe₂ and the black rectangle correspond to the mapping area. b) Hyperspectral map of the sample, here the width of the A exciton peak is reported. c) MoSe₂/Graphene and MoSe₂ spectra, the red line is their Lorentzian fit and double Lorentzian fit respectively. Those fits are used to extract the position intensity and width of each pixels of the hyperspectral map. d) Trion PL Intensity hyperspectral map, the intensity on the MoSe₂/graphene area of the sample is vanishing. e) Exciton PL Intensity hyperspectral map, the intensity on the MoSe₂/Graphene area, the PL intensity is ten times lower than in the MoSe₂ area. f) Trion over exciton intensity ratio hyperspectral map. g) Histogram of MoSe₂ and MoSe₂/Graphene A exciton emission energy in blue and red, MoSe₂ charged A exciton emission energy in green extracted from fit of the hyperspectral above

the A exciton energy, we are creating either excited A exciton (i.e. 2s, 3s ...) or higher lying exciton (i.e. B exciton) that will then cascade non radiatively to either the 1s A exciton or the trion and emit from this state. Trion and exciton are independent [12], meaning that trion does not need an exciton first before being created. It is then mandatory to define the quenching factor with respect to the total trion plus exciton PL intensity instead of the sole A exciton intensity. This will also avoid any trouble with MoSe₂ and MoSe₂/Graphene heterostructure on SiO₂ where the A exciton is more intense on the heterostructure due to the dominant trion on the sole TMD.

Finally, the radiative lifetime for MoSe₂ is around 2ps [12] and with a quenching factor around 20, it gives a lifetime of few hundreds of femtoseconds. This is not true since the exciton lifetime at 4K has been measured on this sample to be 2 ps. This shows again the difficulty to properly define the quenching factor at low temperature. In addition, this result shows that exciton formation rate is probably different in TMD/Graphene than in bare TMD.

Since trions need a charge to be formed, the trion over exciton intensity ratio gives us hints on the TMD doping level. In (Fig. 3.27 d) we found that trion has a vanishing intensity when interfaced with graphene. This highlights that MoSe₂ is probably neutral.

Interestingly, we also found that on one hand, with width ranging from 5 to 10meV (Fig. 3.27 c), we are far from reaching the state of the art width for the BN-encapsulated MoSe₂ A exciton which could be as narrow as 2meV, probably close from the homogeneous broadening. On the other hand, the A exciton width on the MoSe₂/Graphene is reduced down to 4meV, which corresponds, if radiatively limited, to a few hundreds of femtosecond lifetime. This highlights the small, if existing, inhomogeneous broadening and therefore the good quality of our samples.

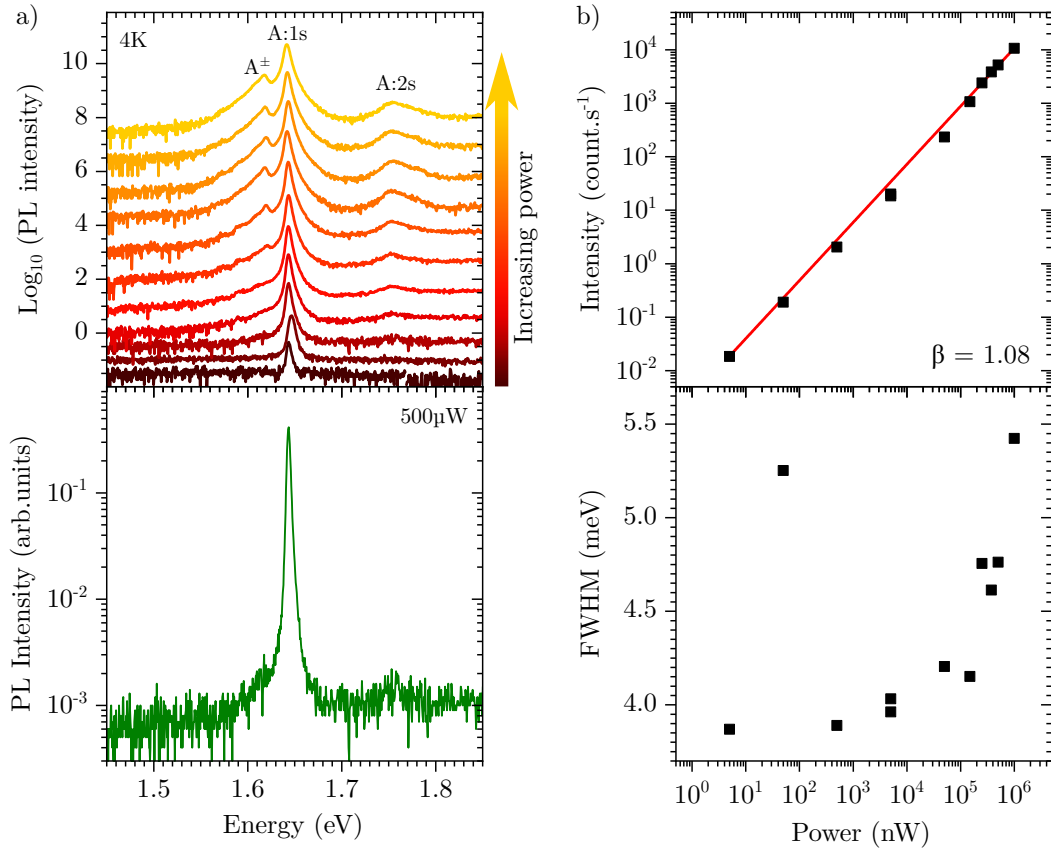


Figure 3.28: Data taken from S6. a) Upper panel, PL spectra at 4K normalized by the photon flux in logarithmic scale. At high photon flux, the trion start to rise as well as the second excitonic state 2s. Lower panel, spectrum taken at 4K with 500 μ W focused with a 50 \times objective. b) Upper panel, integrated A exciton PL intensity with respect to the incoming power. The black squares are the data while the red line is a fit by the power law αx^β with $\beta = 1.08$, showing a strongly linear behaviour of the PL intensity, in the photon flux range we have studied. The lower panel represent the A exciton width with respect to the incident power showing a sharp increase at high flux

TMD are also known to be photodopable [124] with high photon flux even though the microscopic mechanism remains unclear, it could be Auger effect (i.e. exciton exciton annihilation) or some extrinsic effect such as desorption. We try then to increase the trion over exciton ratio by increasing the power. By increasing the power we are able to grow the trion but also the 2s state of the A exciton (Fig. 3.28 a) but surprisingly, we also found a linear behavior of the A exciton photoluminescence intensity (Fig. 3.28 b). As stated before, in our experiments, the linearity of the PL should be define over the whole PL intensity (i.e. the sum of the A exciton and trion PL intensity) but we also found that the exciton/trion intensity ratio decrease and A exciton intensity remain linear while we increase the power. This is a hint of the supra linearity of the heterostructure photoluminescence intensity shedding light on the complex interplay between graphene and TMD.

3.5.4 Exciton and trion dynamics

To further investigate this interlayer coupling between TMD and graphene, we perform time resolved photoluminescence (TRPL) experiment at LPCNO in Xavier Marie's group. The whole specification of these experiments is available in [Chapter or appendix]. At 4K, we record two different TRPL image, one at low power ($1\mu\text{W}$) and one at higher power ($50\mu\text{W}$) (Fig.3.29 a and b).

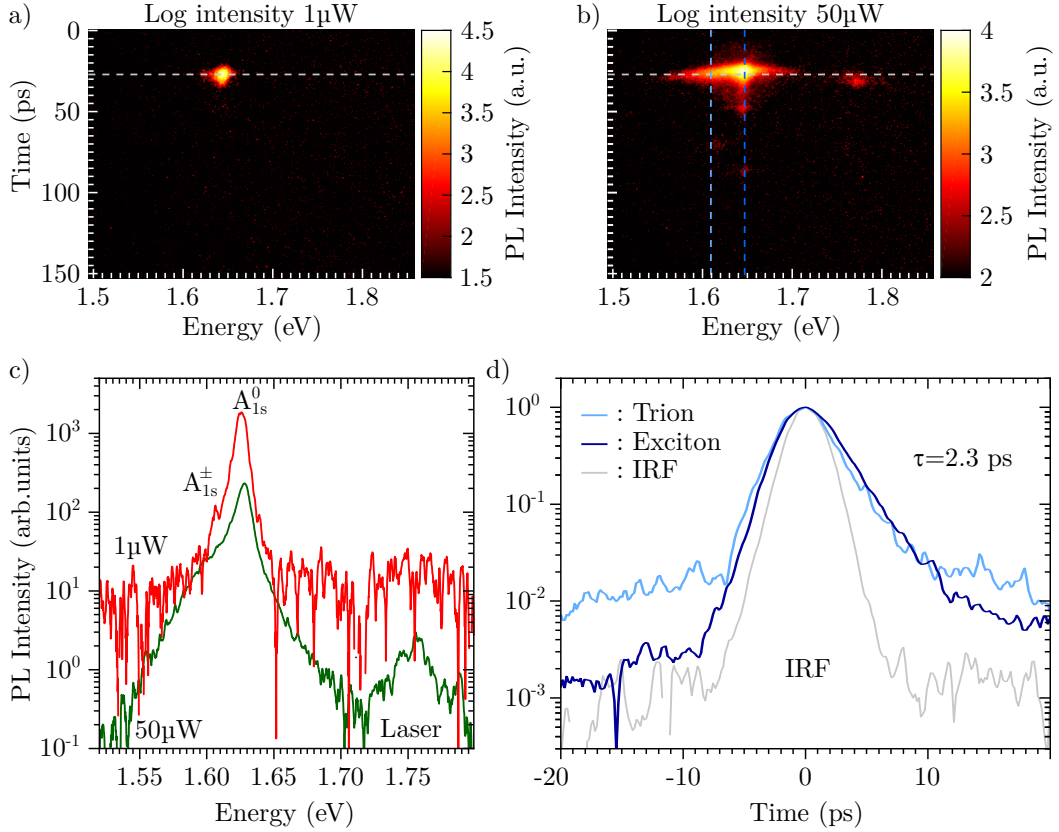


Figure 3.29: Data taken on S3 a) streak camera image in log scale of a $\text{MoSe}_2/\text{Graphene}$ heterostructure PL acquired with a 705nm picosecond pulsed laser, under $1\mu\text{W}$ illumination. In the low excitation power regime, only the A exciton can be seen. b) Same as (a) with an incoming power of $50\mu\text{W}$, in this regime, the trion start to rise up. c) PL intensity spectra in log scale from the temporal integration of the TRPL image in (a) and (b), the dark red spectrum correspond to the low power excitation, only the A is visible while the red spectrum correspond high power excitation, the trion is the red shifted shoulder labelled X_A^\pm . d) Trion (green) and exciton (red) PL decay and IRF (gray).

At $50\mu\text{W}$ a shoulder appears on the red side of the spectrum contrary to the low power one, this could be seen on the spectrum (Fig.3.29 c) which is the integration over time of the image a) and b). At the same time we extract the PL decay time from the exciton and trion which are remarkably the same. Since trion on bare MoSe_2 has a 15 ps lifetime [12], the 2 ps trion lifetime measured for $\text{MoSe}_2/\text{graphene}$ indicates that graphene induced decay time is in the 2 ps range.

3.5.5 Generalization to other TMD

We have shown the neutralization of a MoSe₂ layer when interfaced with graphene. We will now prove that this effect is general for any TMD.

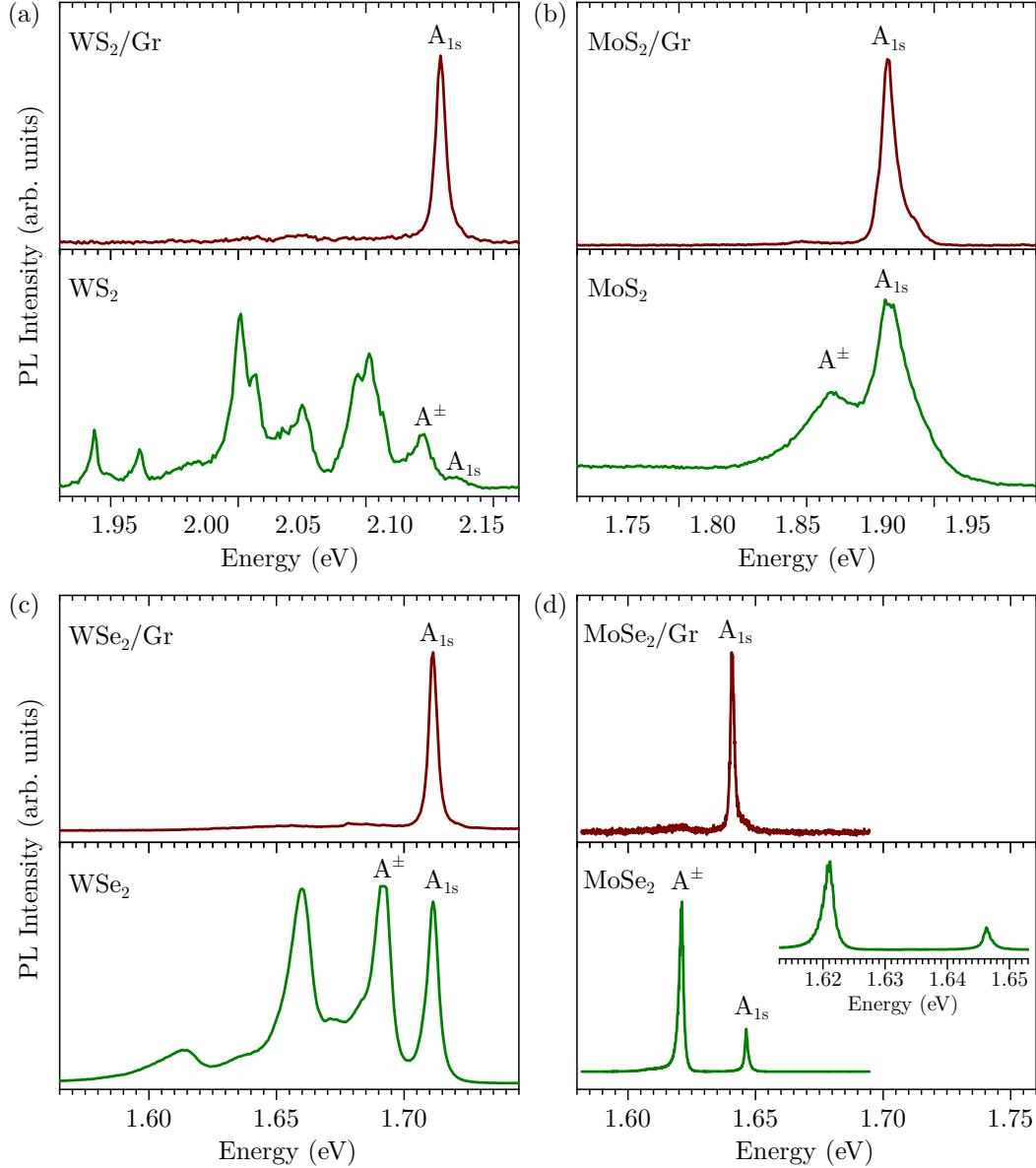


Figure 3.30: PL spectra for BN-encapsulated TMD and BN encapsulated TMD/graphene heterostructure for a) WS₂ b) MoS₂ c) WSe₂ and finally d) MoSe₂

For molybdenum based TMD, two main peaks are present: the trion and the exciton (Fig. 3.30). However, when interfaced with graphene the PL spectra of molybdenum based TMD, has only one peak since doping is vanishing. On the other hand, the effect is much impressive on tungsten based TMD. Bare WS₂ and WSe₂ display many different peak that have been attributed to charged excitons or phonon replica from momentum dark excitons [?]. The absence of the charge exciton is the fingerprint of the TMD neutralization. On the other hand phonon assisted emission is inefficient. Therefore, dark exciton lifetime is high and when interfaced with graphene,

such exciton level populations are completely quenched by the graphene.

3.6 Conclusion

In this chapter, we try to understand the interaction between TMD and graphene monolayer. First, we show the massive PL quenching of the TMD photoluminescence at room temperature. Therefore graphene induce a new efficient decay mechanism for the TMD excitons that could be either charge or energy transfer. We demonstrate a net charge transfer to graphene in TMD/Graphene heterostructure at the sole exception of the MoS₂/graphene heterostructure using Raman spectroscopy. This effect has been shown to be marginal with an extrinsic nature. It is a reversible effect in air but irreversible under vacuum. Finally, changing the substrate block the charge transfer giving a final proof of the extrinsic nature of the net charge transfer. Actually, this process is efficient only when TMD is deposited on SiO₂ or in contact with air. Therefore, we suspect the photoinduced net charge transfer to be adsorbate mediated. The net charge transfer cannot be the efficient decay mechanism induced by graphene to destroy TMD excitons.

We then try to unveil an energy transfer in our structure. We studied the temperature dependent exciton dynamics but the fast dynamics makes it impossible to measure above 80K. The second possibility to investigate energy transfer is to separate spatially donor and acceptor. Looking at the energy transfer efficiency with respect to the donor acceptor distance gives valuable information on the mechanism. However, the donor acceptor separation is so short at the beginning (<1nm) that the usual R^{-4} dependence of the Förster energy transfer breakdown and become closer from an exponential dependence same as the charge mediated Dexter type energy transfer. The Difficulty to fabricate sample with a given distance between TMD and graphene and especially the lack of a proper internal reference forbid us to conclude definitively. However, our observation point toward a charge mediated process.

Finally, when performing low temperature TRPL, we observe a strange mono peak spectrum for MoSe₂ interfaced with graphene instead of the classic double peak consisting of the exciton and the trion. We investigate this effect by reflectivity spectroscopy as well as PL spectroscopy. Surprisingly, we found that TMD when interfaced with graphene is perfectly neutral. Moreover, this effect is the same on any TMD. Being able to neutralize a TMD on large scale, since the only limitation is the size of the graphene layer is an important result. Indeed, it has always been difficult to achieve smooth doping and spectral homogeneity in TMD samples. It would have been even better to demonstrate the modulation of the TMD doping level within this structure. This should be test latter.

Related publication

- G. Froehlicher, [E. Lorchat](#), S. Berciaud
Charge Versus Energy Transfer in Atomically Thin Graphene-Transition Metal Dichalcogenide van der Waals Heterostructures,
Phys.Rev. X, 8, 011007 (2018)

4

Valley physics in TMD heterostructures

The TMD gap is at the corner of its Brillouin zone, the $\pm K$ points. The optical transition at these two points are polarized with opposite polarization, meaning that σ^+ photon are absorbed at the $+K$ point while σ^- photons are absorbed at the $-K$ point (cf Chapter 2). Exciting a TMD with a given circular polarization creates a population of exciton in a given valley. The exciton can be therefore labeled by a valley number, a pseudo-spin. However, both $+$ and $-K$ valleys are coupled, resulting in the exciton pseudo spin relaxation (cf Chapter 2). The exciton spin relaxation times are in the picosecond range, 6 ps at 4 K for WSe₂ decreasing down to 1.5 ps at 120K [125], which is a weak temperature dependence.

To get information on the spin relaxation and decoherence time, we could either use polarization resolved TRPL or pump probe technique such as optical Kerr rotation experiments. Unfortunately we do not have access to such experiments. We adopt then a cw measurement scheme. With polarization resolved steady state PL measurement, we can measure the steady state population in both $\pm K$. Therefore, we can extract the polarization or coherence degree of exciton ρ (cf Chapter 2)

$$\rho = \frac{\rho_0}{1 + 2\frac{\Gamma_s}{\Gamma_d}} \quad (4.1)$$

with Γ_s and Γ_d the exciton spin relaxation rate and the exciton decay rate respectively and ρ_0 the initial population contrast between both valley. ρ_0 is comprised between 0 and 1. Even though the initial population is not perfectly valley polarized, meaning that $\rho_0 < 1$, we will assume a perfect initial polarization. Therefore, we will systematically underestimate the spin lifetime calculated from eq.(4.1).

From (4.1) we found that increasing Γ_d or decreasing Γ_s increases ρ . However, at room temperature, ρ is vanishing since Γ_d is up to three orders of magnitude smaller than Γ_d at 4 K while Γ_s remains within the ps range. Being able to preserve valley polarization (ρ) and coherence (γ) at room temperature would be a major achievement.

In order to do so, we can increase Γ_d while keeping Γ_s constant. This is equivalent to filter the exciton population, since an exciton that lives a shorter time is less subject to spin relaxation process. Exciton decay rate can be separated into two different components, the radiative decay rate and the non radiative one. Even though it is possible to reduce the radiative lifetime within a cavity via Purcell effect [38, 126, 127], the easiest and most efficient way to increase exciton decay rate is to increase its non radiative part by increasing the defect concentration. Steady state, room temperature, valley polarization of defective monolayer TMD have been already demonstrated [94] in WS_2 . The authors show that in WS_2 grown by CVD, the PL is higher at the edge of the sample while the polarization degree is higher at the center of the flake. Unfortunately, this technique has many drawbacks, the first being the small PL yield. In addition, large defect concentration compromise electronic properties and destroy coherence. Since TMD graphene heterostructures have short excitonic lifetime, we have an ideal candidate for the filtering method. Heterostructures still have poor quantum yields. However the PL linearity over a large range of excitation density can be used to bypass the poor quantum yield. In addition, transfer techniques to get TMD/Graphene heterostructure are minimally destructive keeping high quality TMDs and preserving valley contrast at best.

The second possibility is to decrease Γ_s in order to protect exciton from spin relaxation. This would be equivalent to weaken the exciton phonon coupling or the Coulomb exchange, which are the two spin relaxation mechanisms that we will discuss in the following. However, those interaction strengths are mostly intrinsic properties and it is therefore difficult to modify them.

In the following, we will introduce the Mueller polarimetry, a comprehensive polarimetric scheme. We will use this technique to explore the valley properties of TMD/graphene heterostructures, since their excitons are short lived (~ 500 fs) we could recover valley contrast at room temperature in those systems. In addition, the exciton lifetime is weakly temperature dependent in the heterostructure. Therefore, we can discuss the temperature dependence of the exciton spin relaxation mechanism.

After achieving room temperature valley polarization and coherence, we will try to manipulate excitons via their valley pseudo-spin. Using an optical spin-orbit lattice, we will demonstrate room temperature directional coupling (Fig. 4.1).

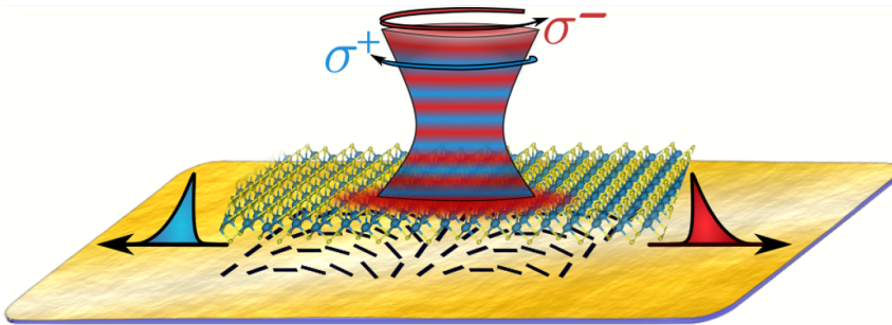


Figure 4.1: Directional coupling of TMD emission routed by the spin-orbit lattice underneath (black lines). The TMD excited by σ^+ photons (red) emit to the right while the σ^- photon (blue) excitation lead to emission to the left.

The directional coupling consists of the photon emission with a positive or negative wavevector depending on the exciton pseudo-spin. Finally, we will discuss the possibility to create countra propagating flows of coherent exciton in the system described in (Fig. 4.1).

The work presented in this chapter have been done in collaboration with the nanostructure lab at Institut de Sience et d'Ingénierie Supramoléculaires de Strasbourg (ISIS), especially with Cyriaque Genet, Stefano Azzini, Thibault Chervy and Thomas Ebbesen.

4.1 Valley Polarization and Coherence in TMD/Graphene van der Waals Heterostructures

In (4.1) ρ measure the ability of a medium to maintain a given polarization during the excitation lifetime before radiative desexcitation. In the following, we will define $\rho = (n_+ - n_-)/(n_+ + n_-)$ as in Chapter 2. We will also define another quantity ρ^{eff} as $\rho^{\text{eff}} = [I_{\sigma^+}(\sigma^+) - I_{\sigma^+}(\sigma^-)]/[I_{\sigma^+}(\sigma^+) + I_{\sigma^+}(\sigma^-)]$. In Chapter 2, we assume that $\rho = \rho^{\text{eff}}$. However, it is not perfectly true and we will demonstrate this point using Mueller formalism.

4.1.1 Mueller algebra and Muller polarimetry

Mueller algebra deals with the description of photon population and their polarization: polarization states. In this formalism, a polarization state is described by a 4 dimensional vector \mathbf{S} and the optical activity of a system is encoded on a 4×4 matrix \mathcal{M} called Mueller matrix. The Mueller formalism is an input output formalism that link the output polarization state \mathbf{S}^{out} from a system with its input polarization state \mathbf{S}^{in} by

$$\mathbf{S}^{\text{out}} = \mathcal{M} \cdot \mathbf{S}^{\text{in}} \quad (4.2)$$

The Mueller vector is defined by

$$\mathbf{S} = \begin{pmatrix} S_0 \\ S_1 \\ S_2 \\ S_3 \end{pmatrix} = \begin{pmatrix} I_{\text{tot}} \\ I_V - I_H \\ I_{+45^\circ} - I_{-45^\circ} \\ I_{\sigma^+} - I_{\sigma^-} \end{pmatrix} \quad (4.3)$$

with I_{tot} the total intensity. The three last components of the vector are balanced measurement of the intensity in a polarization state and in its perpendicular polarization vector. The first component is vertical minus horizontal linearly polarized intensity. The second is the intensity difference between linearly polarized photon at $\pm 45^\circ$. The last one represents the intensity difference between photons circularly polarized right or left. There are only two conditions on the Mueller vectors. The first is $\sqrt{S_1^2 + S_2^2 + S_3^2} \leq S_0$ to avoid getting higher intensity than the total intensity. $\sqrt{S_1^2 + S_2^2 + S_3^2} = S_0$ corresponds to fully polarized photon population. The second is

$S_0 \geq 0$ to have a positive intensity.

The Mueller matrix \mathcal{M} is a 4x4 matrix.

$$\mathcal{M} = \begin{pmatrix} m_{00} & m_{01} & m_{02} & m_{03} \\ m_{10} & m_{11} & m_{12} & m_{13} \\ m_{20} & m_{21} & m_{22} & m_{23} \\ m_{30} & m_{31} & m_{32} & m_{33} \end{pmatrix} \quad (4.4)$$

In a PL spectroscopy experiment, the diagonal component m_{00} corresponds to the system total PL spectrum. Other diagonal coefficients encode the ability of the system to maintain the excitation polarization. In our PL experiment, $m_{11} = m_{22}$ and both measure the ability to maintain linear polarization and are therefore equal to γ . m_{33} is the same for the circular polarization and therefore $m_{33} = \rho$

The m_{i0} correspond to the polarization dependent PL quantum yield. The m_{0i} encodes the dichroism of the medium (linear for $i = 1, 2$ and circular for $i = 3$). Dichroism is the ability of a material to absorb preferentially one polarization state more than the orthogonal one. Finally, the remaining terms correspond to polarization conversion.

Such input/output allows us to fully take into account optical imperfection from our optical element. Since we only need to add a second matrix on the right side of eq. (4.2) that could be finally rewritten as

$$S^{\text{out}} = \mathcal{M}_{\text{det}} \cdot \mathcal{M} \cdot \mathcal{M}_{\text{prep}} \cdot S^{\text{in}} \quad (4.5)$$

with $\mathcal{M}_{\text{prep}}$ the Mueller matrices of the preparation optics block and \mathcal{M}_{det} the matrices of the analysis block (Fig. 5.2).

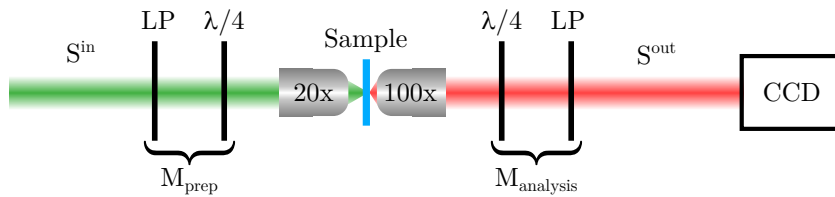


Figure 4.2: *Mueller polarimetry setup scheme.*

The two linear polarizers (Fig. 5.2) can be considered to be perfect while the quarter waveplate cannot. Therefore we modelize quarter waveplate as homogeneous elliptical birefringent materials. Such elliptical birefringent materials are characterized by their energy dependent retardance and ellipticity. Each quarter waveplate characteristics have been measured by our collaborators at ISIS where this setup has been developed. In the end, the Mueller matrix measured without sample is truly the identity as expected. However, using the theoretical Mueller matrix of a

quarter waveplate, the measurement without sample deviate significantly from the identity. The deviation from the identity is a smoking gun of the artefact induced by the imperfection of the optical element.

The first linear polarizer sets the excitation beam polarization to vertical while the last linear polarizer sets the signal polarization to horizontal. The last linear polarizer therefore keeps always the same polarization state before sending the beam into the spectrometer and camera. This to avoid artefact induced by the polarization response of the grating and CCD camera used for the detection. In order to reconstruct the sample Mueller matrix, we need at least 16 independent equations and therefore 16 measurements. However, 16 measurements give large variability of the system solution. Therefore, we use the following protocol [128]. We perform 64 measurements and use a pseudo-inversion algorithm to calculate the system solution since the equation system is over-determine. This method reduces the variability of the solution and gives better results. To perform these 64 measurements, we rotate each quarter wave plate fast-axis by 22.5° step from 22.5 to 180° and record S_0^{out} for each polarizer position.

Since we characterize each optical element and we can take their imperfection into account in their Mueller matrix. Therefore this method is free from artefacts induced by such optical imperfection. Interestingly, Mueller polarimetry is the rigorous way to measure ρ .

From (4.2) we can compute the quantity $\rho^{\text{eff}} = (I_{\parallel} - I_{\perp}) / (I_{\parallel} + I_{\perp})$ to compare ρ^{eff} and $\rho = m_{33}$. ρ^{eff} is measured by exciting the sample with a circularly polarized light and projecting the sample PL signal onto a circular polarization basis. Given the circular polarizer Mueller matrix $\mathcal{M}_{\text{CP}_{\sigma\pm}}$

$$\mathcal{M}_{\text{CP}_{\sigma\pm}} = \begin{pmatrix} 1 & 0 & 0 & \pm 1 \\ 0 & 0 & 0 & 0 \\ 0 & 0 & 0 & 0 \\ \pm 1 & 0 & 0 & 1 \end{pmatrix} \quad (4.6)$$

In this system, we can rewrite (4.2) as

$$S_{\pm}^{\text{out}} = \mathcal{M}_{\text{CP}_{\sigma\pm}} \cdot \mathcal{M} \cdot S^{\text{in}} = \mathcal{M}_{\text{CP}_{\sigma\pm}} \cdot \mathcal{M} \cdot \begin{pmatrix} 1 \\ 0 \\ 0 \\ 1 \end{pmatrix} = \begin{pmatrix} m_{00} + m_{03} \pm m_{33} \pm m_{30} \\ 0 \\ 0 \\ \pm m_{00} + \pm m_{03} + m_{33} + m_{30} \end{pmatrix} \quad (4.7)$$

The vector component $S_{0\pm}^{\text{out}}$ is the intensity we record on the camera in the end. We can therefore write ρ^{eff} as

$$\rho^{\text{eff}} = \frac{I_{\parallel} - I_{\perp}}{I_{\parallel} + I_{\perp}} = \frac{S_{0+}^{\text{out}} - S_{0-}^{\text{out}}}{S_{0+}^{\text{out}} + S_{0-}^{\text{out}}} = \frac{m_{33} + m_{30}}{m_{00} + m_{03}} \neq \rho \quad (4.8)$$

We found in (4.8) that $\rho^{\text{eff}} \neq \rho$. This is also valid for γ , the usual measurement of $\gamma^{\text{eff}} \neq \gamma$. We found a difference between the usually measured ρ^{eff} and ρ even though for symmetry reason, ρ^{eff} should be equal to ρ . However, TMD are quite counter intuitive and the Mueller polarimetry provides us a good sanity check.

Finally, we need a normalization scheme for the Mueller matrices to be able to compare different results. For any matrix element different from m_{00} we choose to normalize it as $m_{ij}^{\text{norm}}(\lambda) = m_{ij}(\lambda)/m_{00}(\lambda)$. However, since such normalization would make $m_{00}(\lambda)$ becomes 1 for any wavelength, we choose another normalization for $m_{00}(\lambda)$. The normalized version of $m_{00}(\lambda)$ then becomes $m_{00}^{\text{norm}}(\lambda) = m_{00}(\lambda)/\max(m_{00}(\lambda))$.

4.1.2 Valley contrast in heterostructures

TMD/Graphene heterostructures have short lifetime, in the ps range without destroying our samples. Such systems are good candidate to recover valley contrast even at room temperature. Even if WS₂ displays strong valley polarization, on the other hand WS₂ has also faint valley coherence at 4K. The latter is not great news to be able to recover valley coherence in WS₂/Graphene heterostructure but WS₂ optical gap at 2 eV is very convenient for us to work with.

We fabricate and characterize a BN encapsulated WS₂/Graphene heterostructure shown in (Fig. 4.3 a-b). As expected, we record a massive PL quenching (Fig. 4.3 b-c) the high intensity region corresponds to encapsulated WS₂ layer while dark ones are interfaced with graphene. The coupling between TMD and graphene is also highlighted by the slight 30 meV redshift of the optical gap. We measure 120 ps lifetime for bare WS₂ (Fig. 4.3 c-d) at $1.21 \times 10^{20} \text{ cm}^{-2} \cdot \text{s}^{-1}$ photon flux which is comparatively twice smaller than the photon flux used to record the PL spectra (Fig. 4.3 c). Combined with the strong PL quenching factor (250 \times) we approximate the WS₂/Graphene A exciton lifetime to 0.5 ps.

We emphasize that $m_{33} = \rho \neq \rho^{\text{eff}}$. However, people usually measure ρ^{eff} which is much more convenient to measure and can be done in much faster ways than using the Mueller matrix measurement scheme. In addition, we will show that in our case, both ρ and ρ^{eff} are equivalent. Therefore, measuring off diagonal term is a necessary sanity check. Non diagonal term should be vanishing in order to get $m_{33} = \rho = \rho^{\text{eff}}$.

In (Fig. 4.4) we display the whole Mueller matrix of the encapsulated WS₂ region. Fortunately, off diagonal term are vanishing. Therefore $\rho = \rho^{\text{eff}}$ and previous results are still valid. Interestingly, all terms vanish except m_{00} as expected from previous measurements.

We measure spatially and spectrally resolved Mueller matrix of our sample. Each time, the off diagonal terms are vanishing. The spatially resolved diagonal terms of the Mueller matrix are presented in (Fig. 4.5). We use wide field excitation using a tunable pulsed laser centered at 2.065eV to image the sample. The laser is filtered but the spectral content is integrated for each pixel. We find a clear anticorrelation between intensity and contrast. As expected, WS₂ interfaced with graphene display valley contrast contrary to the bare WS₂. To be more quantitative, we

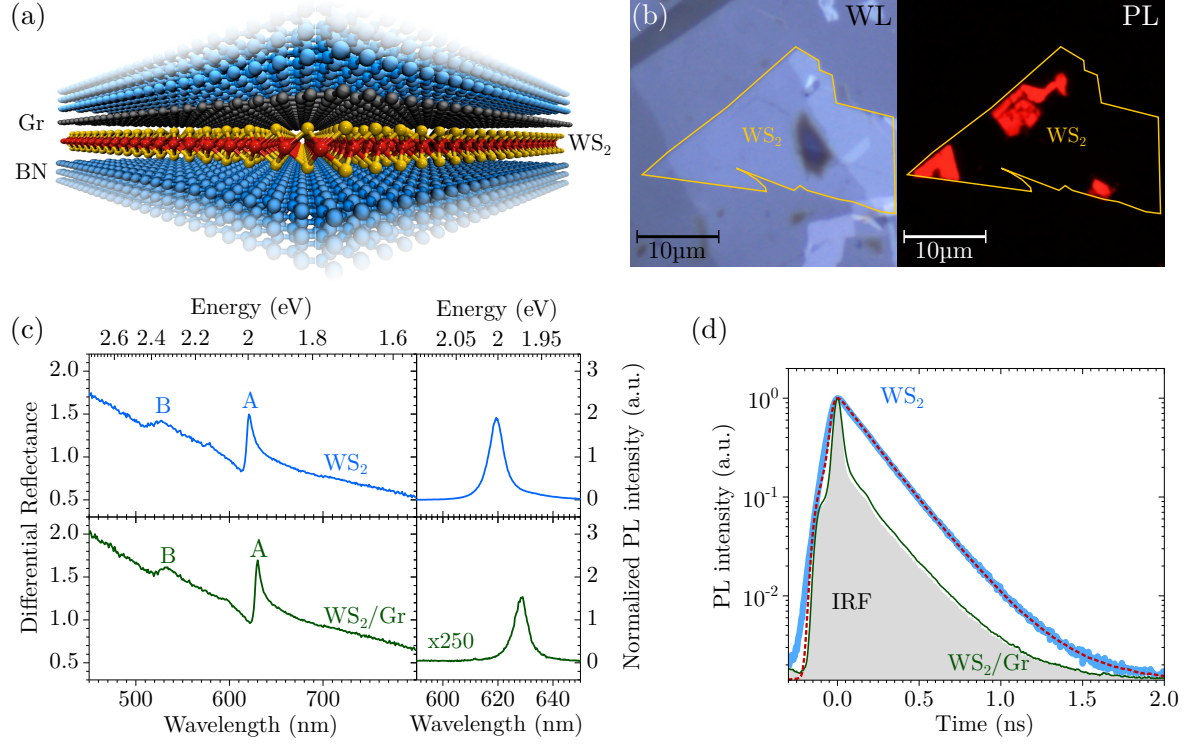


Figure 4.3: *a) Artist's impression of the BN encapsulated WS₂/Graphene heterostructure. b) Optical micrograph (left panel) and fluorescence image, recorded with an ultraviolet light excitation using a fluorescence microscope. The orange line highlights the WS₂ flake. Bright regions correspond to uncoupled or bare TMD region while the dark one corresponds to coupled region. c) Reflectivity and PL spectra at room temperature for WS₂ (blue) or WS₂/graphene (green) region. d) Time resolved photoluminescence for WS₂ in blue and WS₂/Graphene in green. The heterostructure lifetime is the same as the IRF in grey meaning that the heterostructure lifetime is not measurable by our photodiode. Figure reproduced from [112]*

measure the spectrally dependent contrast.

We record spectrally resolved Mueller matrix for both WS₂ and WS₂/Graphene under different excitation condition. The excitonic resonance for WS₂ is at 2.00eV while the WS₂/Graphene one is at 1.97eV. The excitation at 1.959 eV is almost resonant with the heterostructure A exciton resonance while the 2.065 eV is near resonant (Fig. 4.5 e-l). With both excitation, we record contrast that are clearly above zero on the heterostructure but remain at a flat zero for the WS₂ part.

To measure at 1.959 eV, we use BraggGrate filters consisting of three filters, one narrow bandpass to filter the laser to be as narrow as 5 cm⁻¹ and two narrow notch filters with a FWHM of 5 cm⁻¹. With such excitation, WS₂ display strong Raman peaks that are fully polarized. Therefore, Raman signal rises the a contrast, average of the less intense 100% polarized Raman mode with the partially polarized intense PL signal. Such peaks are highlighted by the symbol *

In (Fig. 4.5 i-l) we can extract a 40% valley polarization as well as 20% valley coherence at room temperature. We attribute the increase of contrast at low energy for both m_{11} and m_{22} to the residual, linearly polarized, graphene emission.

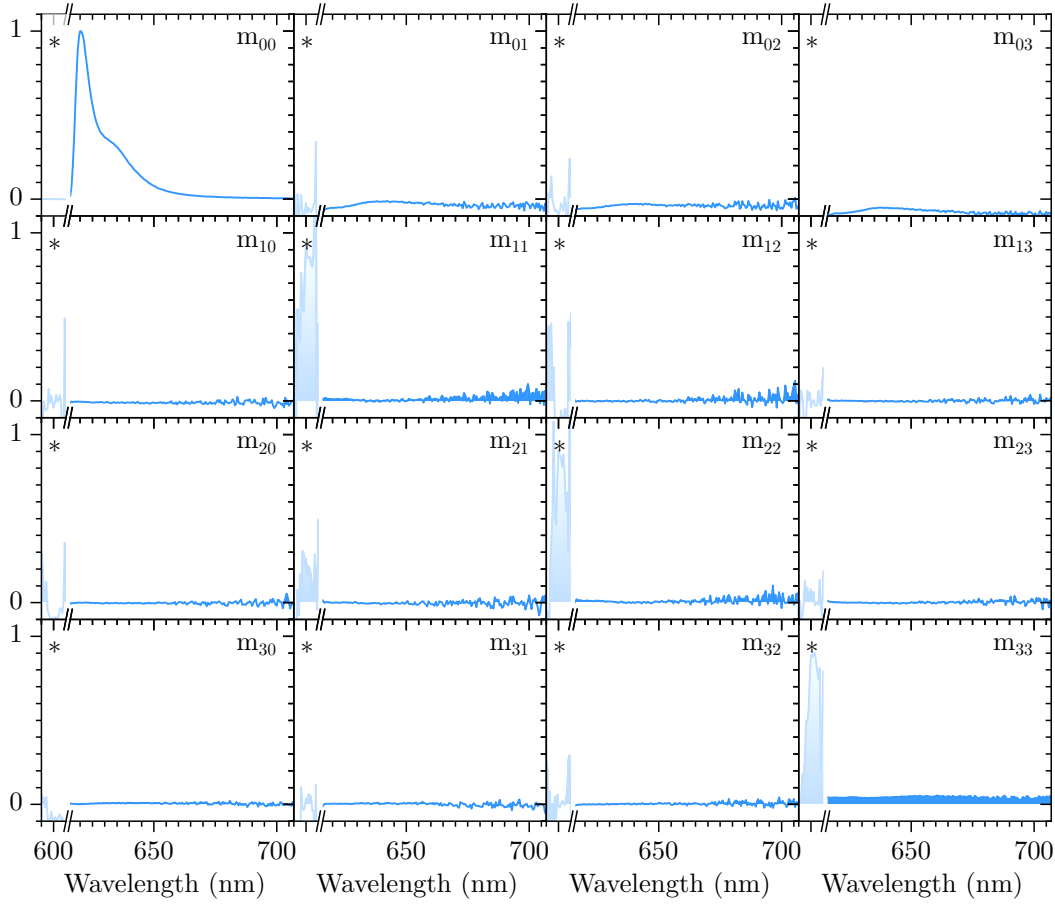


Figure 4.4: WS_2 Mueller matrix, $m_{00}(\lambda)$ is normalized by its maximum while others $m_{ij}(\lambda)$ are normalized by $m_{00}(\lambda)$. The * on the right side of the spectra is the excitation laser signal.

Those measurements have been carried out on many different samples, a not encapsulated WS_2 /Graphene heterostructure deposited on Si/SiO₂ substrate or encapsulated into LiF. Both display similar valley polarization and coherence.

This increase of valley contrast can be understood simply by a lifetime effect as shown in (Fig. 4.6).

Such model allows us to extract the spin relaxation time from the valley contrast together with the exciton lifetime. Injecting a valley polarization of 40% with a 0.5 ps lifetime in eq.(4.1) we extract a 0.7 ps exciton spin relaxation time. To benchmark our system, we decided to perform low temperature polarization resolved PL spectroscopy. For practical reason, we were not able to use the Mueller polarimetry together with our cryostat. Therefore, we use the usual polarimetry scheme, measuring PL intensity in co and cross polarization with respect to the excitation polarization. In order to do so, we use a Wollaston prism to record spectra at the same time

In (Fig. 4.7) we can extract 60% valley coherence and 50% valley polarization. Graphene has the same quenching effect at 300K on MoSe₂ than on WS_2 . It is therefore reasonable to assume

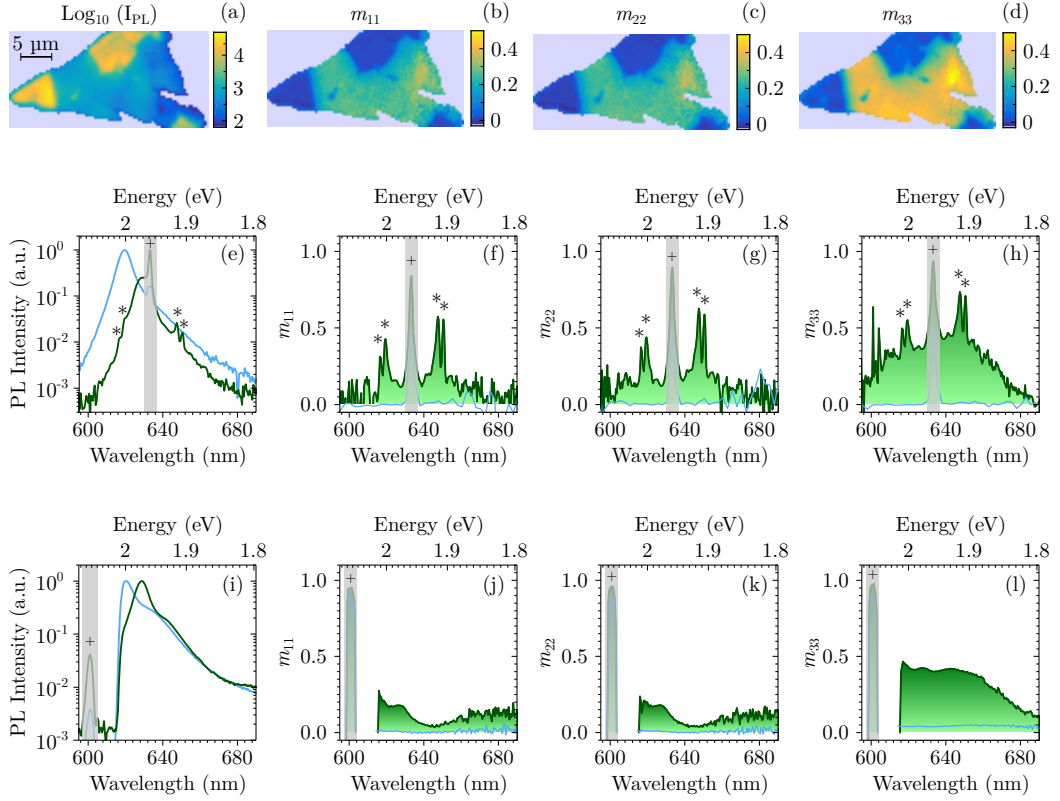


Figure 4.5: *a-d)* Mueller matrix diagonal term, recorded in transmission, at room temperature with a cw 1.96eV He-Ne laser illumination, using BragGrate ultra narrow notch filters to remove the laser line. Those images are measured by wide field illumination. *a)* Wide field PL image in logarithmic scale, *b-c)* m_{11} and m_{22} degree of valley coherence, *d)* m_{33} degree of valley polarization. *e-h)* Spectrally resolved Mueller matrix, the green curves represent data on the heterostructure while the blue one is the WS_2 data. We use an ultra narrow He-Ne cw laser at 1.959eV to excite our sample. Steep and narrow notch filters have been used to filtered out the laser light. The prominent peaks highlighted by * are Raman features. The gray band corresponds to the laser band highlighted by the symbol + *i-l)* same as *e-h)* except excitation done with a tunable pulsed laser centered at 2.065eV. Figure reproduced from [112]

the same effect at low temperature and a picosecond lifetime. Given the valley polarization of 50% and a exciton lifetime of 2 ps, we can extract from (4.1) an exciton spin lifetime of 4 ps. Given the strong lifetime reduction of TMD exciton when interfaced with graphene, it is reasonable to assume that graphene has a negligible effect on the exciton spin lifetime. Therefore, injecting the 10% valley polarization of BN-capped WS_2 in (4.1) we can extract the BN capped WS_2 lifetime: 18 ps. Since BN weakens the TMD exciton-phonon interaction, it gives rise to the population of an intermediate reservoir state that will slowly decay to the optically active exciton state (cf. Chapter 2). Our approximation of the BN capped WS_2 lifetime is therefore probably too crude. It will more likely correspond to the reservoir to optically active state decay time which has been measure in BN capped MoSe_2 sample to be 18 ps [79].

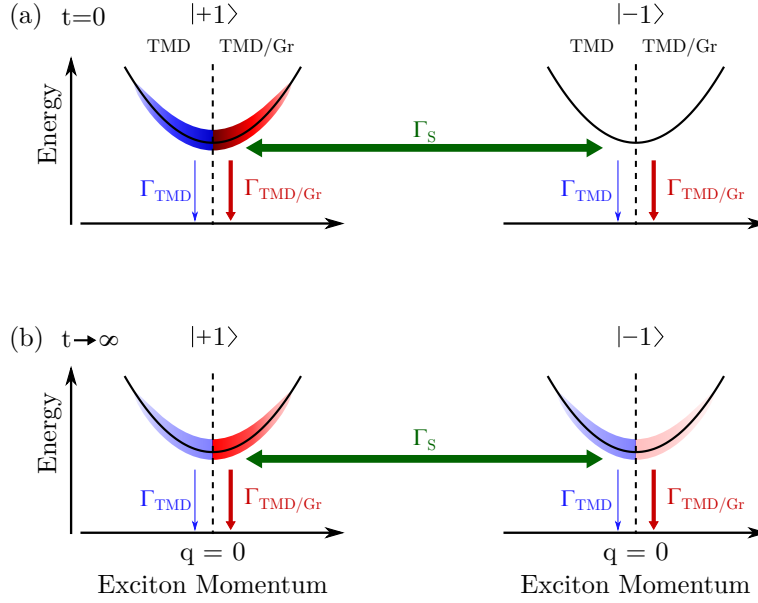


Figure 4.6: *a) initialization of a population just after turning on the laser, only the spin 1 (-1) state are populate, represented by the red (blue) dispersion for the heterostructure (bare TMD) Γ_s is the spin relaxation rate and $\Gamma_{\text{TMD/Gr}}$ (Γ_{TMD}) is the heterostructure (bare TMD) desexcitation rate b) Steady state population, the bare TMD (blue) population is racemized but not the heterostructure one.*

4.1.3 Temperature dependence of valley contrast

The A exciton lifetime of a TMD interfaced with graphene is weakly temperature dependent, it is then interesting to study the temperature dependence of the valley properties to get insight on the spin relaxation microscopic mechanism. The two mechanisms found in the literature are the Maialle, Silva and Sham [85] mechanism based on the Coulomb interaction and phonon mediated spin-flip [129]. Originally derived for III-V Quantum well the coulomb exchange has been adapted to TMD [125]. On the other hand, phonons can flip exciton spins by scattering it from a valley to the other.

We record temperature dependent valley contrast using a Wollaston prism (Fig. 4.8) to spatially separate both polarization contributions and record them at the same time on different regions of the CCD camera.

We use a 50/50 beam splitter (BS) to excite the sample. However, beam splitter usually have a different transmission T_V for vertical and T_H horizontally polarized light. It is not a problem for coherence measurement, since we just need to multiply one of the spectrum by the ratio T_V/T_H . On the other hand, circular polarization will be elliptized by the BS transmission. In order to avoid this problem, we choose to set the quarter waveplate just before the objective (Fig. 4.8). By doing so, we are able to get a good circular polarization at the sample while avoiding polarization dependent transmission or reflection through optical element. A 50x objective with 0.65 numerical aperture and 1 cm working distance is used to focus the excitation beam on the sample and collect the PL signal. We needed to use a long working distance objective since the sample is inside a cryostat while the objective remains out of it. After collecting the PL signal, we send it through

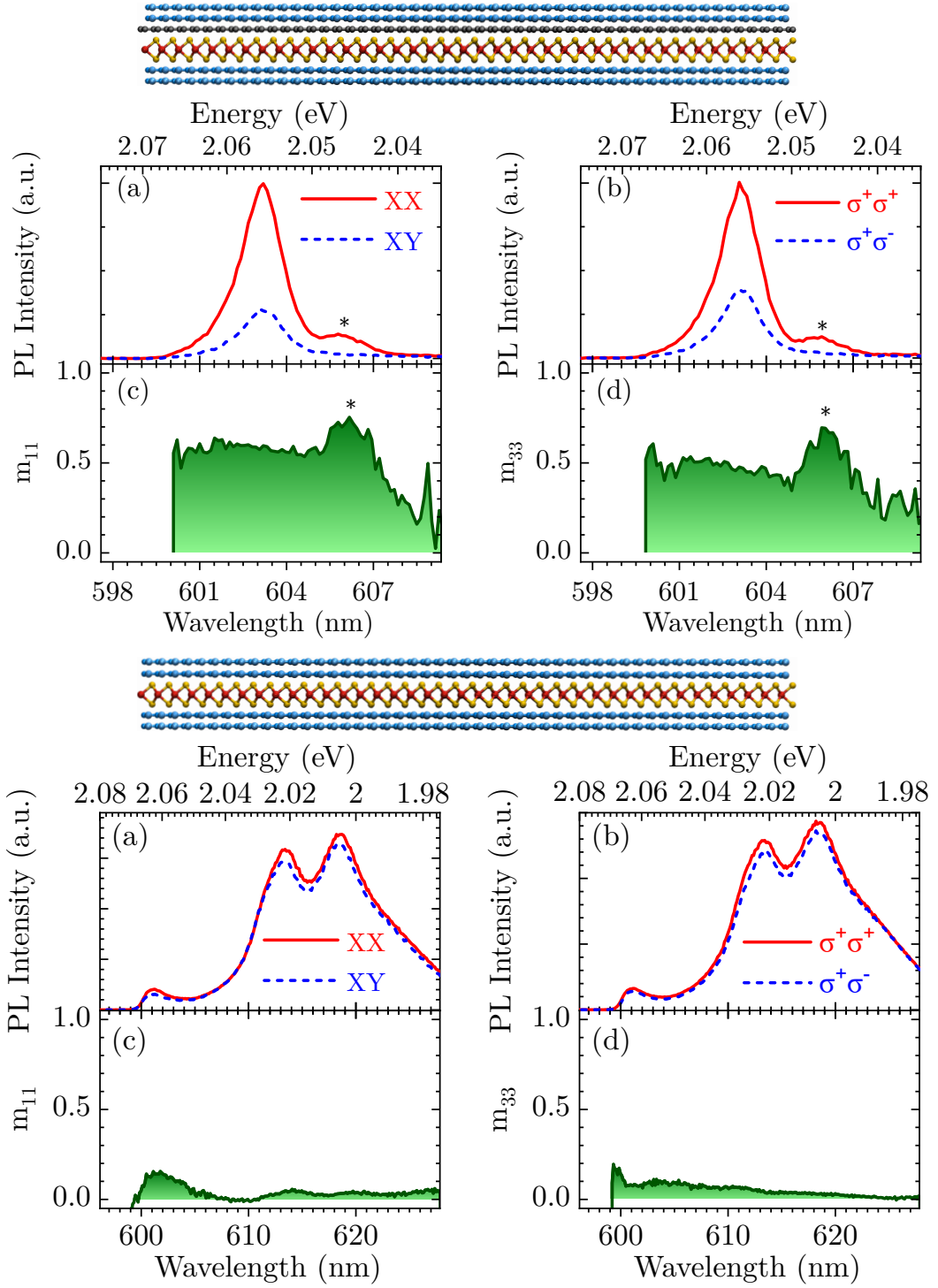


Figure 4.7: a) WS₂/Graphene PL in co and cross polarization at 20 K (upper panel) for linear polarization. Lower panels represent the degree of valley coherence that goes up to 60%. b) Same as (a) for circular polarization, the valley polarization degree is 50%. c) and d) are same as (a) and (b) for WS₂ encapsulated in BN. The degree of valley coherence and polarization are respectively 15% and 10%

the BS to a Wollaston prism that separate spatially vertical and horizontal linear polarization. Each part of the beam will be transmitted with a small, 1°, angle. After the Wollaston prism, we

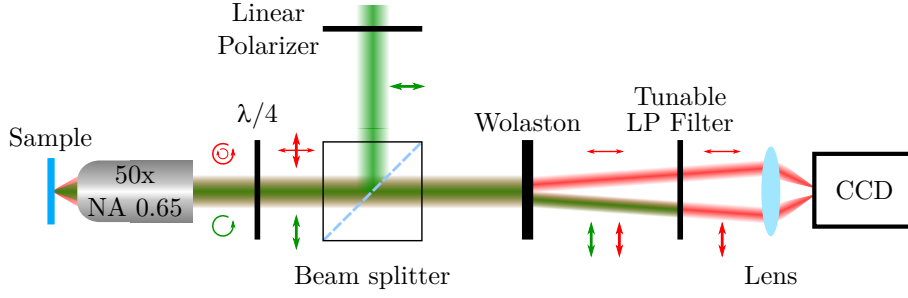


Figure 4.8: Setup representation using Wollaston prism to spatially separate different polarization component. The green (red) line is the excitation (signal) beam the green and red arrows represent the polarization state in different region in the setup.

filter the laser using a tunable long pass filter to finally focus both beam on the spectrometer slit to finally record the intensity on two different region of the CCD.

Valley contrast could be sensitive to the temperature but they are dependent on the detuning between TMD exciton resonance and laser excitation. To avoid any artefact, we carefully adjust the laser frequency to always have the same detuning between the exciton energy and the excitation energy: 50 meV. Therefore, we need a tunable filter to filter the laser.

The BN-capped WS₂ valley polarization depends strongly on the temperature. It has a flat 6% contrast from 4 to 100 K and then drops to zeros between 100 and 150 K. This could be understood by the increase of the exciton lifetime while the fraction of thermalized excitons increases. Such small values of valley polarization can be understood by the increase of the exciton lifetime due to the BN encapsulation of the WS₂. Since the state of the art values are done using non encapsulated TMD sample. However, at 4 K WS₂/graphene displays 70% valley coherence that drops to 20% at room temperature while valley polarization remains almost constant from 4 K to 300 K (Fig. 4.9). though, valley polarization is almost temperature independent ranging from 50 to 40% from 4 K to 300 K.

The temperature dependence of the valley coherence is expected since any exciton-phonon collision could destroy the coherence. Therefore increasing the temperature and then the phonon population, lead to a decrease of the coherence. However, a weakly temperature dependent valley polarization goes hand in hand with a weakly temperature dependent spin relaxation lifetime since exciton lifetime is also quasi temperature independent (cf chapter 4). This result could point toward the Coulomb exchange process. Unfortunately, phonons can mediate spin flip only if they carry a sufficient momentum. Therefore only phonons at the Brillouin zone corner, carry a sufficient momentum to scatter the exciton from one valley to the other. In WS₂ such phonons are ranging from 140 to 180 cm⁻¹ (17 to 22 meV) for the acoustic ones and from 340 to 400 cm⁻¹ (42 to 50 meV) for optical ones [130]. None of those modes are massively populated even at room temperature. Therefore, we do not expect a strong temperature dependence for the phonon mediated process. However, WS₂ acoustic phonons at the K point are populated at room temperature even though it is a small population ($n_{\text{ph}} \approx 1$). At this point a clean modelization is needed to conclude on the spin relaxation mechanism. However, our results can be well explained

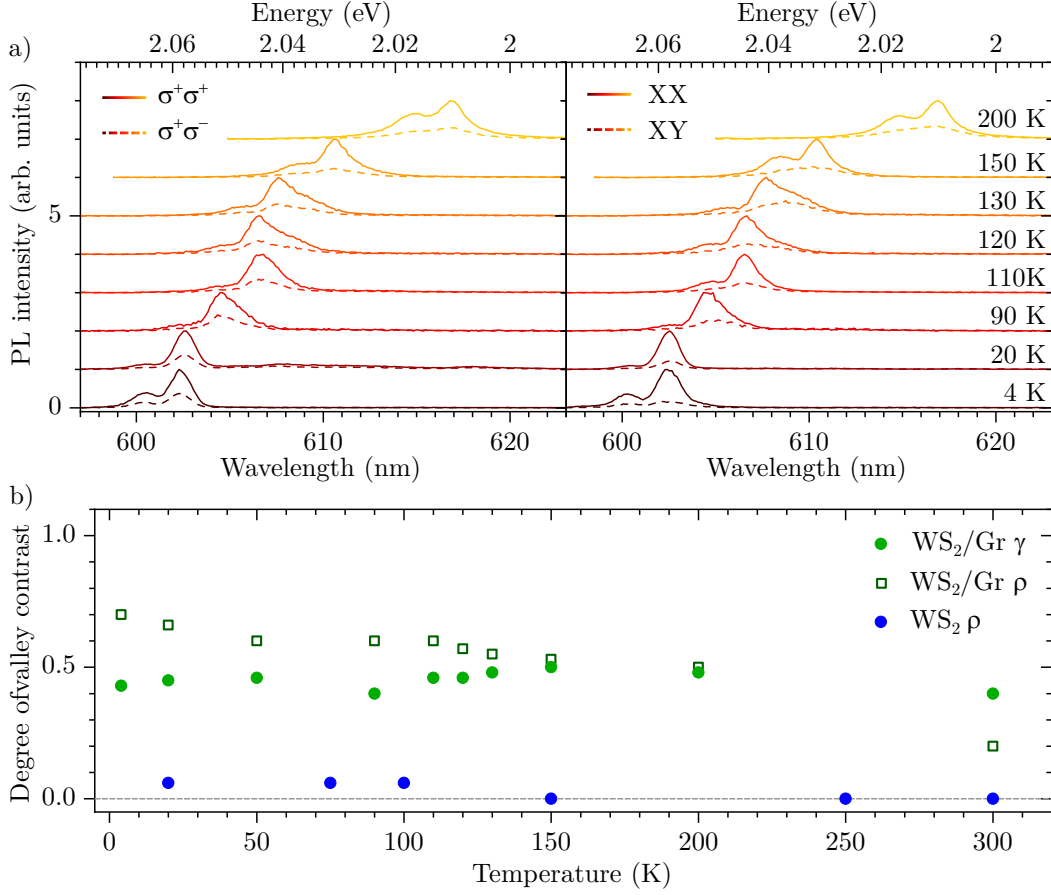


Figure 4.9: a) WS₂/Graphene co and cross polarized spectra at different temperatures b) Contrast with respect to the temperature in dark (light) green the valley coherence (polarization) of WS₂/Grpahene while WS₂ valley polarization is displayed in blue.

by the lifetime reduction that undergoes the WS₂ layer when interfaced with graphene. Finally, a lifetime effect would be enough to recover valley properties at room temperature for any TMD that display valley contrast at low temperature. Since we have already studied in detail MoSe₂ we test our technique to recover valley contrast at room temperature on it.

4.1.4 Discussion

To further characterize the effect of graphene on TMD valley properties, we study encapsulated MoSe₂/Graphene heterostructures because MoSe₂ has no valley contrast even at low temperature or only faint contrast below 5% [91]. Surprisingly, this 5% valley polarization on the A exciton is obtained with excitation resonant with the B exciton. However, in the more common near resonant excitation, the A exciton valley polarization is lowered to 1% ±1.5%. Giving the 2 ps MoSe₂ A exciton lifetime at 4K [12] we can extract a spin relaxation lifetime ranging from 40 to 80 fs

Quasi resonant excitation of the A exciton in MoSe₂/Graphene induces 15% valley coherence and 10% valley polarization (Fig. 4.10 b-d) even at room temperature, the valley coherence is

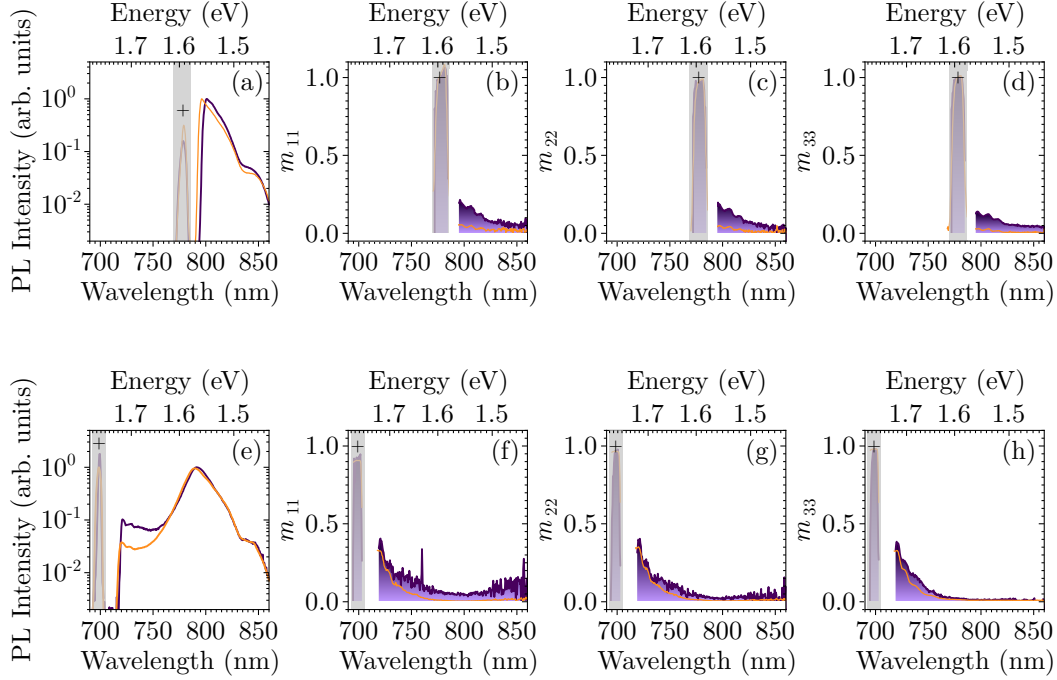


Figure 4.10: *a-d)* MoSe_2 and $\text{MoSe}_2/\text{Graphene}$ Mueller matrix diagonal term in orange and purple respectively, from 0 to 3. Those Muller matrices have been recorded with a tunable pulsed laser centered at 1.590eV . *e-h)* Same as (a-d) with a laser centered at 1.775eV

larger than the polarization highlighting the high quality of our sample. Assuming 500 fs A exciton lifetime we get a spin relaxation time of 100 fs. Interestingly, the spin relaxation time that we extract from our data is smaller than the one measured at 4 K in the same excitation configuration. This could be understood either by an increase of the exciton spin lifetime or by a more selective pumping and therefore a higher initial valley polarization ρ_0 .

B exciton is 200 meV higher in energy than A exciton, at 1.76 eV. Therefore, the excitation at 1.775 eV (Fig. 4.10 e-h) is resonant with the B exciton. However, we do not find larger A exciton valley polarization with this excitation scheme. On the other hand, we found large B exciton valley polarization and coherence, up to 40%. Since B exciton is wide: 100 meV FWHM, we are able to record the red tail of the B exciton and its valley contrast.

Assuming the same spin relaxation time for both A and B exciton, we can extract the lifetime ratio between the A (t_{d_A}) and B (t_{d_B}) exciton using Eq. (4.1)

$$\frac{t_{d_A}}{t_{d_B}} = \frac{1 - \rho_A}{2\rho_A} \times \frac{2\rho_B}{1 - \rho_B} \quad (4.9)$$

with ρ_A and ρ_B the A and B exciton valley polarization. Inserting our experimental value in Eq. (4.9) we end up with a B exciton lifetime six times smaller than the A exciton lifetime. Given the A exciton lifetime between 100 and 500 fs at room temperature, it gives a B exciton lifetime from 17 to 83 fs which is rather short. However, this is consistent with the PL intensity ratio between A and B exciton which is comprised between 2 and 10. Finally, either the B exciton is

short lived and our assumption is right or our assumption is false and the spin relaxation time for the B exciton is not so short. The latest gives us food for thought, because the A exciton in MoSe₂ is a bright exciton, however its B exciton is a dark one (cf. chapter 2) and its spin relaxation time is longer. It is possible then that valley contrast is closely related to the bright or dark character of the exciton. More work has to be done to confirm or deny this idea especially working on the MoS₂ B exciton since this TMD is the sole valley polarized TMD that has a B exciton in a reasonable energy range compared to the A exciton transition.

4.1.5 Conclusion

We make use of Mueller polarimetry to demonstrate that interfacing TMD with graphene allows to recover valley contrast even at room temperature. The spin relaxation time depends slightly on the temperature and decreases from 4 ps at 4 K to 700 fs at 300 K while the exciton lifetime varies from 2 ps to 500 fs. The much smaller contrast in BN capped WS₂ is understood as a smoking gun of the long decay time, 18 ps, from a reservoir to the optically active exciton state. We also demonstrate the same effect on MoSe₂/Graphene heterostructures and demonstrate room temperature valley contrast for a system known to display faint contrast even at 4 K. We record an exciton spin lifetime of 100 fs, higher than what is estimated on bare MoSe₂ at 4 K. We attribute this either to a more selective pumping or to a side effect of graphene that could increase somehow the spin valley lifetime.

Finally, thanks to the strong excitonic lifetime reduction, we demonstrate room temperature chiral emitter. We should be able now to use those systems to achieve directional coupling and by this mean manipulate the excitonic pseudospin degree of freedom. However, we are still looking for a way to recover valley contrast by increasing exciton spin lifetime instead of decreasing exciton lifetime. Both could be achieved by interfacing a TMD layer with a plasmonic cavity. Since cavity is known to increase TMD valley contrast and plasmonic cavity can be designed to get various properties especially directional plasmon launching.

4.2 Chiral Coupling of Valley Excitons with Spin-Momentum Locked Surface Plasmons

Directional coupling has already been demonstrated in various systems [131, 132]. The idea is to couple a chiral waveguide or optical mode with a chiral emitter. Unfortunately, usual chiral emitters are quantum dots that need a magnetic field to get polarized optical transitions and low temperature to avoid coupling between the two polarized states. However, we demonstrate that TMD can be a room temperature chiral emitter without magnetic field, simplifying the experimental setup.

The second ingredient for directional coupling is the chiral optical mode. Pigtail optical fiber, photonic crystal or ultra thin optical fibers are usually used for this purpose. However, optical cavities are known to enhance TMD valley properties. Since we want to use TMD as the chiral emitter, we will try to make a chiral optical resonator. We choose to use a plasmonic cavity as optical resonator, since it offers an efficient way to tailor the optical response.

In the following, we will briefly introduce few concepts of plasmonic and chiral optics to understand the properties of our cavity. We will then interface the plasmonic array with a TMD layer, looking for directional coupling.

4.2.1 Plasmonics in a nutshell

Plasmons are surface (or volume) charge density wave that take place at a positive/negative dielectric constant interface at a given frequency. This is typically a metal air interface in the optical range. Plasmons can also be described as electromagnetic wave confined at the interface [133].

4.2.1.1 Surface plasmons

A surface plasmon is confined at the dielectric/metal interface. Therefore, its intensity decays exponentially out of plane while it can propagate in plane (Fig 4.11).

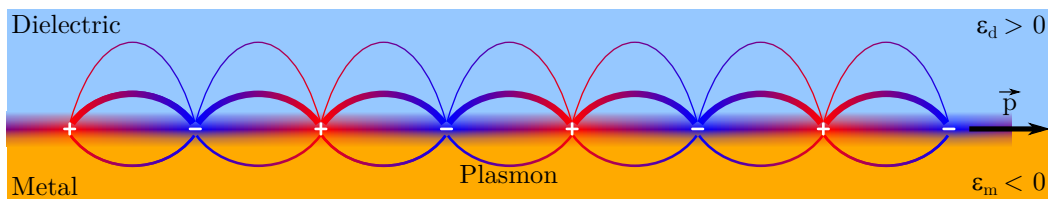


Figure 4.11: Representation of a plasmon at the dielectric/metal interface. The intensity decays exponentially normal to the surface and propagates along the vector \vec{k}

In the near field, plasmons increase the electro-magnetic field density of state, at the plasmon energy. Therefore, a dipole directly in contact with gold can transfer its energy to the plasmon. To get a better picture of the density of state enhancement, we need the surface plasmon dispersion relation. It can be calculated from Maxwell's equations and electro-magnetic wave properties and writes as

$$k_{\text{SP}} = \frac{\omega}{c} \sqrt{\frac{\varepsilon_m \varepsilon_d}{\varepsilon_m + \varepsilon_d}} \quad (4.10)$$

with ε_m and ε_d the dielectric function in the metal and the dielectric respectively. ω is the plasmon frequency and c the speed of light. Since the gold film is isotropic, the surface plasmon wavevector can be along any in plane axis. From (4.10) we found a divergence in the dispersion relation for $\varepsilon_m(\omega_p) = -\varepsilon_d(\omega_p)$, $k_{\text{SP}} \rightarrow \infty$. However, when $\varepsilon_m(\omega) \rightarrow \infty$ then $k_{\text{SP}} \rightarrow \frac{\omega}{c} \sqrt{\varepsilon_d}$. On the other hand, the photon dispersion is given by

$$k_{\text{in}} = \frac{\omega}{c} \sqrt{\varepsilon_d} \quad (4.11)$$

with k_{in} the photon wavevector. Plasmon dispersion relation is always below the lightcone (Fig. 4.12) which means that surface plasmons do not couple to light.

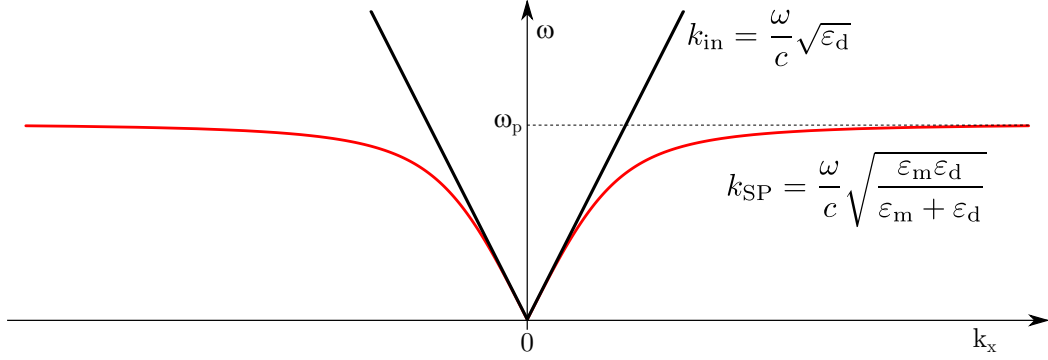


Figure 4.12: Lightcone and plasmon dispersion relation with $\varepsilon_d > 0$ and $\varepsilon_m < 0$

4.2.1.2 Plasmonic arrays

However, we can make use of the grating law to make the plasmon dispersion relation crossing the lightcone. By milling grooves lattice in the metal film we can fold the dispersion relation and by this mean get plasmonic branch inside the lightcone. Such branches can couple to light and therefore can be used to launch plasmon directly with light. The new plasmon dispersion relation can therefore be written as

$$\mathbf{k}_{\text{SP}_L} = \mathbf{k}_{\text{SP}} + \frac{2\pi}{a} n \hat{x} + \frac{2\pi}{b} m \hat{y} \quad (4.12)$$

with a and b the lattice constant along the x and y axis respectively. Plasmonic grating can increase the density of state in the lightcone. Therefore they could be used as optical resonator. The interest of plasmonic arrays resides in their tunability. Since different patterns give different dispersion relations, we can make the plasmon to be resonant with a TMD exciton energy. In

addition, we can make use of geometrical phase to lock the plasmon propagation direction with the excitation photon helicity.

4.2.2 Geometrical phase in plasmonic array

A geometric phase comes from the coupling between the angular momentum of light and the rotation of coordinates. The angular momentum of light could be either orbital or spin momentum. The spin angular momentum of light rises from the photon helicity. The magnetic and electrical field for a circularly polarized photon rotate in the plane perpendicular to the propagation direction. Therefore, a spin angular momentum appears collinear with the propagation vector. Its direction depends on the left or right character of the polarization.

To get the rotation of the coordinates, we decorate our plasmonic lattice. Instead of using square or circular slits, we mill rectangular shaped slits in the gold film. Each step of the lattice, we rotate the rectangle of $\phi = \pi/6$ (Fig. 4.13 a). In such a configuration, the local coordinate of the lattice rotates with respect to the laboratory frame.

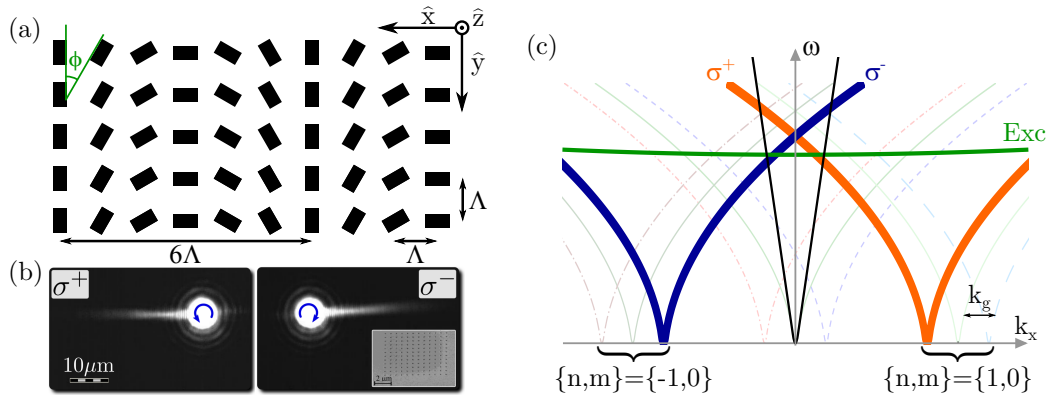


Figure 4.13: *a) plasmonic lattice scheme, each rectangle column is tilted by $\phi = \pi/6$. The distance between two rectangle is Λ . b) Real-space leakage radiation microscope images of the surface plasmons launched by σ^+ and σ^- excitations on an OSO plasmonic resonator. c) Dispersion relation of the OSO lattice along the k_x axis for the $\{-1, 0\}$, $\{0, 0\}$ and $\{1, 0\}$ mode of the lattice. The blue thick solid lines correspond to the $\{-1, 0\}$ lattice mode with the geometrical phase for a σ^- excitation photon while the orange one is the $\{1, 0\}$ lattice mode with the geometrical phase for a σ^+ excitation photon. The green thick solid line corresponds to the exciton dispersion relation. The shaded lines correspond to the other lattice modes.*

The coupling between the spin angular momentum of the incident light and the local coordinate rotation induces an excitation helicity dependent phase.

$$\Phi_G = -\sigma^\pm \phi \quad (4.13)$$

with $\sigma^\pm = \pm 1$ for circularly polarized left or right photons and $\phi = \frac{\pi}{6}$ the rotation angle between two adjacent rectangles (Fig. 4.13 a). Since the rotation of the rectangular slits takes

place along the x-axis, the plasmon wavevector along the x axis is modulated by the geometrical phase.

$$\mathbf{k}_g = \frac{-\sigma\phi}{\Lambda}\hat{x} \quad (4.14)$$

The OSO-lattice wavevector $\mathbf{k}_{\text{SP}_{\text{OSO}}}$ can be written as

$$\mathbf{k}_{\text{SP}_{\text{OSO}}} = \mathbf{k}_{\text{SP}} + \frac{2\pi}{a}n\hat{x} + \frac{2\pi}{b}m\hat{y} + \frac{-\sigma^\pm\phi}{\Lambda}\hat{x} \quad (4.15)$$

Finally, we plot the dispersion relation in (Fig. 4.13 c). At a given energy, the plasmon wavevector is locked on the polarization excitation. Therefore, we can excite plasmon propagating only in one direction (Fig. 4.13 b).

4.2.3 Chiral coupling in a WS_2 /plasmonic array heterostructure

An absorber, namely a TMD A exciton, coupled to a resonant cavity could be either in the weak or strong coupling regime. The weak coupling is characterized by a increase of the radiative desexcitation rate via the Purcell effect. Since the cavity increases the density of mode accessible to desexcite the TMD A exciton. On the other hand, the strong coupling regime is characterized by the hybridization of the optical and excitonic modes giving rise to two new split modes called polaritons (Fig. 4.14).

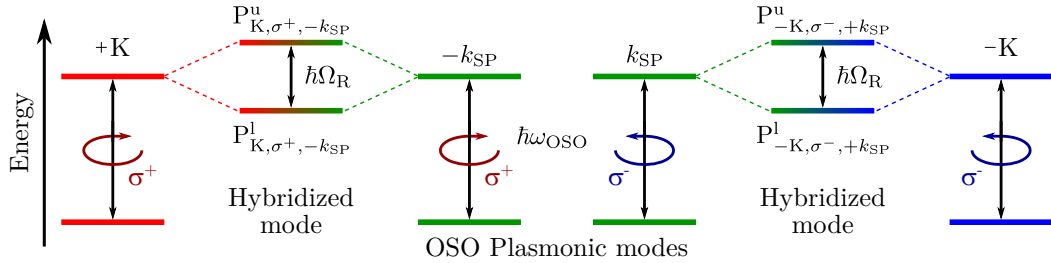


Figure 4.14: Plasmon polaritons arising from the strong coupling between the Optical Spin Orbit lattice and the TMD exciton. We represent in blue and red the TMD exciton at the K and $-K$ valley respectively. In green we show the OSO mode and with the color gradient we represent the hybridized mode, the polaritons P . The superscript u (l) stands for upper (lower) polariton. Ω_R is the Rabi frequency. Adapted from [18]

They originate in the energy exchange between the cavity mode and the excitonic mode, the Rabi oscillations. The splitting between the two mode is the Rabi energy $\hbar\Omega_R$. Since the weak to strong coupling transition is continuous, a figure of merit has been developed to characterize if an absorber is strongly coupled to a cavity

$$C = \frac{2\Omega_R}{\gamma_{\text{ex}} + \Gamma_{\text{cav}}} \quad (4.16)$$

with γ_{ex} the exciton FWHM and Γ_{cav} the cavity FWHM. If $C \geq 1$ then the absorber is strongly coupled otherwise it is in the weak coupling regime.

We have designed an OSO lattice with OSO-modes resonant to the WS₂ A exciton at 2.0 eV and deposit a WS₂ flake onto it. We characterize it by angle resolved reflectivity measurements.

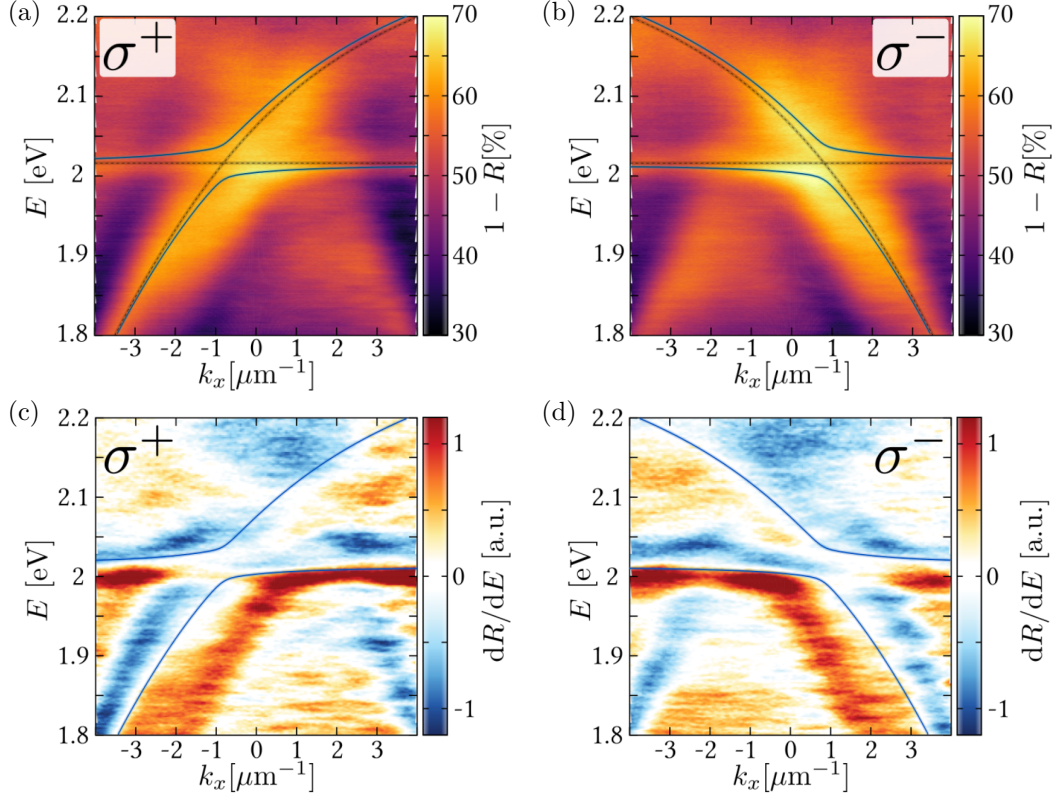


Figure 4.15: a) white light reflectivity measurement under σ^+ insulation and b) under σ^- insulation. The dashed line shows the uncoupled exciton energy level and the green line correspond to the coupled oscillator fit. c-d) derivative with respect to energy of a-b), the coupled oscillator model is represent in blue here.

Due to lattice imperfection, we found that our OSO lattice does not perfectly root the circular polarization. The directionality of the launched plasmons is actually small. It is given by $\eta = (n_{\sigma^+}^r - n_{\sigma^+}^l)/(n_{\sigma^+}^r + n_{\sigma^+}^l)$ with ($n_{\sigma^+}^r$ the number of plasmon launched to the right for a σ^+ excitation. For this lattice $\eta = 15\%$ and could be seen in the low energy part of the image (Fig. 4.15 a-b). In (Fig. 4.15 a-b) we show the reflectivity measurement of our sample with a coupled oscillator fit to check if we enter the strong coupling regime. The upper and lower polaritons absorption peaks are not well resolved but it is clearly seen on the reflectivity first derivative in (Fig. 4.15 c-d). From those data, we can extract the Rabi energy splitting $\hbar\Omega_R = 48$ meV, an excitonic Full Width at Half Maximum (FWHM) $\hbar\gamma_{\text{ex}} = 26$ meV, and a plasmonic mode FWHM $\hbar\Gamma_{\text{OSO}} = 80$ meV. Previous energies allows us to calculate the figure of merit (4.16).

The strong coupling regime is reached if $C = 1$ here we compute $C = 0.9$, at the onset of strong coupling. On the reflectivity, there still absorption induces by the uncoupled part of the exciton population due to the disorder which will broaden as well as asymmetries the reflectivity spec-

trum. Strong coupling or not, let us show how the valley properties of the exciton or polariton evolve.

In (Fig. 4.16) we present polarization and angle resolved PL experiments. First in (Fig. 4.16 a) we show a clear circularly polarized PL emission $\mathcal{F} = 6\%$. As expected, the circular left (right) emission corresponding to exciton in the $-K$ ($+K$) valley are present only on the positive (negative) k_x side. This effect is the imprint of the OSO lattice on the PL emission. It demonstrates that the TMD PL can be routed by an OSO lattice.

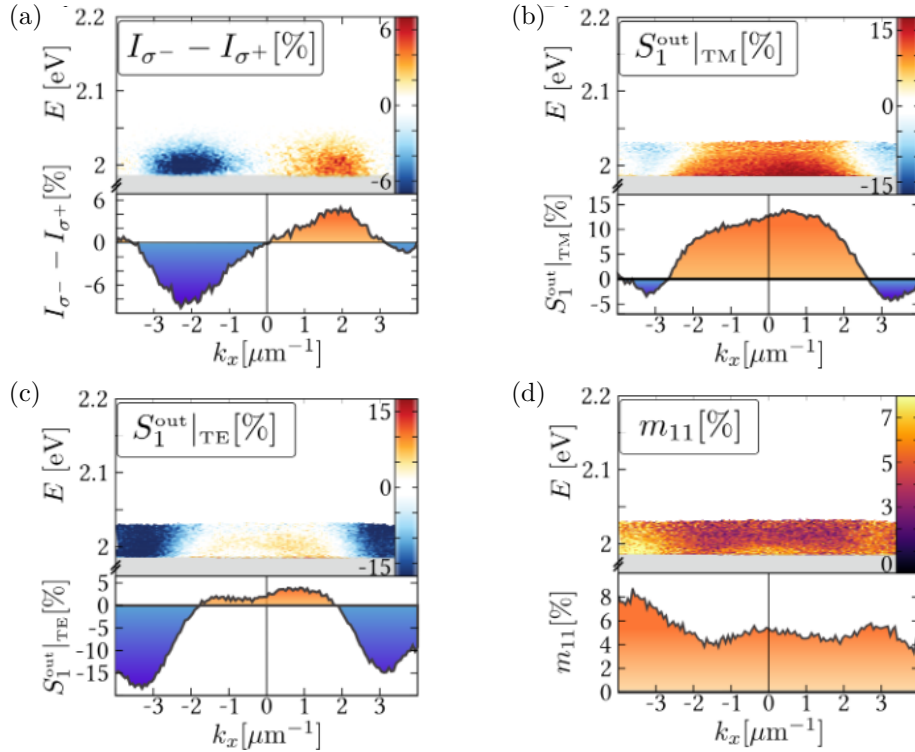


Figure 4.16: In all panel, the cross cuts are taken at 2 eV and the white part of the dispersion correspond to the filtered region. We cut off any signal weaker than 100 counts which cut anything above 2.03eV the laser excitation being at 1.96eV a) angle and polarization resolve circularly polarized PL emission b) Angle-resolved spectrum of the normalized coefficient $S_1^{\text{out}}|_{\text{TE}}/S_0$. c) Same as b) for TM mode. d) Angle resolved second diagonal term of the Mueller matrix m_{11} .

We demonstrate the valley properties of our sample but can we create coherent superposition of polaritons, and how such a coherent superposition will evolve. In (Fig. 4.16 b-c) we plot the second term of the emitted PL stokes vector $S_1^{\text{out}}|_{\text{TE}}/S_0 = (I_V - I_H)/I_{\text{tot}}$ We found a contra-propagating flow of polaritons in both case and a 5% valley coherence at room temperature. Finally, using the previous stokes vectors, we can compute the m_{11} Mueller matrix element measuring the polariton degree of valley coherence. We display the results in (Fig. 4.16 d) the valley coherence at room temperature could be as high as 8%.

4.2.4 Discussion

We measure $\mathcal{F} = 6\%$ and $\gamma = 8\%$. However, \mathcal{F} is the contrast of the whole system while we try to characterize the valley polarization of the TMD. Therefore the valley polarization is the ratio between \mathcal{F} and η the directionality of the plasmons. The TMD valley polarization degree ρ then become 40% at room temperature. To get an idea of the spin relaxation time, we perform time resolved PL measurement to have an idea of the excitation lifetime.

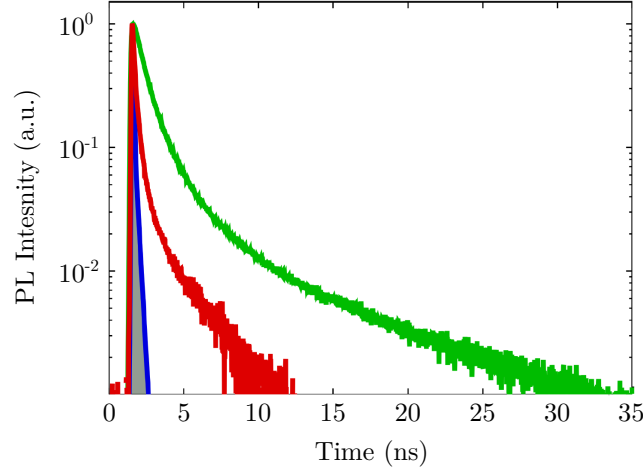


Figure 4.17: Time resolved PL, the blue line correspond to the IRF, the red one to the WS_2 coupled to the plasmonic lattice and the green one to WS_2 supported on PDMS.

The PL lifetime once deconvoluted from the IRF is 192 ps for WS_2 supported on the OSO lattice while it is 1.06 ns for WS_2 on PDMS. Since it is not perfectly clear if WS_2 is strongly coupled to the cavity or not, we have to differentiate this two case. The simplest one is the weak coupling regime. In this regime, the TRPL time is the excitation lifetime. Therefore, we can extract the spin lifetime using the method of the previous section. In this case, $t_s = 256$ ps. which is more than two order of magnitude larger than the spin lifetime in the WS_2 /Graphene heterostructure. This time is the A exciton spin lifetime in the weak coupling regime.

On the other hand in the strong coupling regime, the measured lifetime is most of the time related to a reservoir and is not the direct measurement of the excitation lifetime. However, we still can modelize this system with a simple rate equation model (Fig. 4.19). We excite directly the exciton reservoir that will slowly leak in the polariton mode at rate Γ_r . The polariton lifetime is short, defined by the few hundreds of fs lifetime of plasmons. In this case, both lower polariton population n_p^\pm with a \pm spin and exciton population reservoir n_r^\pm with a \pm spin will undergo spin relaxation with two different rate Γ_{s_i} . Finally, the polariton population will desexcite at a rate $\Gamma_0 \gg \Gamma_r$ (Fig. 4.19). The valley polarization can be written as

$$\rho = \frac{n_p^+ - n_p^-}{n_p^+ + n_p^-} \quad (4.17)$$

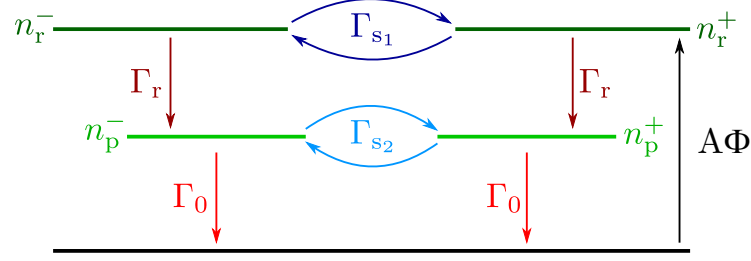


Figure 4.18: Time resolved PL, the blue line correspond to the IRF, the red one to the WS_2 coupled to the plasmonic lattice and the green one to WS_2 supported on PDMS.

The population evolution for the toy model describe in (Fig. 4.19) is given by the following equation

$$\begin{aligned}
 \frac{dn_r^+}{dt} &= \mathcal{A}\Phi - \Gamma_r n_r^+ + \Gamma_{s1} n_r^- - \Gamma_{s1} n_r^+ \\
 \frac{dn_r^-}{dt} &= -\Gamma_r n_r^- - \Gamma_{s1} n_r^- + \Gamma_{s1} n_r^+ \\
 \frac{dn_p^+}{dt} &= \Gamma_r n_r^+ - \Gamma_{s2} n_p^+ + \Gamma_{s2} n_p^- - \Gamma_0 n_p^+ \\
 \frac{dn_p^-}{dt} &= \Gamma_r n_r^- - \Gamma_{s2} n_p^- + \Gamma_{s2} n_p^+ - \Gamma_0 n_p^-
 \end{aligned} \tag{4.18}$$

In the steady state regime, we can calculate the population n_p^+ and n_p^- from (4.2.4). This allow us to calculate ρ in this system.

$$\rho = \frac{1}{1 + 2\frac{\Gamma_{s1}}{\Gamma_r}} \times \frac{1}{1 + 2\frac{\Gamma_{s2}}{\Gamma_0}} = \rho_r \rho_p \tag{4.19}$$

Finally, in the strong coupling regime, both polaritons and exciton in the reservoir will relax their spins. The TRPL measurement gives us access to the reservoir lifetime. Therefore, for polariton spin lifetime much larger than polaritons lifetime, ρ_p becomes 1 and ρ_r is 40%. Finally, the spin lifetime for the reservoir ts_r is the same as before, 256ps. However, if ρ_p smaller than 1, then $\rho_r > 0.4$. This impose ts_r even larger than 256 ps depending on how small is ρ_p .

Whatever the excitation nature, exciton or polaritons, the large valley polarization we have measured as well as the large lifetime shows that coupling to a cavity increase the spin lifetime. Even if the effect is clear, the protection mechanism is not. However, it could not be only attributed to the lifetime reduction due to the interaction with the cavity. Such contrast enhancement for TMD interfaced with cavity has already been observed in other system. Especially TMD coupled to Fabry-Pérot cavity [38, 127]. Here, the TMD is in the strong coupling regime

Here the degree of valley polarization, despite their higher coupling remain below the contrast we have measured on our sample (Fig. 4.19). We could not discuss the spin relaxation time since

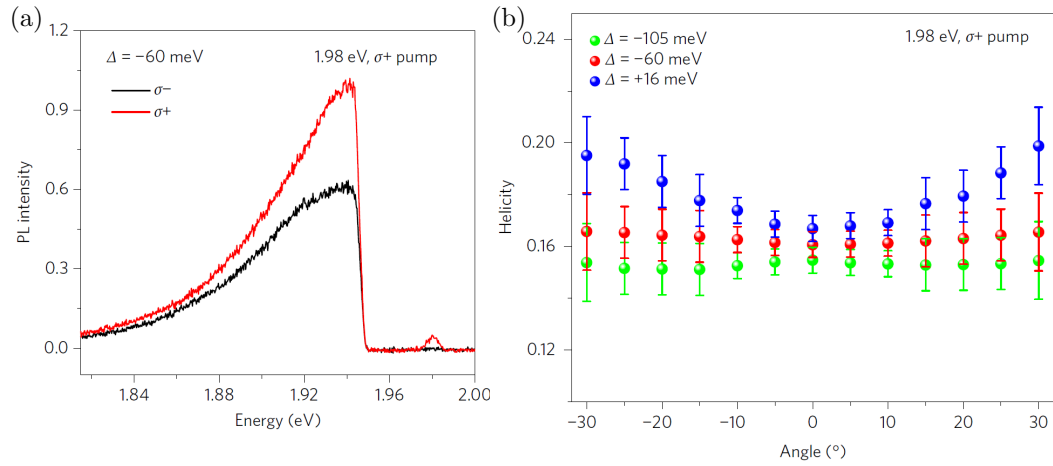


Figure 4.19: *a) WS_2 spectra under σ^+ excitation resonant with the exciton energy analyzed in σ^+ (σ^-) polarization in red (black). b) Angle resolved degree of valley polarization for different detuning between the cavity mode and exciton energy. Data reproduce from [38]*

they do not performed time resolved PL. However, they understand their results by the lifetime effect. However, this explanation needs the direct pumping of the polariton state. Since the reservoir effect is something usual in polariton physics.

4.3 Conclusion

In this chapter, we study the valley properties of transition metal dichalcogenide and propose various way to protect valley contrast at room temperature. We explore both possible ways. First we reduce the exciton lifetime and second we managed to increase the spin lifetime. We make use of graphene to drastically reduce room temperature excitonic lifetime. This allows us to recover both valley polarization and coherence in TMD/Graphene heterostructure. Those 40% valley polarization with a spin relaxation time of 0.7 ps and 20% coherence at room temperature on WS₂/graphene are comparable or higher than the value reported in the literature for bare WS₂ at low temperature.

In addition, the weak temperature dependence of the A exciton lifetime in TMD/Graphene heterostructure allows us to get insight on the exciton spin relaxation mechanism which could be either mediated by phonon or long-range coulomb exchange. The valley coherence drops with the temperature as expected since phonons are efficient to destroy coherence. However, the weak temperature dependence of the valley polarization point toward a coulomb exchange mediated spin relaxation mechanism. Our results on MoSe₂/Graphene heterostructure are much less impressive even though we get 10% valley polarization and 15% valley coherence on a system that display no contrast even at low temperature.

Finally, bright TMD such as MoSe₂ and MoTe₂ present elusive valley contrast even at low temperature, while dark TMD such as WS₂ and WSe₂ display high contrast at low temperature. Here we show that MoSe₂ B exciton which is a dark exciton present robust valley polarization and coherence at room temperature as the WS₂ dark A exciton. This seems to suggest a subtle interplay between spin relaxation and the presence of a dark state reservoir below.

Even if the spin relaxation time in TMD is short, excitation are transferred quickly to the graphene. By this mean, electrons with a given spin can be transferred to graphene using σ^+ or σ^- excitation [37, 134]. This makes this system a nice plateform to study Opto-Valleytronics. Even if we demonstrate room temperature chiral emitter which allows study of chiral light matter interaction at room temperature, graphene reduce heavily the TMD quantum yield and we would like to get the same effect without this drawback.

By making use of an OSO plasmonic cavity, we were able to demonstrate directional flow of polariton or excitation using a given circular polarization for the pump. Therefore we demonstrate that we are able to manipulate valley polarized exciton.

We record 40% valley polarization at room temperature for WS₂ interfaced with our cavity while other group demonstrate only 20% using a Fabry-Pérot cavity. The huge valley polarization we record as well as the long lifetime suggest that we were able to increase the spin relaxation time by two order of magnitude compare to the WS₂/Graphene structure. However, this results needs more study especially on the mechanism that remain unknown.

In the strong coupling regime picture, we have demonstrated room temperature coherence of polaritons as well as the locking of their propagation direction to their valley degree of freedom.

Related publications

- T. Chervy, S. Azzini, E. Lorchat, S. Wang, Y. Gorodetski, J. A. Hutchison, S. Berciaud, T. W. Ebbesen and C. Genet,
Spin-momentum locked polariton transport in the chiral strong coupling regime,
ACS photonics, 5, 1281-1287 (2018)
- E. Lorchat^{*}, S. Azzini^{*}, T. Chervy^{*}, T. Tanigushi, K. Watanabe, T. W Ebbesen, C. Genet, S. Berciaud
Room Temperature valley Polarization and Coherence in Transition Metal Dichalcogenide-Graphene van der Waals Heterostructures,
ACS Photonics, 5, 5047-5054 (2018)

5

Conclusion and perspectives

In this work, we make use of optical spectroscopy that brings us valuable information on TMD/Graphene heterostructure. We found that monolayer TMD/monolayer graphene heterostructures undergoes a drastic PL quenching, smoking gun of the interlayer interaction. We have characterized this interlayer interaction as best as we can. We unveil a photoinduced net charge transfer from TMD to graphene using Raman spectroscopy. We demonstrate that this charge transfer relies on the adsorbate density at the TMD layer surface. As most of adsorbate mediated process, the photo-gating effect is a slow mechanism. Therefore, this process is not the efficient decay mechanism that quenches the TMD PL.

Using TRPL, and exploring the temperature and distance dependence of the exciton dynamics. We show that at zero distance, the exciton lifetime is always below 2 ps at any temperature. However, at 5 nm distance, the exciton lifetime approaches the bare TMD one, showing that Förster type energy transfer is probably not the dominant mechanism at $d = 0$. Despite the large PL quenching, TMD/Gr heterostructure is an interesting emitter. First we demonstrate the neutrality of the TMD, since graphene acts as a local charge reservoir. Second, TMD/Gr is a good chiral emitter with up to 40% valley polarization and 20% valley coherence at room temperature thanks to the filtering of long lived exciton induced by the graphene layer. The low PL yield can be overcome by increasing the excitation power. Since the degree of chiral emission is the most important parameters for chiral optics experiments, this system could be a good alternative to multilayer TMD for instance.

To demonstrate valley degree of freedom protection by interfacing WS_2 with plasmonic resonator. Nonetheless, we also demonstrate directional coupling between WS_2 and our OSO plasmonic lattice. This means that photons emitted by the exciton, have propagation direction locked on the exciton spin. Last but not least, this system also demonstrates the spatial separation of coherent exciton superposition resulting in the contra-propagating flows of excitons.

Perspectives

Our work answers few questions and opens a lot of questions and new paths to explore. I will discuss few of them in the following subsection. The two first points are missing experiments

to better characterize interlayer interactions in TMD/graphene heterostructure. The last point tackle the next system we want to explore in the chiral light chiral matter interaction field.

Interlayer interaction the next step

Adsorbate effect in photodoping effect

We were able to uncover the slow dynamics of the photoinduced net charge transfer. However, we have not understand yet the underlying microscopic mechanism. We demonstrate that, doping occurs when the TMD layer is in contact either with air or with SiO_2 . Therefore, we would like to perform our Raman characterization on $\text{SiO}_2/\text{TMD}/\text{Graphene}/\text{BN}/\text{air}$ or $\text{SiO}_2/\text{BN}/\text{Graphene}/\text{TMD}/\text{air}$ samples. If photoinduced doping needs adsorbates on the TMD layer to occurs, we expect $\text{SiO}_2/\text{BN}/\text{Graphene}/\text{TMD}/\text{air}$ to display photodoping. The $\text{SiO}_2/\text{TMD}/\text{Graphene}/\text{BN}/\text{air}$ sample could also display a photodoping effect since SiO_2 is rough enough for molecule to intercalate at its interface.

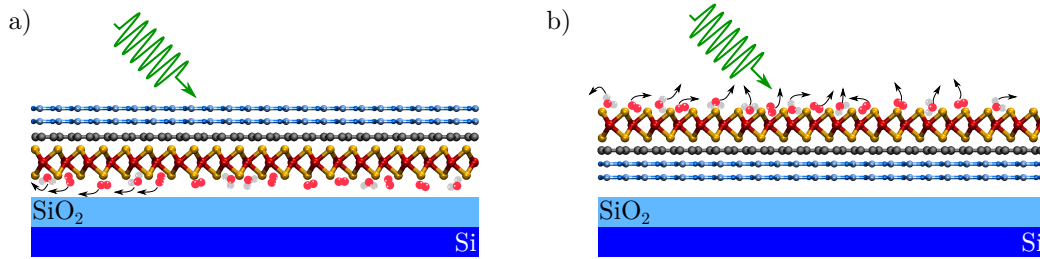


Figure 5.1: *a) TMD/Gr/BN heterostructure supported on SiO_2 adsorbate at the SiO_2/TMD interface can be removed. Therefore, they can release electrons they trapped into the TMD. Those then are transferred to the graphene. b) same as (a) for a BN/Gr/TMD heterostructure.*

Energy transfer : charge or dipole mediated ?

Even though we demonstrate that energy transfer quenches TMD photoluminescence, we do not know yet, which type of energy transfer it is indubitably. Even though we have reason to believe that Dexter energy transfer is the dominant mechanism at zero distance. To better understand the energy transfer mechanism, we need to study the exciton dynamics, at different TMD-graphene distances. Those distances have to be kept small from 1 to 10 layers BN (0.3 to 3 nm) since it seems to be the distance range where the quenching disappears.

TMD valley properties

Valley selective strong coupling

We demonstrate directional coupling using a OSO plasmonic lattice. However, such structure does not carry its own chirality since it could be superimposed with its image in a plane mirror. Therefore, it is not chiral. On the other hand, a plasmonic spiral is a truly chiral structure.

Hence, the density of mode for circular left and right polarization is not the same any more. Therefore, the plasmonic field will interact preferentially with one of the two valley depending on its handedness. Finally, with the good parameters, we could achieve valley selective strong coupling. Such coupling regime would have the same effect as an out of plane magnetic field: the energy splitting between the two valley.

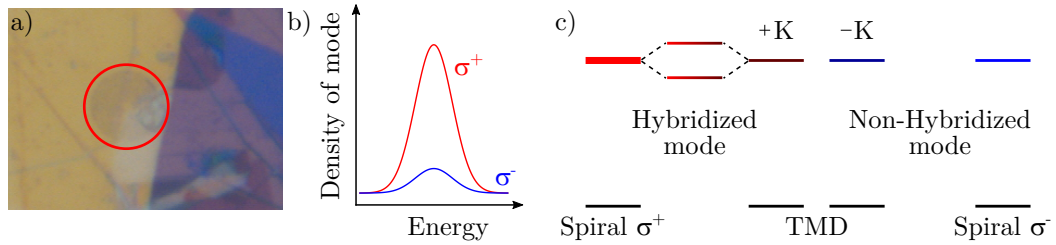


Figure 5.2: a) TMD/Gr/BN heterostructure supported on SiO_2 adsorbate at the SiO_2 /TMD interface can be removed. Therefore, they can release electrons they trapped into the TMD. Those then are transferred to the graphene. b) same as (a) for a BN/Gr/TMD heterostructure.

6

Dans ce manuscrit, nous avons étudié des hétérostructures à base de dichalcogénure de métal de transition (DMT), grâce à des techniques de spectroscopie optique.

Introduction

Matériaux lamellaires

Les DMT font partie de la famille des matériaux lamellaires. Un cristal massif de DMT est donc composé d'un empilement de couches bidimensionnelles cristallines dans lesquelles chaque atome est lié à ses voisins par des liaisons covalentes, alors que les couches ne sont liées entre elles que par des liaisons dites de van der Waals. En 2005, plusieurs cristaux lamellaires massifs ont été exfoliés par K. Novoselov *et al.* [1] en utilisant la méthode du "scotch". Cette méthode permet d'isoler des monocouches de matériaux lamellaires à partir du cristal massif en le séparant en couches de plus en plus fines grâce au ruban adhésif.

Dans cette thèse, nous nous sommes principalement intéressés aux DMT, au graphite et au nitrure de Bohr hexagonal (BN). Matériaux lamellaires massifs et monocouches ont des propriétés électroniques similaires (Fig. 6.1). Le graphite est métallique tandis que sa contrepartie monocouche, le graphène, est semi-métallique. Les DMT sont des semi-conducteurs quel que soit le nombre de couches, bien que les monocouches soient des semi-conducteurs à gap direct tandis que les cristaux multicouches et massifs sont des semi-conducteurs à gap indirect. Finalement, le nitrure de Bohr est un isolant dont la constante diélectrique varie peu avec le nombre de couches. Ces trois types de matériaux : graphène, BN et DMT, sont les briques élémentaires que nous avons utilisées dans ce travail et que nous allons introduire dans ce qui suit.

Graphène

Le graphène est un matériau composé exclusivement d'atomes de carbone, hybridés sp^2 , formant donc trois liaisons σ localisées ainsi qu'une liaison π délocalisée. Ainsi le graphène est un réseau d'atomes de carbone arrangés en nid d'abeille (réseau hexagonal) (Fig. 6.2 a).

De même que le réseau dans l'espace réel, le réseau réciproque est un réseau hexagonal. Les sommets des hexagones sont appelés point K et de même que dans l'espace réel, des sommets

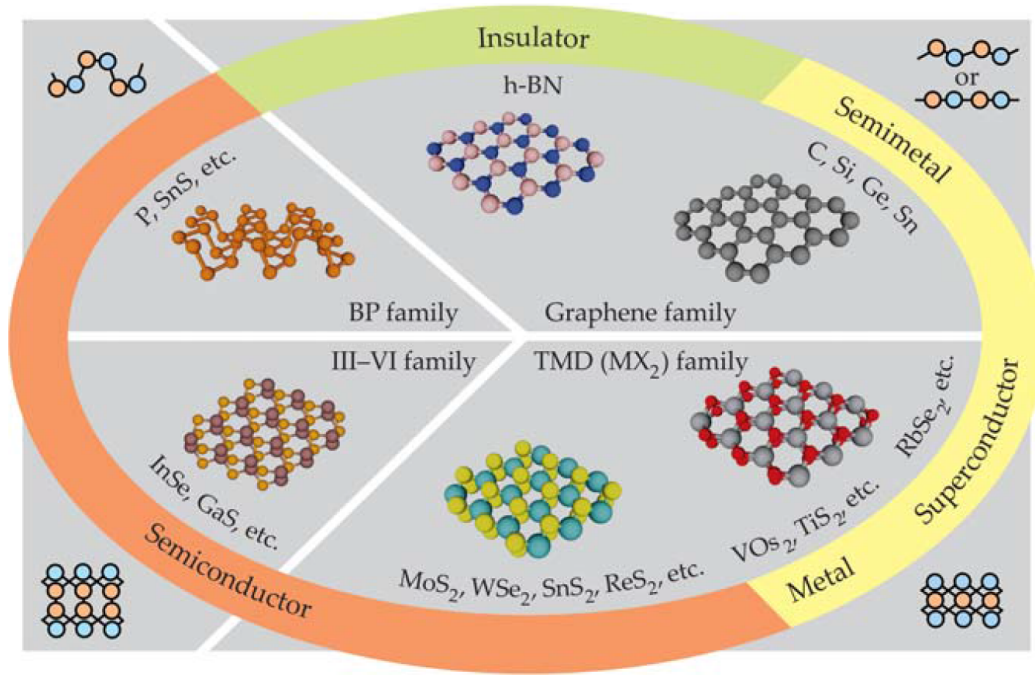


Figure 6.1: Les matériaux lamellaires, leurs propriétés électroniques, leurs structures cristallines et leurs compositions chimiques. Figure reproduite de [2].

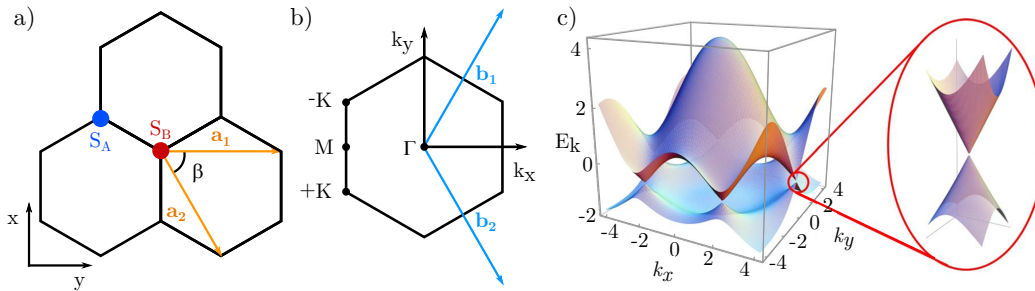


Figure 6.2: a) graphène vu du dessus dans l'espace réel, les deux sites non équivalents A et B sont notés en bleu et rouge respectivement. Les vecteurs cristallins sont notés a_1 et a_2 représentés en orange. b) Représentation de la maille élémentaire du graphène dans l'espace réciproque. Les points de haute symétrie sont notés $\pm K$, M et Γ . Les vecteurs réciproques sont notés b_1 et b_2 représentés en bleu. c) Relation de dispersion électronique du graphène, le zoom au niveau du point K présente la fameuse dispersion conique du graphène. (c) est adapté de [39].

consécutifs sont non équivalents et seront donc libellés $\pm K$. Le point Γ est au centre de l'hexagone (Fig. 6.2 b). La relation de dispersion électronique du graphène présente un point de contact, entre la bande de conduction et la bande de valence, situé au point K (Fig. 6.2 c). C'est ce qui donne le caractère semi-métallique du graphène.

La relation de dispersion conique au point K donne aussi des propriétés optiques et électroniques, accordable par une grille, au graphène. Il est ainsi possible en modulant un voltage de grille de moduler à la fois la résistance d'un canal de graphène ainsi que l'absorption de ce dernier (Fig. 6.3 a-b). Ainsi, moduler l'énergie de Fermi du graphène change la densité de porteur et donc

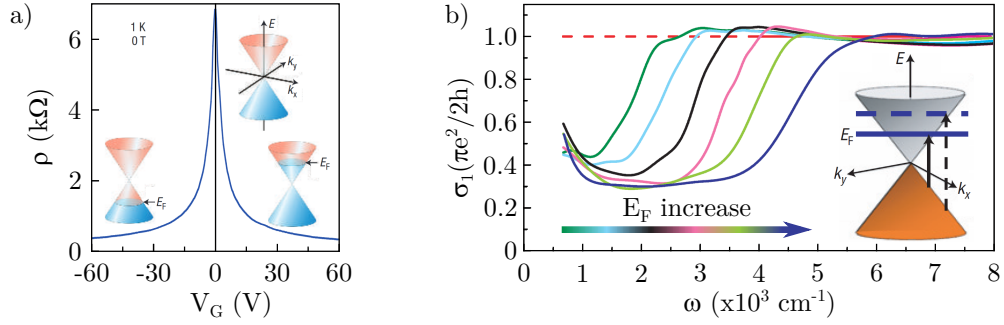


Figure 6.3: a) Résistance d'un canal de graphène en fonction du voltage de grille, adapté de [40]. b) Conductivité optique du graphène en fonction du nombre d'onde du photon. L'augmentation du niveau de Fermi du graphène interdit certaines transitions interbandes augmentant l'énergie minimale nécessaire à un photon pour être absorbé par le graphène. Adapté de [41].

la résistance de ce dernier. C'est donc lorsque l'énergie de Fermi est nulle que la résistance du graphène est maximale (Fig. 6.3 a). D'autre part, la conductivité optique peut aussi être modulée via le changement de l'énergie de Fermi. Ainsi, lorsque l'énergie de Fermi est différente de zéro, certaines transitions interbandes sont bloquées donc, la conductivité optique est, elle aussi, impactée. (Fig. 6.3 b).

Dichalcogénure de métal de transition

Les dichalcogénures de métal de transition peuvent avoir plusieurs structures cristallines mais dans ce manuscrit, nous nous sommes focalisés sur les DMT à structure hexagonale (2H) et plus spécifiquement au : MoS₂, MoSe₂, MoTe₂, WS₂ et enfin WSe₂.

Du point de vue du cristallographe, les DMT ont la même structure que la graphène à une exception près. Dans le graphène, un centre d'inversion relie, par une opération de symétrie, les sites A et B du réseau hexagonal. Par contre, dans les DMT, deux sommets consécutifs sont peuplés d'atomes différents et ne présentent donc pas de centre d'inversion (Fig 6.4).

Les DMT présentent un gap direct en monocouche situé aux points $\pm K$ tout comme le graphène mais contrairement à celui-ci, le DMT est un semi-conducteur. La forme de l'émission de PL, une Lorentzienne, montre que l'absorption et l'émission ne sont pas médiées par des paires électron-trou libres mais par des paires électron-trou liées par interaction de Coulomb appelées excitons.

Le métal de transition induit un fort couplage spin-orbite au sein du semi-conducteur. L'interaction spin-orbite couplée à l'absence de centre d'inversion lève la dégénérescence de spin au point $\pm K$ (Fig. 6.5) donnant aux excitons un nouveau nombre quantique : le pseudo-spin de vallée. Puisqu'un exciton est sous-tendu par une transition électronique entre une bande de valence et une bande de conduction, la levée de dégénérescence des spins donne naissance à une variété d'excitons. Cet effet permet aussi à la PL du DMT de conserver la polarisation de la lumière excitatrice.

Ainsi il a été montré en 2012 [87][82] qu'en illuminant une monocouche de MoS₂ par de la lumière polarisé circulairement la PL du DMT est, elle aussi, polarisée circulairement à plus de

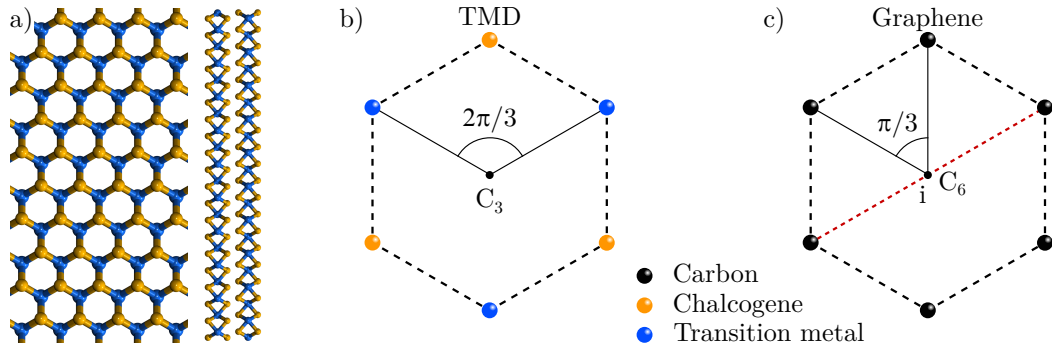


Figure 6.4: a) *vue du dessus et de côté d'une bicouche de DMT.* b) *Vue du dessus de la maille élémentaire d'un DMT monocouche ainsi que l'axe principal de symétrie correspondant à une rotation de $\frac{2\pi}{3}$ autour de C_3 .* c) *Vue du dessus de la maille élémentaire du graphène ainsi que l'axe principal de symétrie correspondant à une rotation de $\frac{\pi}{6}$ autour de C_6 et du centre d'inversion noté i .*

90% à 4 K.

Hétérostructure de van der Waals

De nos jours, les hétérostructures semi-conductrices sont présentes dans beaucoup de dispositifs opto-électroniques, notamment pour des sources lasers compactes et des transistors à haute fréquence (~ 500 GHz) mais de telles applications nécessitent des interfaces sans défaut. Ces hétérostructures sont aujourd'hui fabriquées à base de semi-conducteurs tridimensionnels qui possèdent donc des liaisons pendantes hors du plan. Or, les liaisons pendantes d'un semi-conducteur formeront des liaisons covalentes avec le second semi-conducteur. C'est pourquoi, n'importe quel semi-conducteur ne peut former d'hétérostructure de qualité avec n'importe quel autre semi-conducteur puisqu'un trop grand désaccord de maille entre ces deux espèces entraînera, de fortes contraintes dans les semi-conducteurs.

L'absence de liaisons pendantes hors du plan dans les DMT permet de réaliser des hétérostructures, dites de Van der Waals, qui ne présentent aucune liaison pendante entre deux couches de matériaux lamellaires. Ceci permet de fabriquer des hétérostructures semi-conductrices sans avoir à se soucier du désaccord de maille. De plus, l'interface entre les différents matériaux est auto-nettoyante, puisqu'il est thermodynamiquement plus favorable pour un matériau bidimensionnel d'être directement en contact avec un autre matériau 2D plutôt qu'avec les résidus laissés par le procédé de fabrication. C'est pourquoi les hétérostructures de van der Waals présentent régulièrement des bulles et des rides à leur surface, dans lesquelles sont piégés les résidus d'hydrocarbures.

Afin d'étudier ces hétérostructures, nous avons fabriqué une station de transfert de matériaux 2D avec l'aide de l'atelier mécanique de l'IPCMS. Nous avons choisi d'utiliser la méthode décrite par P.J. Zomer *et al.* [13]. En résumé, un doigt collant fabriqué en polymère nous permet d'empiler différents matériaux sur ce doigt. Un fois que l'hétérostructure est terminée, elle est déposée en faisant fondre le polymère qui permettait la rétention de la structure.

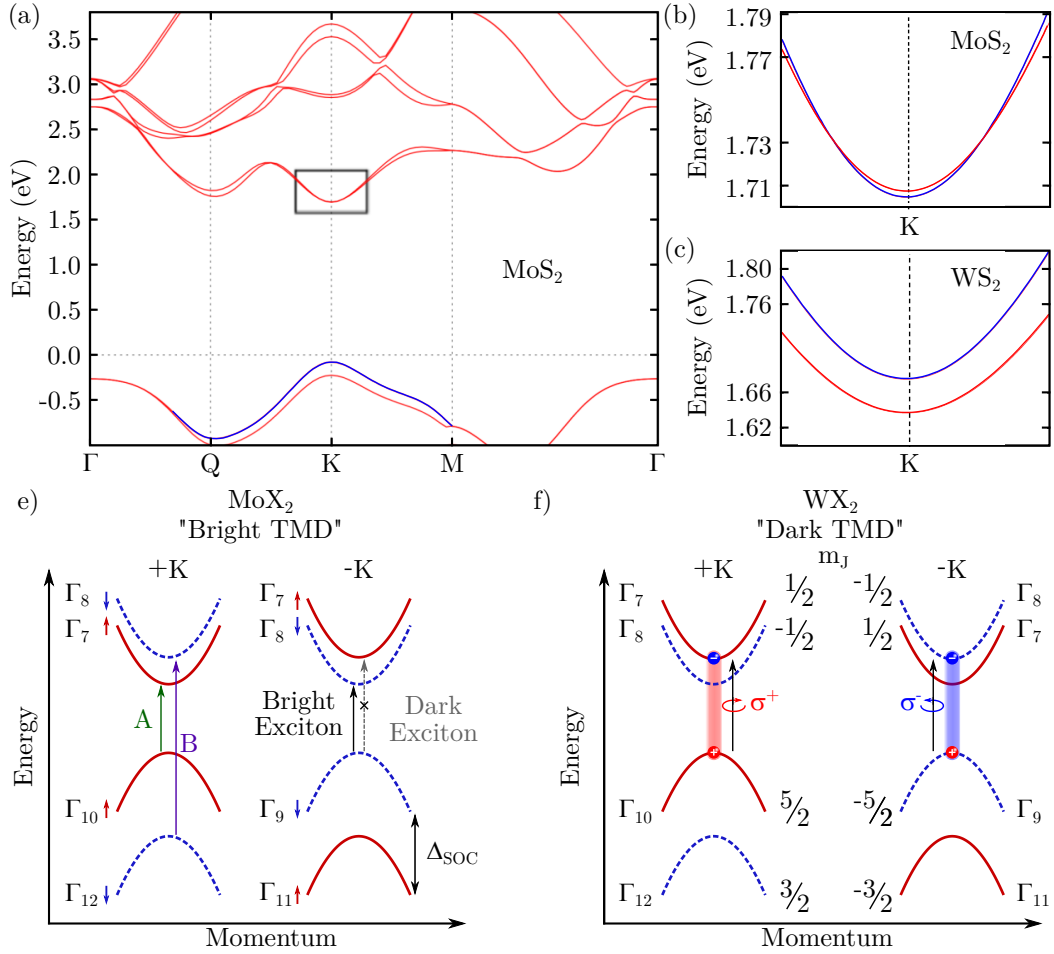


Figure 6.5: a) Structure de bande du MoS_2 monocouche. Le gap électronique à une particule est situé au point K . b-c) Agrandissement de la bande de conduction aux alentours du point K pour MoS_2 (DMT brillant) et WS_2 (DMT sombre) respectivement. e) Structure de bande proche des points $\pm K$ pour un DMT dit brillant, les bandes rouges représentent les spin-up tandis que les bandes bleues pointillées correspondent aux spin-down. Les transitions électroniques correspondant aux excitons A et B sont représentées en vert et violet. f) Structure de bande proche des points $\pm K$ pour un DMT dit sombre. Les moments angulaires totaux sont donnés pour chaque bande, les transitions optiquement actives. Ces transitions électroniques couplent à la lumière polarisée circulairement gauche (droite) dans les vallées opposées.

Finalement, les hétérostructures de Van der Waals forment une nouvelle classe d'interface, atomiquement plane, parfaitement propre et définie sur moins d'un nanomètre. L'interaction entre différentes couches de matériaux bidimensionnels est une question importante et peu étudiée aujourd'hui. Par exemple, les effets de courbures de bandes, bien connus dans les semi-conducteurs tridimensionnels, n'ont été que très peu étudiés dans les hétérostructures de Van der Waals.

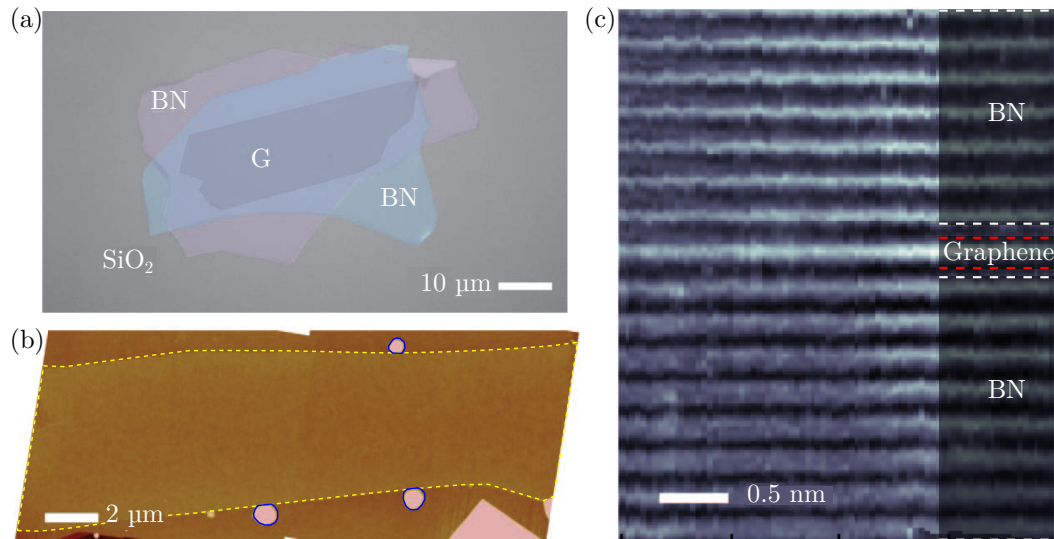


Figure 6.6: a) Image optique d'un échantillon de graphène encapsulé dans le BN. L'hétérostructure est déposée sur SiO₂. b) Topographie AFM de l'échantillon. Les pointillés jaunes entourent le graphène tandis que les bleus montrent les bulles. c) Image TEM d'une coupe de l'échantillon. Le BN est localisé entre les lignes blanches tandis que les lignes rouges délimitent le graphène. Aucun résidu n'est présent à l'interface BN/Graphène. Figure adaptée de [101].

Interaction dans les hétérostructures DMT/Graphène

Dans cette thèse, nous avons étudié les interactions entre une monocouche de DMT et une monocouche de graphène. Nous avons notamment étudié les interactions photo-induites entre les DMT et le graphène. Ces différentes interactions peuvent être notamment du transfert de charge ou d'énergie.

Le transfert d'énergie peut être soit du transfert de Förster ou de Dexter. Celui de Förster est médié par l'interaction dipôle-dipôle dont l'efficacité dépend de la distance entre le donneur (DMT) et l'accepteur (Graphène) en $1/d^n$ avec $n \leq 6$. D'un autre côté, le transfert de Dexter est médié par un échange de charge entre le donneur et l'accepteur avec une efficacité exponentiellement décroissante lorsque la distance donneur-accepteur augmente.

Le transfert de charge peut provenir soit d'un dopage résiduel qui sera transféré au graphène soit des excitons photo-crés dont une des charges pourrait être transférée au graphène.

Pour étudier l'efficacité relative de ces différents transferts, nous avons utilisé des méthodes de spectroscopie optique : photoluminescence, Raman, réflectivité.

spectroscopie optique

La spectroscopie de photoluminescence (PL) consiste à créer une paire électron-trou par l'absorption d'un photon. Ensuite, cette paire électron-trou se recombinera pour réémettre un photon. La PL donne donc des informations sur la dynamique des paires électron-trou (des excitons dans ce cas).

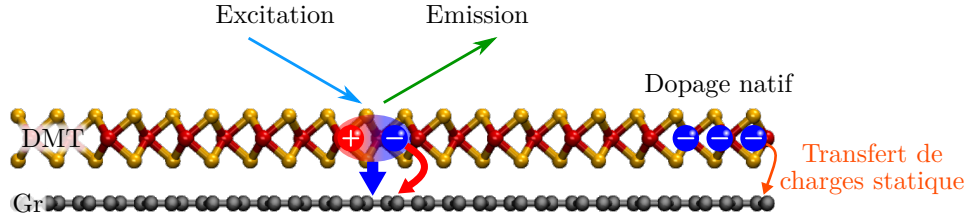


Figure 6.7: Interaction dans les hétérostructures DMT/Graphène. Les flèches fines (bleu et verte) correspondent à l'excitation et l'émission des excitons du DMT. La flèche épaisse bleue représente le transfert d'énergie de l'exciton dans le DMT vers le graphène. La flèche rouge indique la possibilité de transfert de charge photoinduit et finalement le dopage natif du DMT peut être transféré au graphène (flèche orange) même dans le noir.

La photoluminescence résolue en temps (TRPL) permet de mesurer directement le temps de vie de l'exciton de même que l'intensité de photoluminescence mesurée en régime stationnaire. Ainsi, une augmentation de l'intensité sera due soit à l'augmentation du taux de désexcitation radiative soit à la diminution du taux de désexcitation non radiative et inversement pour une diminution de l'intensité de photoluminescence. De plus, la photoluminescence résolue en polarisation permet d'accéder à la dynamique de la polarisation de vallée et de la cohérence de vallée des DMT.

La spectroscopie de diffusion inélastique de la lumière, dite Raman, permet de suivre le dopage des matériaux. Dans le cas du graphène elle permet même la mesure quantitative et locale du niveau de Fermi du graphène lorsque $|E_F| \geq 100$ meV. Due à l'interaction électron-phonon, les fréquences et largeurs des modes de phonon du graphène sont modulées (Fig. 6.8). Pour un graphène parfaitement neutre, un phonon dans le graphène peut transférer son énergie à une paire électron-trou. Ce canal de désexcitation est de moins en moins efficace lorsque le dopage augmente et fini par disparaître lorsque $|E_F| \geq E_{ph}$ avec E_{ph} l'énergie du phonon (Fig. 6.8 d). De plus, l'énergie du phonon augmente avec l'énergie de Fermi du graphène, du fait de l'interaction électron-phonon. Finalement, changer les contraintes dans le cristal modifie la fréquence des phonons du graphène. En étudiant la fréquence et la largeur du pic G ainsi que la corrélation entre la fréquence du pic G et 2D, nous pouvons extraire le dopage ainsi que la nature des dopants dans le graphène (Fig. 6.8). Grâce à un modèle théorique développé par Lazzeri and Mauri [62] nous ajustons la corrélation entre largeur et fréquence du mode G (Fig. 6.8 c). Ensuite, la corrélation entre les fréquences des modes G et 2D. Ainsi, une pente dans cette corrélation de 0.2 correspond à un dopage en électrons, une pente de 0.55 correspond à un dopage en trous, et une pente de 2.2 correspond à des contraintes (Fig. 6.8 e). Finalement, en utilisant ces deux informations, nous pouvons extraire le dopage du graphène (Fig. 6.8 d).

Plan

Dans cette thèse, nous avons d'abord étudié le photodopage dans le graphène et le rôle du DMT dans les hétérostructures DMT/graphène. Nous avons ensuite tenté d'élucider le rôle du graphène dans la dynamique excitonique du DMT, puis nous avons démontré que les hétérostructures DMT/graphène sont des émetteurs chiraux à température ambiante. Finalement, nous avons

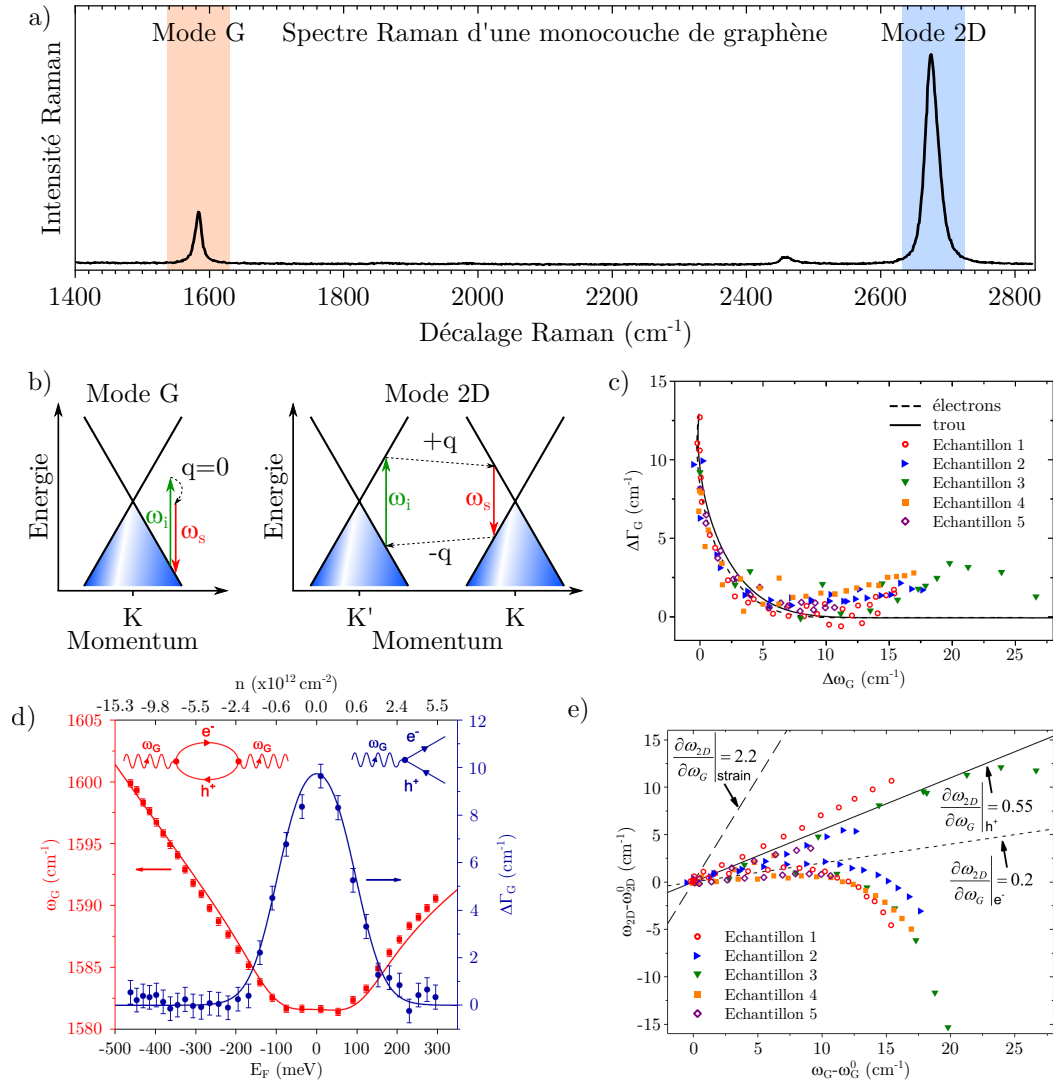


Figure 6.8: a) Spectre Raman typique d'une monocouche de graphène. Le mode G (2D) est surligné en rouge (bleu). b) Schéma de principe de la diffusion inélastique dans le graphène pour le mode G reposant sur un seul phonon (premier ordre) et du mode 2D reposant sur l'interaction avec deux phonons (deuxième ordre). c) Corrélation entre largeur et fréquence du mode G. Chaque point correspond à un dopage différent. d) fréquence (point rouge) et largeur (point bleu) du mode G. Les lignes rouge et bleue correspondent à un modèle théorique développé dans [62]. e) Corrélation entre fréquence du mode G et 2D. Différentes pentes correspondent aux différents dopage et contrainte.

montré que nous pouvons utiliser le degré de liberté interne de vallée pour réaliser un couplage directionnel.

Interactions inter-couche dans les hétérostructures DMT/Graphene

Nous avons utilisé la spectroscopie Raman et de PL pour caractériser des hétérostructures DMT/Gr. De plus, l'utilisation d'une platine de translation piezo nous a permis de faire des cartes hyper-spectrales (Fig. 6.9).

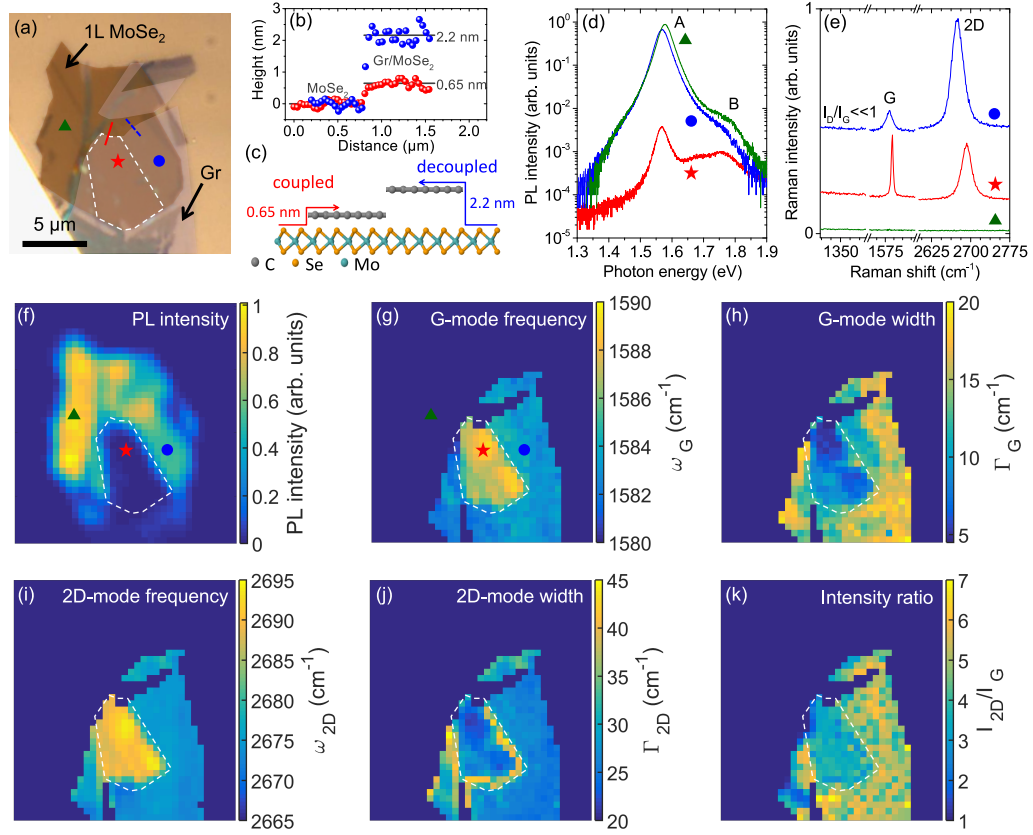


Figure 6.9: a) Image optique de l'échantillon, la région couplée est indiquée par les pointillés blanc. b) profil AFM extrait le long des lignes pointillées bleue et rouge présentées dans (a). c) Schéma de l'hétérostructure, la flèche rouge (bleu) correspond à la région couplée (découplée). d) Spectres de PL de différentes régions données dans (a) : le triangle vert correspond au MoSe₂ nu, le cercle bleu est la région découplée tandis que l'étoile rouge correspond à l'hétérostructure couplée. e) De même que (d) pour les spectres Raman de graphène. f) Carte hyperspectrale de l'intensité de PL, les pointillés blancs entourent la région couplée. g-k) Cartes hyperspectrales Raman de la fréquence (g), et de la largeur (h) du mode G, ainsi que la fréquence (i) et largeur (j) du mode 2D. Finalement (k) est la carte hyperspectrale du ratio d'intensité entre le mode 2D et G. Les échelles des cartes et de l'image optique sont les mêmes. Toutes les cartes ont été faites en utilisant une excitation laser continu à 2.33 eV (532 nm) à un flux de photons $\Phi_{\text{ph}} = 2 \times 10^{19}$ et $\Phi_{\text{ph}} = 2 \times 10^{22} \text{ cm}^{-2} \cdot \text{s}^{-1}$ pour la carte de PL et Raman respectivement. Figure reproduite de [108]

Premièrement, nous avons étudié la topographie de notre échantillon en utilisant un AFM. Nous avons trouvé deux zones sur ce dernier : la région où le graphène est couplé au MoSe₂ avec une distance d'environ 0.7 nm et une région découplée où le graphène est en moyenne à 2.2 nm du MoSe₂ (Fig 6.9 a-c). Dans la région découplée, les spectres de PL sont similaires en intensité aux spectres sur le MoSe₂ nu de même que les spectres Raman sur la zone découplée sont semblables aux spectres sur le graphène nu. Cependant, les spectres Raman et de PL sur la zone couplée sont différents.

Les pics excitoniques sont légèrement décalés vers le rouge et l'intensité de PL est réduite d'un facteur 200 (Fig. 6.9 d,f). Les spectres Raman sont eux aussi fortement modifiés par le couplage avec le MoSe₂. Ainsi, la fréquence du mode G augmente et sa largeur diminue lorsque le graphène est directement en contact avec le MoSe₂, indiquant donc probablement un dopage. De plus, la fréquence du mode 2D est augmentée par le contact avec le DMT, bien que cet effet ne soit pas encore parfaitement compris. Finalement, la réduction du ratio entre l'intensité du mode 2D et du mode G indique lui aussi le dopage (Fig. 6.9 e,g-k). Ainsi, il existe un dopage photo-induit dans le graphène dû à son interaction avec le DMT.

Photodopage

Afin d'étudier le photodopage, nous avons réalisé différentes hétérostructures en utilisant différents DMT : WS₂ WSe₂ MoSe₂ et MoS₂. Dans un premier temps, nous nous sommes focalisés sur les hétérostructures MoSe₂/Graphène. Nous avons enregistré des spectres Raman à différentes puissances, à pression et température ambiante, et utilisé la méthode décrite précédemment pour extraire le dopage.

L'accroissement de la fréquence du pic G ainsi que la pente de 0.11 dans la corrélation entre la fréquence du pic G et 2D indique un dopage en électrons dans le graphène (Fig. ??). Grâce à la fréquence et la largeur du pic G, nous avons pu en extraire le dopage en fonction du flux de photons. Ce dopage est réversible et sature lorsque le flux de photons augmente. Pour aller plus loin, nous avons effectué les mêmes mesures sous vide. Dans ces conditions, bien que le dopage à saturation soit similaire, le dopage n'est plus réversible. Il semblerait donc que les adsorbats aient un rôle à jouer dans le dopage du graphène. Afin de vérifier cette hypothèse, nous avons fabriqué une hétérostructure BN/DMT/Graphène dans laquelle, le DMT n'aura aucun adsorbat à sa surface grâce au caractère autonettoyant des interfaces entre ces matériaux. Dans cette structure, nous n'avons pu mettre en évidence de dopage photo-induit. Ce résultat suggère donc, soit que le dopage photo-induit est médié par la désorption des adsorbats soit que le BN agit comme un réservoir de charge pour l'hétérostructure DMT/Graphène. De plus, il est intéressant de noter que ces effets sont observés sur tous les DMT que nous avons étudié à l'exception du MoS₂ bien qu'un photo-dopage ait été rapporté dans la littérature dans des proportions bien moindre. Quoiqu'il en soit, le transfert de charge photo-induit est négligeable dans la dynamique excitonique.

dynamique excitonique

L'intensité de photoluminescence du MoSe₂ est fortement réduite lorsque le DMT est interfacé avec le graphène. Ceci montre que le temps de vie des excitons dans le MoSe₂ est fortement réduit par le couplage au graphène (Fig. 6.11)

À température ambiante, le temps de vie des excitons est bien supérieur dans le MoSe₂ comparé au MoSe₂/Graphène tandis qu'à 4 K, les temps de vie sont similaires dans les deux cas. Cependant, lorsque le MoSe₂ est encapsulé dans BN, c'est le temps de relaxation des excitons qui est modulé indiquant que le graphène a un effet plus important sur les excitons à grand K.

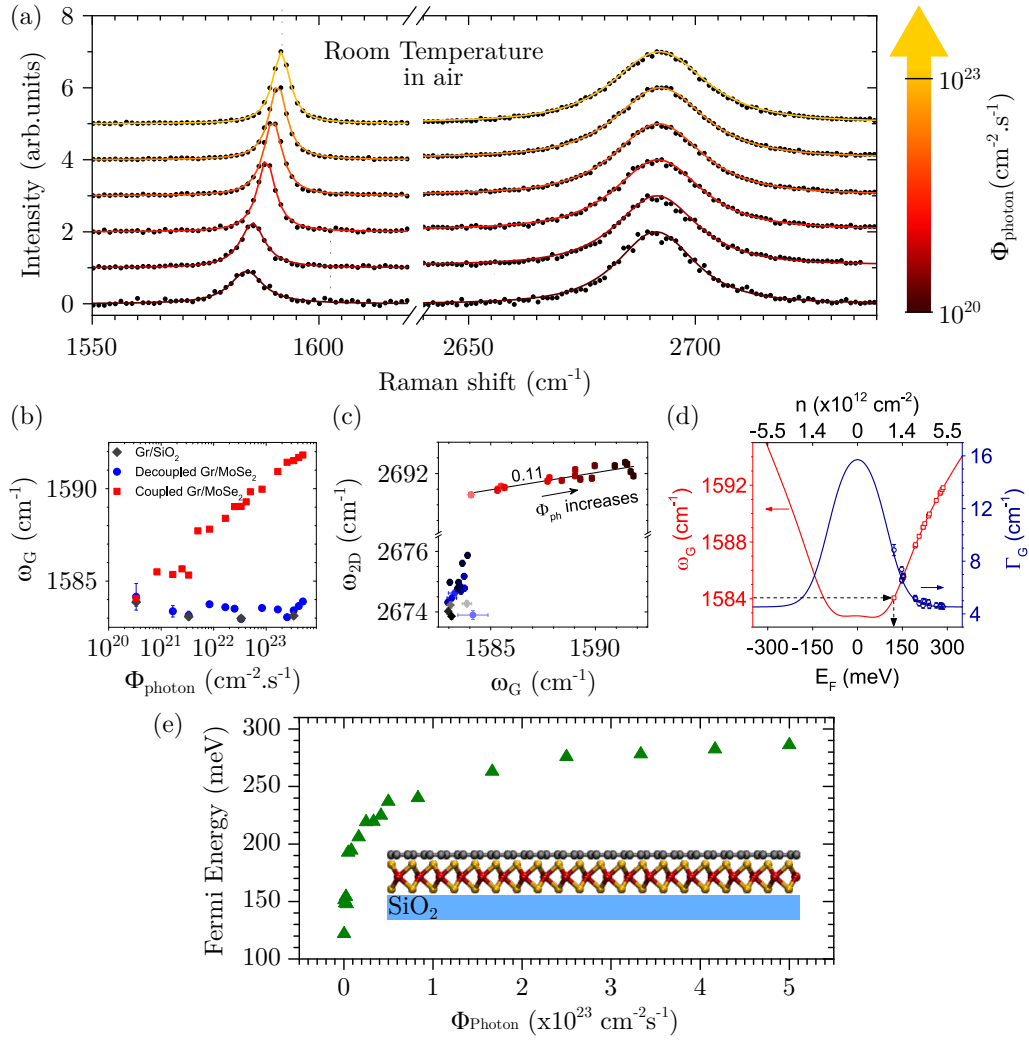


Figure 6.10: a) Spectres Raman enregistrés à différentes puissances, les sphères noires correspondent aux données tandis que les lignes sont des ajustements de ces données. b) Fréquence du mode G extraite des ajustements à différentes puissances. c) corrélation entre fréquence du mode G et 2D, la pente est de 0.11 indiquant un dopage en électrons. d) Ajustement des fréquences et largeurs du pic G avec le modèle théorique de F.Mauri et M.Lazzeri. e) Energie de Fermi du graphène en fonction du flux de photons. Figure reproduite de [108]

Temps de vie court et émission polarisée

Du fait de leur structure de bande particulière, on peut adresser sélectivement une des deux vallées du DMT grâce à la polarisation de l'excitation. Ainsi, une polarisation circulaire droite permet de créer un exciton dans la vallée K tandis que la polarisation circulaire gauche adresse la vallée K'. Cet effet est appelé polarisation de vallée. Grâce à cette propriété, l'émission de photoluminescence des DMT à froid garde partiellement la polarisation de la lumière excitatrice.

L'émission n'est pas parfaitement polarisée car un exciton dans la vallée K (K') peut être diffusé vers la vallée K' (K) avec un temps caractéristique τ_s . Ainsi, une population d'excitons créée dans une des vallées peut être distribuée équitablement entre les deux. Cette redistribution

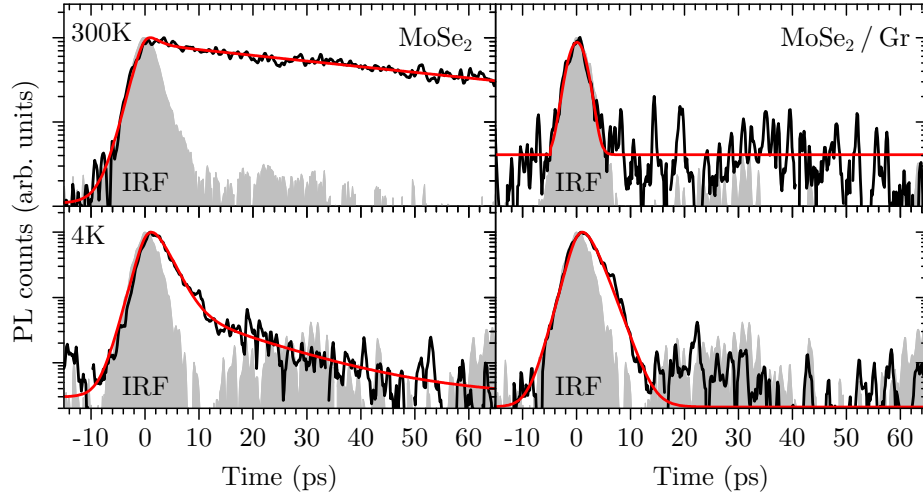


Figure 6.11: Traces temporelles correspondantes à la dynamique des excitons dans $MoSe_2$ et $MoSe_2/Graphène$ à température ambiante et à 4K.

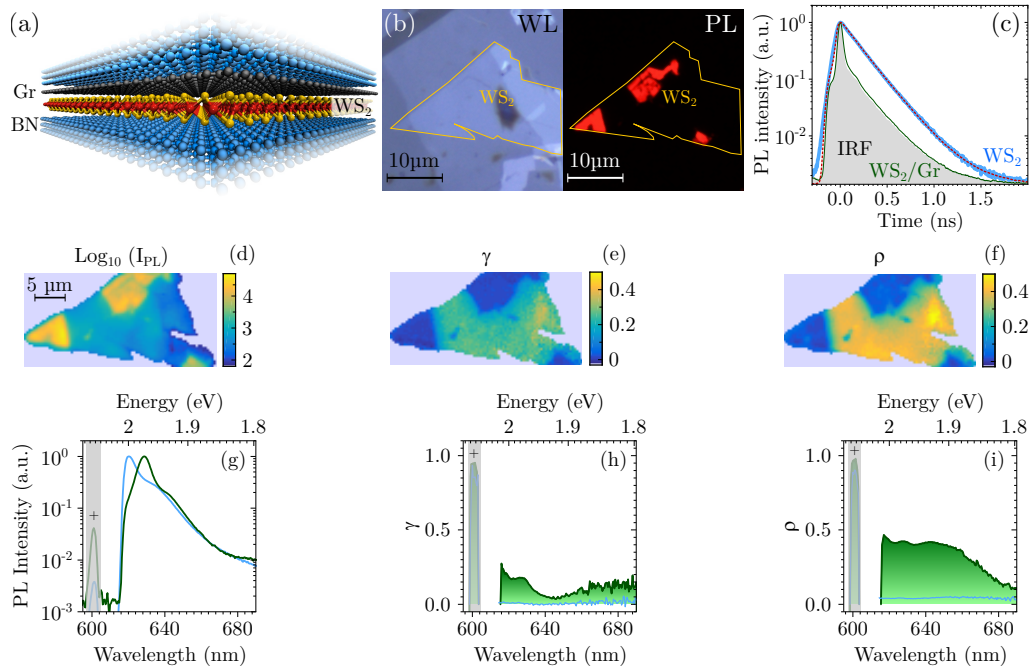


Figure 6.12: a) Schéma de l'échantillon, une hétérostructure $WS_2/Graphène$ encapsulée dans le nitrure de Bohr. b) image optique (gauche) et de fluorescence (droite) de l'échantillon. c) Photoluminescence résolue en temps de l'échantillon pour le WS_2 encapsulé en bleu et pour le $WS_2/graphène$ en vert. d) image de photoluminescence en échelle logarithmique. e,f) image du contraste de polarisation linéaire et circulaire pour la photoluminescence de l'échantillon. g) spectre de photoluminescence normé à 1 pour le WS_2 en bleu et le $WS_2/Graphène$ en vert. La bande grise ainsi que le symbole + correspond au laser. h,i) contraste de polarisation, linéaire (γ) et circulaire (ρ), de la photoluminescence du $WS_2/Graphène$ en vert et du WS_2 en bleu

s'opère pendant le temps de vie de l'exciton τ_x , ainsi, c'est la compétition entre le temps de

vie de l'exciton et le temps de diffusion inter-vallée qui donne le degré de polarisation de la photoluminescence ρ . Dans le cas de la polarisation de vallée (correspondant à une population d'excitons dans une vallée donnée) ρ s'écrit :

$$\rho = \frac{1}{1 + 2\frac{\tau_x}{\tau_s}} \quad (6.1)$$

Pour les DMT, le temps de vie τ_x est court à basse température mais long à haute température. C'est pourquoi à température ambiante, le contraste de vallée ρ est nul. Cependant, les hétérostructures DMT graphène présentent un temps de vie faible, quel que soit la température. Donc, ces hétérostructures présentent un contraste d'environ 40% à température ambiante (Fig. 6.12). De plus, en excitant les DMT avec une polarisation linéaire, qui est une superposition quantique de photons polarisés circulairement droite et gauche, on peut créer un exciton dans une superposition quantique entre vallée K et K'. Une telle superposition permettra d'émettre un photon polarisé linéairement si le temps de décohérence est suffisamment long comparé au temps de vie. Il est important de noter ici que la cohérence est bien plus fragile que la polarisation de vallée. Or une hétérostructure WS₂/graphène permet de conserver la cohérence de vallée à hauteur de 20% (Fig. 6.12) à température ambiante indiquant la très bonne qualité de nos échantillons.

Finalement, nous avons démontré que les hétérostructures WS₂/Graphène peuvent être utilisées comme des émetteurs chiraux à température ambiante afin d'étudier le couplage lumière matière chirale.

Verrouillage entre moment et spin

Nous avons réalisé un couplage directionnel, à température ambiante, dans un DMT en interaction avec un réseau plasmonique, en verrouillant la direction de propagation des excitations sur leur degré de liberté de vallée.

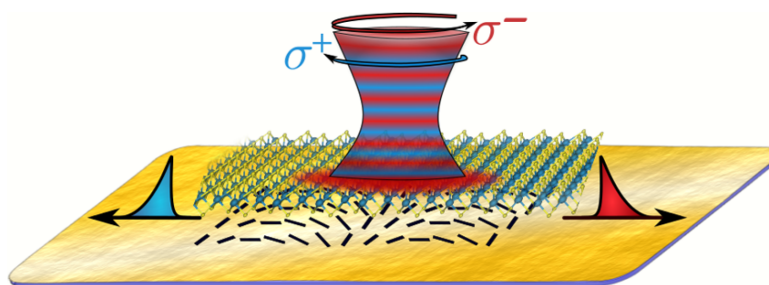


Figure 6.13: Schéma de principe du couplage directionnel, l'excitation avec une polarisation circulaire gauche (droite) crée une excitation propageant vers la gauche (droite).

Pour réaliser cet effet, nous avons besoin d'un résonateur optique chirale ainsi que de la protection des propriétés de vallée des DMT à températures ambiante.

Réseau plasmonique

Un plasmon est une onde électromagnétique confinée à une interface entre un matériau dont la constante diélectrique est négative et un autre dont la constante diélectrique est positive. Cette onde est atténuée exponentiellement en dehors de l'interface. La relation de dispersion d'un plasmon est toujours sous le cône de lumière ce qui le rend impossible à exciter via le champ lointain. De plus, des pertes, dues notamment à l'effet Joule, réduisent l'intensité du plasmon (Fig. 6.14).

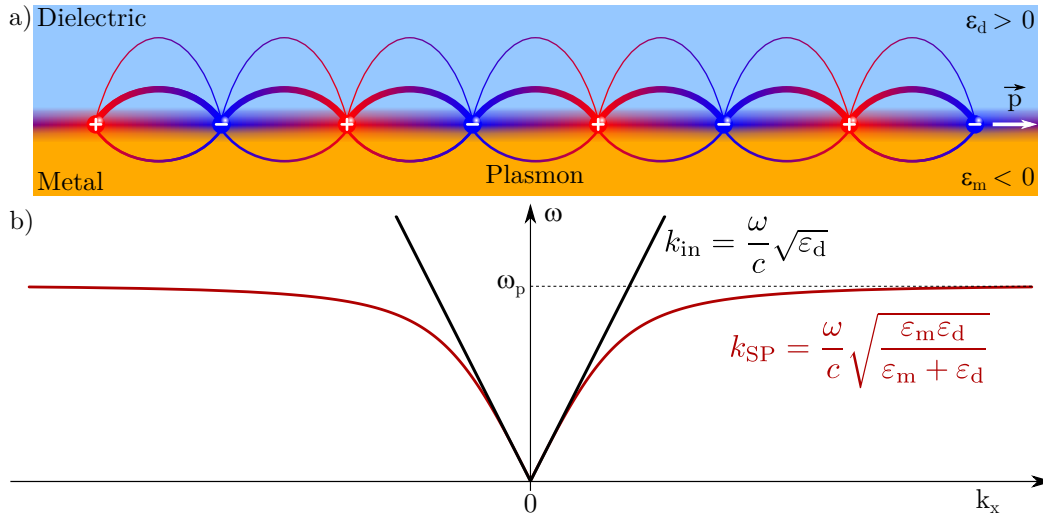


Figure 6.14: a) Schéma d'un plasmon, l'intensité du champ décroît exponentiellement en dehors de l'interface. Ici nous avons représenté un plasmon dans un métal sans perte, c'est pourquoi l'intensité n'est pas réduite avec la distance parcourue. b) Relation de dispersion d'un plasmon en rouge et cône de lumière en noir.

Afin de pouvoir exciter et observer des plasmons dans le champ lointain, une solution est de réaliser un réseau afin de répliquer la relation de dispersion à des moments finis.

Ceci a pour effet de créer des branches plasmoniques à l'intérieur du cône de lumière, qui pourront être excitées via le champ lointain. Ainsi la relation de dispersion du plasmon devient :

$$\mathbf{k}_{\text{SP}_R} = \mathbf{k}_{\text{SP}} + \frac{2\pi}{\Lambda} n \hat{x} + \frac{2\pi}{\Lambda} m \hat{y} \quad (6.2)$$

En utilisant un motif rectangulaire tournant pour le réseau (Fig. 6.15 a), nous pouvons induire une phase supplémentaire \mathbf{k}_g , dite phase géométrique, dépendant de la polarisation, circulaire droite ou gauche, de la lumière incidente. Cette phase dépend aussi de l'angle ϕ entre les motifs rectangulaires successifs et s'écrit.

$$\mathbf{k}_g = \frac{-\phi \sigma^\pm}{\Lambda} \hat{x} \quad (6.3)$$

Avec $\sigma^\pm = \pm 1$ dépendant de la polarisation circulaire gauche ou droite de la lumière et $\phi = \frac{\pi}{6}$. Finalement la relation de dispersion totale de ce réseau de rectangles devient :

$$\mathbf{k}_{\text{SP}_{\text{Rtot}}} = \mathbf{k}_{\text{SP}} + \frac{2\pi}{\Lambda} n \hat{x} + \frac{2\pi}{\Lambda} m \hat{y} \mp \frac{\phi}{\Lambda} \hat{x} \quad (6.4)$$

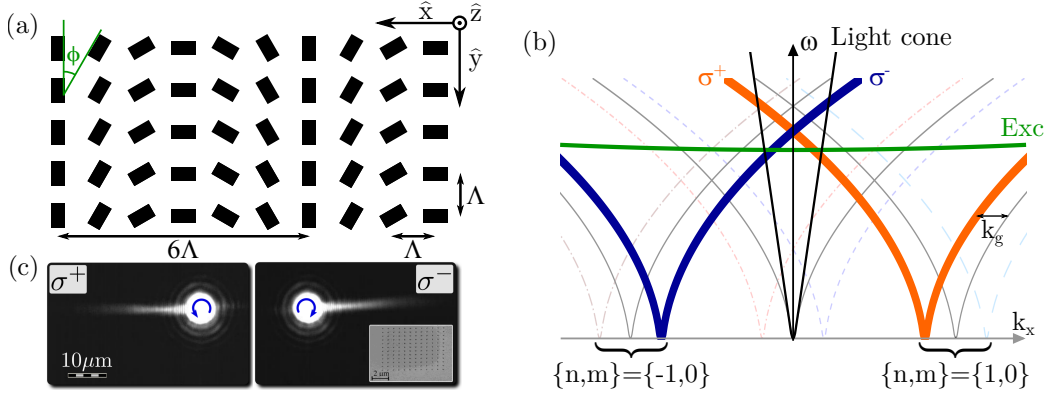


Figure 6.15: *a) Schéma du réseau plasmonique utilisé, les rectangles noirs sont creusés dans un film d'or. b) Relation de dispersion du plasmon correspondant au réseau (a), les lignes grises correspondent aux modes de réseau simple obtenus grâce à l'équation (6.2) tandis que les lignes épaisses orange ou bleu sont les dispersions affectées par la phase géométrique obtenues grâce à l'équation (6.4). c) Image en microscopie de fuite du plasmon lancé dans une direction donnée en fonction de la polarisation de l'excitation.*

Ce réseau plasmonique permet donc de verrouiller la direction de propagation du plasmon et la polarisation de l'excitation.

En ajoutant une monocouche de WS_2 sur ce réseau, nous pouvons obtenir le verrouillage entre le degré de liberté de vallée du TMD et la direction de propagation des excitations à température ambiante.

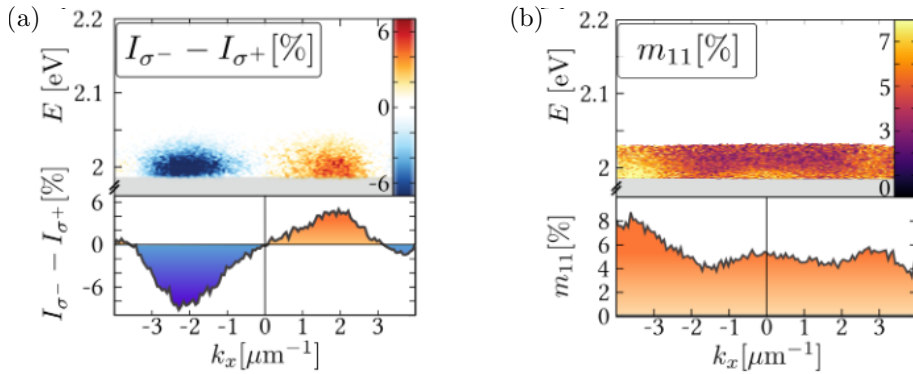


Figure 6.16: *a) Différence des intensités de photoluminescence, résolue en angle, excitée par un laser polarisé circulaire gauche et droite. b) Degré de polarisation linéaire de la photoluminescence du WS_2 couplé au résonateur plasmonique.*

Ainsi, l'émission de polarisation circulaire gauche est liée aux moments négatifs tandis que l'émission de polarisation circulaire droite est liée aux moments positifs (Fig. 6.16 a). De plus, ces résultats sont obtenus à température ambiante. Finalement, nous avons aussi révélé le maintien de la polarisation linéaire dans ce système, révélant ainsi un flux contra-propageant des excitations dans ce système excité par une lumière polarisée linéairement.

Conclusion

Pour conclure, nous avons démontré que les hétérostructures TMD/graphène montrent une forte réduction de la photoluminescence due à un transfert d'énergie efficace du TMD vers le graphène. De plus, le couplage entre graphène et TMD permet d'absorber le dopage natif du TMD qui est transféré au graphène. Finalement, ces hétérostructures permettent de récupérer un degré de polarisation de vallée de 40% ainsi qu'une cohérence de vallée de 20% à température ambiante dans WS₂/graphène. En utilisant ces propriétés de polarisation et de cohérence de vallée, nous avons pu réaliser un verrouillage du degré de liberté de vallée avec la direction de propagation des excitations, en couplant une couche de WS₂ avec un réseau plasmonique bien choisi.

Acknowledgement/Remerciement

Thank you for your attention and patience since you managed to get there you probably read some part of this manuscript. Now I will switch to french.

Bien qu'une thèse soit écrite par une seule personne, le travail qu'elle présente est un travail d'équipe. Il me faut donc remercier mes coéquipiers. En premier lieu, mon directeur de thèse Stéphane Berciaud qui a été mon mentor pendant cette aventure, une sorte de papa scientifique attentionné et bienveillant. Guillaume Froehlicher, grand pédagogue, tu auras su m'enseigner l'art de l'alignement et l'amour des beaux spectres, une signature de l'équipe. François Federspiel et Dominik Metten, thésard dans ce groupe m'ont eux aussi beaucoup appris. J'ai toujours pu compter sur vous et pour cela je vous remercie. Luis tu es arrivé plus tard dans l'équipe mais le travail en ta compagnie a été un plaisir, bonne chance pour ta thèse. Léo tu es arrivé juste avant la fin de ma thèse mais tu m'auras supporté pendant les moments durs de la rédaction merci. Je tiens aussi à remercier Guillaume Schull (habituez-vous aux Guillaumes vous allez en voir défiler quelques-uns) et son équipe avec laquelle j'ai eu la chance de travaillé mais aussi de rigolé, que ce soit durant les parties de tarots ou autour d'un café. Je remercie les théoriciens caché de l'IPCMS : Rodolfo Jalabert, Dietmar Weinman et Guillaume Weick, (mention spécial à Guillaume pour les blagues potaches) ainsi que leur thésard, mon ami François Fernique avec qui je pouvais faire des blagues boiteuses. Tu enquilles sur l'agrégation après la thèse, tu es courageux ! Bonne chance François. Personnes indispensable à nos travaux mais pas assez mis à l'honneur, l'IPCMS a une équipe technique exceptionnelle que je tiens à remercier. Notamment Arnaud Boulard, Manuel Acosta, Fabien Chevrier, Nicolas Beyer, Emmanuel Sternitzky avec lesquelles j'ai travaillé à la conception de la station de transfert pièce maitresse de ma thèse. L'IPCMS, c'était la science mais pas que. Grâce à l'ADDEPT, de multiple sorti bowling, mini-golf etc... ont été organisé. Merci à vous pour l'organisation de tous ces évènements, notamment le fameux tournois de pétanque. J'ai toujours passé d'agréable moment grâce à vous (voir à nous puisque j'en ai été membre en fait). Je remercie chaleureusement Véronique Wernher, la secrétaire du département, efficace, sympathique, et courageuse. D'un point de vue sportif, ma thèse aura aussi été bonne, grâce au fameux RUCK (Rugby Universitaire de Cronembourg et Kronembourg), pour pondre une anagramme pareil il fallait bien quelques docteurs ! Merci à tous les joueurs notamment au deux Guillaume, Rogez et Chaumy (deux nouveaux Guillaume), Anastasia et Claire (parce que oui le rugby ça peut être mixte) ainsi que Jérémie pour y être allé tranquille. J'espère que le RUCK restera d'actualité prenez soin de vous et de notre doyen Thierry Charitat. Je remercie aussi nos collaborateurs à l'ISIS Cyriaque Genet et Stefano Azzini nous avons fait

de belles choses tous ensemble ça a été un plaisir. A l'autre bout de la France, je remercie nos collaborateurs de la ville rose : Xavier Marie, Delphine Lagarde et Cédric Robert. Travailler avec vous était un bonheur et la collaboration fut fructueuse.

Une thèse c'est aussi l'opportunité de rencontrer d'autres personnes embarquées dans la même galère. Ces autres thésards je les croisais chez Oussama le bon lors du fameux groupe lecture (merci pour l'organisation Ous). Il y avait de tout dans ce groupe Thibault le franchouillard, ami et collaborateur, arbitre des élégances et gardien du bon goût. Pedro, le pyromane toujours présent pour lancer les débats houleux et défendre l'indéfendable. Finalement, notre chaman : Ziyad, merci pour Rien mais surtout merci pour tout ! Ce groupe c'était aussi tout un tas d'autres gens que je remercie pour leur bonne humeur Arthur, Meltem, Yul, Matthieu, Jean Yves et bien d'autres. De plus il y a les amis de longue date, les Aventuriers et les amis du PdB, de joyeux lurons, merci pour la rigolade, les concerts etc... Certains ont même eu la foi de venir me voir défendre ma thèse.

Finalement, sans ma famille je n'en serai pas là non plus alors une dernière fois entonnons la fameuse litanie de mon enfance : Papa, Maman, Jean, Marie, Guillaume (le dernier), Philippe, Clémence merci à vous pour les conseils l'éducation et le soutien en général.

Et maintenant, en route vers de nouvelles aventures, et à bientôt !

A

Building van der Waals heterostructure

In this appendix, I will explain in detail how I fabricate a van der Waals heterostructure. It is not the perfect way to build them but it is how I did. The method is based on the process described by P.J. Zomer *et al.*

Someone relying only on optical contrast, between a transparent substrate and a lamellar crystal (e.g. graphite), will struggle to find monolayers. To avoid those problem, we choose to exfoliate our 2D materials on silicon wafer with 90nm silicon oxide on top. These oxide layer enhance optical contrast by interference effect for small number of layers, facilitating the search of monolayers 2D materials.

A.1 Exfoliation

For the exfoliation process, we use :

- commercially available 3M magic tape
- DGL film x4 from *Gelpak* company (6.5mil thickness) polymer similar to PolyDiMethyl-Siloxane (PDMS)
- heating stage to heat up to 100°C

A.1.1 Graphene and Boron Nitride

First, a bulk crystal is placed on a tape, which is folded then unfolded few times in order to have a rather small (2 to 3 cm) but densely covered region (FigA.1 a). Once we have a tape covered with bulk crystal, we stick an empty tape on the bulky one and remove it quiet quickly. Then, we use the previously blank tape as the bulky one and repeat the previous step until the graphite turns light grey. It is worth mentioning that MoS₂ or WS₂ turns green and MoSe₂ or WSe₂ turns reddish. For the BN, the bulk will turn iridescent with a majority of purple/pink colours.

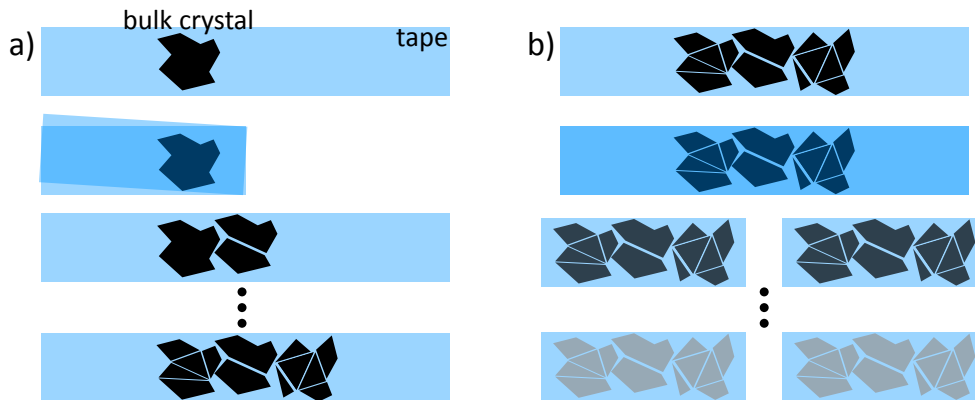


Figure A.1: *a) exfoliation process to cover tape with bulk crystal. First place the bulk then fold up the tape and open it to duplicate bulk crystal. Repeat this step until you have a densely covered region with bulk. b) cover the bulky tape with a second empty tape and remove it to remove few layers from the bulky tape. repeat this process until the bulk graphite turns light grey.*

Then, to drop off crystals on a substrate, the tape is pasted on a Si/SiO₂ substrate, heated up to 100°C for one minute and then removed from the substrate as slowly as possible. To further improve the number of graphene layer on a sample, the Si/SiO₂ substrate are plasma treated with an oxygen plasma at 100 Watts for 5 minutes. This process, provide us many graphene layers on each substrate. Exfoliation of boron nitride follows the same method but TMDs are exfoliated in a slightly different way.

A.1.2 Transition Metal Dichalcogenides

TMDs are not directly dropped off on the silicon substrate they are transferred on the DGL x4 film first and then there is two options. The first one consist of putting the DGL film in contact with a plasma treated Si/SiO₂ substrate, same as before with one extra transfer step. The second option is more deterministic and allows us to find much bigger TMD flake. After the transfer on the DGL film, the first step is to find the right monolayer on the transparent polymer film. Then, using the transfer station, we can drop the monolayer off wherever we want (Fig A.2).

Transferring from the polymer to the substrate is critical, if it is not done well, the chosen monolayer will be destroyed. With this method, we have a perfect control of the contact region between the substrate and the DGL film, meaning that we can make the contact and the withdraw between the layer and the silicon at a very low speed, few microns per second ! If this process is done too fast, The danger here is to induce crack, wrinkles and bubbles are induced in the layer and more problematic, to transfer only a portion of the flake. It is also mandatory to cut the polymer around the region of interest to a roughly 5x5mm square, otherwise the first contact spot between the substrate and the polymer could be far from the targeted flake. At this point, we need to push hard on the polymer stamp inducing ripples at its surface that will degrade the TMD layer. This method provide us 20x10µm TMD monolayers routinely. Those monolayer could be as big as 150x150µm.

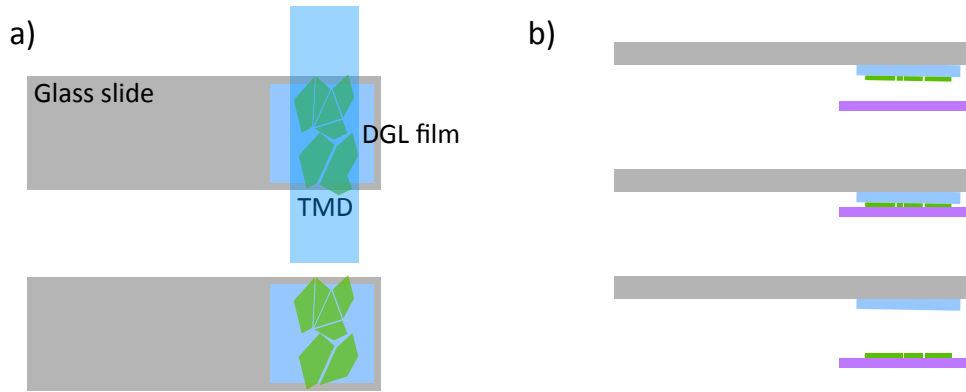


Figure A.2: a) Transfer TMD flake on a DGL film by sticking the tape on the film, remove it by quickly pulling the tape. b) Put the TMD flakes slowly in contact with the substrate, pull the DGL film slowly.

A.2 Van der Waals heterostructure assembly

After exfoliating different 2D layers on silicon substrate, the next step is to stack them. To this aim, we use :

- Poly(Bisphenol A carbonate) 45000 average molar mass
- Chloroform
- PDMS : dow corning Sylgard 184
- Glass slides
- Heat resistant tape (e.g. kapton tape)

This transfer technique use the properties of 2D materials, especially BN, to stick better on a poly(Bisphenol A carbonate) (PC) surface than on a SiO_2 surface. Once we picked up a BN flake, we can stack any 2D material we want below it. To drop off the stack, we just need to melt the polymer in order to release the heterostructure on any substrate.

A.2.1 Recipe for the Polycarbonate stamp

First, we need a PC thin film. To achieve this, we dissolve PC in chloroform (6% PC in mass in chloroform) mix the solid polymer with chloroform in a vial, close it tightly (chloroform is quiet volatile) and stir it at room temperature over the night. Then, we pour few droplets of this mixture on a glass slide and sandwich those droplets with a second glass. By sliding one glass piece relative to the other, we make a nice homogeneous PC thin film (Fig A.3 a and b). This film is dried for fifteen minutes at least before use.

To pick up this film, we use a kapton tape because it resist to high temperature without degrading. We cut a square in its middle and stick it to the PC film, then we notch the PC film alongside the tape to avoid to remove the whole PC film from the glass substrate. Once we picked

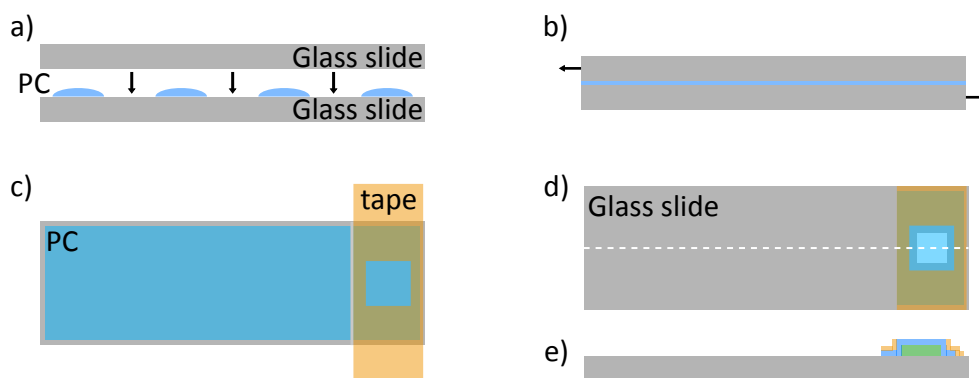


Figure A.3: a), PC droplet in blue, glass slide in grey. b) Slide the two glass pieces to laminate a nice PC thin film. c) pick up a part of the PC film with kapton tape in yellow. d) Grey rectangle is a glass slide, the yellow one is kapton tape, the light blue is the PDMS spacer and the blue rectangle is the PC film. The white dashed line correspond to the cut represented below. e) cut view of the PC stamp in d)

up the PC film, we place a small PDMS spacer on a glass substrate and put the PC film on top of it (Fig A.3 c and d), finishing the PC stamp. To ensure a good adhesion of the PC on the PDMS, the PC stamp is heated at 200°C for ten to thirty second. The stamp is now usable, if there is not too much bubbles or wrinkles on it, otherwise, we discard it to avoid any migration of bubbles that could destroy your sample.

A.2.2 The transfer station

In this part, sample refers to the substrate with a 2D layer that we want to pick up.

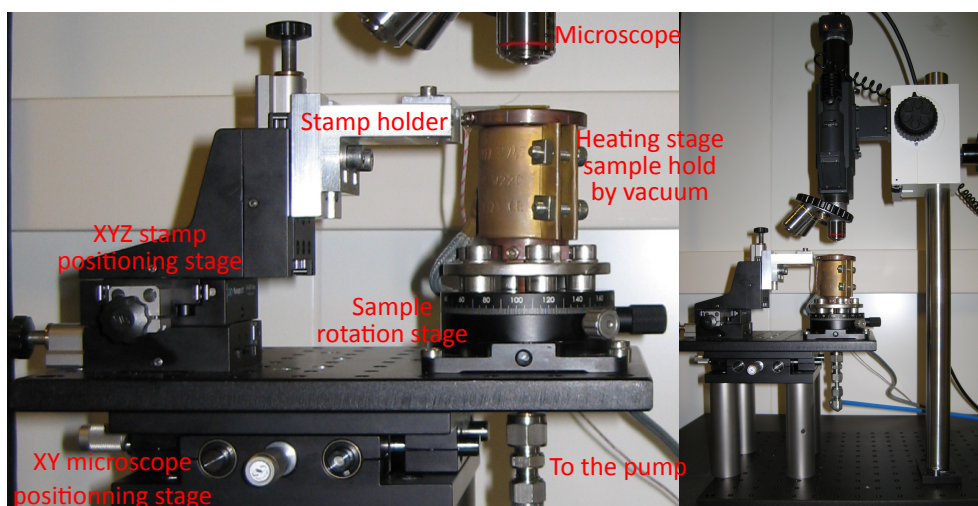


Figure A.4: Transfer station picture, the pole on the right hand side hold the microscope.

The transfer station (Fig A.4) is composed of a microscope with high working distance objectives (here 5x, 10x and 20x), an XY translation stage to move the microscope independently of the stamp and the sample, one XYZ translation stage to position the stamp with respect to the

sample. The sample is held by vacuum on a heating stage that can reach 200°C and this heating stage is placed on a rotational stage to control the orientation of the different 2D layer we want to stack.

A.2.3 Pick up

The PC stamp is now attached to the holder on the transfer station (Fig A.5 a), the sample is placed on the heating stage and hold by vacuum and heated at 40°C. The stamp is then put in contact with the sample, a contact line will appear and it can be moved in two different ways : by pushing the stamp on the sample thanks to the z-axis of the stamp translation stage, or by increasing the temperature of the heating stage. Usually we bring the contact line at few tens of micron by pushing on the stamp and then we start to increase the temperature. When the contact line reach the limit of the 2D layer, it is mandatory to slowly (few μm per second) cover the layer with PC. To achieve this we increase slowly the temperature of the heating stage (few tenth of °C per second).

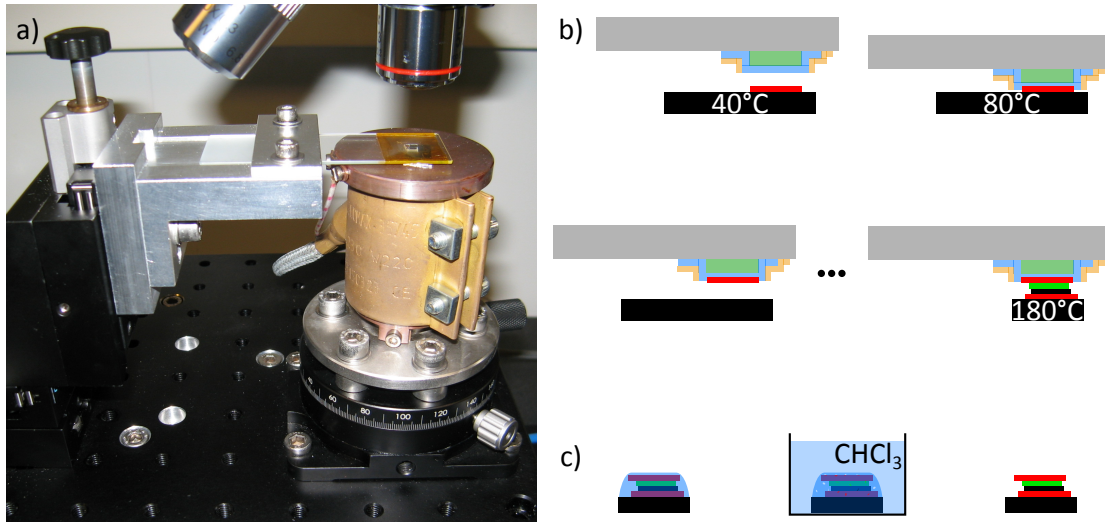


Figure A.5: a) Transfer station picture. b) Different step of the process, the three first step could be repeated several time to produce various stack. c) Cleaning the dropped off stack covered with PC residue in chloroform.

After the contact is made, we increase slowly the temperature when the PC is covering the targeted material, and after the flake is fully covered by the PC, the temperature is set to 80°C and the stamp is withdrawn using the z-axis translation. Again when the contact line is close from the flake, it is essential to slowly remove the PC from the sample to avoid cracks and defect in the layer. After this step, the flake should be picked up, and we can go through this whole process again to stack a second material with the previous one (Fig A.5 b). Once the full stack sit on the PC stamp, it is now time to drop it off on its new substrate. This step is almost the same as the pick up but instead of setting the temperature at 80°C we setting it at 180°C. At this point, the PC start to melt and when we withdrawn the stamp, the PC film remain on the substrate and so is the heterostructure.

Now the last step is to remove the PC residue from the sample. In order to do it, we plunge the sample in chloroform, hermetically close the vial (chloroform still quiet volatile) and leave it under a fume hood over the night. After this, you can clean the sample in ethanol and then isopropanol to finally remove the liquid from the sample with a nitrogen flow (Fig A.5 c).

B

B.1 Optical measurements at IPCMS, a versatile system

At IPCMS, we perform optical spectroscopy, (PL, Raman, reflectivity ...) and time resolve PL. Those techniques rely on three main building blocks. The excitation block, which is shared by every measurement technique, is composed of lasers. The microscope to route and focus the excitation beam on the sample, also shared by every measurement technique. Finally, the detection block is different for spectroscopy measurement than from time resolved measurement. For the former we use a spectrometer combined with a Charge Couple Device (CCD) camera while the latter is an Avalanche Photo-Diode (APD) Fig. B.1.

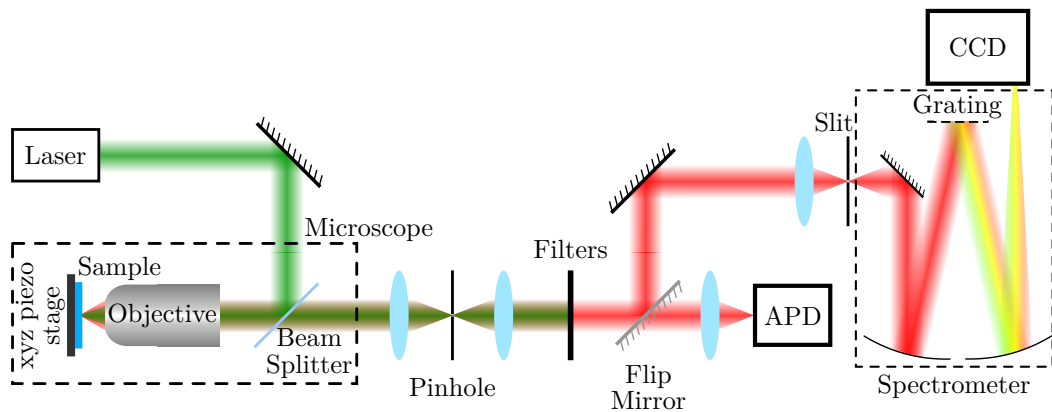


Figure B.1: Scheme of the optical setup at IPCMS. The green beam correspond to the excitation beam and the red to the signal. APD stands for Avalanche Photo-Diode and CCD for Charge Couple Device.

In addition, we have enough free space between the laser and the microscope to prepare the beam. We can modulate its polarization, intensity and collimate the beam. Just like the excitation beam, there is enough room to filter and perform polarization analysis between the microscope and the detection.

B.1.1 Excitation

For the excitation, we can make use of three different lasers. Two continuous wave (cw) narrow line lasers (FWHM < 1 MHz), necessary for the Raman spectroscopy, one at 532 nm (2.33 eV) and one at 633 nm (1.96 eV). The last one is a pulsed laser, mandatory to perform time resolved photoluminescence, tunable from 480 nm (2.58 eV) to 2400 nm (0.52 eV). Its repetition rate can be modulate from 2 to 78 MHz. Before sending the excitation beam into the microscope, we filtered the cw laser beam, using BraggGrate ultra-narrow band pass filter (FWHM = 150 MHz, 5 cm^{-1}). This filter removes the laser background around the laser line Fig. B.2, allowing us to measure signal as near as 5 cm^{-1} from the laser.

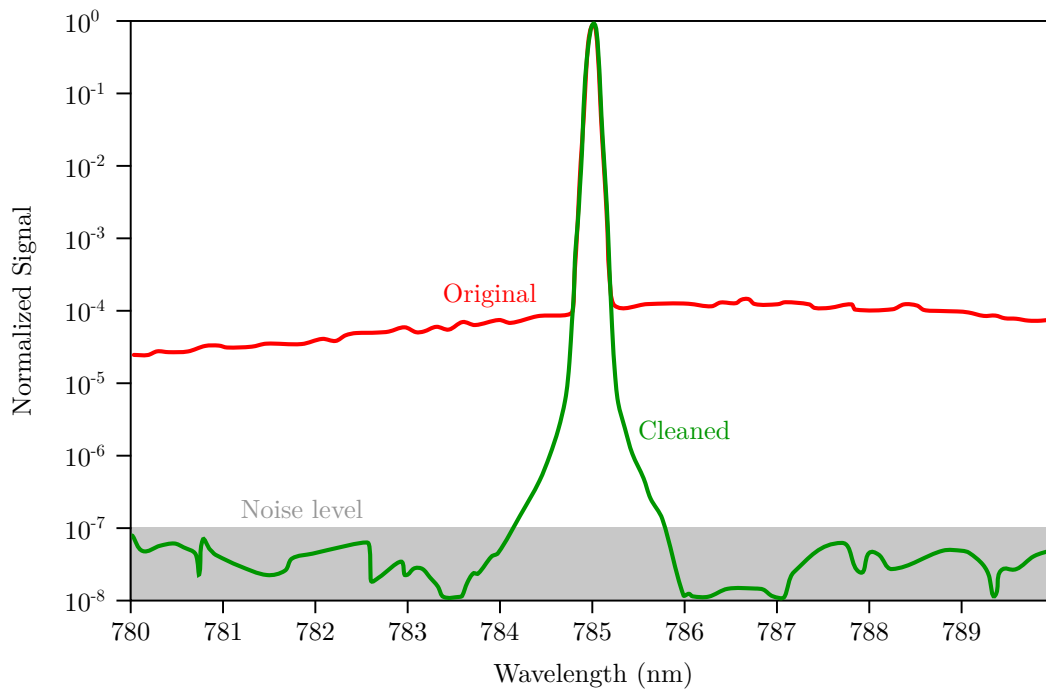


Figure B.2: *Laser intensity with respect to the wavelength. The red line is the original spectral intensity while the green line is the cleaned version with an ultra narrow bandpass filter.*

Our pulsed tunable laser has a temporal FWHM of ≈ 40 ps depending on the emission wavelength. The spectral resolution range from 1 to 10 nm with satellite peak around the main peak.

Since our cw lasers are linearly polarized ($> 1:10\,000$), we modulate the excitation beam intensity using a half waveplate and a linear polarizer. Giving the high polarization of the laser, we can modulate the laser intensity over four decades. On the other hand the pulsed laser is not polarized. However, we can directly modulated the power supplied to the laser cavity and therefore modulate intensity.

B.1.2 Microscopy

B.1.2.1 Measurements in ambient condition

We use a commercial Nikon inverted microscope Ti eclipse for its convenience Fig. B.4. A turret that can load up to 6 objectives allows us to quickly scan our samples and find region of interest with lower magnification objectives before switching to high magnification one for the measurement. In ambient conditions, we use a 100x with 0.9 N.A or a 150x, 0.95 N.A. objectives.

The sample holder is fixed on a xy mechanical translation stage for coarse positioning coupled to a xyz piezo-stage for nano-positioning.

A carousel inside the microscope can hold up to 6 beam splitter and dichroic mirror allowing us to switch from one to another easily with minimum realignment of the excitation beam.

We can choose between three output, one that is linked to a webcam to visualize our sample using white light illumination. The second output is linked to a 500x500 pixels CCD camera cooled by a Peltier device. We use it to perform fluorescence imaging. We adapt a pinhole at the last output to build a confocal microscope Fig. B.1. After the pinhole, we send the signal to the APDs or to the spectrometer.

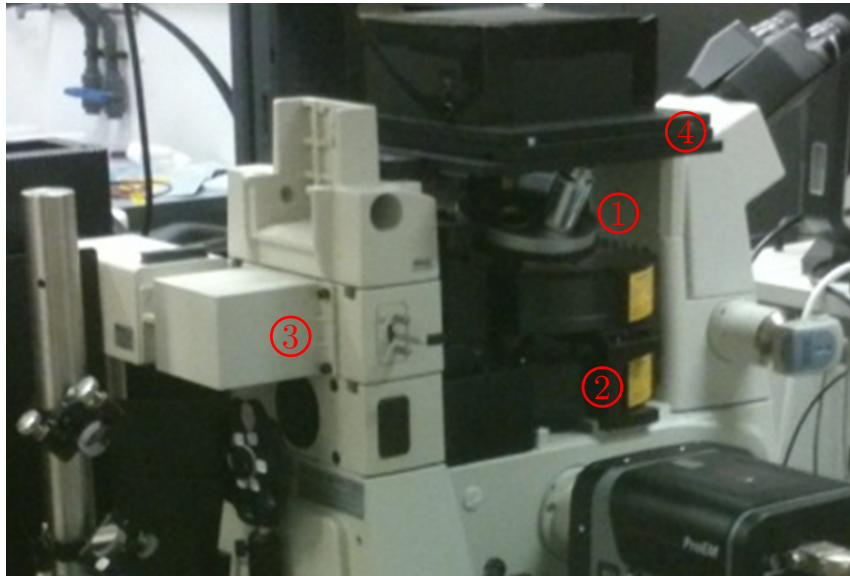


Figure B.3: *Picture of our microscope, 1 is the objective turret, 2 the beam splitter carousel 3 the white light input and the 4 correspond to the positioning stage.*

B.1.2.2 Measurements in vacuum at variable temperature

Cryogenic and vacuum measurement are performed the same way since we use our cryostat as a vacuum chamber for our samples. We use a flux cryostat, pumping liquid helium inside to cool down a cold finger holding our sample. We can adapt this cryostat above the microscope while we adapt the objective on the xyz piezo-stage. In this configuration, we have another xyz mechanical translation stage to move the whole cryostat with respect to the microscope while the

nano-positioning is realized by moving the objective with the piezo stage. For this measurement, we cannot use the 100x and 150x objectives since their working distances are much too short. Therefore, we use a 50x objective 0.65 N.A. with 1 cm working distance.

B.1.3 Detection

The sample signal is sent to the spectrometer or to the APDs. For more convenience we add a flip mirror to easily switch from spectrally resolved to time resolved measurement Fig. B.1. Our time resolved system is composed by a picoquant photo-counting module, linking our ps pulsed laser with the APD. The laser sends a TTL pulse to the photo-counting module each time it emits a pulse. Then each time the APD detects a photon, it sends a pulse to the photo-counting module that measures the time difference between the last laser pulse and the photon arrival time. With such a system, we can record the PL time trace.

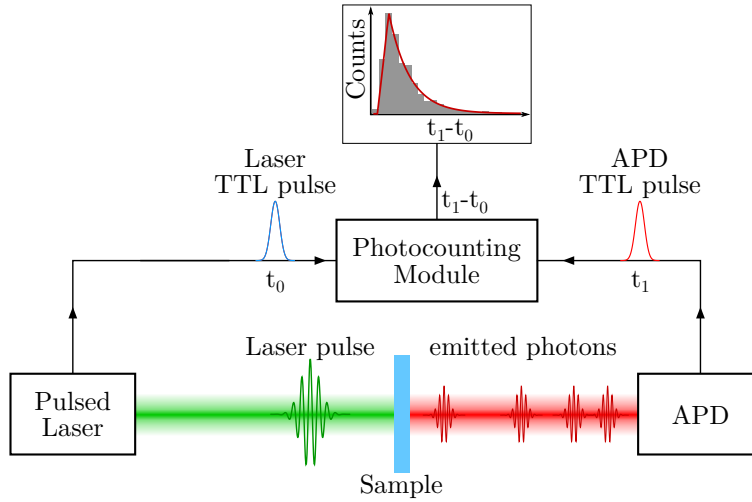


Figure B.4: *PL decay reconstruction scheme*

B.1.3.1 Spectrometer

Our main activity is optical spectroscopy. Since our microscope is confocal, we never perform imaging with this system. Hence, we need a long CCD module, to get the longest spectral window as possible, while the width of the CCD module is not critical. We have therefore a 50 cm focal length spectrometer coupled to a 1340x100 pixels nitrogen cooled CCD camera.

We can adapt several turrets in the spectrometer to change the gratings and hence change our spectral resolution.

B.1.3.2 Grating

The most important parameter of a grating is its number of lines per millimetre. It gives its ability to disperse light, higher lines density lead to larger dispersion. Therefore, the spectral resolution increases with the number of lines per millimetre while the spectral window shrinks.

For TMD Raman spectra measurement, we use a 2400 line per millimetre giving a 0.01 nm spectral resolution. To record Graphene Raman spectra, we took a 900 lines per millimetre grating ending up in a 0.04 nm spectral resolution. Finally, for PL measurement, we need a broader spectral window. Therefore, we use a 150 lines per millimetre that gives us 0.26 nm resolution.

We use the 900 lines per millimetres grating to record graphene Raman spectra when excited with the 532 nm (2.33 eV) laser because we are able to record both G- and 2D-modes in this configuration. However, when we perform the same measurement using a 633 nm laser, the energy resolution $E_1 - E_2$ increase since $E_1 - E_2 \propto 1/\lambda_1 - 1/\lambda_2$. Therefore, we are not able to record both graphene G- and 2D-modes using the 900 line per millimetres grating anymore. To overcome this issue, we also have a 300 lines per millimetres grating to perform graphene Raman spectroscopy excited at 633 nm (1.96 eV).

B.1.4 Hyperspectral mapping

To get the full potential of our system, Michelangelo Romeo interfaced the xyz piezo-stage with the detection device. This allows us to raster scan our sample while recording PL decay or spectra. With this method, we are able to do graphene doping map, follow the emission energy, width distribution over a sample... However, such technique also lead to a large amount of spectra or data to process.

B.1.4.1 Data processing

The typical region of interest on our samples is up to 30x20 μm and we use 0.5 to 1 μm steps. Therefore, we can have up to 1200 spectra for one map. Each spectrum has to be fitted properly in order to extract the relevant parameters such as width or emission energy. Intensity could also be extract from spectrum fitting even though it is not necessary to fit.

Fitting those spectrum one by one is a very painful and time consuming process. Therefore, we choose to develop algorithm that can do this job automatically. We use MATLAB built-in fitting routine (`lsqcurvefit`), that relies on χ^2 (squared difference between the fitting curve and data points) minimisation. After a spectrum has been fitted, we report the fitting parameters at the right position in a $m \times n \times p$ matrix, with $m \times n$ the map size and p the number of parameters in the fitting function. Once each spectrum have been fitted, we can draw hyperspectral map for any fitting parameters.

Our algorithm can fit several Voigt, Lorentzian or Gaussian profile to a spectrum. In addition, minor changes to the algorithm allow us to fit PL decay. However, PL decay are much harder to automatically fit since the guess parameters have to be close from the real values to well fit the decay.

B.2 Angle resolved polarimetric setup at ISIS

We perform angle resolved polarimetric measurement in collaboration with the nanostructure group at ISIS.

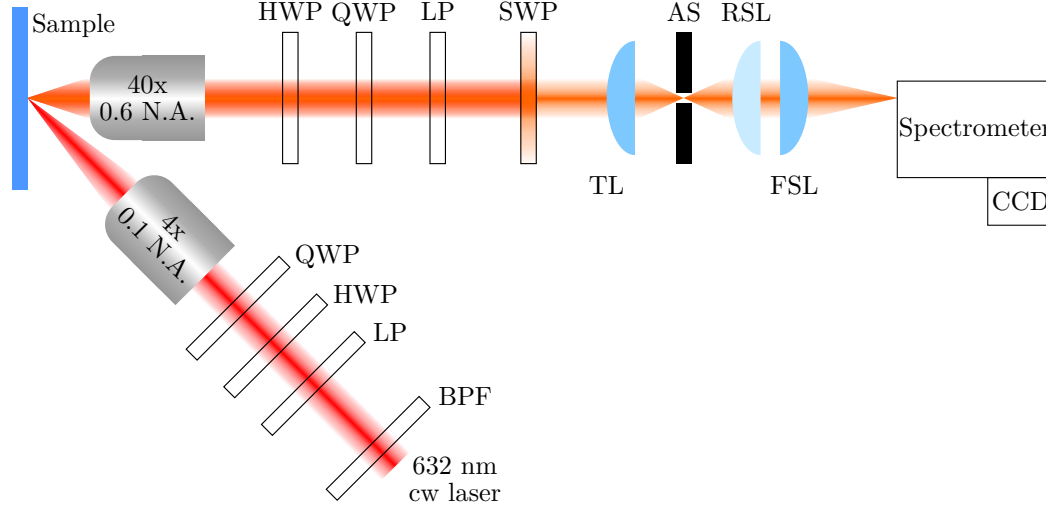


Figure B.5: Angle resolved polarimetric setup. The excitation laser is filtered by a band pass filter centred at the laser frequency. The polarization state is defined by the linear polarizer (LP), a half waveplate (HWP) and a quarter waveplate (QWP). The beam is then focused on the sample using a 4x objective. We collect the emitted light by a 40x objective. The emitted light is then projected on a polarization state using half waveplate, a quarter wave plate and a linear polarizer. We filter the laser light using a short wave pass (SWP). A tube lens forms the image of the sample on the adjustable slit (AS), to select spatially the area of interest on the sample. After the slit, a lens can be added or removed to image the real space image on the camera. The last lens, the Fourier Space Lens (FSL) to image the Fourier Space on the camera.

To get the angular content of an object, we need to Fourier transform its image. This can be done by adding a Fourier space lens (FSL) with its focal plane coinciding with the tube lens image plane [135]. The image plane of the FSL is then coinciding with the spectrometer slit. Adding a lens with a shorter focal distance between the FSL and the tube lens image plane to collimate the beam again allows us to measure the real space spectrum formed on the slit by the FSL Fig. B.5. We adopt an excitation using a second objective tilted from the normal incidence to avoid the necessity of a beam splitter that has different polarization responses for the vertical and horizontal linear polarizations. Since such optical element makes circular polarization elliptical and therefore difficult to manipulate. The Fourier space lens combined with the spectrometer gives access to the dispersion relation ω vs k .

B.3 Time resolved Photo Luminescence at LPCNO

In collaboration with Xavier Marie's group in Toulouse, we perform high resolution TRPL using a streak camera. The setup is the same as the spectral measurement used at IPCMS Fig. B.1 at

the exception of the CCD camera that is replaced by a streak camera. Such system allows us to record time trace at different frequency Fig. B.6.

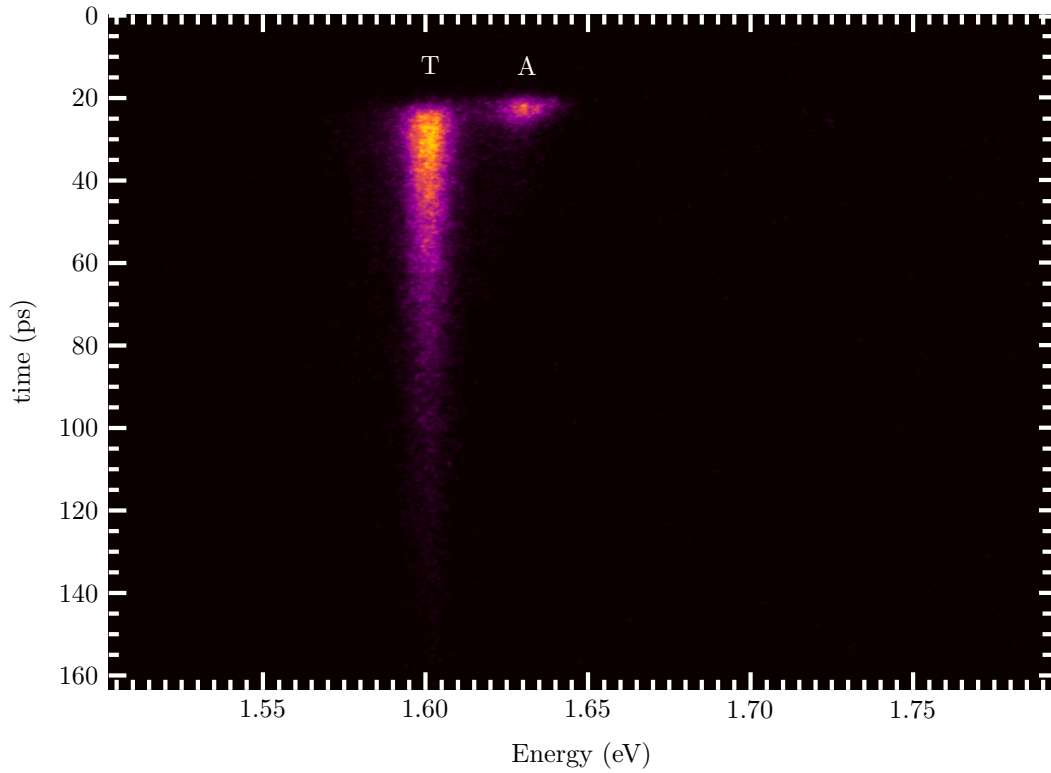


Figure B.6: Streak image of a MoSe_2 flake at 4K . A stands for the A exciton and T for the trion

B.3.1 Streak camera

Photons in a streak camera are first converted to electrons by interacting with a photocathode.

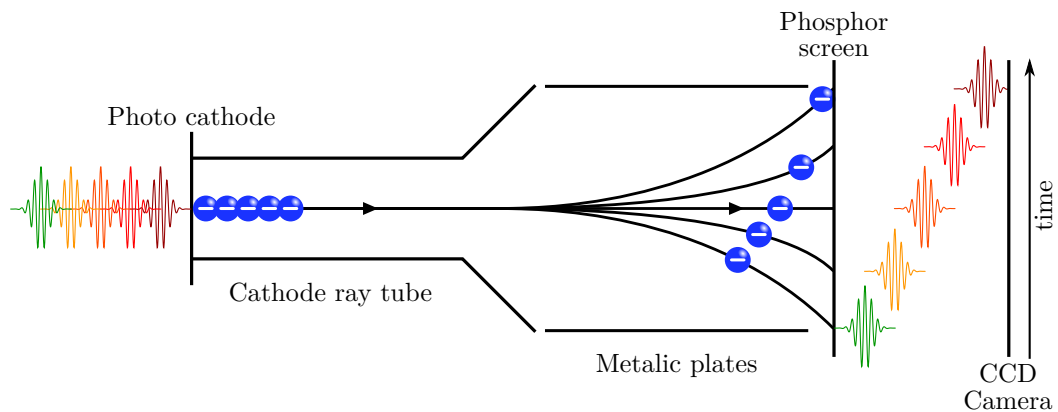


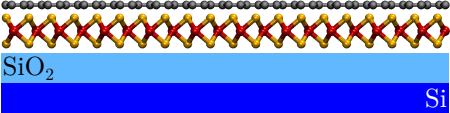
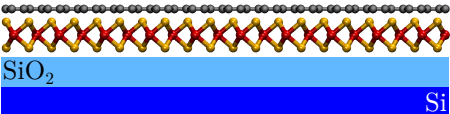
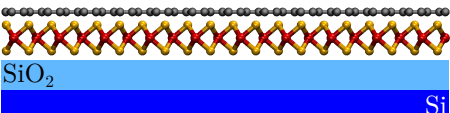
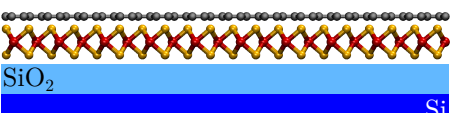
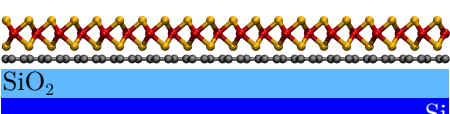
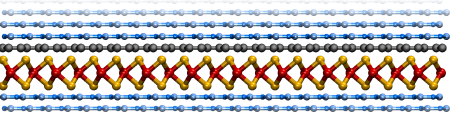
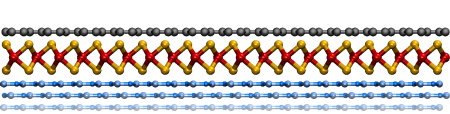
Figure B.7: Scheme of a streak camera

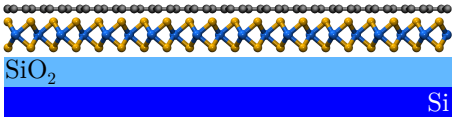
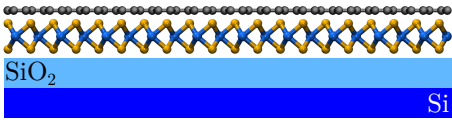
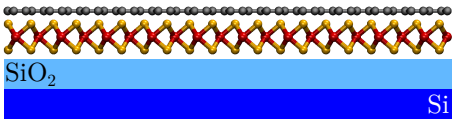
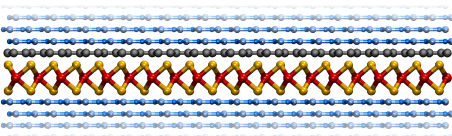
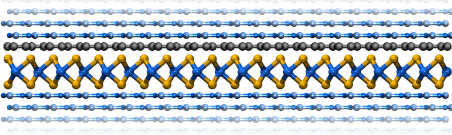
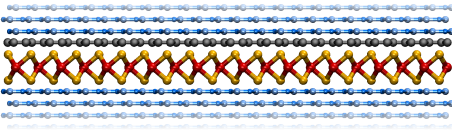
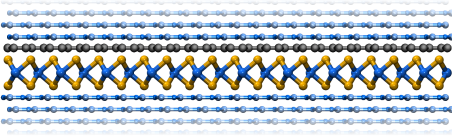
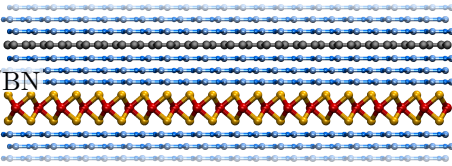
Those electrons are then collected and accelerated by a cathode ray tube before being sent through two metallic plates Fig. B.7. By modulating the electrical potential between both plates,

the deflection undergoes by each electron will be time dependent. By synchronising laser pulses with voltage sweep between the metallic plates, we can make sure that each photon emit a at delay t from the the laser pulse follows always the same path in the streak camera. Once electron have gone through the two plates, they hit a phosphor screen to be re-converted into photons and collected on a CCD camera. The vertical axis on the CCD is the time, while the horizontal one is the frequency since we use a monochromator in this experiment.

C

Samples list

Sample designation	Sample component	Used for
S_1 : MoSe ₂ /Gr		PL, Raman in air, under vacuum and at 4K
S_2 : MoSe ₂ /Gr		PL, Raman in air and under vacuum
S_3 : MoSe ₂ /Gr		PL with respect to T Raman in air in vacuum and at 4K, TRPL
S_4 : MoSe ₂ /Gr		PL, Raman in air and under vacuum
S_5 : MoSe ₂ /Gr		PL, Raman in air and under vacuum
S_6 : BN/MoSe ₂ /Gr/BN		PL in air, under vacuum and at 4K, Raman in air
S_7 : BN/MoSe ₂ /Gr		PL, Raman in air and under vacuum

Sample designation	Sample component	Used for
S ₈ : WSe ₂ /Gr	 <p>The diagram shows a single layer of WSe₂ (represented by yellow and blue spheres) on a graphene (Gr) layer (represented by grey spheres). This is supported by a SiO₂ layer (light blue) on a Si substrate (dark blue).</p>	PL, Raman in air and under vacuum
S ₉ : WS ₂ /Gr	 <p>The diagram shows a single layer of WS₂ (represented by yellow and blue spheres) on a graphene (Gr) layer (represented by grey spheres). This is supported by a SiO₂ layer (light blue) on a Si substrate (dark blue).</p>	PL, Raman in air and under vacuum
S ₁₀ : MoS ₂ /Gr	 <p>The diagram shows a single layer of MoS₂ (represented by red and yellow spheres) on a graphene (Gr) layer (represented by grey spheres). This is supported by a SiO₂ layer (light blue) on a Si substrate (dark blue).</p>	PL, Raman in air and under vacuum
S ₁₁ : BN/MoSe ₂ /Gr/BN	 <p>The diagram shows a MoSe₂ layer (red and yellow spheres) on a graphene (Gr) layer (grey spheres), which is sandwiched between two BN layers (light blue). The entire structure is on a SiO₂ layer (light blue) on a Si substrate (dark blue).</p>	Polarization resolved PL Low temperature TRPL
S ₁₂ : BN/WS ₂ /Gr/BN	 <p>The diagram shows a WS₂ layer (yellow and blue spheres) on a graphene (Gr) layer (grey spheres), which is sandwiched between two BN layers (light blue). The entire structure is on a SiO₂ layer (light blue) on a Si substrate (dark blue).</p>	Polarization resolved PL Low temperature PL
S ₁₃ : BN/MoS ₂ /Gr/BN	 <p>The diagram shows a MoS₂ layer (red and yellow spheres) on a graphene (Gr) layer (grey spheres), which is sandwiched between two BN layers (light blue). The entire structure is on a SiO₂ layer (light blue) on a Si substrate (dark blue).</p>	Polarization resolved PL Low temperature PL
S ₁₄ : BN/WSe ₂ /Gr/BN	 <p>The diagram shows a WSe₂ layer (yellow and blue spheres) on a graphene (Gr) layer (grey spheres), which is sandwiched between two BN layers (light blue). The entire structure is on a SiO₂ layer (light blue) on a Si substrate (dark blue).</p>	Polarization resolved PL Low temperature PL
S ₁₅ : BN/MoSe ₂ /BN/Gr/BN	 <p>The diagram shows a MoSe₂ layer (red and yellow spheres) on a BN layer (light blue), which is on top of a graphene (Gr) layer (grey spheres) sandwiched between two BN layers (light blue). The entire structure is on a SiO₂ layer (light blue) on a Si substrate (dark blue).</p>	Room temperature TRPL

Bibliography

- [1] KS Novoselov, D Jiang, F Schedin, TJ Booth, VV Khotkevich, SV Morozov, and AK Geim. Two-dimensional atomic crystals. *Proc. Natl. Acad. Sci. U.S.A.*, 102(30):10451–10453, 2005.
- [2] P. M. Ajayan, P. Kim, and K. Banerjee. Two-dimensional van der waals materials. *Phys. Today*, 69(9):38–44, September 2016.
- [3] Kin Fai Mak, Changgu Lee, James Hone, Jie Shan, and Tony F. Heinz. Atomically Thin MoS₂: A New Direct-Gap Semiconductor. *Phys. Rev. Lett.*, 105(13):136805, September 2010.
- [4] Alexey Chernikov, Timothy C. Berkelbach, Heather M. Hill, Albert Rigosi, Yilei Li, Ozgur Burak Aslan, David R. Reichman, Mark S. Hybertsen, and Tony F. Heinz. Exciton Binding Energy and Nonhydrogenic Rydberg Series in Monolayer WS₂. *Phys. Rev. Lett.*, 113(7):076802, August 2014.
- [5] A. V. Stier, N. P. Wilson, K. A. Velizhanin, J. Kono, X. Xu, and S. A. Crooker. Magneto-optics of exciton rydberg states in a monolayer semiconductor. *Phys. Rev. Lett.*, 120:057405, Feb 2018.
- [6] Di Xiao, Gui-Bin Liu, Wanxiang Feng, Xiaodong Xu, and Wang Yao. Coupled spin and valley physics in monolayers of mos₂ and other group-vi dichalcogenides. *Phys. Rev. Lett.*, 108:196802, May 2012.
- [7] Kin Fai Mak, Long Ju, Feng Wang, and Tony F Heinz. Optical spectroscopy of graphene: from the far infrared to the ultraviolet. *Solid State Commun.*, 152(15):1341–1349, 2012.
- [8] F. Cadiz, E. Courtade, C. Robert, G. Wang, Y. Shen, H. Cai, T. Taniguchi, K. Watanabe, H. Carrere, D. Lagarde, M. Manca, T. Amand, P. Renucci, S. Tongay, X. Marie, and B. Urbaszek. Excitonic linewidth approaching the homogeneous limit in MoS₂-based van der waals heterostructures. *Phys. Rev. X*, 7:021026, May 2017.
- [9] C. Robert, T. Amand, F. Cadiz, D. Lagarde, E. Courtade, M. Manca, T. Taniguchi, K. Watanabe, B. Urbaszek, and X. Marie. Fine structure and lifetime of dark excitons in transition metal dichalcogenide monolayers. *Phys. Rev. B*, 96:155423, Oct 2017.
- [10] Xiao-Xiao Zhang, Ting Cao, Zhengguang Lu, Yu-Chuan Lin, Fan Zhang, Ying Wang, Zhiqiang Li, James C Hone, Joshua A Robinson, Dmitry Smirnov, et al. Magnetic bright-

- ening and control of dark excitons in monolayer wse 2. *Nature nanotechnology*, 12(9):883, 2017.
- [11] You Zhou, Giovanni Scuri, Dominik S Wild, Alexander A High, Alan Dibos, Luis A Jau-regui, Chi Shu, Kristiaan De Greve, Kateryna Pistunova, Andrew Y Joe, et al. Probing dark excitons in atomically thin semiconductors via near-field coupling to surface plasmon polaritons. *Nature nanotechnology*, 12(9):856, 2017.
- [12] C. Robert, D. Lagarde, F. Cadiz, G. Wang, B. Lassagne, T. Amand, A. Balocchi, P. Renucci, S. Tongay, B. Urbaszek, and X. Marie. Exciton radiative lifetime in transition metal dichalcogenide monolayers. *Phys. Rev. B*, 93:205423, May 2016.
- [13] P. J. Zomer, M. H. D. Guimarães, J. C. Brant, N. Tombros, and B. J. van Wees. Fast pick up technique for high quality heterostructures of bilayer graphene and hexagonal boron nitride. *Appl. Phys. Lett.*, 105(1):013101, July 2014.
- [14] Wenjing Zhang, Chih-Piao Chuu, Jing-Kai Huang, Chang-Hsiao Chen, Meng-Lin Tsai, Yung-Huang Chang, Chi-Te Liang, Yu-Ze Chen, Yu-Lun Chueh, Jr-Hau He, Mei-Yin Chou, and Lain-Jong Li. Ultrahigh-Gain Photodetectors Based on Atomically Thin Graphene-MoS₂ Heterostructures. *Sci. Rep.*, 4, January 2014.
- [15] M Massicotte, P Schmidt, F Vialla, KG Schädler, A Reserbat-Plantey, K Watanabe, T Taniguchi, KJ Tielrooij, and FHL Koppens. Picosecond photoresponse in van der Waals heterostructures. *Nat. Nanotechnol.*, 11(1):42–46, 2016.
- [16] Xiaoze Liu, Tal Galfsky, Zheng Sun, Fengnian Xia, Erh-chen Lin, Yi-Hsien Lee, Stéphane Kéna-Cohen, and Vinod M Menon. Strong light-matter coupling in two-dimensional atomic crystals. *Nat. Photonics*, 9(1):30–34, 2015.
- [17] Su-Hyun Gong, Filippo Alpeggiani, Beniamino Sciacca, Erik C. Garnett, and L. Kuipers. Nanoscale chiral valley-photon interface through optical spin-orbit coupling. *Science*, 359(6374):443–447, 2018.
- [18] Thibault Chervy, Stefano Azzini, Etienne Lorchat, Shaojun Wang, Yuri Gorodetski, James A. Hutchison, Stéphane Berciaud, Thomas W. Ebbesen, and Cyriaque Genet. Room temperature chiral coupling of valley excitons with spin-momentum locked surface plasmons. *ACS Photonics*, page doi:10.1021/acsp Photonics.7b01032, 2018.
- [19] Cory R Dean, Andrea F Young, Inanc Meric, Chris Lee, Lei Wang, S Sorgenfrei, K Watanabe, T Taniguchi, P Kim, KL Shepard, et al. Boron nitride substrates for high-quality graphene electronics. *Nat. Nanotechnol.*, 5(10):722–726, 2010.
- [20] Jason S Ross, Sanfeng Wu, Hongyi Yu, Nirmal J Ghimire, Aaron M Jones, Grant Aivazian, Jiaqiang Yan, David G Mandrus, Di Xiao, Wang Yao, et al. Electrical control of neutral and charged excitons in a monolayer semiconductor. *Nat. Commun.*, 4:1474, 2013.

-
- [21] Frank Ceballos, Matthew Z Bellus, Hsin-Ying Chiu, and Hui Zhao. Ultrafast charge separation and indirect exciton formation in a MoS_2 – MoSe_2 van der Waals heterostructure. *ACS Nano*, 8(12):12717–12724, 2014.
- [22] Pasqual Rivera, John R Schaibley, Aaron M Jones, Jason S Ross, Sanfeng Wu, Grant Aivazian, Philip Klement, Kyle Seyler, Genevieve Clark, Nirmal J Ghimire, et al. Observation of long-lived interlayer excitons in monolayer MoSe_2 – WSe_2 heterostructures. *Nat. Commun.*, 6, 2015.
- [23] Ajit Srivastava, Meinrad Sidler, Adrien V Allain, Dominik S Lembke, Andras Kis, and Atac Imamoglu. Valley zeeman effect in elementary optical excitations of monolayer wse 2. *Nature Physics*, 11(2):141, 2015.
- [24] C. H. Lui, Zhipeng Ye, Chao Ji, Kuan-Chang Chiu, Cheng-Tse Chou, Trond I. Andersen, Casie Means-Shively, Heidi Anderson, Jenn-Ming Wu, Tim Kidd, Yi-Hsien Lee, and Rui He. Observation of interlayer phonon modes in van der waals heterostructures. *Phys. Rev. B*, 91:165403, Apr 2015.
- [25] Archana Raja, Andrey Chaves, Jaeun Yu, Ghidewon Arefe, Heather M. Hill, Albert F. Rigosi, Timothy C. Berkelbach, Philipp Nagler, Christian Schüller, Tobias Korn, Colin Nuckolls, James Hone, Louis E. Brus, Tony F. Heinz, David R. Reichman, and Alexey Chernikov. Coulomb engineering of the bandgap and excitons in two-dimensional materials. *Nature Communications*, 8:15251, 2017.
- [26] Masaru Onga, Yijin Zhang, Toshiya Ideue, and Yoshihiro Iwasa. Exciton hall effect in monolayer mos_2 . *Nature materials*, 16(12):1193, 2017.
- [27] G. Wang, C. Robert, M. M. Glazov, F. Cadiz, E. Courtade, T. Amand, D. Lagarde, T. Taniguchi, K. Watanabe, B. Urbaszek, and X. Marie. In-plane propagation of light in transition metal dichalcogenide monolayers: Optical selection rules. *Phys. Rev. Lett.*, 119:047401, Jul 2017.
- [28] Patrick Back, Sina Zeytinoglu, Aroosa Ijaz, Martin Kroner, and Atac Imamoglu. Realization of an electrically tunable narrow-bandwidth atomically thin mirror using monolayer mose_2 . *Phys. Rev. Lett.*, 120:037401, Jan 2018.
- [29] Branimir Radisavljevic, Aleksandra Radenovic, Jacopo Brivio, i V Giacometti, and A Kis. Single-layer mos_2 transistors. *Nature nanotechnology*, 6(3):147, 2011.
- [30] CR Dean, L Wang, P Maher, C Forsythe, F Ghahari, Y Gao, J Katoch, M Ishigami, P Moon, M Koshino, et al. Hofstadter’s butterfly and the fractal quantum hall effect in moire superlattices. *Nature*, 497(7451):598–602, 2013.
- [31] K. F. Mak, K. L. McGill, J. Park, and P. L. McEuen. The valley Hall effect in MoS_2 transistors. *Science*, 344(6191):1489–1492, June 2014.

- [32] Meng-Lin Tsai, Sheng-Han Su, Jan-Kai Chang, Dung-Sheng Tsai, Chang-Hsiao Chen, Chih-I Wu, Lain-Jong Li, Lih-Juann Chen, and Jr-Hau He. Monolayer mos_2 heterojunction solar cells. *ACS nano*, 8(8):8317–8322, 2014.
- [33] Chul-Ho Lee, Gwan-Hyoung Lee, Arend M. van der Zande, Wenchao Chen, Yilei Li, Minyong Han, Xu Cui, Ghidewon Arefe, Colin Nuckolls, Tony F. Heinz, Jing Guo, James Hone, and Philip Kim. Atomically thin p–n junctions with van der Waals heterointerfaces. *Nat. Nanotechnol.*, 9(9):676–681, September 2014.
- [34] F. Withers, O. Del Pozo-Zamudio, A. Mishchenko, A. P. Rooney, A. Gholinia, K. Watanabe, T. Taniguchi, S. J. Haigh, A. K. Geim, A. I. Tartakovskii, and K. S. Novoselov. Light-emitting diodes by band-structure engineering in van der Waals heterostructures. *Nat. Mater.*, 14(3):301, March 2015.
- [35] Wu Shi, Jianting Ye, Yijin Zhang, Ryuji Suzuki, Masaro Yoshida, Jun Miyazaki, Naoko Inoue, Yu Saito, and Yoshihiro Iwasa. Superconductivity series in transition metal dichalcogenides by ionic gating. *Scientific reports*, 5:12534, 2015.
- [36] Masaru Onga, Yijin Zhang, Ryuji Suzuki, and Yoshihiro Iwasa. High circular polarization in electroluminescence from mose_2 . *Applied Physics Letters*, 108(7):073107, 2016.
- [37] Ahmet Avsar, Dmitrii Unuchek, Jiawei Liu, Oriol Lopez Sanchez, Kenji Watanabe, Takashi Taniguchi, Barbaros Özyilmaz, and Andras Kis. Optospintronics in graphene via proximity coupling. *ACS Nano*, 11(11), 2017.
- [38] Zheng Sun, Jie Gu, Areg Ghazaryan, Zav Shotan, Christopher R. Consideine, Michael Dollar, Biswanath Chakraborty, Xiaoze Liu, Pouyan Ghaemi, Stéphane Kéna-Cohen, and Vinod M. Menon. Optical control of room-temperature valley polaritons. *Nature Photonics*, 11:491, July 2017.
- [39] A. H. Castro Neto, F. Guinea, N. M. R. Peres, K. S. Novoselov, and A. K. Geim. The electronic properties of graphene. *Rev. Mod. Phys.*, 81:109–162, Jan 2009.
- [40] A. K. Geim and K. S. Novoselov. The rise of graphene. *Nat. Mater.*, 6:183–191, Mar 2007.
- [41] Z. Q. Li, E. A. Henriksen, Z. Jiang, Z. Hao, M. C. Martin, P. Kim, H. L. Stormer, and D. N. Basov. Dirac charge dynamics in graphene by infrared spectroscopy. *Nat. Phys.*, 4(7):532–535, July 2008.
- [42] Rahul Raveendran Nair, Peter Blake, Alexander N Grigorenko, Konstantin S Novoselov, Tim J Booth, Tobias Stauber, Nuno MR Peres, and Andre K Geim. Fine structure constant defines visual transparency of graphene. *Science*, 320(5881):1308–1308, 2008.
- [43] Marcos H. D. Guimarães, Hui Gao, Yimo Han, Kibum Kang, Saien Xie, Cheol-Joo Kim, David A. Muller, Daniel C. Ralph, and Jiwoong Park. Atomically thin ohmic edge contacts between two-dimensional materials. *ACS Nano*, 10(6):6392–6399, 2016. PMID: 27299957.

-
- [44] Marius Eich, Riccardo Pisoni, Hiske Overweg, Annika Kurzmann, Yongjin Lee, Peter Rickhaus, Thomas Ihn, Klaus Ensslin, František Herman, Manfred Sigrist, Kenji Watanabe, and Takashi Taniguchi. Spin and valley states in gate-defined bilayer graphene quantum dots. *Phys. Rev. X*, 8:031023, Jul 2018.
- [45] Rajesh Koppera, Damien Voiry, Sibel Ebru Yalcin, Brittany Branch, Gautam Gupta, Aditya D. Mohite, and Manish Chhowalla. Phase-engineered low-resistance contacts for ultrathin MoS₂ transistors. *Nat. Mater.*, 13(12):1128–1134, December 2014.
- [46] Andor Kormányos, Viktor Zólyomi, Neil D. Drummond, and Guido Burkard. Spin-orbit coupling, quantum dots, and qubits in monolayer transition metal dichalcogenides. *Phys. Rev. X*, 4:011034, Mar 2014.
- [47] Maciej Koperski, Maciej R Molas, Ashish Arora, Karol Nogajewski, Artur O Slobodeniuk, Clement Faugeras, and Marek Potemski. Optical properties of atomically thin transition metal dichalcogenides: observations and puzzles. *Nanophotonics*, 6(6):1289–1308, 2017.
- [48] K. Kośmider, J. W. González, and J. Fernández-Rossier. Large spin splitting in the conduction band of transition metal dichalcogenide monolayers. *Phys. Rev. B*, 88:245436, Dec 2013.
- [49] M R Molas, C Faugeras, A O Slobodeniuk, K Nogajewski, M Bartos, D M Basko, and M Potemski. Brightening of dark excitons in monolayers of semiconducting transition metal dichalcogenides. *2D Materials*, 4(2):021003, 2017.
- [50] Yilei Li, Alexey Chernikov, Xian Zhang, Albert Rigosi, Heather M. Hill, Arend M. van der Zande, Daniel A. Chenet, En-Min Shih, James Hone, and Tony F. Heinz. Measurement of the optical dielectric function of monolayer transition-metal dichalcogenides: MoS₂, MoSe₂, WS₂, and WSe₂. *Phys. Rev. B*, 90:205422, Nov 2014.
- [51] Giovanni Scuri, You Zhou, Alexander A. High, Dominik S. Wild, Chi Shu, Kristiaan De Greve, Luis A. Jauregui, Takashi Taniguchi, Kenji Watanabe, Philip Kim, Mikhail D. Lukin, and Hongkun Park. Large excitonic reflectivity of monolayer mose₂ encapsulated in hexagonal boron nitride. *Phys. Rev. Lett.*, 120:037402, Jan 2018.
- [52] Jessica Lindlau, Cedric Robert, Victor Funk, Jonathan Förste, Michael Förg, Léo Colombier, Andre Neumann, Emmanuel Courtade, Shivangi Shree, Takashi Taniguchi, et al. Identifying optical signatures of momentum-dark excitons in transition metal dichalcogenide monolayers. *arXiv preprint arXiv:1710.00988*, 2017.
- [53] Jessica Lindlau, Malte Selig, Andre Neumann, Léo Colombier, Jonathan Förste, Victor Funk, Michael Förg, Jonghwan Kim, Gunnar Berghäuser, Takashi Taniguchi, et al. The role of momentum-dark excitons in the elementary optical response of bilayer wse₂. *Nature communications*, 9(1):2586, 2018.

- [54] H Yanagisawa, T Tanaka, Y Ishida, M Matsue, E Rokuta, S Otani, and C Oshima. Analysis of phonons in graphene sheets by means of hreels measurement and ab initio calculation. *Surf. Interface Anal.*, 37(2):133–136, 2005.
- [55] Dominik Metten, François Federspiel, Michelangelo Romeo, and Stéphane Berciaud. All-optical blister test of suspended graphene using micro-Raman spectroscopy. *Phys. Rev. Appl.*, 2:054008, Nov 2014.
- [56] Guillaume Froehlicher and Stéphane Berciaud. Raman spectroscopy of electrochemically gated graphene transistors: Geometrical capacitance, electron-phonon, electron-electron, and electron-defect scattering. *Phys. Rev. B*, 91:205413, May 2015.
- [57] Bo Peng, Hao Zhang, Hezhu Shao, Yuchen Xu, Xiangchao Zhang, and Heyuan Zhu. Thermal conductivity of monolayer mos₂, mose₂, and ws₂: interplay of mass effect, interatomic bonding and anharmonicity. *RSC Advances*, 6(7):5767–5773, 2016.
- [58] R. Loudon. The raman effect in crystals. *Adv. Phys.*, 13:423, 1964.
- [59] Mildred S Dresselhaus, Gene Dresselhaus, and Ado Jorio. *Group theory: application to the physics of condensed matter*. Springer Science & Business Media, 2007.
- [60] Andrea C. Ferrari and Denis M. Basko. Raman spectroscopy as a versatile tool for studying the properties of graphene. *Nat. Nanotechnol.*, 8(4):235–246, April 2013.
- [61] Simone Pisana, Michele Lazzeri, Cinzia Casiraghi, Kostya S. Novoselov, A. K. Geim, Andrea C. Ferrari, and Francesco Mauri. Breakdown of the adiabatic born-oppenheimer approximation in graphene. *Nat. Mater.*, 6(3):198–201, March 2007.
- [62] Michele Lazzeri and Francesco Mauri. Nonadiabatic kohn anomaly in a doped graphene monolayer. *Phys. Rev. Lett.*, 97(26):266407, December 2006.
- [63] Jun Yan, Yuanbo Zhang, Philip Kim, and Aron Pinczuk. Electric field effect tuning of electron-phonon coupling in graphene. *Phys. Rev. Lett.*, 98(16):166802, April 2007.
- [64] A. Das, S. Pisana, B. Chakraborty, S. Piscanec, S. K. Saha, U. V. Waghmare, K. S. Novoselov, H. R. Krishnamurthy, A. K. Geim, A. C. Ferrari, and A. K. Sood. Monitoring dopants by Raman scattering in an electrochemically top-gated graphene transistor. *Nat. Nanotechnol.*, 3(4):210–215, April 2008.
- [65] Guillaume Froehlicher, Etienne Lorchat, François Fernique, Chaitanya Joshi, Alejandro Molina-Sánchez, Ludger Wirtz, and Stéphane Berciaud. Unified description of the optical phonon modes in N -layer MoTe₂. *Nano Lett.*, 15(10):6481–6489, 2015.
- [66] Bastian Miller, Eric Parzinger, Anna Vernickel, Alexander W Holleitner, and Ursula Wurstbauer. Photogating of mono-and few-layer MoS₂. *Appl. Phys. Lett.*, 106(12):122103, 2015.
- [67] Biswanath Chakraborty, Achintya Bera, D. V. S. Muthu, Somnath Bhowmick, U. V. Waghmare, and A. K. Sood. Symmetry-dependent phonon renormalization in monolayer MoS₂ transistor. *Phys. Rev. B*, 85(16):161403, April 2012.

-
- [68] Hartmut Haug and Stephan W Koch. *Quantum Theory of the Optical and Electronic Properties of Semiconductors: Third Edition*. World Scientific Publishing Company, 1994.
- [69] Timothy C. Berkelbach, Mark S. Hybertsen, and David R. Reichman. Theory of neutral and charged excitons in monolayer transition metal dichalcogenides. *Phys. Rev. B*, 88:045318, Jul 2013.
- [70] A. Molina-Sánchez and L. Wirtz. Phonons in single-layer and few-layer MoS₂ and WS₂. *Phys. Rev. B*, 84(15):155413, October 2011.
- [71] JS Blakemore. Semiconducting and other major properties of gallium arsenide. *Journal of Applied Physics*, 53(10):R123–R181, 1982.
- [72] Heather M Hill, Albert F Rigosi, Cyrielle Roquelet, Alexey Chernikov, Timothy C Berkelbach, David R Reichman, Mark S Hybertsen, Louis E Brus, and Tony F Heinz. Observation of excitonic rydberg states in monolayer mos₂ and ws₂ by photoluminescence excitation spectroscopy. *Nano letters*, 15(5):2992–2997, 2015.
- [73] LV Keldysh. Coulomb interaction in thin semiconductor and semimetal films. *Soviet Journal of Experimental and Theoretical Physics Letters*, 29:658, 1979.
- [74] B. Han, C. Robert, E. Courtade, M. Manca, S. Shree, T. Amand, P. Renucci, T. Taniguchi, K. Watanabe, X. Marie, L. E. Golub, M. M. Glazov, and B. Urbaszek. Exciton states in monolayer mose₂ and mote₂ probed by upconversion spectroscopy. *Phys. Rev. X*, 8:031073, Sep 2018.
- [75] Liang Wang, Yayun Pu, Ai Kah Soh, Yuping Shi, and Shuangyi Liu. Layers dependent dielectric properties of two dimensional hexagonal boron nitridenanosheets. *AIP Advances*, 6(12):125126, 2016.
- [76] Matteo Barbone, Alejandro R-P Montblanch, Dhiren M Kara, Carmen Palacios-Berraquero, Alisson R Cadore, Domenico De Fazio, Benjamin Pingault, Elaheh Mostaani, Han Li, Bin Chen, et al. Charge-tuneable biexciton complexes in monolayer wse₂. *Nature Communications*, 2018.
- [77] Philipp Steinleitner, Philipp Merkl, Philipp Nagler, Joshua Mornhinweg, Christian Schüller, Tobias Korn, Alexey Chernikov, and Rupert Huber. Direct observation of ultrafast exciton formation in a monolayer of wse₂. *Nano Letters*, 17(3):1455–1460, 2017.
- [78] Tobias Korn, Stefanie Heydrich, Michael Hirmer, Johannes Schmutzler, and Christian Schüller. Low-temperature photocarrier dynamics in monolayer mos₂. *Appl. Phys. Lett.*, 99(10):102109, 2011.
- [79] H. H. Fang, B. Han, C. Robert, M. A. Semina, D. Lagarde, E. Courtade, T. Taniguchi, K. Watanabe, T. Amand, B. Urbaszek, M. M. Glazov, and X. Marie. Control of the exciton radiative lifetime in van der waals heterostructures. *arXiv preprint arXiv:1902.00670*, 2019.

- [80] Marvin Kulig, Jonas Zipfel, Philipp Nagler, Sofia Blanter, Christian Schüller, Tobias Korn, Nicola Paradiso, Mikhail M. Glazov, and Alexey Chernikov. Exciton diffusion and halo effects in monolayer semiconductors. *Phys. Rev. Lett.*, 120:207401, May 2018.
- [81] Gui-Bin Liu, Di Xiao, Yugui Yao, Xiaodong Xu, and Wang Yao. Electronic structures and theoretical modelling of two-dimensional group-vib transition metal dichalcogenides. *Chemical Society Reviews*, 44(9):2643–2663, 2015.
- [82] G. Sallen, L. Bouet, X. Marie, G. Wang, C. R. Zhu, W. P. Han, Y. Lu, P. H. Tan, T. Amand, B. L. Liu, and B. Urbaszek. Robust optical emission polarization in MoS₂ monolayers through selective valley excitation. *Phys. Rev. B*, 86:081301, Aug 2012.
- [83] Bairen Zhu, Hualing Zeng, Junfeng Dai, Zhirui Gong, and Xiaodong Cui. Anomalously robust valley polarization and valley coherence in bilayer ws₂. *Proceedings of the National Academy of Sciences*, 111(32):11606–11611, 2014.
- [84] Qihang Liu, Xiuwen Zhang, and Alex Zunger. Intrinsic Circular Polarization in Centrosymmetric Stacks of Transition-Metal Dichalcogenide Compounds. *Phys. Rev. Lett.*, 114(8):087402, February 2015.
- [85] M. Z. Maialle, E. A. de Andrada e Silva, and L. J. Sham. Exciton spin dynamics in quantum wells. *Phys. Rev. B*, 47:15776–15788, Jun 1993.
- [86] Gang Wang, Alexey Chernikov, Mikhail M. Glazov, Tony F. Heinz, Xavier Marie, Thierry Amand, and Bernhard Urbaszek. Colloquium: Excitons in atomically thin transition metal dichalcogenides. *Rev. Mod. Phys.*, 90:021001, Apr 2018.
- [87] Kin Fai Mak, Keliang He, Jie Shan, and Tony F Heinz. Control of valley polarization in monolayer MoS₂ by optical helicity. *Nat. Nanotechnol.*, 7(8):494–498, 2012.
- [88] Aaron M Jones, Hongyi Yu, Nirmal J Ghimire, Sanfeng Wu, Grant Aivazian, Jason S Ross, Bo Zhao, Jiaqiang Yan, David G Mandrus, Di Xiao, , W Yao, and X Xu. Optical generation of excitonic valley coherence in monolayer WSe₂. *Nat. Nanotechnol.*, 8(9):634–638, 2013.
- [89] Ting Cao, Gang Wang, Wenpeng Han, Huiqi Ye, Chuanrui Zhu, Junren Shi, Qian Niu, Pingheng Tan, Enge Wang, Baoli Liu, and Ji Feng. Valley-selective circular dichroism of monolayer molybdenum disulphide. *Nature Communications*, 3:887, Jun 2012.
- [90] Hualing Zeng, Junfeng Dai, Wang Yao, Di Xiao, and Xiaodong Cui. Valley polarization in mos₂ monolayers by optical pumping. *Nature nanotechnology*, 7(8):490–493, 2012.
- [91] G. Wang, E. Palleau, T. Amand, S. Tongay, X. Marie, and B. Urbaszek. Polarization and time-resolved photoluminescence spectroscopy of excitons in MoSe₂ monolayers. *Appl. Phys. Lett.*, 106(11), 2015.
- [92] Ashish Arora, Robert Schmidt, Robert Schneider, Maciej R Molas, Ivan Breslavetz, Marek Potemski, and Rudolf Bratschitsch. Valley zeeman splitting and valley polarization of

- neutral and charged excitons in monolayer MoS_2 at high magnetic fields. *Nano letters*, 16(6):3624–3629, 2016.
- [93] D. Lagarde, L. Bouet, X. Marie, C. R. Zhu, B. L. Liu, T. Amand, P. H. Tan, and B. Urbaszek. Carrier and polarization dynamics in monolayer MoS_2 . *Phys. Rev. Lett.*, 112:047401, Jan 2014.
- [94] Kathleen M. McCreary, Marc Currie, Aubrey T. Hanbicki, Hsun-Jen Chuang, and Berend T. Jonker. Understanding variations in circularly polarized photoluminescence in monolayer transition metal dichalcogenides. *ACS Nano*, 11(8):7988–7994, 2017.
- [95] Kenji Watanabe, Takashi Taniguchi, and Hisao Kanda. Direct-bandgap properties and evidence for ultraviolet lasing of hexagonal boron nitride single crystal. *Nature materials*, 3(6):404, 2004.
- [96] Akash Laturia, Maarten L Van de Put, and William G Vandenberghe. Dielectric properties of hexagonal boron nitride and transition metal dichalcogenides: from monolayer to bulk. *npj 2D Materials and Applications*, 2(1):6, 2018.
- [97] Yuan Cao, Valla Fatemi, Shiang Fang, Kenji Watanabe, Takashi Taniguchi, Efthimios Kaxiras, and Pablo Jarillo-Herrero. Unconventional superconductivity in magic-angle graphene superlattices. *Nature*, 556(7699):43, 2018.
- [98] Filippo Pizzocchero, Lene Gammelgaard, Bjarke S. Jessen, José M. Caridad, Lei Wang, James Hone, Peter Bøggild, and Timothy J. Booth. The hot pick-up technique for batch assembly of van der Waals heterostructures. *Nat. Commun.*, 7:11894, 2016.
- [99] KS Novoselov, A Mishchenko, A Carvalho, and AH Castro Neto. 2D materials and van der Waals heterostructures. *Science*, 353(6298):aac9439, 2016.
- [100] K. I. Bolotin, K. J. Sikes, J. Hone, H. L. Stormer, and P. Kim. Temperature-dependent transport in suspended graphene. *Phys. Rev. Lett.*, 101:096802, Aug 2008.
- [101] L Wang, I Meric, PY Huang, Q Gao, Y Gao, H Tran, T Taniguchi, K Watanabe, LM Campos, DA Muller, et al. One-dimensional electrical contact to a two-dimensional material. *Science*, 342(6158):614–617, 2013.
- [102] Cheng Gong, Hengji Zhang, Weihua Wang, Luigi Colombo, Robert M. Wallace, and Kyeongjae Cho. Band alignment of two-dimensional transition metal dichalcogenides: Application in tunnel field effect transistors. *Appl. Phys. Lett.*, 103(5):053513, 2013.
- [103] Young-Jun Yu, Yue Zhao, Sunmin Ryu, Louis E Brus, Kwang S Kim, and Philip Kim. Tuning the graphene work function by electric field effect. *Nano Lett.*, 9(10):3430–3434, 2009.
- [104] Pramoda K Nayak, Yevhen Horbatenko, Seongjoon Ahn, Gwangwoo Kim, Jae-Ung Lee, Kyung Yeol Ma, A-Rang Jang, Hyunseob Lim, Dogyeong Kim, Sunmin Ryu, et al. Probing

- evolution of twist-angle-dependent interlayer excitons in $\text{mose}_2/\text{wse}_2$ van der waals heterostructures. *ACS nano*, 11(4):4041–4050, 2017.
- [105] Haiming Zhu, Jue Wang, Zizhou Gong, Young Duck Kim, Martin Gustafsson, James Hone, and Xiaoyang Zhu. Interfacial charge transfer circumventing momentum mismatch at 2D van der Waals heterojunctions. *arXiv preprint arXiv:1702.06366*, 2017.
- [106] Daichi Kozawa, Alexandra Carvalho, Ivan Verzhbitskiy, Francesco Giustiniano, Yuhei Miyauchi, Shinichiro Mouri, AH Castro Neto, Kazunari Matsuda, and Goki Eda. Evidence for fast interlayer energy transfer in $\text{MoSe}_2/\text{WS}_2$ heterostructures. *Nano Lett.*, 2016.
- [107] François Federspiel, Guillaume Froehlicher, Michel Nasilowski, Silvia Pedetti, Ather Mahmood, Bernard Doudin, Serin Park, Jeong-O Lee, David Halley, Benoît Dubertret, et al. Distance dependence of the energy transfer rate from a single semiconductor nanostructure to graphene. *Nano Lett.*, 15(2):1252–1258, 2015.
- [108] Guillaume Froehlicher, Etienne Lorchat, and Stéphane Berciaud. Charge versus energy transfer in atomically thin graphene-transition metal dichalcogenide van der waals heterostructures. *Phys. Rev. X*, 8:011007, Jan 2018.
- [109] Malte Selig, Ermin Malic, Kwang Jun Ahn, Norbert Koch, and Andreas Knorr. Theory of optically induced förster coupling in van der waals coupled heterostructures. *Phys. Rev. B*, 99:035420, Jan 2019.
- [110] Jiaqi He, Nardeep Kumar, Matthew Z Bellus, Hsin-Ying Chiu, Dawei He, Yongsheng Wang, and Hui Zhao. Electron transfer and coupling in graphene–tungsten disulfide van der Waals heterostructures. *Nat. Commun.*, 5, 2014.
- [111] Long Yuan, Ting-Fung Chung, Agnieszka Kuc, Yan Wan, Yang Xu, Yong P. Chen, Thomas Heine, and Libai Huang. Photocarrier generation from interlayer charge-transfer transitions in ws_2 -graphene heterostructures. *Science Advances*, 4(2):e1700324, 2018.
- [112] Etienne Lorchat, Stefano Azzini, Thibault Chervy, Takashi Taniguchi, Kenji Watanabe, Thomas W Ebbesen, Cyriaque Genet, and Stéphane Berciaud. Room-temperature valley polarization and coherence in transition metal dichalcogenide–graphene van der waals heterostructures. *ACS Photonics*, 5(12):5047–5054, 2018.
- [113] Kallol Roy, Medini Padmanabhan, Srijit Goswami, T. Phanindra Sai, Sanjeev Kaushal, and Arindam Ghosh. Optically active heterostructures of graphene and ultrathin MoS_2 . *Solid State Commun.*, 175–176:35–42, December 2013.
- [114] Ermin Malic, Heiko Appel, Oliver T Hofmann, and Angel Rubio. Förster-induced energy transfer in functionalized graphene. *The Journal of Physical Chemistry C*, 118(17):9283–9289, 2014.
- [115] Archana Raja, Andrés Montoya-Castillo, Johanna Zultak, Xiao-Xiao Zhang, Ziliang Ye, Cyrielle Roquelet, Daniel A Chenet, Arend M van der Zande, Pinshane Huang, Steffen

- Jockusch, et al. Energy transfer from quantum dots to graphene and MoS₂: The role of absorption and screening in two-dimensional materials. *Nano Lett.*, 16(4):2328–2333, 2016.
- [116] D. L. Mafra, G. Samsonidze, L. M. Malard, D. C. Elias, J. C. Brant, F. Plentz, E. S. Alves, and M. A. Pimenta. Determination of Γ and π phonon dispersion relations of graphene near the dirac point by double resonance raman scattering. *Phys. Rev. B*, 76:233407, Dec 2007.
- [117] F. Forster, A. Molina-Sanchez, S. Engels, A. Epping, K. Watanabe, T. Taniguchi, L. Wirtz, and C. Stampfer. Dielectric screening of the Kohn anomaly of graphene on hexagonal boron nitride. *Phys. Rev. B*, 88:085419, Aug 2013.
- [118] Stéphane Berciaud, Sunmin Ryu, Louis E. Brus, and Tony F. Heinz. Probing the intrinsic properties of exfoliated graphene: Raman spectroscopy of free-standing monolayers. *Nano Lett.*, 9(1):346–352, 2008.
- [119] Christoph Neumann, Luca Banszerus, Michael Schmitz, Sven Reichardt, Jens Sonntag, Takashi Taniguchi, Kenji Watanabe, Bernd Beschoten, and Christoph Stampfer. Line shape of the raman 2d peak of graphene in van der waals heterostructures. *physica status solidi (b)*, 253(12):2326–2330, 2016.
- [120] Sunmin Ryu, Li Liu, Stéphane Berciaud, Young-Jun Yu, Haitao Liu, Philip Kim, George W. Flynn, and Louis E. Brus. Atmospheric oxygen binding and hole doping in deformed graphene on a SiO₂ substrate. *Nano Lett.*, 10(12):4944–4951, 2010.
- [121] Axel Eckmann, Alexandre Felten, Ivan Verzhbitskiy, Rebecca Davey, and Cinzia Casiraghi. Raman study on defective graphene: Effect of the excitation energy, type, and amount of defects. *Phys. Rev. B*, 88(3):035426, July 2013.
- [122] Duoming Wang, Guorui Chen, Chaokai Li, Meng Cheng, Wei Yang, Shuang Wu, Guibai Xie, Jing Zhang, Jing Zhao, Xiaobo Lu, Peng Chen, Guole Wang, Jianling Meng, Jian Tang, Rong Yang, Congli He, Donghua Liu, Dongxia Shi, Kenji Watanabe, Takashi Taniguchi, Ji Feng, Yuanbo Zhang, and Guangyu Zhang. Thermally induced graphene rotation on hexagonal boron nitride. *Phys. Rev. Lett.*, 116:126101, Mar 2016.
- [123] Biswanath Chakraborty, HSS Matte, AK Sood, and CNR Rao. Layer-dependent resonant raman scattering of a few layer mos₂. *J. Raman Spectrosc.*, 44(1):92–96, 2013.
- [124] M Currie, AT Hanbicki, G Kioseoglou, and BT Jonker. Optical control of charged exciton states in tungsten disulfide. *Applied Physics Letters*, 106(20):201907, 2015.
- [125] M. M. Glazov, E. L. Ivchenko, G. Wang, T. Amand, X. Marie, B. Urbaszek, and B. L. Liu. Spin and valley dynamics of excitons in transition metal dichalcogenide monolayers. *physica status solidi (b)*, 252(11):2349–2362, 2015.
- [126] Yen-Jung Chen, Jeffrey D. Cain, Teodor K. Stanev, Vinayak P. Dravid, and Nathaniel P. Stern. Valley-polarized exciton-polaritons in a monolayer semiconductor. *Nature Photonics*, 11:431, Jun 2017.

- [127] N. Lundt, S. Stoll, P. Nagler, A. Nalitov, S. Klemmt, S. Betzold, J. Goddard, E. Frieling, A. V. Kavokin, C. Schüller, T. Korn, S. Höfling, and C. Schneider. Observation of macroscopic valley-polarized monolayer exciton-polaritons at room temperature. *Phys. Rev. B*, 96:241403, Dec 2017.
- [128] F Le Roy-Brehonnet and B Le Jeune. Utilization of mueller matrix formalism to obtain optical targets depolarization and polarization properties. *Progress in Quantum Electronics*, 21(2):109–151, 1997.
- [129] Alejandro Molina-Sánchez, Davide Sangalli, Ludger Wirtz, and Andrea Marini. Ab initio calculations of ultrashort carrier dynamics in two-dimensional materials: Valley depolarization in single-layer WSe₂. *Nano Letters*, 17(8):4549–4555, 2017.
- [130] Ayse Berkdemir, Humberto R. Gutiérrez, Andrés R. Botello-Méndez, Néstor Perea-López, Ana Laura Elías, Chen-Ing Chia, Bei Wang, Vincent H. Crespi, Florentino López-Urías, Jean-Christophe Charlier, Humberto Terrones, and Mauricio Terrones. Identification of individual and few layers of WS₂ using raman spectroscopy. *Scientific Reports*, 3:1755, 2013.
- [131] Immo Söllner, Sahand Mahmoodian, Sofie Lindskov Hansen, Leonardo Midolo, Alisa Javadi, Gabija Kiršanskė, Tommaso Pregnolato, Haitham El-Ella, Eun Hye Lee, Jin Dong Song, et al. Deterministic photon-emitter coupling in chiral photonic circuits. *Nature nanotechnology*, 10(9):775, 2015.
- [132] Peter Lodahl, Sahand Mahmoodian, Søren Stobbe, Arno Rauschenbeutel, Philipp Schneeweiss, Jürgen Volz, Hannes Pichler, and Peter Zoller. Chiral quantum optics. *Nature*, 541(7638):473, 2017.
- [133] Lukas Novotny and Bert Hecht. *Principles of nano-optics*. Cambridge university press, 2012.
- [134] Yunqiu Kelly Luo, Jinsong Xu, Tiancong Zhu, Guanzhong Wu, Elizabeth J. McCormick, Wenbo Zhan, Mahesh R. Neupane, and Roland K. Kawakami. Opto-valleytronic spin injection in monolayer MoS₂/few-layer graphene hybrid spin valves. *Nano Letters*, 17(6):3877–3883, 2017.
- [135] Eugene Hecht. *Optics (4th Edition)*. Addison-Wesley, 2001.

Optical spectroscopy of heterostructures based on atomically-thin semiconductors

Résumé

Au cours de cette thèse, nous avons fabriqué et étudié par spectroscopie optique, des hétérostructures de van der Waals, composées de monofeuillets semi-conducteurs (dichalcogénures de métaux de transition, DMT) couplés à une monocouche de graphène ou à un résonateur plasmonique. Nous avons observé des modifications importantes de la dynamique des états excités optiquement dans le DMT (excitons) lorsque celui-ci est en contact avec le graphène. Le graphène neutralise la couche de DMT et permet un transfert non-radiatif d'excitons en moins de quelques picosecondes. Ce transfert d'énergie peut s'accompagner d'un photodopage extrinsèque considérablement moins efficace. La réduction de la durée de vie des excitons du DMT en présence de graphène a été exploitée pour montrer que leur pseudo-spin de vallée maintient un degré de polarisation et de cohérence important jusqu'à température ambiante. Enfin, en couplant fortement les excitons d'un DMT aux modes d'un résonateur plasmonique à phase géométrique, nous avons mis en évidence, à température ambiante, le verrouillage du pseudo-spin de vallée sur la direction de propagation des polaritons chiraux (chiralitons) issus du couplage.

Mots clés : Matériaux 2D, spectroscopie optique, exciton, hétérostructures de Van der Waals

Résumé en anglais

During this thesis, we have fabricated and studied by optical spectroscopy, van der Waals heterostructures composed of semiconductor monolayers (transition metal dichalcogenides, TMD) coupled to a graphene monolayer or to a plasmonic resonator. We have observed significant changes in the dynamics of the TMD optically excited states (excitons) when it is in direct contact with graphene. Graphene neutralizes the TMD monolayer and enables non-radiative transfer of excitons within less than a few picoseconds. This energy transfer process may be accompanied by a considerably less efficient, extrinsic photodoping. The reduced lifetime of TMD excitons in the presence of graphene has been exploited to show that their valley pseudo-spin maintains a high degree of polarization and coherence up to room temperature. Finally, by strongly coupling TMD excitons to the modes of a geometric phase plasmonic resonator, we have demonstrated, at room temperature, that the momentum of the resulting chiral polaritons (chiralitons) is locked to their valley pseudo-spin.

Keywords : 2D materials, optical spectroscopy, exciton, van der Waals heterostructures